The University Of Sheffield.

The spatiotemporal coherence as an indicator of the stability in swirling flows

By:

Oscar Farias Moguel

A thesis submitted in partial fulfilment of the requirements for the degree of Doctor of Philosophy

The University of Sheffield
Faculty of Engineering
Department of Mechanical Engineering

September 2018

The candidate confirms that the work submitted is his own, except where work, which has formed part of jointly authored publications, has been included. The contribution of the candidate and the other authors to this work has been explicitly indicated below. The candidate confirms that appropriate credit has been given within the thesis where reference has been made to the work of others.

The work in Chapter 4 of this thesis is based on the following publication:

O. Farias Moguel, J. Szuhánszki, A.G. Clements, D.B. Ingham, L. Ma, M. Pourkashanian, "Oscillating coal and biomass flames: A spectral and digital imaging approach for air and oxyfuel condition", Fuel Processing Technology, Volume 173, 2018, Pages 243-252.

The implementation of the Sigma SGS model employed in Chapter 5 and 6 and the FSCK model for the calculation of the absorption coefficient in the gas phase used in Chapter 6 were carried out by Dr. Alastair G. Clements. Credits for the experimental data employed to validate the numerical calculations have been given in Chapter 6 by citing the relevant publications.

Acknowledgements

I would like to express my gratitude to my supervisors Prof. Mohamed Pourkashanian, Prof. Derek B. Ingham and Prof. Lin Ma for giving me the opportunity to conduct my studies at the Energy 2050 group, but most importantly for the confidence placed on me to successfully accomplish this piece of research.

I would also like to acknowledge Dr. Alastair G. Clements for his guidance and constant inspiration during my studies. His contributions were crucial at many stages of my research and allowed me to develop the desire to always pursuit excellence.

In addition, I would like to thank the assistance provided by Dr. Janos Szuhánszki throughout this research. His motivation and endless patience made the long days of the experimental campaigns a joyful experience.

I would like to thank to the staff and fellow PhD students of the Energy 2050 group for lighten my time at Sheffield and for providing me a place to share the vicissitudes of this stage in my life.

Furthermore, I would like to express my eternal gratitude to my family for always providing me the support required to carry on with this endeavour and for all the sacrifices they had made during this time. Their presence was paramount to fully enjoy the achievements and to obtain the necessary encouragement while in my time of need.

Finally, I would like to acknowledge the National Council for Science and Technology (CONACyT) in Mexico for funding my studies

Abstract

Combustion has played a key role in the development of human society; it has driven the evolution in the manufacturing processes, transportation, and it is used to produce the vast majority of the global energy consumed. The emission of pollutants from the combustion of fossil fuels in power plants lead to the development of advanced clean energy technologies, such as carbon capture and storage. Oxyfuel combustion is part of the carbon capture and storage techniques, and consists in the replacement of the air as oxidiser in the reaction with a mixture of oxygen and recycled flue gas, thus allowing a rich CO_2 outflow stream that can subsequently be compressed, transported and safely stored.

The number of phenomena in combustion that are inherently dynamic impede the convention of a unique conception of flame stability. However, the quantification of the flow repeatability can produce insights on the efficiency of the process. This thesis presents the assessment of the stability in swirling flows through the calculation of their spatiotemporal coherence. The experimental data obtained from a 250 kW_{th} combustor allows the assessment of the flame by means of spectral and oscillation severity analyses. A similar methodology is developed to analyse the data from large eddy simulations. The spectral analysis, the proper orthogonal decomposition and the dynamic mode decomposition have been employed to account for the temporal, spatial and spatiotemporal coherence of the flow, respectively. The spatiotemporal coherence is employed as a comprehensive term for the characterisation of the dynamic behaviour in the swirling flows and as a measurable indicator of the stability. This concept can be incorporated into the design of novel combustion technologies that will lead into a sustained reduction in pollutants and to the mitigation of the noxious effects associated to them.

Table of contents

Acknowledgements i
Abstract iii
Table of contents v
List of figures ix
List of tables xvi
1. Introduction 1
1.1. Global warming and climate change 2
1.2. Power generation using coal 3
1.3. Carbon capture and storage technologies 5
1.3.1. Pre-combustion capture 5
1.3.2. Post-combustion capture 6
1.3.3. Oxyfuel combustion 6
1.4. Flame stability and coherence 8
1.5. Modelling of coal combustion 9
1.6. Aims and objectives 11
1.7. Thesis outline 12
2. Literature review 13
2.1. Computational fluid dynamics modelling for coal combustion 13
2.1.1. Governing equations 14
2.1.2. Turbulence simulation 17
2.1.2.1. The Reynolds-averaged Navier-Stokes approach 23
2.1.2.2. The large eddy simulation approach 28
2.1.3. Combustion modelling in coal particles 37
2.1.3.1. Particle dynamics 37
2.1.3.2. Particle combustion 39
2.1.3.2.1. Moisture evaporation and devolatilisation 40
2.1.3.2.2. Combustion of volatiles 42
2.1.3.2.3. Combustion of char 46
2.1.4. Radiative heat transfer 52
2.1.4.1. Radiative heat transfer in a participating medium 52
2.1.4.2. Radiative heat transfer in particles 60
2.2. Spatial and temporal coherence assessment 62
2.2.1. Spectral analysis and signal correlations 62
2.2.2. The proper orthogonal decomposition 70
2.2.3. The dynamic mode decomposition 73
2.3. Summary 77

3. Experimental facilities and data collection 79
3.1. Introduction 79
3.2. 250 kW Combustion Test Facility 79
3.2.1. Coal burner 79
3.2.2. Furnace 81
3.2.3. Oxidiser and fuel supply system 83
3.2.4. Experimental capabilities 86
3.2.4.1. Gas analysis 86
3.2.4.2. Temperature measurements 88
3.2.4.3. Heat flux measurements 88
3.2.4.4. Flame imaging 88
3.2.5. Conditions analysed 89
3.3. Isothermal swirling flow apparatus 90
3.3.1. Swirling flow duct 91
3.3.2. Water inlet plenum and swirler arrangement 91
3.3.3. Flow visualization techniques 92
3.3.4. Flow conditions reported 93
3.4. Summary 94
4. Spectral and digital imaging analysis of coal flames 96
4.1. Experimental set-up 96
4.2. Methodology 98
4.2.1. Digital luminance 100
4.2.2. The two colour pyrometer 101
4.2.3. Temporal coherence 102
4.2.4. The oscillation severity index 103
4.3. Spectral analysis 107
4.3.1. Full flame region 108
4.3.2. Near burner region 111
4.4. Oscillation severity analysis 113
4.4.1. Full flame region 113
4.4.2. Near burner region 114
4.5. Summary 115
5. The coherence of an isothermal swirling flow 117
5.1. Case description 118
5.2. Numerical settings 119
5.3. Velocity field results 121
5.3.1. RANS turbulence models and grid size assessment 122
5.3.2. Transient velocity distributions and vortex identification 127

5.3.3. Temporal coherence analysis 132
5.3.3.1. Axial position 1 133
5.3.3.2. Axial position 2 136
5.3.3.3. Axial position 3 139
5.3.3.4. Axial position 4 142
5.3.4. Spatial coherence analysis 145
5.3.4.1. Axial position 1 146
5.3.4.2. Axial position 2 150
5.3.4.3. Axial position 3 154
5.3.4.4. Axial position 4 158
5.3.5. Spatiotemporal coherence analysis 162
5.3.5.1. Axial position 1 163
5.3.5.2. Axial position 2 167
5.3.5.3. Axial position 3 171
5.3.5.4. Axial position 4 175
5.4. Summary 179
6. The coherence of the flow in a coal combustor 182
6.1. Case description 183
6.2. Numerical settings 185
6.3. Steady state reactive flow results 188
6.4. Transient results 194
6.4.1. Aerodynamics and vortex identification 195
6.4.2. Temporal coherence analysis 197
6.4.2.1. Axial position 1 198
6.4.2.2. Axial position 2 202
6.4.2.3. Axial position 3 204
6.4.3. Spatial coherence analysis 208
6.4.3.1. Axial position 1 209
6.4.3.2. Axial position 2 213
6.4.3.3. Axial position 3 217
6.4.3.4. Midplane 221
6.4.4. Spatiotemporal coherence analysis 225
6.4.4.1. Axial position 1 226
6.4.4.2. Axial position 2 230
6.4.4.3. Axial position 3 234
6.4.4.4. Midplane 238
6.5. Summary 242
7. Conclusions and further work 248

7.1. Conclusions....248
7.2. Further work....256
Bibliography....260

List of figures

Figure 1.1 Share by fuel of total power generation..... 1
Figure 1.2 The increase in the average temperature relative to the pre-industrial era and concentration of CO_2..... 2
Figure 1.3 Schematic representation of coal boilers..... 3
Figure 1.4 A process flow diagram of an oxy-coal power plant. 7
Figure 2.1 Turbulent jet motion captured by laser-induced fluorescence. 18
Figure 2.2 Energy spectrum for a turbulent flow. 21
Figure 2.3 Graphical representation of the detail of a flow variable captured by RANS, LES and DNS approaches. 22
Figure 2.4. A schematic of the combustion process for a coal particle. 39
Figure 3.1 Photograph of the front view of the Doosan Babcock 250 kW coal burner and cross-section of the computer aided drawing of the coal burner. 80
Figure 3.2 Schematic of the cross section of the 250 kW CTF 81
Figure 3.3 Photographs of the 250 kW coal furnace.....82
Figure 3.4 Photograph of the oxidiser supply manifold of the 250 kW CTF. 83
Figure 3.5 Photograph of the mechanical feeder used in the coal delivery system. 84
Figure 3.6 Calibration curves for the frequency of the geared motor and for the fuel mass flow of the fuel supply system. 85
Figure 3.7 Photograph of the cluster of gas analysers of the 250 kW CTF...87
Figure 3.8 Photograph of the flame imaging system. 89
Figure 3.9 A computer-aided representation of the isothermal swirling flow test rig.....91
Figure 3.10. Schematic of the design characteristics of the blade arrangement installed in the isothermal swirling flow apparatus. 92
Figure 4.1 A Cartesian representation of the RGB colour space and a three-dimensional colour cube used to capture the light spectrum 98
Figure 4.2 Schematic representation of the array of matrices used to represent an image in RGB colour space. 99
Figure 4.3. Three-dimensional representation of the HSI colour space 104
Figure 4.4 Original snapshot recovered from the recorded videoand the correspondent processed frames for luminance and temperature 109
Figure 4.5 Spectrum of frequencies constructed after the digital luminance and temperature parameters computed using the full flame region. 110
Figure 4.6 Trend of the characteristic oscillation frequencies for the luminance and temperature approach using the full flame region. 110
Figure 4.7 Original and processed snapshots used in the assessment of the characteristic frequency in the near burner region. 111
Figure 4.8 Spectrum of frequencies obtained after the luminance and temperature parameters in the near burner region. 112
Figure 4.9 Characteristic oscillation frequencies for the digital luminance and temperature of the flame in the near burner region. 112
Figure 4.10 Oscillation severity index computed for the full flame region...114
Figure 4.11 Oscillation severity index for the near burner region of the coal flame. 115
Figure 5.1 Cross section of the isothermal swirling flow apparatus. 119

Figure 5.2 Comparison of the axial velocity for different RANS models using Grid 1 122
Figure 5.3 Comparison of the axial velocity for the different RANS models using Grid 2..... 123
Figure 5.4 Comparison of the axial velocity produced by different RANS models using Grid 3..... 124
Figure 5.5 Comparison of the axial velocity at different axial positions for the evaluation of the near-wall treatment functions 125
Figure 5.6 Axial velocity a various positions used to evaluate the effect of the refinement of the three-dimensional grids in the RANS computations. 126
Figure 5.7 Assessment of the mesh suitablity for LES..... 126
Figure 5.8 Comparison of the axial velocities obtained for different SGS models and for the RANS approach. 128
Figure 5.9 Distribution of the axial velocity at the cross-section of the test section. 129
Figure 5.10 Plots of the axial velocity distribution at different positions along the axis. 130
Figure 5.11 Isosurface for the vorticity magnitude, Q criterion and Lambda-2 criterion 131
Figure 5.12 Location of the different monitor points used in the analysis of the temporal coherence. 132
Figure 5.13 Spectrum of frequencies obtained for the monitors at position 1 using the Smagorinsky-Lilly SGS model. 133
Figure 5.14 Cross-correlations of the signals recorded at consecutive points at position 1 using the Smagorinsky-Lilly model..... 134
Figure 5.15 Frequency spectrums produced by the Sigma model for the different points located at position 1. 135
Figure 5.16 Plots of the cross-correlation for the temporal signals obtained using the Sigma model across the different points at position 1. 135
Figure 5.17 Frequency spectrums obtained at different point in the position 2 using the results produced by the Smagorinsky-Lilly SGS model. 136
Figure 5.18 Value for the cross-correlation of the signals produced at the axial position 2 for the Smagorinsky-Lilly SGS model 137
Figure 5.19 Frequency spectrums for the signals produced by the LES simulation using the Sigma SGS model at the axial position 2..... 138
Figure 5.20 Plot of the cross-correlations of the different transient signals obtained at the axial position 2 by the LES computation that employs the Sigma SGS model. 138
Figure 5.21 Distribution of frequencies produced by the transient signals recorded at different points at the axial position 3 employing the Smagorinsky-Lilly SGS model..... 139
Figure 5.22 The cross-correlations of the transient signals obtained using the Smagorinsky-Lilly approach at the axial position 3 140
Figure 5.23 Frequency spectrums for the points located at position 3, computed using the Sigma model..... 141
Figure 5.24 Cross-correlation of the transient signals recorded at different points located on axial position 3 while employing the Sigma model. 141
Figure 5.25 Frequency spectrums calculated using the Smagorinsky-Lilly model at the axial position 4..... 142

Figure 5.26 Cross-correlations of the transient signals sampled at position 4 using the Smagorinsky-Lilly SGS model. 143
Figure 5.27 Frequency spectrums obtained for LES using the Sigma model at the axial position 4. 144
Figure 5.28 Cross correlations for the temporal signals generated at the axial position 4 by LES incorporating the Sigma SGS model. 144
Figure 5.29 Distribution of the energy contained per POD mode and vector plot of the mean velocity components obtained by the LES that incorporates the Smagorinsky-Lilly SGS model 146
Figure 5.30 POD modes produced by the LES using the Smagorinsky-Lilly model for the SGS tensor at the axial position 1. 147
Figure 5.31 Plot of the distribution of the energy of the system in the POD modes and the vector field of the mean velocities produced by the Sigma model in the LES framework at the axial position 1. 148
Figure 5.32 POD modes for the set of snapshots produced for the axial position 1 by the LES with Sigma model for the SGS effects 149
Figure 5.33 The contained energy across the POD modes produced by analysing the transient data of the LES with Smagorinsky-Lilly formulation for the SGS effects and the vector plot of the mean velocity components for the same study 150
Figure 5.34 POD modes computed for the LES that employs the Smagorinsky-Lilly SGS model at the axial position 2. 151
Figure 5.35 Plot of the distribution of energy in the POD modes computed for the results of the LES with the Sigma model for the SGS stresses and vector plot of the mean velocity field at the axial position 2 152
Figure 5.36 POD modes calculated for the data sampled at the axial position 2 and that is produced by the LES using the Sigma approach for the SGS effects. 153
Figure 5.37 Plot of the distribution of energy in the POD modes calculated for the axial position 3 using results of the LES with the Smagorinsky-Lilly SGS model and the vector plot of the mean velocity 154
Figure 5.38 POD modes for the LES results, at the axial position 3, employing the Smagorinsky-Lilly model 155
Figure 5.39 Energy distribution in the POD modes and vector plot of the mean velocity obtained from the LES with the Sigma model for the position 3 ... 156
Figure 5.40 POD modes for the transients results obtained for the Sigma SGS model at the axial position 3. 157
Figure 5.41 Plot of the distribution of the energy in the POD modesand mean velocity vector plot computed for the results produced by the LES with the Smagorinsky-Lilly SGS model at position 4. 158
Figure 5.42 POD modes obtained for the data produced by the LES using the Smagorinsky-Lilly model at position 4. 159
Figure 5.43 Plot of the distribution of energy across the POD modes and vector plot for the mean velocity components computed for the transient data generated by the LES with the Sigma model to compute the SGS stresses at position 4. 160
Figure 5.44 POD modes computed at position 4 for LES results that were used in the Sigma model for the SGS stresses. 161

Figure 5.45 Frequency spectrum and steady state DMD mode calculated at position 1 for the LES data that was employed in the Smagorinsky-Lilly SGS model. 163
Figure 5.46 DMD modes for the axial position 1 calculated for the data obtained by performing LES with the Smagorinsky-Lilly approach as the SGS model. 164
Figure 5.47 Spectrum of frequencies for the DMD modes computed for the LES with the Sigma SGS model and the steady state DMD mode at the axial position 1 165
Figure 5.48 DMD modes calculated from the results of the LES with the Sigma SGS model and the transient data was obtained at the axial position 1. ... 166
Figure 5.49 Frequency spectrum of the DMD modes computed for the transient data gathered at the axial position 2 for the LES with the Smagorinsky-Lilly model and the steady state DMD mode 167
Figure 5.50 The DMD modes for the transient data at the axial position 2 that was obtained from a LES using the Smagorinsky-Lilly SGS model 168
Figure 5.51 Frequency spectrum for the DMD modes and the steady state DMD mode calculated for the LES using the Sigma SGS model at the axial position 2. 169
Figure 5.52 The DMD modes produced for the transient data at the axial position 2, generated by a LES with the Sigma SGS model. 170
Figure 5.53 Normalised power contained by the DMD modes and the DMD mode at 0 Hz produced for the transient data produced by the LES with the Smagorinsky-Lilly SGS model at position 3. 171
Figure 5.54 The DMD modes obtained for the LES data for the Smagorinsky-Lilly case at position 3. 172
Figure 5.55 Distribution of the power in the DMD modes and the steady state DMD mode for the data produced by the LES with the Sigma SGS model at the axial position 3. 173
Figure 5.56 The DMD modes computed for the LES data for the Sigma case at the axial position 3. 174
Figure 5.57 Frequency spectrum of the DMD modes and the steady stated DMD mode calculated at position 4 for the LES results with the Smagorinsky-Lilly approach to model the SGS stresses. 175
Figure 5.58 The DMD modes for the transient data at the axial position 4 produced by the LES with the Smagorinsky-Lilly SGS model. 176
Figure 5.59 Distribution power in the DMD modes and the DMD mode at 0Hz computed for the results at position 4 using the Sigma SGS model for the LES computations. 177
Figure 5.60 The DMD modes computed for the data generated by the LES with the Sigma SGS model at position 4. 178
Figure 6.1 Schematic of the solid-fuel furnace of the PACT facilities. 186
Figure 6.2 Location of the different axial positions and monitor points used in the analysis of the temporal coherence in a coal combustor. 189
Figure 6.3 Comparison of the predicted gas composition at the axial position 1 against the values measured during the experimental campaign 190
Figure 6.4 Comparison of the gas composition predicted by the RANS computations against the experimental values at the axial position 2. 191

Figure 6.5 Comparison of the distribution of species predicted by the RANS computations against the experimental measurements obtained at the axial position 3. 192
Figure 6.6 Contours of the temperature and axial velocity distributions predicted by steady state CFD computations for the coal combustion under air and oxyfuel conditions. 193
Figure 6.7 Comparison of the axial velocity distribution for the reactive RANS calculations and the isothermal LES. 196
Figure 6.8 Isosurfacces for the vorticity magnitude, Q criterion and Lambda-2 criterion employed as vortex core detection mechanisms in the flow of a coal combustor 196
Figure 6.9 Frequency spectrums obtained for the transient data recorded at the axial position 1 using the air conditions....199
Figure 6.10 Cross-correlations for the transient signals generated by the fluctuations of the axial velocity for the air case at the axial position 1. 200
Figure 6.11 Spectrum of frequencies produced by the velocity fluctuations observed for the Oxy27 case at the axial position 1. 200
Figure 6.12 Cross-correlations for the transient signals obtained for the Oxy27 flow conditions at the axial position 1....201
Figure 6.13 Frequency spectrums obtained for the axial velocity fluctuations in the air conditions recorded at the axial position 2. 202
Figure 6.14 Cross-correlations computed for the transient variations in the axial velocity obtained for the air case at the axial position 2. 203
Figure 6.15 Spectrum of frequencies obtained for the transient data produced by the monitor points at the axial position 2 in the Oxy 27 case....203
Figure 6.16 Cross-correlations for the transient signals obtained at the axial position 2 in the LES of the coal combustor under Oxy27 conditions.....204
Figure 6.17 Frequency spectrums obtained for the fluctuations of the axial velocity for the air case at the axial position 3....205
Figure 6.18 Cross-correlations calculated for the transient oscillations in the axial velocity computed for the air case at the axial position 3. 206
Figure 6.19 Frequency spectrum of the transient fluctuations in the axial velocity produced by the LES of the Oxy27 flow conditions and measured at the axial position 3....206
Figure 6.20 The cross-correlations calculated for the transient signals of the axial velocity fluctuations at the axial position 3 in the coal combustor.....207
Figure 6.21 Distribution of the energy in the POD modes and the vector plot for the mean velocities for the air conditions at the axial position 1. 209
Figure 6.22 POD modes computed for the snapshots produced by the LES for the air case at the axial position 1. 210
Figure 6.23 Energy distribution in the POD modes and vector plot of the mean velocity at the axial position 1 for the Oxy27 flow conditions in the coal combustor. 211
Figure 6.24 POD modes computed for the results obtained at the axial position1 of the LES of the coal combustor under Oxy27 conditions. 212
Figure 6.25 Distribution of the energy in the POD modes for the air case at the axial position 2 and the vector plot of the mean velocity values....213
Figure 6.26 POD modes for the transient data of the air case at the axial position 2. 214

Figure 6.27 Distribution of the energy in the POD modes for the results at the axial position 2 in the coal combustor under the Oxy27 flow condition. 215
Figure 6.28 POD modes computed for the snapshots captured at the axial position 2 of the coal combustor under the Oxy27 flow conditions..... 216
Figure 6.29 Distribution of the energy in the POD modes for the air conditions and the vector plot for the mean velocity components at the axial position 3 (right)..... 217
Figure 6.30 Modes produced by the POD of the LES data generated for the air flow conditions in the coal combustor at the axial position 3..... 218
Figure 6.31 Distribution of the energy contained in the POD modes and vector plot for the mean velocities at the axial position 3 in the LES for the coal combustor under the Oxy27 flow conditions..... 219
Figure 6.32 POD modes calculated for the transient data-set obtained at the axial position 3 un the coal combustor under the Oxy27 flow conditions... 220
Figure 6.33 Energy distribution in the POD modes under air conditions at the cross-section of the furnace and a vector plot of the mean velocity values. 221
Figure 6.34 POD modes computed for the transient results obtained at the cross-section plane for the air conditions in the coal combustor..... 222
Figure 6.35 Distribution of energy in the POD modes calculated for the results at the cross-section plane in the simulation for the Oxy27 flow conditions in the coal combustor and mean velocity vectors 223
Figure 6.36 POD modes calculated at the cross-section of the coal combustor in a LES of the Oxy27 flow conditions. 224
Figure 6.37 Frequency spectrum of the DMD modes and steady state DMD mode obtained for the LES of the air flow conditions. 226
Figure 6.38 DMD modes obtained for the transient data generated for the air case at the axial position 1. 227
Figure 6.39 Spectrum of frequencies of the DMD modes for the flow at the axial position 1 in the coal combustor under Oxy27 conditions and steady state of the flow 228
Figure 6.40 DMD modes computed for the results obtained at the axial position 1 of the coal combustor under the Oxy27 conditions..... 229
Figure 6.41 Distribution of power contained in the DMD modes and steady state DMD mode at the axial position 2 of the air conditions in the coal combustor..... 230
Figure 6.42 DMD modes computed for the flow in the coal combustor at the axial position 2 under air conditions..... 231
Figure 6.43 Distribution of power across the DMD modes and steady state DMD mode at the axial position 2 in the coal combustor under the Oxy27 conditions. 232
Figure 6.44 POD modes calculated for the LES results of the flow at the axial position 2 in the coal combustor under the Oxy27 conditions. 233
Figure 6.45 Distribution of power contained in the DMD modes and steady state vector plot at the axial position 3 of the coal combustor under air flow conditions. 234
Figure 6.46 DMD modes produced for the snapshots sampled at the axial position 3 in the LES of the flow in the coal combustor for the air flow conditions. 235

Figure 6.47 Spectrum of frequencies produced by the power contained in the DMD modes and steady state DMD mode at the axial position 3 of the coal combustor under the Oxy27 conditions. 236
Figure 6.48 DMD modes calculated for the flow in the coal combustor under the Oxy27 conditions at the axial position 3. 237
Figure 6.49 Distribution of power in the DMD modes for the flow of air in the coal combustor and steady state of the flow 238
Figure 6.50 DMD modes obtained at the cross-section of the coal combustor for the LES results of the air case. 239
Figure 6.51 Distribution of power in the DMD modesand steady state DMD mode at the cross-section of the coal combustor under the Oxy27 flow conditions. 240
Figure 6.52 DMD modes generated for the transient results obtained at the cross-section of the coal combustor under the Oxy27 conditions. 241

List of tables

Table 3.1 Properties of the 'El Cerrejon' coal. 86
Table 3.2 Operating conditions used in the coal combustion experimental campaign. 90
Table 3.3 Experimental conditions evaluated in the isothermal swirling flow test array. 94
Table 5.1 Characteristics of the flow condition used to develop the methodology for assessment of the coherence in swirling flow. 118
Table 5.2 Details of the numerical grids employed in the evaluation of different RANS models for turbulence modelling and in the LES computations..... 120
Table 5.3 Summary of the monitors employed in the assessment of the coherence in an isothermal swirling flow. 122
Table 6.1 Combustion conditions employed in the analysis of the flow coherence in a coal combustor. 184
Table 6.2 Modelling parameters employed in the CFD studies of the flow in a coal combustor 187

1. Introduction

Energy consumption is often referred to as a main indicator of social and economic development of nations worldwide [1]. An expected global population of 8.3 billion people by 2030, in addition to the sustained industrialisation of emerging countries, such as China, Russia and India will generate a 36% higher energy demand, which will be more complex to satisfy [2], [3].

Most of the global energy demand is accounted by the power generation industry, which relies on a mixture of different fuels and technologies to fulfil the population requirements. The power generation miscellanea is highly dynamic, varying accordingly to the fuel source availability, market price and the implementation and amendments to their usage policies. As a result, it is expected that usage of some of the available alternatives tends to increase, especially those recent developments such as renewable technologies. Nevertheless, fossil fuels are predicted to remain the major the contributor in the energy mixture with steady values of more than 80% of the overall primary consumption, as shown in Figure 1.1 [4].

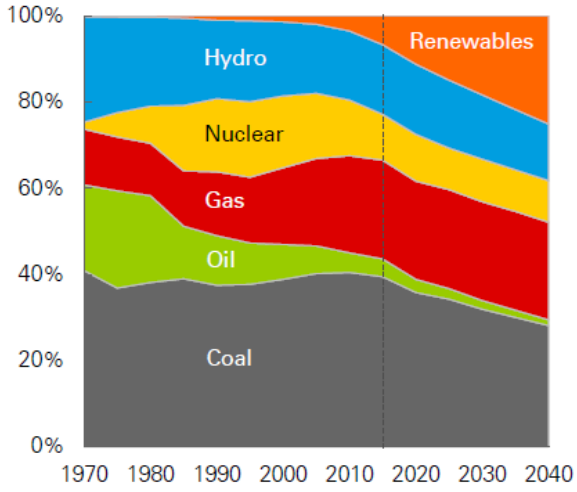

Figure 1.1 Share by fuel of total power generation from 1970 to 2040.

Among the fossil fuels, coal has been used historically as a primary source of energy due to its wide availability and relative easy way of extraction. The actual proven coal reservoirs are estimated to be more than a 100 years, thus making it a key asset in the power production industry for the foreseeable future [2].

Contrary to its benefits, several drawbacks associated to the employment of coal for power generation have been widely reported. Coal-based power plants are a major source of air pollutants such as nitrogen and sulphur oxides, particulate matter, heavy metals and greenhouse gases [5].

Carbon dioxide (CO_2), a product of the combustion of coal, is acknowledged as a major contributor to the greenhouse house effect in the atmosphere due to its higher concentration in comparison to other pollutants. The direct relationship between the levels of greenhouse gases in the atmosphere and the rise in ambient temperature, known as global warming, is of prime concern due to its repercussions to the global life balance [6].

1.1. Global warming and climate change

The increasing trend in the atmospheric and surface temperatures recorded in the last century is known as global warming. The planetary average temperature is reported to have increased 0.9 K, relative to the baseline of mid-20th century as shown in Figure 1.2. It has been concluded that global warming is mainly driven by the increasing emission in greenhouse gases to the atmosphere since the industrial revolution [7].

Carbon dioxide is by far the largest anthropogenic greenhouse gas emitted to the atmosphere. The concentration of CO_2, presented in Figure 1.2, has increased from approximately 280 parts per million in the pre-industrial era to more than 400 ppm nowadays. The sustained increase in CO_2 emissions is a direct consequence of the reliance in fossil fuels [8], [9].

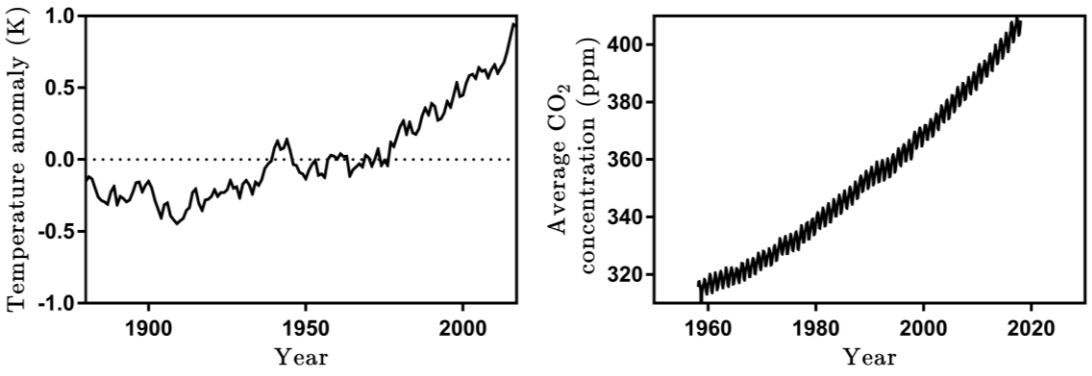

Figure 1.2 The increase in the average temperature relative to the pre-industrial era (right) [7]. Concentration of CO_2 measured at Mauna Loa observatory (left) [9].

The climate equilibrium is a direct consequence of the planetary energy balance. A large part of the energy emitted by the sun is absorbed, while the remaining energy is either reflected or emitted back to space. The changes in the composition of the atmosphere as a result of the larger concentration of greenhouse gases modifies the overall energy balance; the alteration in the absorption coefficient is reported to be the direct cause of the greenhouse effect [10].

In addition to global warming, a wide range of phenomena are directly associated to the greenhouse effect, these include the melting and detachment of large fragments of ice in glaciers, the rise in the sea level, alterations to the natural sprout cycles of many crops and extreme weather systems [7].

An increment of more than 2 K on the planetary average temperature is agreed to be potentially irreversible and its consequences are predicted to be devastating. The large effort made by the scientific community in terms of awareness and contingence of the climate change effect has lead to the drafting of several laws and global policies aimed at reducing the greenhouse gas emissions [11]–[13].

1.2. Power generation using coal

Coal, as a fuel, represents a major contributor in the power generation industry. In general, coal-based power plants use the heat obtained from the combustion of coal particles to evaporate water. The generated steam is used as a working fluid in a turbine, thus generating torque. The power shaft of the turbine is finally coupled to a generator in order to produce electricity.

The more common coal combustion or gasification processes in the power generation industry include the fixed bed, fluidised bed and entrained flow reactors. A representation of these types of boilers is presented in Figure 1.3 [14].

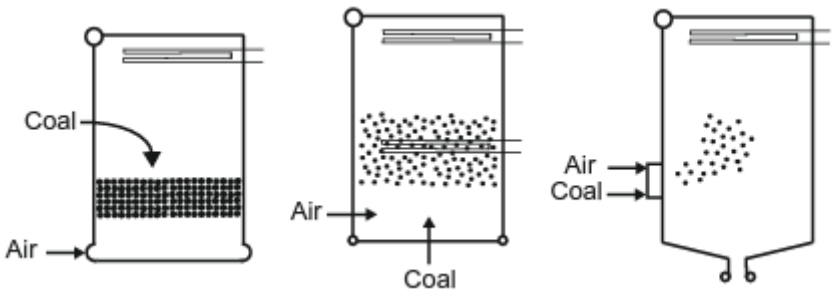

Figure 1.3 Schematic representation of coal boilers, fixed bed reactor (left), fluidised bed (middle), and entrained flow (right).

In fixed bed boilers, the fuel is supplied by a conveyor into a moving grate, hence forming a compact bed of particles. The coal particles are heated as the grate moves within the boiler, releasing their volatile matter and later burning as char. A stream of air is pushed through the coal bed in order to drive the formed gases into the volatile combustion zone, usually at the top. The stoichiometry of the volatile combustion is adjusted by introducing a secondary air flow after the coal particle bed. Fixed bed boilers are capable of using a wide range of coal types; however, their efficiency is severely penalized by the excess air required by the process.

Fluidised bed boilers require smaller particles than those used to form fixed beds, being usually 5 to 10 mm in size. The coal particles are injected into a hot mixture of inert solids, such as ash or limestone, and air. The particle devolatilisation and subsequent combustion occurs within this zone. The air velocity supplied must be sufficiently large to overcome the inertial force of the particles and set them in motion; the lower value for this purpose is known as the fluidisation velocity. The air with velocities above the fluidisation threshold flows in the form of bubbles through the particle bed; for velocities being much higher, the particles are lifted out of the bed, thus making necessary the addition of a cyclone separator in order to recirculate the entrained particles. The possibility to recirculate coal particles into the system increases their residence time, thus providing these types of systems with a large capability to use a wide range of coal types.

In the entrained flow systems, the coal particles are carried by a small portion of the total air required for the reaction in the primary flow channel; the temperature of the primary air is maintained low, less than 373 K for safety purposes. Coal particles are milled into a fine dust, usually below 70 μm, thus securing a proper displacement into the furnace. The remaining part of the air is preheated prior to entering the furnace, and is often swirled by an arrangement of blades in a burner. The residence time for these types of systems is usually about 1 to 2 s, a value much lower in comparison to the bed-based boilers. Pulverised coal is the most common fuel in the installed power plants, mainly due to its high reliability, wide range of fuel capability and their relative simplicity in increasing the unit size. However, the efficiency of the system directly relies on the aerodynamic profile generated by the installed burner and its capability to produce a stable flame. In addition, the energy required in the milling process, the high particulate and noxious gas emissions, represent major disadvantages.

In order to mitigate the contribution of coal-fired power plants to the concentration of greenhouse gases in the atmosphere, different technologies, such as carbon capture and storage have been proposed.

1.3. Carbon capture and storage technologies

A large socioeconomic endeavour has recently been put in place to successfully tackle the challenges of future energy security and to mitigate the adverse climate change effects. Recent policies and amendments to the law have pressured large companies into sustained economic investments towards the development and deployment of advanced clean energy alternatives, such as carbon capture and storage (CCS).

Carbon capture and storage comprises a group of technologies aimed at removing the carbon dioxide generated as part of many industrial processes. In power generation from fossil fuels, the fundamental chemical process is the exothermic oxidation of carbon, thus the generation of carbon dioxide is unavoidable. The captured carbon dioxide is subsequently compressed for simpler transportation and finally stored in a safe site or reused as part of a different industrial process. The removal of the generated carbon emissions can be achieved at different stages in the process [15]:

- Elimination of carbon from the fuel prior to its combustion (pre-combustion capture)
- Dissociation of carbon dioxide from the products of combustion (post-combustion capture)
- Modify the combustion process to produce a pure carbon dioxide stream as its product (oxyfuel combustion)

1.3.1. Pre-combustion capture

The removal of CO_2 prior to combustion relies on the processing of the fuel in a gasification reactor to produce hydrogen. The gasification process involves the reaction of the fuel with a mixture of water vapour and insufficient oxygen to fully complete the combustion reaction. The product obtained from the gasification of the fuel is a mixture known as synthetic gas or syngas, consisting mainly of carbon monoxide, carbon dioxide, methane, and hydrogen [16]. The preliminary syngas is re-processed with a second stream of water vapour in a shifting reactor to convert it to a mixture of only carbon dioxide and hydrogen. The CO_2 is then separated and the remaining hydrogen-rich gas is further

processed to be used in a fuel cell or combusted as part of the gas turbine cycle [6].

The energy required for the capture and compression of CO_2 in pre- combustion processes is reported to be lower in comparison to other CCS technologies [15]. However, the large capital cost of the gasifier requires a constant full load operation of the reactor in order to make the process affordable. In addition, some technical challenges are currently being addressed; these include the reduction of the amount of steam required in the process, the development of gas turbines for flameless combustion and the appropriate materials for their construction [15].

1.3.2. Post-combustion capture

In post-combustion capture, the carbon dioxide is trapped from the products of the reaction before they are released to the atmosphere. The post-combustion treatment of flue gases allows the capture of air pollutants such as NO_x and SO_x in addition to CO_2. Chemical absorption is considered the most mature treatment for post-combustion CO_2 capture [15]. In chemical absorption, the CO_2 is removed from the flue gases after the formation of a chemically bounded compound by the presence of a liquid solvent [17]. The absorption reaction takes place in a column in which the gas is exposed directly to the solvent. The absorber column is often filled with a porous inert material in order to increase the superficial area and the absorption rate as consequence. The captured CO_2 is stripped from the solvent mixture by a stream of steam in a posterior column; the water vapour is condensed afterwards, thus producing a rich CO_2 product suitable for compression. Organic solvents, such as monoethanolamine (MEA) are the most widely used in post-combustion capture systems [18].

Despite its technological maturity and feasibility for retrofitting, the large energy penalty associated with the low CO_2 content in the flue gases from air-fired combustion (7–14% for coal and 4% for gas) represents a major challenge to address [19], [20].

1.3.3. Oxyfuel combustion

In oxyfuel combustion, the nitrogen (N_2), an inert gas that accounts for almost 80% of the air composition, is effectively removed from the oxidizer stream in the reaction. The fuel is burned in a mixture of oxygen and recycled flue gas, the process was initially developed to produce a rich CO_2 gas to be used for enhanced oil recovery [21]. In addition to replacing the nitrogen within the

combustor, the recycled flue gas is used to control the temperature of the reaction [22]. The resulting products obtained from the oxyfuel process are solely those associated with the combustion reaction, mainly CO_2 and water vapour. The CO_2 concentration obtained from oxyfuel combustion has been reported to be up to 95% on a dry basis measurement, in comparison to 14% achieved under air-fired conditions, thus facilitating and increasing the efficiency of the later compression process [23]. A schematic diagram of an oxy-coal power plant is shown in Figure 1.4 [24].

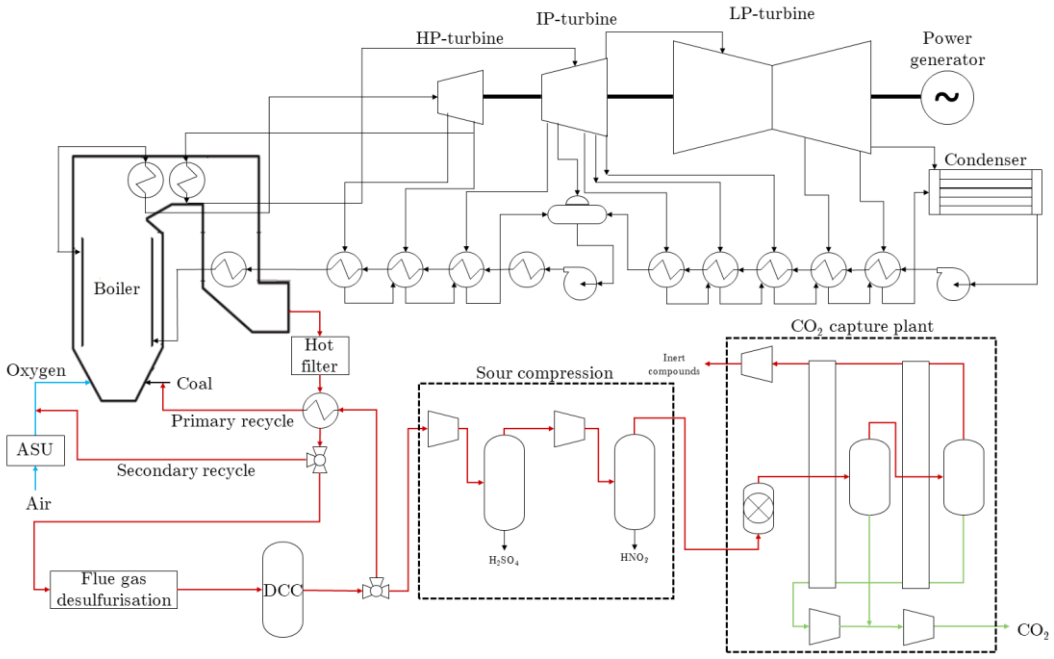

Figure 1.4 A process flow diagram of an oxy-coal power plant.

Oxyfuel combustion systems represent an attractive alternative towards the decarbonisation of power generation. The feasibility for retrofitting power plants to oxyfuel combustion, while retaining the capability to be able to operate under air-fired conditions, currently represents its major advantage [25]. The flame front generated under oxyfuel combustion produce a lower conversion of fuel-bounded nitrogen to NO_x gases, and SO_2 to SO_3, both gases that are removed as liquid acids in CO_2 purification units [24], [26].

In addition to the different composition in the emissions, oxyfuel combustion produce a lower adiabatic flame temperature and delayed ignition in comparison to its counterpart under air-fired conditions. These effects are mainly attributed to differences in the physicochemical properties of the diluting gases, N_2 and CO_2 for air and oxyfuel conditions, respectively [27], [28]. In order to

achieve a similar temperature profile, a larger amount of oxygen is required for oxyfuel combustion, between 27 and 30%, rather than the 21% required for air [25], [27]. The alterations in the combustion environment could potentially disrupt the overall stability of the system, thus making crucial a suitable assessment of the flame repeatability.

In oxyfuel combustion, there is no energy penalty directly associated to the steam cycle in the power production process, however a large amount of energy is required for the separation of air into its components [29]. Novel technologies for air separation, such as electrolytic separation and chemical looping, are currently under development in order to replace the use of cryogenic distillation which has been adopted as the standard technique in oxyfuel systems [30].

1.4. Flame stability and coherence

In order to embrace oxyfuel combustion as a viable technology in the CO_2 abatement strategy, safe and reliable operation must be ensured in power plants. A burner is considered as stable if is able to maintain the fuel ignition without the assistance of a pilot across the range of operational parameters ordinarily used [31].

The stability of the generated flame is directly influenced by the capability of the burner to attain and maintain the minimum ignition temperature; provide enough momentum so the oxidant is continuously mixed with the fuel and the flammability limit is surpassed and the entrained velocity equalizes the flame speed [22]. The oscillatory patterns of the flame characteristics, such as size, colour and shape are desired to remain low. An unstable coal flame will exhibit a noticeable erratic behaviour in the near burner region as the fuel and the oxidizer are mixed, then the instability will be propagated through the flame front [32].

The effect of the higher concentration of CO_2 in oxyfuel combustion, and the changes in physicochemical properties associated with it are expected to modify the stability of the flame [33]. Both the flame propagation speed and flammability limits are affected by the higher heat capacity of CO_2 in comparison to N_2, and the ignition delay in the oxyfuel environments [34], [35]. A common flame stabilization measure is to induce a stronger recirculation of the hot combustion products to compensate for the higher heat capacity of CO_2, and this is achieved by altering the combustor aerodynamics [14], [25], [36]–[38].

The assessment of the stability of a flame is often carried out by analysing the temporal repeatability of its characteristics. Since coal combustion comprises several associated phenomena, the different parameters measured from the flame will lead to different insights in the flame stability. The stability analysis in terms of the flow field is directly related to the presence of turbulent coherent structures within the domain [39], while the analysis using the size, shape, brightness or temperature of the flame is used as an indicator of the efficiency of the chemical reactions involved [40]. The transient data obtained from the flame is often converted into a more comprehensive type in the frequency domain by performing fast Fourier transforms (FFT). The constructed frequency spectrum accounts for the temporal repeatability of the flame parameter oscillation [41]. In addition to the temporal repeatability, the physical space in which the flame front resides is of primary concern. Data driven models, such as the Proper Orthogonal Decomposition (POD), are used to determine the zone in which the flame is oscillating. The Dynamic Mode Decomposition (DMD) was formulated as an extension of the POD methodology by including fast Fourier transforms in time for the calculated spatial oscillations, hence accounting for the spatial and temporal repeatability [42]. A stable flame will display a discernible oscillation frequency across a delimited physical space, thus representing its spatiotemporal coherence.

1.5. Modelling of coal combustion

Combustion engineering is focused on improving the process efficiency, and particularly to reduce the greenhouse gas emissions. A thorough study of all the parameters involved and their effect on the overall combustion phenomena is often required as part of the design or retrofit process. The development of accurate mathematical models that are able to predict the response of the system to a wide range of conditions provides a valuable insight into the operational behaviour of the system. The effects of the oxy-fuel environment in the combustion performance and plant efficiency as a consequence are the primary concern during the development and implementation of low carbon technologies for power generation.

Combustion is often regarded as one of the most complex phenomenon in engineering due to the strong interaction between the physical and chemical processes involved. A typical combustion analysis comprises the solution for the turbulent motion of the fluid, heat transfer, chemical reactions and fuel particle interactions. Computational fluid dynamics (CFD) is a numerical tool used for

modelling the combustion process and the related phenomena. The set equations that represent all the intertwined processes involved are numerically solved across a finite discrete space that represents the domain of interest. The coupling of different sub-models in the same CFD analysis provides a large adaptability of the methodology into different research topics. The implementation of CFD models provides a fast and relative inexpensive alternative to investigate different oxy-fuel ratios and to predict the adequate laws when adjusting the scale of the application [43]–[45].

Coal combustion modelling is often analysed as a two-phase reacting flow in a three-dimensional space. The integration of the fluid motion and reacting particles of pulverised coal leads to the solution of sub-models for the turbulent mixing, heat transfer mechanisms, reaction kinetics and pollutants formation [46]. Many of the sub-models employed in CFD analyses are developed for a wide range of applications, however comparisons against experimental results for the particular case under investigation are often necessary to ensure their validity. In case that none of the available sub-models is suitable, amendments to their assumptions, inputs or, if necessary, a new model must be made prior to their implementation [22].

The chaotic essence of turbulent flows compel the employment of detailed mathematical models in order to predict its motion. Steady-state solutions for the flow field and temperature distributions are still the most desired data for industrial applications; the solution of the Reynolds-Averaged Navier-Stokes (RANS) equations are commonly used for this purpose. The additional terms in the transport equations produced by the time-averaging procedure in RANS simulations needs to be approximated by a suitable model [47]. Contrary to the RANS approach, the solution for all the scalars in the Navier-Stokes equations can be obtained by performing Direct Numerical Simulations (DNS). However, due to the large computational cost associated with the DNS simulations, these are currently limited to simple geometries and low Reynolds number flows, thus restricting its use for practical purposes. A third approach in the solution of turbulent motion is to partially solve the turbulent spectrum in the flow domain; this alternative is known as the Scale-Resolving Simulation (SRS). Large Eddy Simulation (LES) is a widely known SRS method. In LES simulations, a filtration function is introduced in order to limit the portion of the turbulent spectrum to be solved. The detailed solution obtained from SRS methods allows a comprehensive overview of the unsteady nature of turbulent flows and their related phenomena [48]–[51].

The heat transfer mechanisms in coal combustion are strongly dependant on the gas heat capacity and temperature; both properties are directly influenced by the gas composition [52]. The major contributor to the energy balance is the thermal radiation from the combusting particles and the products of combustion. The prediction of the radiative heat flux is therefore affected by the uncertainties in the gas emission and absorption rate modelling. The higher concentrations of CO_2 and H_2O reached in oxyfuel combustion, impose changes in the overall heat flow throughout the furnace and eventually might lead into increasing the formation of pollutants and compromise the stability of the reaction [53]–[55]. The selection of an adequate model to account for all the variables in the heat transfer phenomena across different scenarios is paramount for the accuracy of the simulation of coal combustion [56].

1.6. Aims and objectives

The combustion of coal for power generation purposes will remain to play a key role in fulfilling the global energy demand over the next decades. Therefore, the deployment of novel combustion technologies such as oxyfuel combustion is paramount to reduce the associated carbon dioxide emissions.

The alteration of the oxidant affects the whole set of processes related to the combustion phenomena and the burner aerodynamics. The changes in the fuel ignition point, residence time, flame shape and its proper spatial and temporal propagation are among the parameters that influence the stability of the system and are potentially disruptive if not controlled. The adoption of CFD modelling techniques in conjunction to experimental results can be employed to investigate the effects of the oxyfuel environment in the early stages of the retrofit or design process is therefore

In this framework, it is crucial to develop an adequate methodology to assess and predict the overall stability of flame, as an indicator of the quality of the combustion process. The main objectives of this work are presented as follows:

- Implementation of flame imaging techniques for the assessment of the temporal coherence and stability of a series of experimental coal flames under different oxyfuel conditions.

- Development of a CFD model and an adequate methodology to account for the spatial and temporal coherence of an isothermal swirling flow.

- Application of the spatiotemporal coherence assessment methodology to estimate for the stability of a series of different CFD oxyfuel scenarios.

1.7. Thesis outline

The work presented in this thesis comprises the development of a methodology to assess and predict the stability of coal flames under different oxyfuel conditions. In this chapter an introduction into the context and motivation of this research is presented. In Chapter 2, a summary of the literature available is provided. A review of the different techniques available for the spatial and temporal coherence analysis is introduced alongside an examination of the CFD models for coal combustion under air and oxyfuel conditions.

The technical details of the experimental facility and data collection procedures used in the experimental flame imaging campaign are presented in the first sections of Chapter 3. The details of the isothermal chamber and its measurements, used in the development of the methodology for the spatiotemporal coherence analysis are contained in the subsequent sections.

Chapter 4 presents the analysis of different coal flames using spectral and digital imaging techniques. The stability of the flames are estimated after their repeatability in time and the severity of the oscillations in their parameters.

In Chapter 5, the development and test of a methodology to account for the repeatability in time and space of CFD simulations of an isothermal swirling flow is introduced. Reduction order models and spectral analysis techniques are compared among them and evaluated after the results produced.

Chapter 6 describes the estimation of the stability in a coal combustor under different oxyfuel ratios produced by CFD simulations. The stability assessment of the flow was performed in terms of the temporal, spatial and spatiotemporal coherence of the flow scalars.

Finally, Chapter 7 provides a summary of the general conclusions obtained, and it offers an insight into the further work required.

2. Literature review

The tightening of policies on pollutant emissions in the power industry, besides the progression towards novel and more efficient combustion systems, compel the generation of reliable and reproducible methodologies in the evaluation of combustion processes. The assessment of the flame stability, as an indicator of the combustion efficiency, is a challenging task due to the large amount of phenomena involved in the combustion reaction and the lack of universal criteria in its definition.

The quantification of the influence of new technologies in the overall process efficiency, such as the different combustion environment in oxy-fuel techniques, is crucial in its successful implementation. Measurable data obtained experimentally from the flame front, including digital imaging, have been used in the development of mathematical models that are used to evaluate the combustion reaction performance. Additionally, computational tools, such as computational fluid dynamics, have been recently applied in the prediction of the dynamic behaviour of the combustion reaction. The data generated, from both experimental and numerical approaches, are of a critical importance in the continuous development of cleaner combustors for future power generation applications.

A review of the available literature for the modelling of coal combustion and for the assessment of the spatial and temporal coherence of the obtained data is presented in this chapter. The mathematical expressions and models used in the computational fluid dynamics simulations are introduced in Section 2.1. The governing equations employed in the simulation of combusting coal particles are described in Section 2.1.1. The concepts behind the modelling of turbulent flows, combustion reactions and radiative heat transfer are reviewed in Sections 2.1.2, 2.1.3 and 2.1.4, respectively. In addition, the approaches used in the quantification of the spatial and temporal coherence of the coal flames are presented in Section 2.2. Finally, a summary of the models employed throughout this thesis is provided in Section 2.3.

2.1. Computational fluid dynamics modelling for coal combustion

The ability to accurately predict the combustion performance is key in the design and implementation of novel technologies in the power generation industry. Different techniques have been developed for this purpose; computer-

based analyses, such as computational fluid dynamics, have gained relevance recently due to the amount of data produced and the insights on the process dynamics that are possible to infer after interpreting those techniques [43].

Computational fluid dynamics (CFD) is a numerical tool that allows different operational conditions to be tested across different scales without any major adjustments to the algorithms. The results produced by CFD analyses have been used in coal combustors across different scales, such as in laboratory devices [57]–[59], pilot scale [60]–[69] and for industrial size applications [56], [70]–[72]. In CFD simulations, the behaviour of the fluid flow is bounded by the conservation laws of physics and are expressed through a series of governing equations.

2.1.1. Governing equations

The mathematical expressions used in the representation of the fluid motion are known as the governing equations. In CFD analyses, the molecular motion of the fluid constituents, as well as the structure of the matter are regularly ignored, hence considering the fluid as a continuum. The fluid flow is depicted through its macroscopic properties, such as the velocity, pressure, density and temperature, and spatial and temporal derivatives [44].

The mass conservation equation across a differential element of the fluid is given by:

$$\frac{\partial \rho}{\partial t} + \frac{\partial}{\partial x_i}(\rho u_i) = 0 + S_{DPM} \tag{2.1}$$

where S_{DPM} is the mass released by the particle in the form of moisture, volatiles or char. The external forces acting on a fluid particle, assuming a Lagrangian approach, will produce changes to its momentum if a closed system is assumed. The momentum conservation convention is evidenced in Newton's second law; in the CFD approach the fluid motion is governed by the momentum equations, namely the Navier-Stokes equations [44]:

$$\frac{\partial}{\partial t}(\rho u_i) + \frac{\partial}{\partial x_i}\left(\rho u_i u_j\right) = -\frac{\partial p}{\partial x_i} + \frac{\partial \tau_{ij}}{\partial x_i} + F_i + F_{DPM} \tag{2.2}$$

where F_i is a body force, such as gravity, acting on the continuum, F_{DPM} is the exchange of momentum between the coal particles and the fuid and τ_{ij} is the stress tensor, which for Newtonian fluids may be written as

$$\tau_{ij} = \mu\left(\frac{\partial u_i}{\partial x_j} + \frac{\partial u_j}{\partial x_i} - \frac{2}{3}\frac{\partial u_k}{\partial x_k}\delta_{ij}\right) \tag{2.3}$$

For fluid flows with a finite number of reacting species, k, the transport equation for the mass fraction, Y_k, is given by

$$\frac{\partial}{\partial t}(\rho Y_k) + \frac{\partial}{\partial x_i}(\rho u_i Y_k) = \frac{\partial}{\partial x_i}\left(\rho D_k \frac{\partial Y_k}{\partial x_i}\right) + \dot{\omega}_k \tag{2.4}$$

where $\omega_k$is a source term that accounts for the volumetric rate of either the generation or the destruction of a species due to chemical reactions. The species diffusion coefficient, D_k, is calculated from the Schmidt number

$$Sc_k = \frac{\mu}{\rho D_k} \tag{2.5}$$

The thermodynamic state and the composition of the mixture determines the temperature reached in combusting flows. The enthalpy resulting from the exothermal chemical reactions is obtained by solving the energy transport equation, given by

$$\begin{aligned}\frac{\partial}{\partial t}(\rho h) + \frac{\partial}{\partial x_i}(\rho u_i h) \\ = \frac{\partial}{\partial x_i}\left[\frac{\mu}{Pr}\frac{\partial h}{\partial x_i} + \mu\left(\frac{1}{Sc_k} - \frac{1}{Pr}\right)\sum_{k=1}^{N} h_k \frac{\partial Y_k}{\partial x_i}\right] + \frac{\partial p}{\partial t} \\ + S_{rad}\end{aligned} \tag{2.6}$$

with S_{rad} being a source term for the radiation exchange; the enthalpy of the mixture per unit mass is represented by h, while h_k is the specific enthalpy of the species k. The summation of enthalpies on the right hand side of the equation contains all the number of species, N, that are contained in the mixture. The Prandtl number, Pr, accounts for the ratio of momentum and temperature transport, and it is defined as

$$Pr = \frac{c_p \mu}{k} \tag{2.7}$$

Different assumptions in the combustion simulations are regularly made in order to reduce the complexity of the governing equations. The assumption of a single diffusion coefficient, D, for all the species k present in the reacting flow is commonly adopted in the transport equations. In addition, turbulence is acknowledged as the driven mechanism in the transport of species and temperature, hence the convention of a unitary ratio among them [73], [74]. The Lewis number accounts for the ratio of energy transport against species transport rates, and it is given by

$$Le_k = \frac{Sc_k}{Pr} = \frac{k}{\rho c_p D_k} \tag{2.8}$$

Further, in the case of low-speed combustion applications, such as in an unpressurized coal furnace, the temporal pressure oscillation term, $\partial p/\partial t$, can be effectively disregarded. When adopting the unitary diffusion coefficient and a unitary Lewis number for low-speed combusting flows, the energy transport equation (2.6) can be simplified to an expression that resembles the species transport equation, and it is given by

$$\frac{\partial}{\partial t}(\rho h) + \frac{\partial}{\partial x_i}(\rho u_i h) = \frac{\partial}{\partial x_i}\left[\frac{\mu}{Pr}\frac{\partial h}{\partial x_i}\right] + S_{rad} \tag{2.9}$$

The transient turbulent motion of a reacting flow can be characterized through the simultaneous solution of Equations 2.1, 2.2, 2.4 and 2.9. The analytical solution for the set of governing equations can only be accomplished for elementary flow configurations, such as laminar flows in simple geometries, thus reducing its significance in practical applications. However, numerical methods are often applied to obtain approximate solutions that, within a finite range of error, provide useful information of the fluid flow. The numerical approximation is usually performed by employing a three-dimensional domain which, as well as the temporal terms of the governing equations, is conveniently discretised. In order to decrease the computing time required to obtain a solution, mathematical formulations involving the averaging or filtering operations are included in the governing equations. Additional terms are often created as a result of the averaging or filtering operations, hence requiring the selection of a suitable model to obtain a solution. The details regarding the model selected for the simulation of coal combustion by means of computational fluid dynamics will be detailed in the subsequent sections.

2.1.2. Turbulence simulation

Turbulence is a phenomenon present in the majority of both naturally occurring and engineering fluid flows. In turbulent flows, the thermo-hydrodynamic properties of the fluid, such as temperature, pressure and velocity, experience fluctuations caused by the presence of eddies. The size and number of the eddies in turbulent flows is extremely irregular and their dynamics is chaotic by nature; as a result of the inhomogeneous variations of the fluid properties, its motion is random in space and time [75], [76]. An image of a turbulent jet is presented in Figure 2.1 [77].

The ratio between the inertial and viscous forces of a fluid in motion, represented by the Reynolds number, provides a measure to characterize the uniformity of the flow. For fluid flows with Reynolds number values, Re, below a characteristic threshold, known as the critical Reynolds number, a well distinguished arrangement of fluid layers is observed and the flow is smooth and consistent, these types of flows are known as laminar. In contrast, for fluid flow characterized by Reynolds numbers above the critical value, the fluid flow becomes erratic and instabilities arise, even when constant boundary conditions are enforced, and the flow becomes turbulent. The Reynolds number used in the characterization of the motion of a fluid is given by

$$Re = \frac{UL}{\nu} \tag{2.10}$$

where U is the velocity of the fluid, L is a characteristic length scale and ν is the kinematic viscosity.

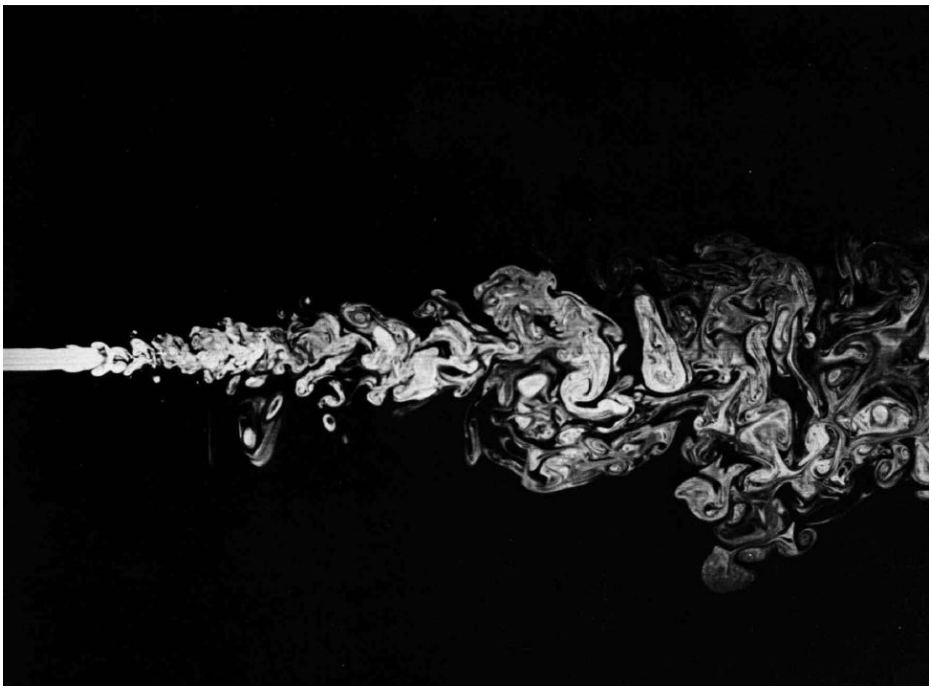

Figure 2.1 Turbulent jet motion captured by laser-induced fluorescence at $Re = 2300$.

Turbulent fluid flows exhibit a high degree of randomness in their motion, thus forbidding a deterministic approach for their solution. In addition, high vorticity regions naturally occur within the domain, which eventually leads to the generation of discernible three-dimensional structures [44]. The turbulent structures interact with the surrounding fluid and suffer alterations in their shape driven by elongation, stretching and ultimately break-up. The turbulent structures, especially those of larger size, evince a certain degree of repeatability and therefore are classified as coherent. The presence of three-dimensional eddies enhances the transport processes and, as a consequence, the exchange of heat, mass and transfer is more efficient than in laminar flows [78], [79].

The size range of the eddies present in turbulent flows ranges vastly for practical applications. The largest eddies sustain their turbulent motion by extracting energy from the mean flow through a process known as vortex stretching.

The characteristic length and velocity of the larger eddies, ℓ_0 and u_0 respectively, are of the same order of magnitude as those of the mean flow; in large eddies the viscous effects are negligible and only the influence of inertial forces are relevant. The smaller eddies are stretched predominantly by the larger ones and, to a lesser extent, by the mean flow. The process in which the kinetic energy is progressively ceded by the larger eddies into the smaller ones is known as the energy cascade [80]. The energy transfer will be extended until the recipient eddy is small enough that the viscous forces are able to halt their motion and dissipate the kinetic energy as thermal internal energy [44].

The first process in the energy cascade sequence, in which energy from the mean flow is gathered from the largest eddies, is determined by the rate of dissipation, ϵ. The energy contained by the large eddies is of an order u_0^2 and the timescale is $\mathcal{T}_0 = \ell_0/u_0$, hence the dissipation rate scales as

$$\epsilon \sim \frac{u_0^3}{\ell_0} \tag{2.11}$$

and is independent of the viscosity, ν, under the assumption of a high Reynolds number [81]. The value of the dissipation rate can be approximated to U^3/L if the large eddy length scale is sufficiently close to the characteristic values of the domain, as in wall-bounded flows. The larger eddies are generally considered as anisotropic, hence their behaviour is strongly influenced by the boundary conditions of the flow.

In contrast, the smallest turbulent structures ($\ell \ll \ell_0$) can be considered as statistically isotropic for high Reynolds number flows [82]. A characteristic length scale, $\ell_{EI} = \ell_0/6$, can be used as a threshold for the size of the turbulent eddies [81]. In addition, the statistics of the small turbulent eddies, contained in the universal equilibrium range ($\ell < \ell_{EI}$), are assumed to be a direct relationship of uniquely ν and ϵ. The definition for the unique length, velocity and time scales are known as the Kolmogorov scales and they are defined as [81]

$$\ell_\eta = (\nu^3/\epsilon)^{1/4} \tag{2.12}$$

$$u_\eta = (\nu\epsilon)^{1/4} \tag{2.13}$$

$$\mathcal{T}_\eta = (\nu/\epsilon)^{1/2} \tag{2.14}$$

Following the energy cascade concept, it can be stated that the Reynold number associated to the smallest dissipative eddies is equal to one, thus regarding the viscous effects as being larger than the inertial forces. From the definition of the Kolmogorov scales, ratios between the smallest and largest eddies can be defined as [81]

$$\ell_\eta/\ell_0 \sim Re^{-3/4} \tag{2.15}$$

$$u_\eta/u_0 \sim Re^{-1/4} \tag{2.16}$$

$$\mathcal{T}_\eta/\mathcal{T}_0 \sim Re^{-1/2} \tag{2.17}$$

From the length scales relationship introduced in Equation 2.15, it can be inferred that for fluid flows with high Reynolds number there is a range of eddies that are very small in comparison to ℓ_0, yet large enough to not be effectively dissipated as heat. Further, it can be stated that flows at sufficiently high Reynolds number, the statistics of the turbulent eddies of a scale ℓ, within the range $\ell_{EI} > \ell > \ell_{DI}$, have a universal form that is determined exclusively by ϵ and thus being independent of ν. The lengthscale, $\ell_{DI} = 60\ell_\eta$, is introduced in order to conveniently split the universal equilibrium range in two, namely the inertial and dissipation subranges. The motions in the inertial subrange ($\ell_{EI} > \ell > \ell_{DI}$) are driven entirely by inertial forces, whereas the viscous effects are only relevant to the motions contained in the dissipation

subrange ($\ell < \ell_{DI}$). A typical energy spectrum of a turbulent flow is presented in Figure 2.2.

The governing equations, introduced in Section 2.1.1, provide a mathematical representation of fluid flows and analytical solutions can be obtained for simple geometric configurations under a laminar regime. In contrast, solutions for more complex configurations, such as many engineering applications, need to be solved through a numerical approach. Various numerical methodologies have been developed for this purpose, with different degrees of simplicity, and accuracy. In Direct Numerical Simulations (DNS), the governing equations are solved by applying discretisation techniques exclusively. The lack of averaging or approximation procedures within the DNS approach allows one to obtain the most accurate representation of the flow field possible. However, the spatial and temporal discretisation required for DNS must be small enough to capture the motion of the turbulent eddies up to the Kolmogorov scales. The range of sizes for the eddies in turbulent flow conditions dramatically escalates the amount of computational resources required to perform DNS analyses, hence making it unusable for practical purposes.

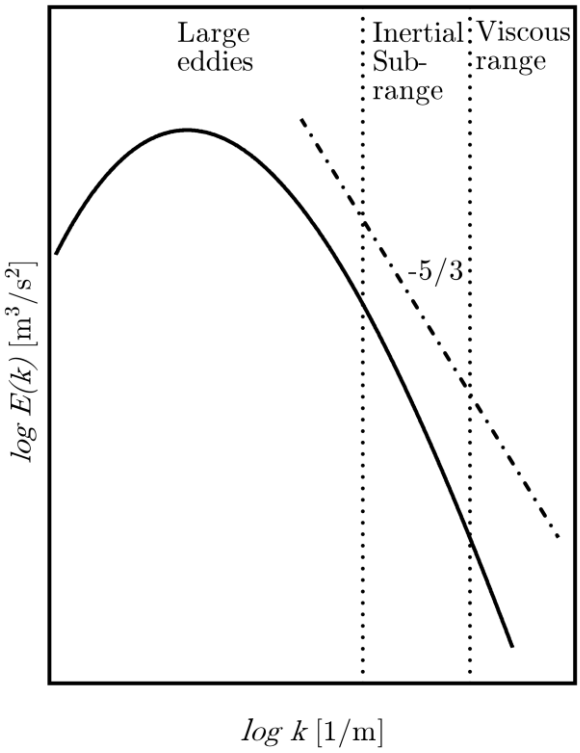

Figure 2.2 Energy spectrum for a turbulent flow, plotted on a log-log scale. The line has $-5/3$ slope and this indicates that the separation scale is insufficient to capture the inertial sub-range.

In order to solve complex flows, a different numerical definition of the flow scalars, known as the Reynolds decomposition, is often used. The Reynolds decomposition employs an averaging procedure to the governing equations, in which only the mean values of the flow scalars are retained; the filtered equations obtained are commonly referred to as the Reynolds-averaged Navier-Stokes (RANS) equations [44]. The additional terms generated in the governing equations by the Reynolds-averaging procedure needs to be modelled in order to be able to solve the governing system of partial differential equations. The results obtained from the RANS computations will only represent the steady state of the flow, often desirable for engineering applications but ineffective to capture highly dynamic transient phenomena such as combustion instabilities [74].

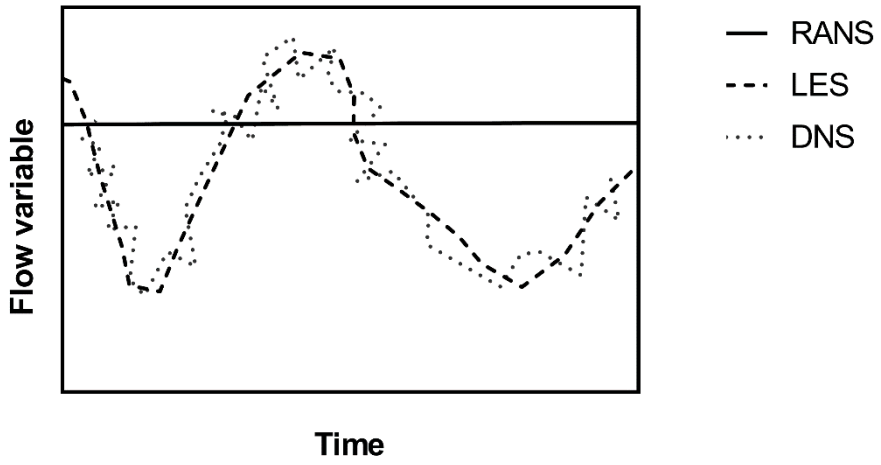

Figure 2.3 Graphical representation of the detail of a flow variable captured by RANS, LES and DNS approaches.

A different approach to simulate turbulent flows is to exclusively resolve the motion of the larger, and more energetic, eddies while a suitable mathematical model accounts for the smaller structures [48]. This approach, known as large eddy simulation (LES), employs a spatial filter to dissociate the larger turbulent structures from the flow field; the additional terms in the governing equations, produced by the filtering operation, describe the contribution of the smaller scales into the flow and these are required to be modelled [83]. In LES computations, the grid resolution must be fine enough in order to successfully capture the motion of the larger turbulent eddies, thus imposing a higher computational cost in comparison to the RANS approach but significantly lower than in DNS. In addition, the three-dimensional nature of turbulent flows impede the simplification of the geometry and compel the implementation of high-

order discretization algorithms. In LES, the natural oscillatory behaviour of turbulent flows can be captured, thus giving a better prediction of the turbulent transport phenomena and in the development of turbulent coherent structures [81], [84]. A graphical representation of the captured detail for each CFD approach in turbulence is presented in Figure 2.3.

2.1.2.1. The Reynolds-averaged Navier-Stokes approach

A common practice to characterise the instantaneous values of the scalars comprised in turbulent flows, ϕ, is to describe them as the addition of the mean $\bar{\phi}$ and fluctuating part ϕ'; this approach was introduced by Reynolds [85] and can be written as

$$\phi = \bar{\phi} + \phi' \tag{2.18}$$

where $\bar{\phi}$ denotes the statistical mean of the scalar ϕ across time. For practical applications, the period of time in which the averaging procedures take place is considerably larger than that associated to the motion of the slower turbulent structures, thus representing a statistically stationary turbulent flow. The Reynolds-averaged scalar is represented by

$$\bar{\phi} = \frac{1}{T}\int_{t}^{t+T} \phi \, dt \tag{2.19}$$

Following, the mean value of the fluctuating contribution, ϕ', is therefore characterised by

$$\overline{\phi'} = \frac{1}{T}\int_{t}^{t+T} \phi' dt = 0 \tag{2.20}$$

In reacting flows, such as in combusting environments, the density of the fluid will fluctuate, thus requiring an additional averaging procedure. The Favre

averaging procedure is applied to all the field scalars but the pressure; the Favre averaged scalars are defined as [86], [87]

$$\tilde{\phi} = \frac{\overline{\rho\phi}}{\bar{\rho}} \tag{2.21}$$

The instantaneous scalars therefore can be re-written as

$$\phi = \tilde{\phi} + \phi'' \tag{2.22}$$

where ϕ'' comprises the effects of the fluctuating density; for incompressible flows, the density is assumed constant, and therefore $\tilde{\phi} = \bar{\phi}$ and, consequently, $\phi'' \equiv \phi'$. The governing equations for reacting flows resulting from the Favre-averaging procedure are given by

$$\frac{\partial \bar{\rho}}{\partial t} + \frac{\partial}{\partial x_i}(\bar{\rho}\tilde{u}_i) = 0 \tag{2.23}$$

$$\frac{\partial}{\partial t}(\bar{\rho}\tilde{u}_i) + \frac{\partial}{\partial x_j}\left(\bar{\rho}\tilde{u}_i\tilde{u}_j\right) = -\frac{\partial \bar{p}}{\partial x_i} + \frac{\partial}{\partial x_j}\left(\bar{\tau}_{ij} - \bar{\rho}\widetilde{u_i''u_j''}\right) + \bar{F}_i \tag{2.24}$$

$$\begin{aligned}\frac{\partial}{\partial t}\left(\bar{\rho}\tilde{Y}_k\right) + \frac{\partial}{\partial x_j}\left(\bar{\rho}\tilde{u}_j\tilde{Y}_k\right) \\ = \frac{\partial}{\partial x_j}\left(\bar{\rho}D_k\frac{\partial \tilde{Y}_k}{\partial x_j} - \bar{\rho}\widetilde{Y_k''u_j''}\right) + \frac{\partial}{\partial x_j}\left(\bar{\rho}D_k\frac{\partial \widetilde{Y_k''}}{\partial x_j}\right) + \tilde{\dot{\omega}}_k\end{aligned} \tag{2.25}$$

$$\begin{aligned}\frac{\partial}{\partial t}\left(\bar{\rho}\tilde{h}\right) + \frac{\partial}{\partial x_j}\left(\bar{\rho}\tilde{u}_j\tilde{h}\right) \\ = -\frac{\partial}{\partial x_j}\left(\bar{\rho}\widetilde{u_j''h''}\right) + \frac{\partial}{\partial x_i}\left[\widetilde{\frac{\mu}{Pr}\frac{\partial h}{\partial x_i}}\right] + \frac{\partial \bar{p}}{\partial t} + S_{rad}\end{aligned} \tag{2.26}$$

The additional term, $\widetilde{u_i''u_j''}$, contained in Equation 2.24 is known as the Reynolds-stress tensor and requires to be modelled, this is commonly regarded as the closure problem of turbulence, and is addressed by selecting a suitable mathematical approximation [88], [89].

The direct relationship between the Reynolds stresses and the mean rate of deformation introduced by Boussinesq is often used as the basis in turbulence modelling; according to this postulate, the Reynolds stresses are then estimated by

$$-\bar{\rho}\widetilde{u_i''u_j''} = \mu_t\left(\frac{\partial\widetilde{u_i}}{\partial x_j}+\frac{\partial\widetilde{u_j}}{\partial x_i}\right)-\frac{2}{3}\bar{\rho}\hbar\delta_{ij} \tag{2.27}$$

where μ_t is the turbulent viscosity, a field variable that, in contrast to the molecular viscosity, depends on the flow characteristics rather than on the intrinsic properties of the fluid; $\hbar = 1/2\left(\widetilde{u''^2}+\widetilde{v''^2}+\widetilde{w''^2}\right)$ is the turbulent kinetic energy and δ_{ij} is the Kronecker delta operator. For simplification purposes, the turbulent viscosity is often obtained as an analogous correlation between the characteristic length $\mathcal{L}$ and velocity $\mathcal{U}$, of the turbulent structures developed [44].

Different mathematical models have been proposed to approximate the turbulent viscosity. The earliest, and most simplistic, approach for the turbulent viscosity estimation is known as the mixing-length model, and it relies on a dimensionless constant of proportionality introduced to an algebraic relation between turbulent viscosity and the length scales of the mean flow [44], [88], [90]. Subsequently, a differential transport equation was employed to obtain a more accurate solution for the turbulent kinetic energy, hence the one-equation models, such as the Spalart-Allmaras [91], were developed.

The most widely used models for turbulence modelling are those that make use of two complementary transport equations for the flow variables which are then employed to evaluate the characteristic turbulent length and velocity. The calculation of characteristic turbulent velocity, in the two-equation models, is performed using a similar convention and it is given by [44]

$$\mathcal{U} = \mathcal{k}^{1/2} \tag{2.28}$$

The calculation of the turbulent length scale imposes a greater degree of complexity; therefore, different interpretations have been used to develop suitable mathematical models [88]. A common approach among the two-equation models for computing the turbulence characteristics, is through computing the rate of dissipation of kinetic energy, ϵ; this approach is known as the $\mathcal{k} - \epsilon$ model [92], [93]. The characteristic turbulent length scale is defined in terms of both $\mathcal{k}$ and ϵ, as

$$\mathcal{L} = \frac{\mathcal{k}^{3/2}}{\epsilon} \tag{2.29}$$

while the turbulent viscosity can be specified as

$$\mu_t = C_\mu \rho \frac{\mathcal{k}^2}{\epsilon} \tag{2.30}$$

where C_μ is a dimensionless constant that, in addition to those contained in the transport equations for $\mathcal{k}$ and ϵ, can be adjusted for particular applications [89]. The $\mathcal{k} - \epsilon$ model was devised to be used in turbulent flows with high Reynolds number. Therefore, the equations postulated are not applicable for the near-wall region in enclosed domains due to its inability to capture the logarithmic decay in the proximity of the wall. In wall-bounded flows, such as in a coal combustion furnace, a value of zero for the velocity and for the gradient of $\mathcal{k}$ in the normal direction are imposed as boundary conditions for the walls. The transport equation for ϵ is not solved up to the wall, and semi-empirical equations, known as wall functions, are used instead to associate the solution of the field scalars in the turbulent region to that obtained for the zone adjacent to the wall [44]. Different formulations have been proposed as wall functions, such as the standard approach, which is based on the law-of-the-wall; and the scalable and two-layer approaches [93], [94].

The $k - \epsilon$ turbulence model has been modified to improve its performance for different applications. The renormalisation group (RNG) analysis was included in the standard $k - \epsilon$ formulation in order to obtain a better representation for the low-Reynolds regions and more complex arrangements, such as swirling flows [95]. The RNG $k - \epsilon$ model has been successfully implemented for the solution of highly swirled coal combustion cases [96]–[99]. In addition, the realisation of the velocity, assumed as a random variable, has been employed in order to satisfy the mathematical constraints of the flow when it is aligned to the physical motion [94]. The realisable $k - \epsilon$ turbulence model also provides a revised formulation for the turbulent viscosity [100] that has produced good agreement in reacting flows [72], [101], [102].

Different turbulence models, such as the $k - \omega$ model [103], have been specifically devised to be used in the low-Reynolds regimes, thus requiring a finer spatial discretization of the computational domain that effectively envelops the viscous sublayer. In the $k - \omega$ model, the transport equation for the specific turbulent dissipation rate, ω, is solved alongside the equation for the turbulent kinetic energy. The specific turbulent dissipation rate is defined as [103]

$$\omega = \frac{\epsilon}{k} \tag{2.31}$$

Different modifications and improvements have been made to the original formulation of the $k - \omega$ model in order to overcome the limitations associated to the turbulent viscosity assumption. The SST model [104], which results from blending the transport equations for ϵ and ω, and the revised version of the $k - \omega$ model [105] are two noteworthy improvements.

A more detailed model, known as the Reynolds-stress model [106], in which the stress-isotropy assumption is dropped, hence requiring a transport equation for each component of the stress tensor. Furthermore, an additional equation for the rate of dissipation ϵ is solved, thus solving for a total of seven transport equations. The larger number of transport equations impose an increase in the computation time in comparison to the two-equation models.

The results obtained from the RANS computations are often the steady-state solution in which all the time-dependant effects are disregarded, leading to inaccuracies when detailed information of the flow is required. In addition, since turbulent motions are entirely modelled, RANS computations are completely unsuitable to produce instantaneous values for the field variables.

2.1.2.2. The large eddy simulation approach

In large eddy simulations (LES), unlike the RANS approach, the motion of the larger and more energetic turbulent structures are directly solved, while the smaller eddies are assumed to be isotropic, and therefore are modelled [48]. A spatial filtering operation is employed to the field variables as a threshold to isolate the small-scale structures from the filtered part that is defined as [107]

$$\bar{\bar{\phi}}(\mathrm{x}) = \int \phi(\mathrm{x}^*, t) G(\mathrm{x},\mathrm{x}^*, \Delta) d\mathrm{x}^* \tag{2.32}$$

where $G(\mathrm{x},\mathrm{x}^*,\Delta)$ is the spatial filtering function and Δ is the cutoff filter width, which determines the part of the field variable that is either retained for direct computations or rejected [44]. Following, the instantaneous values for the field variables can effectively be described in terms of their resolved component $\bar{\bar{\phi}}$ and the residual part ϕ^* as

$$\phi = \bar{\bar{\phi}} + \phi^* \tag{2.33}$$

The filtering functions commonly used in LES computation employ a box [108], a Gaussian filter [83], or the spectral cutoff technique [109], and the implementation of the filter can be made either explicit or implicitly. In the explicit approach, the filtering operation is performed to the governing equations through a previously constructed function [48]. The filtered equations that are composed from both resolved and modelled scales are solved numerically. The solutions obtained from the explicit approach exhibit grid independence due to the separation of the filtering and discretization procedures. However, the grid resolution needs to be sufficiently small to capture the smallest scales produced by explicit filter, thus imposing an increase in the computational cost [110],

[111]. In contrast, while using the implicit filtering technique, the grid size and the numerical scheme employed for the discretization procedure are considered to be the spatial filter function [48]. The solutions obtained while using an implicit filter are, therefore, directly dependant on the grid resolution. However, an examination of the statistical behaviour for the field variables across different grid resolutions will show that they become invariant as they reach a sufficiently small cell size, thus ensuring the validity of the computation [48]. As a consequence, the accuracy of the LES calculations improves as the grid resolution approaches to the Kolmogorov scale [112].

In CFD computations, the cutoff width Δ, a measure for the size of the resolved eddies, is set to be a direct function of the grid size, and it is defined as[108]

$$\Delta = \sqrt[3]{\mathrm{V}_{cell}} = \sqrt[3]{\Delta x \Delta y \Delta z} \tag{2.34}$$

where Δx, Δy and Δz are the length of the cell contained in the grid in each direction of the Cartesian coordinate system [108].

The instantaneous transport equations obtained after the implicit filtering operation, can be obtained by a Favre-filtering operation, similar to that employed for the RANS approach. The Favre-filtering operation is defined by [81]

$$\bar{\bar{\rho}}\tilde{\phi}(\mathrm{x}) = \int \rho\phi(\mathrm{x}^*, t) G(\mathrm{x},\mathrm{x}^*, \Delta) d\mathrm{x}^* \tag{2.35}$$

The Favre-filtered instantaneous fluctuation $\widetilde{\phi^*}$, unlike in the averaged equation, does contain a value that is usually different form zero. The Favre-filtered governing equations for mass, momentum species and enthalpy transport are presented as

$$\frac{\partial \bar{\bar{\rho}}}{\partial t} + \frac{\partial}{\partial x_j}\left(\bar{\bar{\rho}}\tilde{u}_j\right) = 0 \tag{2.36}$$

$$\frac{\partial}{\partial t}(\bar{\bar{\rho}}\tilde{u}_i) + \frac{\partial}{\partial x_j}(\bar{\bar{\rho}}\tilde{u}_i\tilde{u}_j) = -\frac{\partial}{\partial x_j}\left(\bar{\bar{\rho}}\left(\widetilde{u_i u_j} - \tilde{u}_i\tilde{u}_j\right)\right) + \frac{\partial}{\partial x_j}\bar{\bar{\tau}}_{ij} + \bar{\bar{F}}_i \tag{2.37}$$

$$\begin{aligned}\frac{\partial}{\partial t}(\bar{\bar{\rho}}\widetilde{Y_k}) + \frac{\partial}{\partial x_j}(\bar{\bar{\rho}}\widetilde{Y_k}\tilde{u}_j) \\ = -\frac{\partial}{\partial x_j}\left(\bar{\bar{\rho}}\left(\widetilde{Y_k u_j} - \tilde{Y}_k\tilde{u}_j\right)\right) - \frac{\partial}{\partial x_j}\left(\bar{\bar{J}}_j^k\right) + \bar{\bar{\omega}}_k\end{aligned} \tag{2.38}$$

$$\begin{aligned}\frac{\partial}{\partial t}(\bar{\bar{\rho}}\widetilde{h_t}) + \frac{\partial}{\partial x_j}(\bar{\bar{\rho}}\widetilde{h_t}\tilde{u}_j) \\ = -\frac{\partial}{\partial x_j}\left(\bar{\bar{\rho}}\left(\widetilde{h_t u_j} - \tilde{h}_t\tilde{u}_j\right)\right) - \frac{\partial}{\partial x_j}\left(\overline{\overline{J_j^{h_t}}}\right) + \bar{\bar{\omega}}_{h_t}\end{aligned} \tag{2.39}$$

From the spatial filtering operation in Equation 2.37, an unknown term, known as the SGS stress tensor, is generated and a suitable model is required for the solution of the system. The SGS stress tensor is defined as [81]

$$\tau_{ij,SGS} = \widetilde{u_i u_j} - \tilde{u}_i\tilde{u}_j \tag{2.40}$$

Additionally, it can be noted from Equations 2.38 and 2.39 that, resembling the Reynold-averaging procedure, a general form for a Favre-filtered field variable can be written as

$$\frac{\partial}{\partial t}(\bar{\bar{\rho}}\tilde{\phi}) + \frac{\partial}{\partial x_j}(\bar{\bar{\rho}}\tilde{\phi}\tilde{u}_j) = -\frac{\partial}{\partial x_j}\left(\bar{\bar{\rho}}\left(\widetilde{\phi u_j} - \tilde{\phi}\tilde{u}_j\right)\right) - \frac{\partial}{\partial x_j}\left(\overline{\overline{J_j^{\phi}}}\right) + \bar{\bar{\omega}}_{\phi} \tag{2.41}$$

where $\bar{\bar{\omega}}_{\phi}$ is a sink term that depends on the definition of ϕ, $\overline{\overline{J_j^{\phi}}}$ is a filtered diffusion flux that usually is evaluated a molecular level and $\widetilde{\phi u_j} - \tilde{\phi}\tilde{u}_j$ is the SGS flux of the scalar ϕ. Both, the SGS stress tensor, $\tau_{ij,SGS}$, and the SGS scalar flux represent the effect of the modelled turbulent structures on the large resolved eddies [81]. The SGS scalar fluxes are approximated as [113]

$$\phi_{SGS} = \bar{\rho}\left(\widetilde{\phi u_j} - \tilde{\phi}\tilde{u}_j\right) = -\frac{\mu_{SGS}}{Sc_{turb,\phi}}\frac{\partial \tilde{\phi}}{\partial x_j} \tag{2.42}$$

where μ_{SGS} is the turbulent sub-grid viscosity.

The SGS stress tensor, contrary to the Reynolds stresses in the RANS equations, is comprised of different contributions whose nature can be determined after the decomposition of the flow variable ϕ, presented in Equation 2.33. The SGS stress tensor can be written as [114]

$$\tau_{ij,SGS} = \overline{u_i u_j} - \bar{u}_i\bar{u}_j = \overline{\bar{u}_i\bar{u}_j} - \bar{u}_i\bar{u}_j + \overline{\bar{u}_i u_j'} + \overline{u_i'\bar{u}_j} + \overline{u_i'u_j'} \tag{2.43}$$

where $L_{ij} = \overline{\bar{u}_i\bar{u}_j} - \bar{u}_i\bar{u}_j$ are the Leonard stresses, $C_{ij} = \overline{\bar{u}_i u_j'} + \overline{u_i'\bar{u}_j}$ are known as the cross-stresses and $R_{ij} = \overline{u_i'u_j'}$ are the LES Reynolds stresses. The contribution of the Leonard stresses are unique due to the interactions among the resolved turbulent structures, while the cross-stresses arise from the interactions of the larger eddies and the SGS eddies. Finally, the LES Reynolds stresses are a consequence of the convective momentum transfer within the SGS structures and are modelled through a suitable SGS turbulence model [44]. A typical assumption to model the SGS stress tensor is to ignore both the Leonard and cross-stresses and only account for their effects while modelling the LES Reynolds stresses [108], [115].

A common approach to approximate the SGS stress tensor is by, resembling the RANS models, assuming the isotropy of the smaller eddies, thus employing the Boussinesq relationship. The SGS stress tensor is modelled as [81]

$$\tau_{ij,SGS} = -2\mu_{SGS}\bar{S}_{ij} + \frac{1}{3}\tau_{ii}\delta_{ij} = -\mu_{SGS}\left(\frac{\partial \bar{u}_i}{\partial x_j} + \frac{\partial \bar{u}_j}{\partial x_i}\right) + \frac{1}{3}\tau_{ii}\delta_{ij} \tag{2.44}$$

where $\mu_{SGS}$is the sub-grid turbulent viscosity. A direct analogy to the mixing-length theorem is employed by the Smagorinsky-Lilly model [116], where the sub-grid turbulent viscosity is defined in terms of a filter length Δ as

$$\nu_{SGS} = \frac{\mu_{SGS}}{\rho} = (C_m \Delta)^2 \mathcal{D}_s \tag{2.45}$$

where C_m is a proportionality constant that can be adjusted depending on the type of flow, and $\mathcal{D}_s$ is the rate-of-strain differential operator acting on the velocity field, defined as

$$\mathcal{D}_s = \sqrt{2\bar{S}_{ij}\bar{S}_{ij}} \tag{2.46}$$

The value of $C_{m,S}$ was suggested to be contained within a range of 0.065 and 0.3 [117], [118]. However, later studies evidenced that a value between 0.1 and 0.13, if the grid was fine enough, produced less damping of the solution and therefore was appointed as being more suitable [108], [119]. The simplicity and numerical stability of the Smagorinsky-Lilly model has made it a popular choice among the scientific community. However, the dependence on a singular constant and its subsequent high level of turbulence prediction in the near wall region are regarded as the major handicaps for its implementation. In order to ensure a zero value for the viscosity at the wall, different mathematical functions have been developed, thus giving the Smagorinsky-Lilly model a wider usability [94], [120]. In addition, a mathematical postulate has been used to dynamically compute the value of C_m, thus eliminating the necessity of previously assess its value [114].

The Wall-Adapting Local Eddy Viscosity (WALE) model was developed to overcome the limitations of the Smagorinsky-Lilly approach [121] while correcting the behaviour of the solution in the near-wall region. The differential operator for the WALE model is introduced as

$$\mathcal{D}_w = \frac{\left(\bar{S}_{ij}^d \bar{S}_{ij}^d\right)^{3/2}}{\left(\bar{S}_{ij}\bar{S}_{ij}\right)^{5/2} + \left(\bar{S}_{ij}^d \bar{S}_{ij}^d\right)^{5/4}} \tag{2.47}$$

where $\bar{S}_{ij}^{d}$ is the symmetric part of the velocity gradient tensor given by $g_{ij}^{2} = g_{ik}g_{kj}$, and is defined by

$$\bar{S}_{ij}^{d} = \frac{1}{2}\left(g_{ij}^{2} + g_{ij}^{2}\right) - \frac{1}{3}g_{kk}^{2}\delta_{ij} \tag{2.48}$$

The model constant $C_{m,W}$ is set to be 0.325 for all purposes.

A mathematical model, of recent development, known as the Sigma SGS stress model [122] has been acknowledged to comply to all the requirements for accurate LES calculations. The singular values,$\sigma_1 \geq \sigma_2 \geq \sigma_3$, obtained from the Eigen-decomposition of the tensor $\mathbf{G} = \mathrm{g}^{\mathrm{t}}\mathrm{g}$ are used to obtain a differential operator. The singular values are defined by

$$\sigma_1 = \left(\frac{\mathfrak{T}_1}{3} + 2\sqrt{\alpha_1}\cos\alpha_3\right)^{1/2} \tag{2.49}$$

$$\sigma_2 = \left(\frac{\mathfrak{T}_1}{3} - 2\sqrt{\alpha_1}\cos\left(\frac{\pi}{3} + \alpha_3\right)\right)^{1/2} \tag{2.50}$$

$$\sigma_3 = \left(\frac{\mathfrak{T}_1}{3} - 2\sqrt{\alpha_1}\cos\left(\frac{\pi}{3} - \alpha_3\right)\right)^{1/2} \tag{2.51}$$

where

$$\alpha_1 = \frac{\mathfrak{T}_1^2}{9} - \frac{\mathfrak{T}_2}{3} \tag{2.52}$$

$$\alpha_2 = \frac{\mathfrak{T}_1^3}{27} - \frac{\mathfrak{T}_1\mathfrak{T}_2}{6} + \frac{\mathfrak{T}_3}{2} \tag{2.53}$$

$$\alpha_3 = \frac{1}{3}\cos^{-1}\frac{\alpha_2}{\alpha_1^{3/2}} \tag{2.54}$$

and

$$\mathfrak{T}_1 = \mathrm{tr}(\mathbf{G}) \tag{2.55}$$

$$\mathfrak{T}_2 = \frac{1}{2}\left(\mathrm{tr}(\mathbf{G})^2 - \mathrm{tr}(\mathbf{G}^2)\right) \tag{2.56}$$

$$\mathfrak{T}_3 = \det(\mathbf{G}) \tag{2.57}$$

The differential operator for the Sigma SGS stress model is defined as

$$\mathcal{D}_\sigma = \frac{\sigma_3(\sigma_1 - \sigma_2)(\sigma_2 - \sigma_3)}{\sigma_1^2} \tag{2.58}$$

and a model constant, $C_{m,\sigma}$, of 3 is used in all flow configurations. Comparisons among different SGS models shown that the Sigma SGS stress model produced more accurate results than the fixed-constant models, and in some cases, surpassed the performance of the Dynamic model approach [123]. The Sigma SGS stress model has been successfully implemented in reacting flow simulations [124], [125], and has been reported to improve the prediction of the naturally developed turbulent coherent structures [126].

The errors produced in the LES simulations are an aggregate of those associated to the numerical methods such as the discretization algorithms, e_{num}, and those intrinsically related to the sub-grid modelled part e_{SGS} [127]. In scale-resolved simulations, such as in LES, a direct relationship between the contributions of numerical and modelled associated errors is acknowledged, being this more relevant when the implicit filtering operation is employed [128].

In order to assess the accuracy of the LES solution, the results obtained are often compared against reliable data; this methodology is known as the a posteriori approach and involves either experimental data or results obtained from DNS [129]. In addition, the performance of the SGS stress model can be evaluated by exclusively comparing the results obtained from the modelled part to the filtered data acquired from experiments or DNS. However, the resolution of the data used for comparison must be high enough to account for the smaller structures contained in the modelled part of the LES; this approach is known as the a-priori assessment [129], [130].

Different quality indices for the mesh resolution have been developed based on the direct relationship between the grid resolution and the accuracy of the LES solution, especially while using and implicit spatial filtering operation. These qualitative assessments are intended to decrease the dependability on high-resolution data, which often is only available for simple flow configurations, to validate the LES calculations. However, the grid quality indicators, only evaluate the capability of the grid to capture the larger turbulent structures, hence the pertinence of the boundary conditions and any other additional inputs are not considered, and their contributions towards the final solution are excluded [127].

A ratio between the turbulent kinetic energy that has been directly computed and that corresponding to the modelled part is frequently used as an indicator of the solution quality. The quality index can be defined as

$$\mathcal{Q} = \frac{\mathbb{k}_{SGS}}{\mathbb{k}_{tot}} \tag{2.59}$$

where $\mathbb{k}_{tot} = \mathbb{k}_{SGS} + \mathbb{k}_{res}$. The index $\mathcal{Q}$ produces values ranging between 0 and 1, being 0 the corresponding value of a solution where all the turbulent kinetic energy was resolved, such as a DNS solution; in contrast; an index value of 1 represents a fully modelled solution, as in the RANS results. It is acknowledged that an LES solution in which at least 80% for the turbulent kinetic energy is resolved will produce accurate results [44], [81].

The definition of $\mathcal{Q}$ relies on the results obtained from the LES computation, thus imposing computational time in their assessment. An additional method-

ology for the estimation of the quality in LES was proposed after the characteristic turbulent length scale. The characteristic length of the larger, anisotropic eddies is described in terms of the universal equilibrium range as $\ell_{EI} = \mathcal{L}/6$ [81]. In addition, a characteristic filtering length, based on the mesh size, is introduced by $\mathcal{L}_{grid} = \Delta = \sqrt[3]{\Delta x \Delta y \Delta z}$. In order to successfully resolve at least 80% of the turbulent kinetic energy, it was estimated that, for highly turbulent flows, a filter size of $\Delta \approx \mathcal{L}/12$ is required [81], [127], [128]. Following these criteria, the quality of the grid for an LES computation can be evaluated as [81]

$$\frac{\mathcal{L}_{grid}}{\mathcal{L}/12} \begin{cases} \leq 1 & \text{the grid is adequate} \\ > 1 & \text{the grid requires refinement} \end{cases} \tag{2.60}$$

The value of $\mathcal{L}$ can be estimated as $\mathcal{L} = \mathcal{k}^{1.5}/\epsilon$, where the values of $\mathcal{k}$ and ϵ are often obtained from a preliminary RANS computation [81].

The boundary conditions employed in LES and their ability to capture the dynamic behaviour of the flow are of prime concern due to the influence that they impose in the final solution. In RANS calculations, mean values for the transported scalars of the flow usually will suffice to obtain a valid solution. In LES, however, the instantaneous fluctuations of the flow are directly resolved, thus requiring the implementation of a time-dependant boundary condition, that comprises these effects. The implementation of time-varying components for the velocity and related scalars will improve the authenticity of the solution; these boundary conditions can be obtained from experimental sampling or DNS data. The complexity associated to the acquisition of transient data that can be used in LES boundary conditions compel the utilization of numerical algorithms that generate stochastic variations in the flow field. Different algorithms have been developed for this purpose, such as the vortex method [131]–[133], which employ a 2D approach for generating variations in the axial velocity. Additional algorithms that produce flow variations using the spatial orthogonality [134] and white noise [135] have been reported to decrease the number of synthetic coherent structures developed as a direct result of the boundary condition, thus enhancing their usability in the assessment of the flow coherence [126].

2.1.3. Combustion modelling in coal particles

The combustion models for solid fuels, such as coal, are often derived using a single particle approach. However, in reality a large number of particles are simultaneously combusted in the furnace. The cluster of coal particles are entrained by the gaseous phase into the furnace where they sustain an increase in their temperature and eventually ignite. The lack of detailed experimental data in association to the complexity of the chemical reaction compel the utilization of simplified mathematical models to account for more involved phenomena. Furthermore, the modification to the combustion environment under oxyfuel condition will require to either modify the mathematical models that were developed for air-fired conditions or to develop a suitable methodology that comprehends the possible alterations to the combustion environment composition. In this section, the models employed in the simulation of turbulent reacting flows will be reviewed, including the prediction of the particle dynamics and the combustion of volatiles and char.

2.1.3.1. Particle dynamics

In the combustion of coal, different phases interact and the differences in the thermo-physical properties among them require that each phase be treated separately. Three different approaches, namely Euler-Euler, Euler-Lagrange and probabilistic formulations, are usually employed in the calculation of multiphase flows [70]. The Euler-Lagrange approach is often preferred to account for particulate flows, especially when the volume of the solid phase is low in comparison to that of the entire domain, such as in coal combustion [94], [136]. In the Euler-Lagrange approach, the gaseous phase is modelled as a continuum, thus following the governing equations introduced in the previous sections. However, the dynamics of the particle entrained in the carrier phase is obtained after a set of differential equations for the rate of change in mass, momentum and energy. The set of equations to compute the change sustained by the properties of the coal particles as it travels through the gas is defined by [70]

$$\frac{\mathrm{d}}{\mathrm{d}t}\left(m_p\right) = -R_p \tag{2.61}$$

$$m_p \frac{\mathrm{d}}{\mathrm{d}t}\left(u_p\right) = \sum F_p \tag{2.62}$$

$$\frac{\mathrm{d}}{\mathrm{d}t}(mh)_p = \sum Q_p \tag{2.63}$$

where the variable m_p is the mass of the particle and R_p is the rate of mass loss due to different phenomena such as moisture evaporation, devolatilisation or char oxidation; u_p is the velocity of the particle and F_p is the effect of numerous forces acting on the particle, such as the drag and gravitational forces; $(mh)_p$ is the enthalpy of the particle and Q_p is the sum of the energy sources in the particle including conduction or convection from the gaseous flow, radiative energy and heat liberated from the reaction. The local properties of the fluid along the particle trajectory are used to determine the boundary conditions required for the solution of the set of governing differential equations. Different constitutive relationships for the drag and heat transfer coefficients are employed to compute the exchange rates of momentum and heat transfer between the phases. In addition, the mass exchange rate is estimated after incorporating various relationships for the wide range of phenomena occurring in the combustion of the coal particle.

Several simplifications are often adopted in coal combustion simulations in order to reduce the complexity of the analysis; commonly, the particles are assumed to be spherical thus obtaining the drag force coefficient from simpler correlations [72], [137]. Furthermore, the effects of the thermophoretic force and Brownian motion are neglected after the assumption that the vast majority of the particles are larger than 1 μm and their velocity is large enough to not suffer any disruption in their trajectory due to these effects. In contrast, the effects of the random turbulent motion of the gas in the particle path are significant and must be included through a suitable model in computations involving multiphase flows. The turbulent dispersion of particles is often accounted for by the particle cloud model or by employing the stochastic tracking approach, the latter model being the most common in coal combustion studies. In the particle cloud model, the concentration of particles within the domain is approximated as a Gaussian probability density function that directly depends on the turbulent fluctuations of the velocity [138]. The stochastic tracking approach estimates the turbulent dispersion of the particles as an integral of the trajectories described by a cluster of particles; the motion of each particle is estimated after the mean and fluctuating parts of the velocity field for the gas phase [139]. The fluctuating component of the velocity can be incorporated by a model, such as the discrete random walk model, in which the variations

the velocity are assumed to be a piecewise constant functions of time, and are only computed over a finite time interval based on the characteristic lifetime of the turbulent eddies [140].

2.1.3.2. Particle combustion

As the particle temperature increases, the moisture is evaporated in a first stage followed by the release of light volatile matter. The released volatiles are transported within the furnace and mixed with oxygen until they are ignited. The char particles, that remains after the volatiles are released, undergo into an oxidation process that is slower than the combustion of the volatiles. After the completion of the combustion process, the constitution of the particle will be reduced to ash, a material assumed to be inert but relevant in the heat exchange within the furnace.

A sequential approach in which the combustion reaction is assumed to be a series of consecutive steps is often employed for CFD calculations; each step in the process is modelled as an isolated event, hence requiring its completion to trigger the subsequent stage. However, overlapping and simultaneous sub-processes in the combustion reaction does occur in reality, which are more notorious for air fired conditions [141]. A schematic of the coal combustion process is presented in Figure 2.4.

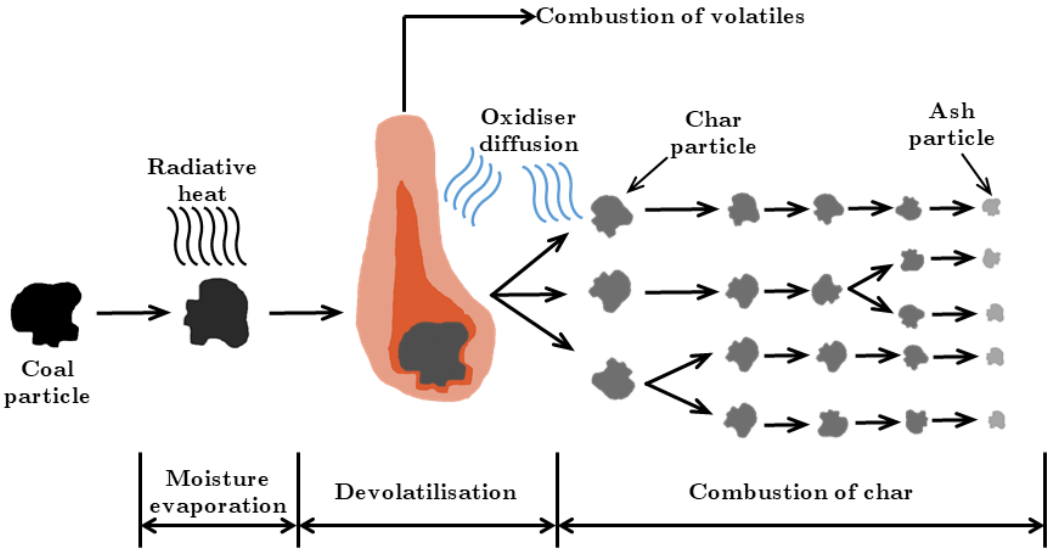

Figure 2.4. A schematic of the combustion process for a coal particle.

2.1.3.2.1. Moisture evaporation and devolatilisation

The rise in the temperature of the particle prompt the evaporation of the moisture contained on the surface, known as free-water, in a first stage, and the dissociation of the water molecules bounded to the particle in a following process. The water vapour is released through the pores in the particle causing shrinking and reducing its structural integrity, and eventually leading to internal cracking and breakup [136]. The moisture evaporation is a low-temperature phenomenon that takes place in the vicinity of the burner, hence influencing the overall behaviour of the flame. The water vapour removes heat from the flame zone, thus causing lower flame temperatures and inducing stabilization issues due to the lower particle heating rate and ignition delay [142]. In order to reduce the effect of the moisture content in the combustion process, fuels are stored in dry conditions whenever it is possible or dried in low temperature desiccants prior to their utilisation [32].

The further heating of the particle will produce a thermo-chemical decomposition of the constitutive compounds of the particle material, thus producing the release of volatile matter; this process is known as devolatilisation. The gases are physically trapped within the particle, such as CO_2 and CH_4, and these are released in the first stage of the devolatilisation process, followed by the light volatiles and the latter heavier compounds, which require more energy to break their chemical bonds [143]. The volatiles are released through the particle pores, which can melt and fuse afterwards, thus trapping any additional gas and forming bubbles. Depending on the heating rate, size, temperature and morphology of the particle, the trapped gas will either cause swelling or, eventually, rupture. The alteration in the particle structure due to the devolatilisation process influences the particle trajectory, distribution and directly affects the ignition and reactivity [144], [145].

The devolatilisation process is often modelled using mathematical relationships obtained after two different approaches. The first approach is based on the evolution of the coal molecular structure during the devolatilisation, and the models derived after it are usually regarded as part of the functional group. These models are able to produce high fidelity predictions of the rate and yield of the volatile production as well as its composition. However, their implementation requires a large amount of detailed input data that often is difficult to obtain experimentally [146]. Among the functional group models, the most widely used are the Functional-Group, Depolymerization, Vaporization, Cross-

linking (FG-DVC) [145], [147], the FLASHCHAIN [148]–[150] and the Chemical Percolation and Devolatilization [151]–[154].

The second approach employs empirical relationships based on the kinetic rates of the governing equations that can be obtained either experimentally or after more detailed models, such as those in the functional group [72]. This method includes different approaches, such as the single rate [155] and two-competing-rates models [156]. In the single rate model, an Arrhenius equation is used to compute a kinetic rate that is used to estimate the amount of volatiles released by the particle, the mathematical relationship is given by

$$\frac{\mathrm{d}}{\mathrm{d}t}(m_p) = -m_v A \exp\left(-\frac{E_a}{RT_p}\right) \tag{2.64}$$

where m_v is the mass of released volatiles, R is the universal gas constant, T_p is the temperature of the particle; terms A and E_a are a constant and the activation energy, respectively, and they need to be estimated for each analysis. The suitable parameters for the single rate model are often obtained after temporal data of the mass loss in the particle under a controlled environment. The transient data is usually acquired by thermo-gravimetric measurements and drop-tube tests [157], [158].

The single rate model represents the most simplistic approach to the mathematical representation of the devolatilisation process; the two-competing-rates model incorporates the notion of the evolution in the particle constituents as it heats up, thus employing two kinetic rates for low and high hating rates [156]. The production of volatiles in the two-competing-rates model is defined as

$$\frac{\mathrm{d}}{\mathrm{d}t}(m_p) = -m_c \int_0^t (\alpha_1 k_1 + \alpha_2 k_2) \exp\left(\int_o^t (k_1 + k_2)\mathrm{d}t\right)\mathrm{d}t \tag{2.65}$$

where m_c is the mass of the char particle assuming full combustion, k_1 and k_2 are Arrhenius expressions that account for the kinetic rate of devolatilisation

under each condition, and α_1 and α_2 are weighting parameters that require to be adjusted.

Despite the differences in the combustion environments, and the effects of the high CO_2 concentration in the combustion kinetics, no noticeable changes have been observed in the devolatilisation rate [158]. The empirical models for devolatilisation are usually implemented in CFD analyses due to their simplicity and robustness. However, the composition of the volatiles is often simplified to a single compound that comprehensively represents the overall chemical structure. The simulated compound is obtained after the ultimate and calorific analyses of the fuel in order to maintain the relevant mass and energy balance.

2.1.3.2.2. Combustion of volatiles

In the context of combustion studies, flames are often categorised under three groups based on how the fuel and the oxidiser are combined [159]. In premixed flames, the fuel and the oxidiser are thoroughly mixed, up to the molecular level, before they encounter their way into the combustion chamber. The flame front produced in the premixed regime is well defined and usually its shape is retained during the process [32]. Further, the possibility to accurately control the combustion stoichiometry allows them to operate under lean conditions with a lower risk of quenching. In contrast, non-premixed flames are obtained after the streams of the fuel and the oxidiser are mixed within the combustion chamber. The mixing process of the reactants, mainly driven by the diffusion mechanisms, will constrain the ignition and subsequent flame propagation in the combustion chamber; hence, these types of flames are often referred to as diffusion flames [74]. The diffusion flames are characterised by a wrinkled front that visibly oscillates both in space and in time; furthermore, an oxygen rich mixture is generally used to ensure the complete combustion of the fuel and to inhibit instability phenomena, such as flame detachment [32]. Otherwise, the partially premixed flames are those obtained after a flow in which only a part of the fuel and the oxidiser were fully mixed. The flow regime of the reactants greatly influences the combustion process, thus encouraging the adoption of turbulent and laminar flows as a sub classification for each flame group. In turbulent flames, the transport of heat and species occurring at large scales will control the reaction, while those under laminar conditions will rely on the diffusion at the molecular level [74], [136]. The modelling approach for the simulation of non-premixed turbulent flames, typical of coal combustion, will be detailed henceforth; the models employed in the computation of both pre-

mixed and partially premixed flames can be reviewed in the relevant literature [74], [160], [161].

The interaction between turbulence and chemistry is paramount in the combustion reaction, with the evolution of the reactants occurring at scales smaller than those resolved in RANS and even LES calculations [162]. The range of scales involved in combustion compel the adoption of a suitable model that is able to account for the turbulent-chemistry interaction in the sub-grid scale [74].

The composition of the volatiles released by the coal particles is difficult to estimate as it is directly related to the fuel and the dynamic heating rates that the particles undergo as they travel in the furnace. A single compound, $C_aH_bO_cN_d$, that is representative of the overall devolatilised species is often preferred in order to simplify the reaction complexity.

The intermediate species from the volatile combustion, which are a consequence of up to thousands of reactions, are neglected. Simplified chemical mechanisms, including a few hundreds of reactions, such as the GRI 3.0 model, are available. However, their implementation in CFD analyses of coal combustion are still not common due to the elevated computational cost and the numerical stability issues associated to the solution of a large number of transport variables [163]. The diffusion of oxygen into the particle and the subsequent effects on the composition of the volatiles is neglected, thus assuming that the mixing process will take place after the devolatilisation.

The volatile combustion reaction is governed by the more relevant phenomenon in place, being physically limited when the turbulent mixing of the reactants is slower than the reaction kinetics. In contrast, the kinetically controlled combustion will assume a reaction kinetics slower than the mixing of chemical species. In coal combustion studies, the concept of an infinitely fast reaction kinetic is adopted, thus obtaining models for reaction rate that are directly dependant on the mixing mechanisms.

The simplest modelling approach in volatile combustion is to consider that combustion will take place as soon as mixing occur, this approach is known as the mixed-is-burnt (MIB) model [164]. The stoichiometric ratio of the flow will limit the extent of the reaction, which is assumed in a global expression given by

$$C_aH_bO_cN_d + \alpha_{MIB}O_2 \rightarrow aCO_2 + \frac{b}{2}H_2O + \frac{d}{2}N_2 \qquad \text{(R 2.1)}$$

where $\alpha_{MIB} = \left(a + (b/4) - (c/2)\right)$. The estimation of a reaction rate in the MIB model is obviated after the assumption of the full combustion of the reactants.

An improvement to the mixed-is-burnt model is the eddy break-up (EBU) model [165] and its latter upgrade, the eddy dissipation model (ED) [166]. The combustion is assumed to be controlled entirely by the turbulent mixing in the ED model and the effects of the reaction kinetics are neglected. The turbulent mixing time, $\mathcal{T}_t$, in addition to the mass fractions of the participating species, is used to estimate the reaction rate [58]

$$R_R = A\rho\frac{1}{\mathcal{T}_t}\min\left(\tilde{Y}_f, \frac{\tilde{Y}_{ox}}{\mathcal{S}}, B\frac{\tilde{Y}_p}{\mathcal{S}+1}\right) \qquad (2.66)$$

where R_R is the fuel burning rate, $\tilde{Y}_f$ is the Favre-averaged mass fraction of the fuel, $\tilde{Y}_{ox}$ is the Favre-averaged mass fraction of the oxidiser, assumed to be O_2, $\tilde{Y}_p$ is the Favre-averaged mass fraction of the products of the reaction, $\mathcal{S}$ is the stoichiometric coefficient calculated as the mass of oxidant per unit mass of fuel and A and B are model constants. The turbulent mixing time can be estimated in RANS computations as the ratio of the turbulent kinetic energy and the dissipation rate $\mathcal{T}_t = \mathcal{k}/\epsilon$. Moreover, the implementation of the ED model in LES will require the introduction of the relevant spatially filtered variables and the estimation of the turbulent mixing time in terms of the rate of strain as $1/\mathcal{T}_t = |\tilde{S}| = \left(2\tilde{S}_{ij}\tilde{S}_{ij}\right)^{1/2}$ [167], [168]. The value for the constants A and B will mainly depend on the type of fuel and usually were assumed to be 4 and 0.5, values that were obtained for a methane flame. However, further studies evidenced that setting values of 0.5 and 0.7 for A and B, respectively, yield more accurate results [56], [61], [62]. In the ED model, an irreversible two step reaction is assumed for the evolution of the volatiles into CO_2 as follows [169]

$$C_aH_bO_cN_d + \alpha_{ED}O_2 \rightarrow aCO + \frac{b}{2}H_2O + \frac{d}{2}N_2 \quad \text{(R 2.2)}$$

$$CO + \frac{1}{2}O_2 \rightarrow CO_2 \quad \text{(R 2.3)}$$

where $\alpha_{ED} = ((a - c)/2) + (b/4)$. The assumption of a turbulent controlled reaction for the ED model reduces its accuracy in particular regions of the simulated domain where the effects of the chemistry kinetics are more important, such as in low temperature regions. The finite-rate eddy dissipation (FR-ED) model, which is a stem of the ED model, incorporates an Arrhenius rate to account for the chemically-limited part of the reaction. The net reaction rate is then assumed to be whichever is the minimum between the chemically-limited part and the turbulence-driven mixing process. The Arrhenius rate in the FR-ED model is obtained after the averaged or filtered flow properties, which are not representative of the mixture, thus reducing its relevance in the reaction limiting.

The eddy dissipation concept (EDC) model is an upgrade to the ED model that allows a full integration of a kinetic mechanism and the turbulent mixing process [170]. In the EDC model, combustion is assumed to occur at characteristic scales in time and space given by [170], [171]

$$\ell_{EDC} = \left(\frac{3C_{D2}}{4C_{D1}^2}\right)^{1/4} \left(\frac{\nu\epsilon}{\mathcal{k}^2}\right)^{1/4} \quad (2.67)$$

$$\mathcal{T}_{EDC} = \left(\frac{C_{D2}}{3}\right)^{1/2} \left(\frac{\nu}{\epsilon}\right)^{1/2} \quad (2.68)$$

where $\mathcal{k}$ is the turbulent kinetic energy, ϵ is the dissipation rate, ν is the kinematic viscosity and C_{D1} and C_{D2} are model constants with values of 0.134 and 0.5, respectively. The EDC has been successfully implemented in RANS simulations using 2 [172] and 4 [173] reaction mechanisms, the results evidenced a better prediction in temperatures and heat flux. However, the associated computational cost was significantly higher in comparison to the ED and ED-FR

cases [174]–[176]. Furthermore, the EDC has been extended into the LES frame, however the case of studies have been focused on gaseous fuels [168], [177], [178].

The possibility of modelling volatile combustion in terms of the transported scalars for the fuel and the oxidiser have been recently employed as an alternative approach to the kinetically controlled models. An additional transported variable that characterize the mixing in the flow field is introduced, it ranges from 0 to 1, corresponding to pure oxidiser and pure fuel, respectively, and it is known as the mixture fraction. Instantaneous relationships that includes the mixture fraction, the thermodynamic state of the species, temperature and the detailed chemistry are tabulated into a database that is used in the prediction of the flame front. Furthermore, a probability density function (PDF) is introduced as a representation of the variation in the mixture fractions at the subgrid level; a β function is often adopted for RANS calculations, while simpler functions, such as the top-hat, are implemented for LES [179].

A turbulent diffusion flame can be considered as an ensemble of one-dimensional flamelet structures that represent the interface between the oxidiser and the fuel [180]. Each flamelet is assumed as a laminar diffusion flame and depends on the local conditions of the flow. The association of the laminar flamelet hypothesis to the calculation of a PDF yields a more accurate prediction of the combustion process; however, its practicality in CFD analyses decreases due the computational time that imposes. The laminar flamelet and variable tracking models had been successfully applied for hydrogen flames [181] and recently in the modelling of pulverised coal combustion [69], [182]–[185]. A detailed characterization of the chemical composition of the volatiles is fundamental for the proper implementation of combustion models that include detailed chemistry. However, this data is often difficult to obtain and simpler approaches, such as the ED model, are preferred for large applications.

2.1.3.2.3. Combustion of char

The progression of the coal particle into char occurs as the volatile matter is released. Char is a porous solid material consisting in large hydrocarbon structures packed around condensed rings of aromatic compounds and usually accounts for 30 to 70% of the mass fraction of the original coal particle. The heterogeneous reaction of char with the oxidiser stream accounts for the majority of the time required for particle burnout [136]. The characteristics of the

char depend on different parameters, such as the type of coal, the devolatilisation temperature, pressure, heating rate and size of the particle; char is mainly constituted of carbon and ash, with presence of hydrogen, oxygen, nitrogen and sulphur in smaller quantities [14].

The oxidising of the char is directly is governed by the chemical structure of the particle, the reactivity of the surface and the composition of the gases surrounding the particle. The char reaction kinetics can be summarized as eight steps, whose two are assumed as reversible thus giving a total of ten heterogeneous reactions given by

$$2C+O_2 \longrightarrow C(O)+CO \quad \text{(R 2.4)}$$

$$C+C(O)+O_2 \longrightarrow CO_2+C(O) \quad \text{(R 2.5)}$$

$$C(O) \longrightarrow CO \quad \text{(R 2.6)}$$

$$C+CO_2 \leftrightarrow C(O)+CO \quad \text{(R 2.7)}$$

$$C(O) \longrightarrow CO \quad \text{(R 2.8)}$$

$$C+H_2O \leftrightarrow C(O)+H_2 \quad \text{(R 2.9)}$$

$$C(O) \longrightarrow CO \quad \text{(R 2.10)}$$

$$C+2H_2 \longrightarrow CH_4 \quad \text{(R 2.11)}$$

where R 2.4 to 2.6 are the oxidation mechanisms and R 2.7 to 2.11 the gasification reactions and $C(O)$ is the oxide complex developed in the carbon surface [186]. The limiting factors in the combustion of char can be due to the superficial reaction kinetics or due to the diffusion of the surrounding gases across the boundary layer and into the particle through the pores. Different processes

predominantly influence the different stages of the char combustion process, thus three different zones occur, namely [22], [169], [187]

i. Zone I is a low temperature and chemically limited region where the relative slow reaction rate allows the replenishing of the burnt oxygen from the surrounding gas.

ii. Zone II is characterized by being both chemically and diffusion controlled. The temperature and the reaction kinetics are faster than in Zone I, and the intrinsic concentration of the oxidiser is lower than in the surrounding gas due to a slower diffusion rate. The density and size of the particle undergoes a reduction process.

iii. Zone III is a high temperature region in which the superficial reactions occurs faster than the diffusion of oxygen through the pores into the particle. The combustion reaction will be take place exclusively at the surface, thus reducing the particle size whilst the density does not suffer sizeable alterations.

The environment achieved under the typical operation of pulverised coal boilers, both in pilot and industrial scales, suggest that the char combustion will develop under Zone II and III conditions [188].

The limit in the diffusion of the oxidiser into the char particle is used as a premise in the simplest models for char combustion [155], [189], however the limiting effect of the chemical kinetics was included into the estimation of the overall reaction rate as an improvement of the diffusion approach [190]. Following, the reaction rate for the combustion of char can be written in terms of the kinetic rate and the oxidiser diffusion as [191], [192]

$$\frac{dm_c}{dt} = A_{s,p} R_d \left(p_{o,\infty} - p_{o,s}\right) = R_c \left(p_{o,s}\right)^n \tag{2.69}$$

where m_c is the mass of the char particle, $A_{s,p}$ is the external superficial area of the particle, R_d is the diffusion rate coefficient, $p_{o,\infty}$ is the bulk partial pressure of the oxidiser, $p_{o,s}$ is the partial pressure of the oxidiser at the particle

surface, R_c and R_d are, respectively, the reaction rate coefficients for the chemically limited and diffusion limited reaction, and n is the apparent reaction order. The chemically controlled kinetic rate, R_c, can be estimated as [187]

$$R_c = A_{s,i} k_c \tag{2.70}$$

where $A_{s,i}$ is the internal superficial area of the char particle and k_c is the overall kinetic rate of the combustion reaction, usually expressed as an Arrhenius expression given by

$$k_c = A_c \exp(-E_c / R T_c) \tag{2.71}$$

where A_c and E_c are the pre-exponential factor and the activation energy of the reaction, R is the universal gas constant and T_c is the temperature of the particle. The reaction rate limited by the diffusion of species is obtained by applying the Fick's law to the boundary layer, in addition the assumption of spherical particles yields [187]

$$R_d = \frac{12 \lambda D_c}{\rho_c {d_c}^2} \left(C_{o,\infty} - C_{o,s} \right) \tag{2.72}$$

where λ is the molar-based stoichiometric coefficient, D_c is the binary diffusion coefficient, ρ_c is the apparent density, d_c is the particle diameter and $\left(C_{o,\infty} - C_{o,s} \right)$ is the difference in the oxidiser concentration between the bulk and the surface of the particle. The diffusion coefficient, D_c, can be approximated following

$$D_c(T,p) = D_c(T_0,p_0)\left(\frac{p_0}{p}\right)\left(\frac{T}{T_0}\right)^{7/4} \tag{2.73}$$

where T_0 and p_0 are reference temperature and pressure, respectively.

In addition to the chemical and diffusion limiters in the char combustion reaction, the particle reactivity, which relies on the extent and accessibility to the oxidiser from the internal pores of the particle is included. The intrinsic reactivity of the char particle can defined as the reaction rate per unit area of pore surface if no restrictions in the mass-transfer mechanisms are assumed [193]. An effectiveness factor, η_c, is introduced to the chemically limited rate expression, given in Equation 2.70, thus

$$R_c = \eta_c A_{s,i} k_c \tag{2.74}$$

The effectiveness factor is the ratio of the actual rate per particle to that obtained under the assumption of no pore diffusion resistance, and it is a function of the Thiele modulus, ϕ, and is given by [187]:

$$\eta_c = \frac{3}{\phi}\left(\frac{1}{\tanh\phi} - \frac{1}{\phi}\right) \tag{2.75}$$

The Thiele modulus is defined as [193]:

$$\phi = \frac{d_c}{2}\left(\frac{A_{s,i}\rho_c R_c C_{o,s}^{n-1}}{D_e}\right)^{1/2} \tag{2.76}$$

where n is the order of reaction and D_e is the effective diffusion coefficient of the oxidiser through the particle pores which is highly dependent on the particle structure and the properties of the oxidiser. The value for the effective diffusion coefficient is obtained by including the effects of the diffusion in the

large and micro scale, usually known as Knudsen diffusion, of the porous structure, thus [187]

$$D_e = \frac{\varphi}{\tau^2}\left[\frac{1}{R_d} + \frac{1}{D_{Kn}}\right]^{-1} \tag{2.77}$$

with

$$D_{Kn} = \frac{d_p}{3}\left(\frac{8RT_c}{\pi M_o}\right)^{1/2} \tag{2.78}$$

where φ is the porosity of the char, τ is the tortuosity, d_p is the pore diameter and M_o is the molecular weight of the oxidiser. Furthermore, the reaction rate of the char combustion that includes the effects from the three different combustion zones can be written as:

$$\frac{dm_c}{dt} = R_c\left(p_{o,\infty} - \frac{dm_c}{dt}\frac{1}{A_{s,p}R_d}\right)^n \tag{2.79}$$

which requires a suitable numerical method for its solution.

The changes in the char particle size and density associated to the combustion process are accounted through a relationship of their initial value and the fractional degree of burnoff, ψ, and it is given by:

$$d_p = d_{p,0}(1-\psi)^{\alpha} \tag{2.80}$$

$$\rho_c = \rho_{c,0}(1-\psi)^{1-3\alpha} \tag{2.81}$$

where $d_{p,0}$ and $\rho_{c,0}$ are the diameter and the density of the char particle prior to the combustion process and α is the burnout mode. The value of α will vary according to the different combustion conditions; for Zone I $\alpha = 0$, thus burning under a constant diameter; in the Zone III region $\alpha = 1/3$, thus allowing the particle to shrink at a constant density. The value of α for the Zone II conditions is dynamic as both the size and density changes, however a value of 0.25 is commonly used [56].

The dynamic variability in the physical structure of the coals and the large difference in length-scales associated to the different phenomena involved, increases the complexity of the char combustion process. Therefore, it is common to employ global reaction rates and optimize them to improve their prediction under certain conditions, such as in oxyfuel combustion.

2.1.4. Radiative heat transfer

Radiative heat transfer describes the energy exchange caused by electromagnetic waves. All materials continuously emit and absorb electromagnetic waves, or photons, at a particular level and wavelengths that directly depends on the temperature of the emitting body [194].

The largely radiative environment of the furnace, and its adequate mathematical representation, is of prime concern in coal combustion modelling, as it considerably influences the prediction of the temperature distributions. In addition, the variations in the combustion environment, as a consequence of the different oxygen enrichment levels in oxyfuel combustion, will alter the reaction kinetics and the overall heat transfer mechanisms [195].

2.1.4.1. Radiative heat transfer in a participating medium

The radiative energy that travels through a continuum is weakened by other bodies absorbing it and the scattering effects, whilst the radiative emissions from the surroundings and the in-scattering phenomena increases it. The radiative flux in a medium can be described through the radiative transfer equation (RTE) given by [194]

$$\frac{\mathrm{d}I_\eta(\mathbf{r},\hat{\mathbf{s}})}{\mathrm{d}\hat{\mathbf{s}}} = \kappa_\eta I_{\eta,b}(\mathbf{r}) - \left(\kappa_\eta + \sigma_\eta\right) I_\eta(\mathbf{r},\hat{\mathbf{s}}) + \frac{\sigma_\eta}{4\pi}\int_{4\pi} \Phi_\eta(\hat{\mathbf{s}},\hat{\boldsymbol{s}}_\iota)\, I_\eta(\mathbf{r},\hat{\boldsymbol{s}}_\iota)\mathrm{d}\Omega \tag{2.82}$$

where $\eta = 1/\lambda$ is a wavenumber and λ is a wavelength in the radiation spectrum, $I_\eta(\mathbf{r},\hat{\mathbf{s}})$ is the radiative intensity at a position $\mathbf{r}$ and direction of propagation $\hat{\mathbf{s}}$, $I_{\eta,b}$ is the Planck function obtained at the temperature observed in the position $\mathbf{r}$, κ_η and σ_η are the absorption and the scattering coefficients, respectively, Φ_η is the scattering phase function and Ω is a solid angle used to compute the integral over a unitary sphere. The terms on the right-hand side of the Equation 2.82 represent the radiative emission, attenuation due to scattering and absorption, and the in-scattering augmentation effect, respectively.

In the CFD calculations, the contribution of the radiative heat transfer to the enthalpy balance, depicted in Equation 2.6, is accounted for by means of the source term S_{rad}. The radiation source term is defined as the divergence of the radiative heat flux in the fluid domain, and is given by

$$S_{rad} = \nabla \cdot q_\eta(\mathbf{r}) = \int_0^\infty \kappa_\eta \left(4\pi I_{\eta,b}(\mathbf{r}) - \int_{4\pi} I_\eta(\mathbf{r},\hat{\mathbf{s}}) \mathrm{d}\Omega \right) \mathrm{d}\eta \tag{2.83}$$

where q_η is the radiative heat flux at a position $\mathbf{r}$ within the domain. The thermal radiation to the walls accounts for the largest portion of the total heat flux in furnaces, thus making its accurate calculation a paramount parameter in the simulation of the overall process. The heat flux at the boundary walls is obtained by means of an energy balance similar to equation 2.83, is as follows

$$q_\eta(\mathbf{r_w}) \cdot \hat{\mathbf{n}} = \int_0^\infty \epsilon_w \left(\int_{\hat{\mathbf{s}}\cdot\hat{\mathbf{n}}<\mathbf{0}} I_\eta(\mathbf{r},\hat{\mathbf{s}}) |\hat{\mathbf{s}} \cdot \hat{\mathbf{n}}| \mathrm{d}\Omega \right) - \epsilon_w \pi I_{\eta,b}(\mathbf{r_w}) \mathrm{d}\eta \tag{2.84}$$

where $\mathbf{r_w}$ is a location in the wall, $\hat{\mathbf{n}}$ is the vector normal to the surface of the wall and ϵ_w is the emissivity of the wall, a property of the material that represents the effectiveness in the emission of thermal radiation. The solution of the RTE involves the spatial integration of the radiative heat flux, hence the evaluation over the discretized spectrum is often employed. Different numerical approaches have been developed for this purpose based on the spatial and

angular discretization of the domain space, and these techniques include the discrete transfer (DTM), the discrete ordinates (DOM) and the Monte Carlo method [194].

The DTM method employs the direction between two points, $\mathbf{r}_n$ and $\mathbf{r}_{n+1}$, in the domain for the estimation if the radiative intensity, which is defined as [196]

$$I_\eta(\mathbf{r}_{n+1},\hat{\mathbf{s}}) = I_\eta(\mathbf{r}_{n+1},\hat{\mathbf{s}})\tau_{n\to n+1} + S_\eta(1-\tau_{n\to n+1}) \tag{2.85}$$

where $\tau_{n\to n+1}$ is defined as the transmissivity across the path between $\mathbf{r}_n$ and $\mathbf{r}_{n+1}$, and S_η is the radiative source function. The nodal transmissivity is given by

$$\tau_{n\to n+1} = \exp\left(\int_n^{n+1} -\beta \mathrm{d}s\right) \tag{2.86}$$

where the integration operation is performed over the path $s = |\mathbf{r}_{n+1} - \mathbf{r}_n|$, and $\beta = (\kappa + \sigma)$ is known as the extinction coefficient. Moreover, the radiative source function can be described as

$$S_\eta = (1-\varpi)I_{\eta,b,n+1/2} + \frac{\varpi}{4\pi}\left[\frac{4\pi\sum_i \bar{I}(\hat{\boldsymbol{s}}_i)\delta\Omega_i}{\sum_i \delta\Omega_i}\right] \tag{2.87}$$

where $\varpi = \sigma/\beta$, $\bar{I}(\hat{\boldsymbol{s}}_i)$ is the mean intensity between that measured at $\mathbf{r}_n$ and $\mathbf{r}_{n+1}$, $\delta\Omega$ represents the discrete intervals of the solid angle.

A finite number of rays are traced from the boundaries through the domain; the radiative energy absorbed and emitted from each of the control volumes is calculated and a radiative source function is obtained after the net intensity in the volume. The solution of the radiative intensity becomes iterative as the

traced rays are scattered or reflected from the wall. Further, the accuracy of the results is directly proportional to the number of traced rays.

The DOM method employs a finite volume approach for the approximation of the spatial evolution of the radiative intensity while a Gaussian quadrature is used in the estimation of the angular integral, hence [197]

$$\int_{4\pi} I(\mathbf{r},\hat{\mathbf{s}})\mathrm{d}\Omega \approx \sum_{i=1}^{n} w_i I(\mathbf{r},\hat{\mathbf{s}}_i) \tag{2.88}$$

where w_i is a weighting factor associated to the radiative intensity of the direction $\hat{\mathbf{s}}_i$ and n is the number of directions, or ordinates, used in the quadrature estimation. As the number of directions in the quadrature increases, the accuracy of the prediction is enhanced, thus reaching an exact solution if the number of ordinates tend to infinity. The employment of the DOM in CFD calculations is very popular as its implementation is straightforward and the level of accuracy obtained is directly proportional to the computational power.

A stem of the DOM model is known as the finite volume method (FVM) for the radiation and employs a discretisation of the angular integral into a finite number of non-overlapping intervals that are subsequently solved using the finite volume method [198]. The advantage of the angular discretisation in the FVM is that it can be easily adapted to irregular geometries and unstructured meshes without losing accuracy, thus illustrating a great flexibility in its usability [199].

The Monte Carlo approach employs a statistical sampling technique to obtain the radiative intensity; the history of a statistically meaningful random sample of photons are traced from their point of emission to their point of absorption or up to its intensity depletion. The position of the traced rays and its wavenumber in the spectrum is assigned stochastically, usually between 10^5 and 10^7 sampled paths are drawn in a Monte Carlo simulation. The fast selection of the ray origins and paths is important for the simulation efficiency, and sets of random numbers from previous tabulations were stored in separate files and used as an index for the allocation of the sampled rays. However, the amount of storage required for these files imposed additional restrictions in the implementation of the Monte Carlo method. The use of parallel routines, known as

pseudorandom number generators have been adopted lately, but they still need to be tested and adjusted before their coupling into the simulation [194]. The inclusion of all the important associated phenomena in radiative heat transfer without requiring numerical approximations is the major attribute to the Monte Carlo method, nevertheless the large number of rays required to achieve an accurate solution, and the associated computer cost, diminish its suitability for CFD analyses [200].

The differences observed in the absorption coefficient for each of the wavelengths contained in the energy spectrum represents a challenge in the modelling of radiative environments. Different numerical approaches have been developed in order to predict the properties of the participating medium, such as the absorption coefficient, without the necessity of a high resolution partitioning of the energy spectrum. The composition of the combustion environment, and its alterations while under oxyfuel conditions, directly influences the overall radiative heat transfer, as the absorption and emission properties of the different compounds in the medium vastly differ between them [201]. The models derived for the calculation of the spectral radiative heat transfer can be grouped into the line-by-line, narrow and wide band calculations and the global approach.

The line-by-line model applies detailed information for each of the spectral lines that are usually gathered from databases of the spectrometry measurements, such as HITRAN [202] or HITEMP [203]. Due to the large variations in the absorption coefficient, the integration over the spectrum of the radiative heat transfer must be performed using several hundred thousand wavenumbers. The results produced by the line-by-line model are highly accurate; however, they take up a large amount of computational power. Nevertheless, the line-by-line method is commonly used as a benchmark in order to validate further developments in spectral modelling [194].

In narrow band calculations, the line-based absorption coefficient is replaced for a smoothened value that is valid over a narrow range of the spectrum. Different models have been developed under this assumption, including the statistical narrow band model, the Elasser approach and the narrow band k-distribution. The spectrally averaged, or narrow band, values of the absorption coefficient and the emissivity are computed after the spacing and the relative strength of each band contained within the partition. The Elasser model assumes that the lines in the band are equally spaced and hold equal intensities, whilst the statistical model assume randomness in both the line spacing and in

the intensity value [194]. In the narrow band k -distribution, the spectrally averaged absorption coefficient is re-ordered using a k-distribution function based on the field variables relevant to the absorption coefficient, such as the pressure, temperature and gas composition [204].

Wide band models rely on the relative constant value for the blackbody intensity across a rotational-vibrational band of the energy spectrum. Wide band correlations can be obtained by integrating the results of the narrow band approach over the entire band. A well-known approach is the exponential wide band model which employs a direct integral of the spectral absorptivity over the band width [205]. The wide band models were popular in the past due to the simplicity in their calculations and the lack of highly detailed spectral data, however it is acknowledged that, in some cases, the error might be as high as 70% [194]. Recent developments have used the high definition data available nowadays to produce highly efficient computer codes that compute the radiative intensity using a wide band approach faster than the counterpart using a global approach [206].

A more practical approach is to obtain mean values for the absorption and emissivity of a gas based on its composition and the conditions of the environment, such as the temperature and pressure. A function fitted to experimental data or more detailed results, such as the narrow band or line-by-line models, is used to estimate the radiative properties of the gas [52], [194]. Furthermore, different models have been developed to account for the total radiative intensity using a global approach, noteworthy methodologies are the weighted sum of grey gases (WSGG) model and the full-spectrum correlated k-distribution (FSCK).

The WSGG model was developed in the context of the zonal method, however it was later applied to the general radiative transfer equation depicted in Equation 2.82 [207]. In the WSGG model the emissivity of the fluid is approximated as the weighted contribution of N gases assumed to be grey, namely

$$\epsilon = \sum_{n=0}^{N} a_n [1 - \exp(\kappa_n p \mathbf{s})] \tag{2.89}$$

where ϵ is the overall emissivity of the medium, a_n is the weighting coefficient for the grey gas n, κ_n is the absorption coefficient of the grey gas n, p is the partial pressure of the species contained in the medium, and $\mathbf{s}$ is the path length of the emission. Tabulated values for the gas emissivity obtained from more detailed models are used to acquire values for the weighting and absorption coefficients, the tabulated data is often produced as a relationship of the gas composition, temperature, pressure and beam lengths [194]. Moreover, the gas evaluated in $n = 0$ is considered as a transparent gas, hence containing an absorption coefficient $\kappa_0 = 0$ and is used to encompass the windows that might be generated while computing the spectrum. The beam length is often estimated as a geometric relationship following [194]

$$\mathbf{s} = \frac{3.6V}{A} \tag{2.90}$$

where V is the volume of the domain and A is the surface area that intervenes in the radiative exchange. A rearrangement of Equation 2.89 allows the calculation of an effective absorption coefficient for the grey gas given by

$$\kappa_{eff} = -\frac{\ln(1-\epsilon)}{\mathbf{s}} \tag{2.91}$$

The tabulated data employed in the WSGG model are usually generated under controlled conditions or numerically by the narrow band or line-by-line models, therefore its validity must be examined prior to its implementation. In oxyfuel conditions, the higher concentration of CO_2 and water vapour affects the overall transfer of the radiative heat. Recent studies have documented updated values for air-fired combustion that were obtained using different refinements and high definition experimental databases such as HITEMP2010 [208], [209]. In addition, weighting coefficients suitable for oxy-fuel environments have been obtained after different models such as the exponential wide band model [210], statistical narrow band model [211], [212] and the line-by-line approach [213], [214].

The WSGG model is a computationally cheap approach in the calculation of the radiative heat transfer, however the reliance on the fluid composition, usually a simulated variable itself, for the estimation of the weighting coefficient increase the uncertainty in the predictions [56], [215], [216]. Despite its acknowledged drawbacks, the WSGG model is a common approach for CFD calculations [71], [217], [218], but advising caution while employing it.

The full-spectrum correlated k-distribution (FSCK) is a global model that employs the Planck function as weighting mechanism for a set of k-distributions and it is given by [219]

$$f(\bar{\phi},T,k) = \frac{1}{I_b(T)} \int_0^{\infty} I_{\eta,b}(T,\eta)\, \delta\left(k - \kappa(\bar{\phi})\right) \mathrm{d}\eta \tag{2.92}$$

where $f(\bar{\phi},T,k)$ is the full-spectrum k-distribution, $\bar{\phi}$ is the conditions that influence the absorption coefficient arrange in a vector form, $I_b(T)$ is the blackbody intensity, $I_{b\eta}(T,\eta)$ is the Planck function and δ is the Dirac delta. Following, the local absorption coefficient, $\kappa(\bar{\phi})$, is calculated as a value correlated to a reference state $\bar{\phi}_0$

$$\kappa(\bar{\phi}) = k^*\left(\bar{\phi}, \kappa(\bar{\phi}_0)\right) \tag{2.93}$$

where k^* is the correlation function. In addition, the k-distributions for the full-spectrum can be obtained from pre-computed narrow band k-distributions and thus

$$f(\bar{\phi},T,k) = \sum_{n}^{N_{bands}} \frac{\int_{\Delta\eta} I_{\eta,b}(T)\mathrm{d}\eta}{I_b(T)} f_n(\bar{\phi},k) \tag{2.94}$$

where N_{bands} corresponds to the number of bands in the narrow band calculation, $\Delta\eta$ is the width of the band and $f_n(\bar{\phi}, k)$ is the k-distribution of the narrow band n. The implementation of the FSCK model into the CFD calculations require to pre-compute the full-spectrum of the k-distributions for different conditions and then interpolate them to the desired state [204], [220], [221]. Comparison of the CFD results generated by the FSCK model to the benchmark cases using line-by-line and narrow band results [222]–[224], as well as in combustion applications [56], suggests that the model produces accurate results without the computational cost of the spectral approaches.

2.1.4.2. Radiative heat transfer in particles

In coal combustion furnaces, a large amount of particulate matter remains entrained thus contributing to the transfer of radiative heat. The temperature reached at the particle surface, as a result of the heterogeneous reactions, is often higher than that measured in the surrounding medium. In addition, the thermal properties of the particle evolve from the highly radiative behaviour of coal, char and soot particles to the large scattering effect of the ash. Furthermore, the effects of oxyfuel conditions in the radiative heat transfer of the particle are directly associated to the localized high temperature regions.

An equivalent coefficient for the absorption and scattering contribution from a cloud of particles is calculated using a cross-sectional approach [194], namely

$$\kappa_p = \int_0^\infty n(r) C_{abs} \mathrm{d}r \tag{2.95}$$

$$\sigma_p = \int_0^\infty n(r) C_{sca} \mathrm{d}r \tag{2.96}$$

where κ_p is the effective absorption coefficient and σ_p is the effective scattering coefficient, $n(r)$ is a particle distribution function in a volume of radius r, C_{abs} is the absorption cross-section and C_{sca} is the scattering cross section. Similarly, the energy dispersed by the particle cloud can be obtained through an integration over the cross section, however the Planck function evaluated at the particle temperature, T_p, is included as weighting factor, thus giving

$$E_{\eta,p} = \int_0^{\infty} n(r) C_{abs} I_{\eta,b}(T_p) \mathrm{d}r \tag{2.97}$$

The scattering phase function is obtained from

$$\Phi_p(\hat{\mathbf{s}}, \hat{\boldsymbol{s}_i}) = \frac{1}{\sigma_p} \int_0^{\infty} n(r) C_{sca} \Phi(\hat{\mathbf{s}}, \hat{\boldsymbol{s}_i}) \mathrm{d}r \tag{2.98}$$

where $\Phi_p(\hat{\mathbf{s}}, \hat{\boldsymbol{s}_i})$ is the effective phase function in the scattering direction $(\hat{\mathbf{s}}, \hat{\boldsymbol{s}_i})$ and $\Phi(\hat{\mathbf{s}}, \hat{\boldsymbol{s}_i})$ is the phase function of a single particle. The incorporation of the particulate effects into the RTE presented in Equation 2.82 yields [194]

$$\begin{aligned} \frac{\mathrm{d}I_\eta(\mathbf{r},\hat{\mathbf{s}})}{\mathrm{d}\hat{\mathbf{s}}} = \kappa_\eta I_{\eta,b}(\mathbf{r}) + E_{\eta,p} - \left(\kappa_\eta + \sigma_\eta + \kappa_p + \sigma_p\right) I_\eta(\mathbf{r},\hat{\mathbf{s}}) \\ + \frac{\sigma_p}{4\pi} \int_{4\pi} \Phi_p(\hat{\mathbf{s}}, \hat{\boldsymbol{s}_i})\, I_\eta(\mathbf{r},\hat{\boldsymbol{s}_i}) \mathrm{d}\Omega \end{aligned} \tag{2.99}$$

The size of the particles affect the transfer of the radiative heat; for the case of small particles, such as soot and molecular gaseous particles, the scattering and extinction efficiencies are evaluated after the Rayleigh scattering theory. In contrast, the larger particles, such as coal, char and ash, exhibit noticeable scattering effects and their contribution to the radiative exchange must be accounted for through a more comprehensive methodology, such as the Mie theory [194].

In cloudy combustion environments, a common approach in the calculation of the optical properties is to assume a constant absorption and scattering efficiency. The estimation of an overall value for the radiative properties is based on experimental data, such as the Fourier-transform infrared (FT-IR) spectroscopy [225], [226]. The absorption efficiency of the char is commonly set between 0.85 and 0.95, furthermore the value for the suspended ash is agreed to be inferior however it has not been widely validated. The optical properties

evaluated for environment filled with both coal and char particles remain similar across different coal types, nevertheless data is available for a wide range of coal ranks [227], [228].

In addition to the vibration-rotation bands in the spectrum that account for the majority of the radiative heat transfer, there are some wavelengths that emit radiation in the form of light. The vast majority of the combustion processes are luminous and therefore are visible to the human eye. The luminous emission in coal combustion comes from soot particles, and their contribution to the radiative heat transfer is often enclosed in the estimation of the optical properties of the suspension. The light emitted, in contrast, does not contributes to a great extent in the heat transfer but it can be used in the evaluation of the overall combustion performance [194].

2.2. Spatial and temporal coherence assessment

The classical definition of turbulent flows implies a chaotic and random arrangement of vortices that move and interact within a continuum. The asymptotic, or mature, turbulence generated as the fluid flows through the domain is often considered as more important than the level of turbulence observed as initial conditions. However, in turbulent flows, a certain amount of the initial conditions of the flow are retained despite the complexity of the phenomenon. The lingering turbulence information is associated to the dynamic invariants of the flow which are a direct result of the laws of conservation of linear and angular momentum [79].

The evolution of the turbulent motion after the initial conditions provides, up to certain degree, repeatability or coherence to the flow and in some cases allows the formation of three-dimensional structures. The ability of a flow to repeat itself in an orderly fashion enhances the sustainability of more complex phenomena, such as combustion. Furthermore, the adequate analysis and prediction of the flow coherence is paramount in the control and improvement of any associated processes. In the following sections, different methodologies for the assessment of the coherence of a flow are introduced. These methodologies are based on a statistical and data-driven approaches, and includes techniques for the evaluation of the temporal, spatial and spatiotemporal coherence.

2.2.1. Spectral analysis and signal correlations

Turbulence is dominated by the motion of the large, energy bearing, eddies which subsequently enhance the diffusivity and the stresses in the flow. Large eddies remain in the domain longer and can travel large distances, therefore

the diffusivity and the stresses are built upon the flow history and are not necessarily functions of local properties. Furthermore, the large turbulent structures dictate the rate of dissipation of energy through the smaller turbulent eddies and eventually the viscous effects, thus effectively influencing the overall fluid flow. The motion at any point in the turbulent flow affects the motion of distant points downstream by means of the pressure field, thus preventing the utilization of mean values associated to single particles in the representation of the flow. It can be established that turbulent flows are less random and more organised than the molecular motion, and that in order characterise the organization of the flow, instantaneous and mean values of the flow variables for two or more particles, and the interactions among them must be included [88], [229].

The temporal evaluation of the fluid properties at a particular location in the domain will produce a signal. In experimentation and CFD modelling is common to sample or record fluid variables at a certain rate, thus creating discrete-time signals. The rapid fluctuations of the flow variables often generate signals that are complex to analyse qualitatively, thus requiring to be analysed by different means. The discrete Fourier transforms (DFT) allow the conversion of the evidence of the temporal evolution of the flow into the frequency domain where underlying information, such as the temporal repeatability of the signal, can be acquired. The signal is decomposed into its constituent frequency components, the range of frequencies in which the signal is contained is known as the frequency spectrum [230].

For a function $u(t)$, which contains information of the flow and is time-dependant, with a period T, sampled at N equally spaced times during the period, the discrete Fourier transform will define N coefficients related to a Fourier series that represent a discrete spectral representation of $u(t)$. The time interval, Δt, is defined by

$$\Delta t = \frac{T}{N} \tag{2.100}$$

with sampling times given by

$$t_j \equiv j\Delta t, \quad \text{for} \quad j = 0,1,\ldots,N-1 \tag{2.101}$$

Each sample of $u(t)$ is defined as

$$u_j \equiv u(t_j) \tag{2.102}$$

The complex coefficients of the DFT, $\tilde{c}_k$, are determined for $1 - 1/2\,N \leq k \leq 1/2\,N$, where k is a wavenumber, by

$$\tilde{c}_k \equiv \frac{1}{N}\sum_{j=0}^{N-1} u_j \exp^{-i\omega_k t_j} = \frac{1}{N}\sum_{j=0}^{N-1} u_j \exp^{-2\pi i jk/N} \tag{2.103}$$

where, in analogy to the Fourier series, the frequency ω_k is given by

$$\omega_k = \frac{2\pi k}{T} \tag{2.104}$$

One of the advantages of the DFT is that the generated modes are orthogonal, thus giving independence among the modes [81]. The DFT is only defined for a sequence of finite-duration and despite that it can be directly computed, the straightforward implementation is inefficient for large number of samples. In order to obtain one sample of $\tilde{c}_k$ using the direct DFT approach, N complex multiplications and $N-1$ complex additions are required, thus forcing the solution of N^2 complex multiplications and $N(N-1) \simeq N^2$ complex additions to obtain the complete set of coefficients. In addition, the overall set of coefficients will have a size N^2 which might produce complications for its digital storage and manipulation. Since the number of DFT computations is a quadratic ratio of N, its implementation for a large data set is not practical [231]. Different

methodologies have been developed to improve the efficiency of DFT calculations; these are collectively known as the fast Fourier transform (FFT) algorithms [232].

The FFT algorithms are constructed in a way that the number of computations is constant per data sample, thus the total amount of operations will vary linearly with respect to N. Most of the operations realized while computing DFT are repetitive, hence periodicity and symmetry properties can be applied. For $W_N = \exp^{-2\pi i/N}$, the periodicity property is given by [231]

$$W_N^{kj} = W_N^{k(j+N)} = W_N^{(k+N)j} \tag{2.105}$$

while the symmetry property is as follows

$$W_N^{kj+N/2} = -W_N^{kj} \tag{2.106}$$

Furthermore, the sequence N can be divided into M smaller sections of length L, thus $N = LM$ and $L^2 + M^2 \ll N^2$ for a large N. The divide-and-combine approach take M smaller L-point DFT, and combine them into a larger transform using L smaller M-point DFT. Then j and k can be re-written as [231]

$$j = M\ell + m, \;\; 0 \leq \ell \leq L-1, \;\; 0 \leq m \leq M-1 \tag{2.107}$$

$$k = p + Lq, \;\; 0 \leq p \leq L-1, \;\; 0 \leq q \leq M-1 \tag{2.108}$$

Since $\tilde{c}_k$ and u_j can be written as the arrays $\tilde{c}(p,q)$ and $u(\ell,m)$, respectively, Equation 2.103 takes the form

$$\begin{aligned}\tilde{c}(p,q) &= \sum_{m=0}^{M-1}\sum_{\ell=0}^{L-1} u(\ell,m) W_N^{(M\ell+m)(p+Lq)} \\ &= \sum_{m=0}^{M-1}\left\{W_N^{mp}\left[\sum_{\ell=0}^{L-1} u(\ell,m) W_N^{M\ell p}\right]\right\} W_N^{Lmq} \\ &= \underbrace{\sum_{m=0}^{M-1}\left\{W_N^{mp}\underbrace{\left[\sum_{\ell=0}^{L-1} u(\ell,m) W_L^{\ell p}\right]}_{L\text{-point DFT}}\right\} W_M^{mq}}_{M\text{-point DFT}}\end{aligned} \tag{2.109}$$

The solution of Equation 2.109 is usually implemented as a three-step procedure, starting by the calculation of the L-point DFT array for each of the columns $m = 0,\ldots,M-1$ given by

$$F(p,m) = \sum_{\ell=0}^{L-1} u(\ell,m) W_L^{\ell p}; \quad 0 \le p \le L-1, \tag{2.110}$$

Followed by the modification of the array $F(p,m)$, thus obtaining

$$G(p,m) = W_N^{pm} F(p,m); \qquad \begin{matrix} 0 \le p \le L-1 \\ 0 \le m \le M-1 \end{matrix} \tag{2.111}$$

where W_N^{pm} is known as the twiddle factor. Finally, the M-point DFT for the rows $p = 0,\ldots,L-1$, is obtained following

$$\tilde{c}(p,q) = \sum_{m=0}^{M-1} G(p,m) W_M^{mq}; \quad 0 \le q \le M-1 \tag{2.112}$$

The total number of complex multiplications, C_N, for this approach is less than in the direct DFT approximation, and can be accounted for by the following expression:

$$C_N = ML^2 + N + LM^2 < N^2 \tag{2.113}$$

The divide-and-combine procedure can be repeated whenever M or L are composite numbers, and it becomes more efficient when N is a highly composite number in the form of $N = R^v$. The algorithms that employs the multiple divide-and-combine approach are called the radix-R algorithms, with the radix-2 FFT calculation being the most widely employed [231].

In the radix-2 FFT calculation $N = 2^v$ with $M = 2$ and $L = N/2$, moreover $u(k)$ is separated into two point sequences of $N/2$ in length according to

$$\begin{matrix} g_1(j) = u(2j) \\ g_2(j) = u(2j+1) \end{matrix} \; ; \quad 0 \le j \le \frac{N}{2} - 1 \tag{2.114}$$

where $g_1(j)$ and $g_2(j)$ contain the even-ordered and the odd-order samples of $u(j)$, respectively. For the assumption of $G_1(k)$ and $G_2(k)$ as the respective DFT of $g_1(j)$ and $g_2(j)$, the solution for the coefficients is obtained through a merging operation given by [231]

$$\tilde{c}_k = G_1(k) + W_N^k G_2(k), \quad 0 \le k \le N - 1 \tag{2.115}$$

The number of complex multiplications, after using the radix-2 FFT methodology, is reduced to

$$C_N = \frac{N^2}{2} + N \tag{2.116}$$

which is of the same order of magnitude as N^2 for large values of N. The procedure can be repeated continuously, thus decimating the sequence and combining the smaller DFT. The decimation process will effectively terminate when a number of N one-point sequences are generated and their correspondent DFT are obtained. The procedure resulting from the solution of the coefficients is known as the decimation-in-time FFT algorithm which has an associated number of complex multiplications given by [231]

$$C_N = N\nu = N\log_2 N \tag{2.117}$$

which satisfies the linearity condition for large values of N. The methodology for the decimation-in-time FFT of a finite signal is available on a wide variety mathematical processing softwares, such as MATLAB, where additional subroutines are incorporated in order to accelerate the computation and improve the storage of intermediate data [231].

The analysis of the spectrum of frequencies derived from transient signals that contains flow information allows a better comprehension of the temporal dynamics of the turbulent motion, however these only represent the behaviour of the flow in a particular location. In contrast, the degree of interdependence between different locations, and the similarity of the flow information across various recorded signals provides a comprehensive characterisation of the flow [81].

For two data sequences, $u_1(j)$ and $u_2(j)$, of the flow information that were simultaneously sampled and contain N data, the cross-correlation is defined as [230]

$$r_{12} = \frac{1}{N}\sum_{j=0}^{N-1} u_1(j)u_2(j) \tag{2.118}$$

The general definition of the cross-correlation given in Equation 2.118, might produce inaccurate results when the signals are out of phase. The phase difference, or lag, in signals might be the result of a delay in the measurement or evidence of the influence of one location on the other. In order to avoid the miscalculation of the cross-correlation, one of the signals is shifted in order to improve the alignment. The signal $u_2(j)$ is effectively converted to $u_2(j+s)$, where s is the amount of sampling points shifted that were required in the alignment of the signals. The cross-correlation is then obtained by [230]

$$r_{12}(s) = \frac{1}{N}\sum_{j=0}^{N-1} u_1(j)u_2(j+s) \tag{2.119}$$

The phase shift between two signals is usually unknown, so the cross-correlation is commonly computed for different lags and the largest value of the correlation is assumed to be the most relevant. The shifting of the signal will inevitably shorten it and values with no pair products will be produced. This is known as the end effect and it is corrected by adding the value of $sr_{12}(0)/N$ to the remaining samples of the signal [233].

In order to standardize the analysis of the cross-correlations, a normalization procedure is often employed, and this allows the direct comparison of the correlation of finite signals regardless of the absolute data values. The normalized expression for the cross-correlation is known as the cross-correlation coefficient and its given by [234]

$$\chi_{12}(s) = \frac{r_{12}(s)}{\frac{1}{N}\left[\sum_{j=0}^{N-1} u_1^2(j)\ \sum_{j=0}^{N-1} u_2^2(j)\right]^{1/2}} \tag{2.120}$$

A particular case of the auto-correlation occurs when the signal is correlated to itself and no lag is assumed. This is known as the autocorrelation and is calculated by

$$r_{11}(0) = \frac{1}{N}\sum_{j=0}^{N-1} u_1^2(j) = E_{11} \tag{2.121}$$

where E_{11} is the normalized energy contained in the signal.

The spectral analysis has been widely used in fluid dynamics to analyse the behaviour of flows [128], [235], [236], while employing data collected experimentally [237]–[239] and, later, numerically [240]–[244]. However, the availability of high resolution data in addition to the increment in the computational power has led to the development of more efficient methodologies for the analysis of turbulent flows. Nevertheless, the results obtained from the direct spectral analysis still represents the workhorse in the evaluation of the fluid coherence due to its simplicity and wide implementation in commercial software.

2.2.2. The proper orthogonal decomposition

In order to understand the dynamics of flows and the transport processes associated to it, the underlying coherent features must be estimated and carefully analysed. The assessment of the disturbances in intricate geometries and complex applications, such as in combustion chambers, allows a better understanding of the transitional phenomena and instability mechanisms [245].

Analyses of the global stability by direct methods, such as the spectral analyses, become prohibitively as the number and the resolution of the samples increase, thus requiring iterative schemes to acquire the stability modes. Furthermore, the iterative approaches rely on statistical values of the flow from which a series of artificial flow fields are constructed until convergence is reached. The statistical values of the flow field, however, are commonly unknown, hence a robust methodology for the coherence analysis of the flow should be based exclusively on the sampled data[245].

The proper orthogonal decomposition (POD) is a global analysis technique that decomposes the field of any flow scalar into a sum of weighted, linear, basis functions known as modes [246], [247]. The development of the POD analysis spans across nearly three decades and it has received different names based on its application and fellow developers, such as the principal component analysis [248], the Hottelling transform [249], the Karhunen-Loeve transform [250], [251] and singular value decomposition [252]. The pertinence of the application of the POD analyses to finite data became noticeable as the size in the databases generated either empirically or numerically increased, however

a common misconception that the classical method [246] could only be employed for one-dimensional data prevented its popularization. A further evolution of the classical method known as the snapshot method, demonstrated that it was possible to compute the empirical eigenfunctions of three-dimensional data without requiring any approximations [253]. The method of snapshots for the calculation of the POD is the preferred approach in the analysis of turbulent flows as it provides the versatility to analyse sampled data in two or three dimensions by using the same algorithm. Different numerical algorithms have been designed to improve the computation process of the POD, with the calculation in terms of the singular value decomposition (SVD) being regarded as the most efficient and straightforward [254]. The procedure for the calculation of the POD using the snapshot method in terms of the SVD will be describe thereafter.

In the snapshots method is required to obtain a finite series of data in the form of a vector field given by

$$a(\mathbf{r}, t_j) = \begin{bmatrix} a(\mathbf{r}_{1,1}, t_j) & a(\mathbf{r}_{1,2}, t_j) & \cdots & a(\mathbf{r}_{1,q}, t_j) \\ a(\mathbf{r}_{2,1}, t_j) & a(\mathbf{r}_{2,2}, t_j) & \cdots & a(\mathbf{r}_{2,q}, t_j) \\ \vdots & \vdots & \ddots & \vdots \\ a(\mathbf{r}_{p,1}, t_j) & a(\mathbf{r}_{p,2}, t_j) & \cdots & a(\mathbf{r}_{p,q}, t_j) \end{bmatrix} \tag{2.122}$$

where a is the flow variable of interest, $\mathbf{r}$ is a spatial coordinate and the index j denotes the j-ith time step of the sample. Each vector field is compressed into a single column vector in the form of [42]

$$a(j) = \begin{bmatrix} a(\mathbf{r}_{1,1}, t_j) \\ a(\mathbf{r}_{1,2}, t_j) \\ \vdots \\ a(\mathbf{r}_{2,1}, t_j) \\ \vdots \\ a(\mathbf{r}_{q,p}, t_j) \end{bmatrix} \tag{2.123}$$

The vector $a(j) \in \mathbb{R}^m$ is called a snapshot of the data; the value of m will depend on the size of the original vector field and the number of flow variables

contained in the sample and this value is usually a big number. The arrangement of the vector field into a single column removes the spatial relationship between neighbours but allows to perform inner vector products to compare different temporal states. The set of flattened snapshots obtained from the original data can be arranged into a single matrix, thus [42]

$$A = \begin{bmatrix} | & | & & | \\ a(1) & a(2) & \cdots & a(n) \\ | & | & & | \end{bmatrix} \tag{2.124}$$

The POD of the data matrix A is obtained by performing the SVD that is defined as

$$A = U\Sigma V^T \tag{2.125}$$

where U and V are orthogonal matrices of size $U \in \mathbb{R}^{q\times q}$ and $V \in \mathbb{R}^{p\times p}$. The matrix Σ is of a diagonal type where the values are the non-negative square roots of the eigenvalues of A^TA and they are known as singular values or principal values [255]–[257].

A matrix consisting of the inner products of the columns of A is used to compute the values of V and Σ by correlating its eigendecomposition to the SVD as follows [42]

$$A^TA = V\Sigma U^T U\Sigma V^T = V\Sigma^2 V^T \tag{2.126}$$

$$A^TAV = V\Sigma^2 \tag{2.127}$$

The spectral decomposition of A^TA allows the generation of the n leading columns of U, which are the POD modes, as

$$U = AV\Sigma^{-1} \tag{2.128}$$

It is common practice in the analysis of inhomogeneous flows to subtract the mean value of the scalar $a(j)$ prior to the computation of the POD modes, thus providing more significance to the oscillatory modes computed [42]. The matrices U and V contain the spatial and temporal correlations of A, respectively. In POD analyses, however, only the spatial coherence information contained in U is often desired and the remaining data of Σ and V is disregarded. Further developments in reduced order modelling have been made in order to incorporate the temporal component into the assessment of the coherence in dynamics systems, and that is the case of the dynamic mode decomposition.

POD analyses have be widely used in the assessment of complex phenomena such as swirling flows [258]–[262] and combustion applications [263]–[269]. Furthermore, the application of the POD technique for results obtained from CFD analyses allowed the characterization of the flow field in terms of its spatial coherence and provided a deeper insight into the complex dynamics of the turbulent motion and its associated phenomena, such as the system stability. The coupled POD-CFD studies have been successfully applied to isothermal, non-reacting flows [270]–[275] and in combustion environments [276]–[280].

Despite broadening the comprehension of the turbulent flows, POD analyses exhibit two major acknowledged drawbacks, namely the incorrect procedure to rank the importance of the structures captured by the methodology and the loss of phase information due to the second-order statistics employed in the formulation of the decomposition. Different weighting function have been employed to provide a better arrangement on the modes, thus overcoming the first handicap. The second shortcoming is more complex to solve and requires the reconstruction of the decomposition procedure [245].

2.2.3. The dynamic mode decomposition

The purpose of the experimental and computational fluid dynamics is to provide a description of the flow that is objective and that can be quantified. An accurate description of the flow is paramount in the comprehension of the underlying, relevant processes and it is the foundation for the development of novel fluid technologies. A well-known approach to obtain the relevant information from the flow is to employ a series of measurements, from experimental tests or computer simulations, to extract the dynamic characteristics of the

fluid motion [281]. The dynamic mode decomposition (DMD) is a data-driven method used for the analysis of complex and dynamic systems. Unlike POD analyses, the DMD utilize the time correlations and rearrange the spatial coherent modes, thus enforcing that the dominant patterns remain coherent both in time and space [42], [282].

In the DMD, the relationship between pairs of measurements is analysed. The measurements $a(j)$ and $a(j+1)$, where j denotes a temporal iteration in the data, are assumed to be correlated by a linear operator given by [283]

$$a(j+1) \approx Ba(j) \tag{2.129}$$

where $a \in \mathbb{R}^m$ and $B \in \mathbb{R}^{m \times m}$, and it is adopted for all pairs of measurements. The principle of the DMD methodology is to find the best fit-solution for B.

For finite transient data sets, each measurement, $a(t)$, is collected at regular time intervals Δt, described as $a(j) = a(j\Delta t)$. Each measurements in known as a snapshot of the field in similar fashion to the POD analysis. Two sequence of snapshots can be constructed as following

$$A = \begin{bmatrix} | & | & & | \\ a(1) & a(2) & \cdots & a(n-1) \\ | & | & & | \end{bmatrix} \tag{2.130}$$

$$A' = \begin{bmatrix} | & | & & | \\ a(2) & a(3) & \cdots & a(n) \\ | & | & & | \end{bmatrix} \tag{2.131}$$

where n is the number of samples obtained from the flow, and A' is the time-shifted snapshot matrix. Appling the relationship described in Equation 2.129, it can be written that

$$A' = BA \tag{2.132}$$

The DMD of the pair of data matrices A and A' is defined as the eigendecomposition of the matrix B and it is given by

$$B = A'A^{\dagger} \tag{2.133}$$

where the superscript † denotes the Moore-Penrose pseudoinverse which can be efficiently computed using the SVD. The SVD of A yields a decomposition in the form of Equation 2.125, which can be further expanded to [283]

$$A = U\Sigma V^T = [\widetilde{U} \quad \widetilde{U}_{rem}] \begin{bmatrix} \tilde{\Sigma} & 0 \\ 0 & \tilde{\Sigma}_{rem} \end{bmatrix} \begin{bmatrix} \tilde{V}^T \\ \tilde{V}_{rem}^T \end{bmatrix} \tag{2.134}$$

$$\approx \widetilde{U}\tilde{\Sigma}\tilde{V}^T \tag{2.135}$$

where $U \in \mathbb{R}^{m\times m}$, $\Sigma \in \mathbb{R}^{m\times n-1}$, $V^T \in \mathbb{R}^{n-1\times n-1}$, $\widetilde{U} \in \mathbb{R}^{m\times r}$, $\tilde{\Sigma} \in \mathbb{R}^{r\times r}$, $\tilde{V}^T \in \mathbb{R}^{r\times n-1}$, the subscript rem indicates the remaining singular values given as $n-1-r$, and the superscript T represent the complex conjugate transpose. The Equation 2.135 shows that the dimension of the data matrix A can be adequately reduced by choosing a suitable value of the cutoff threshold r. The remaining terms are eliminated for the computation, thus allowing a much faster calculation of the pseudoinverse [284].

After the SVD of the matrix A, an approximation of the matrix B can be obtained as follows

$$B \approx \breve{B} = A'\tilde{V}\tilde{\Sigma}^{-1}\widetilde{U}^T \tag{2.136}$$

A dynamic model of the process can be then constructed for the data set following the analogy of Equation 2.129, namely

$$a(j+1) = \breve{B}a(j) \tag{2.137}$$

The dynamic modes of system are obtained by the eigenvalue analysis of the matrix $\breve{B}$. The eigenvalue analysis of matrix $\breve{B}$ can become computationally expensive for large values of m, however a projection of $a(j)$ onto a subspace of dimension r will vastly reduce the requirements for the calculation. The transformation of $a(j)$ is in the form $Pa = \tilde{a}$, where $P = \widetilde{U}^T$. The reduced order model is therefore derived as [283]

$$\tilde{a}(j+1) = \widetilde{U}^T \breve{B} \widetilde{U} \tilde{a}(j) = \widetilde{U}^T A' \tilde{V} \tilde{\Sigma}^{-1} \tilde{a}(j) = \tilde{B}\tilde{a}(j) \tag{2.138}$$

From which it can be concluded that

$$\tilde{B} = \widetilde{U}^T A' \tilde{V} \tilde{\Sigma}^{-1} \tag{2.139}$$

The eigendecomposition of $\tilde{B}$ is therefore more efficient and yields information that can be used in the analysis of the spatiotemporal coherence of the flow [42], [283]. The eigendecomposition of $\tilde{B}$ is written as

$$\tilde{B}w = \lambda w \tag{2.140}$$

where each non-zero eigenvalue, λ, is a DMD eigenvalue. The DMD mode that corresponds to λ is defined as [284], [285]

$$\varphi = \frac{1}{\lambda} A' \tilde{V} \tilde{\Sigma}^{-1} w \tag{2.141}$$

The DMD modes obtained from Equation 2.141 need to be re-arranged by computing their optimal amplitudes. This procedure allows the improvement in the physical meaning of each set of the DMD mode and the associated eigenvalue. The construction of an index matrix based by on a convex optimisation problem for the SVD values allows to sort the arrangement of the DMD modes in terms of their relevant growth/decay rate and, as consequence, as per their contribution to the dynamic state of the flow [286]. In addition, different supplementary operations have been incorporated into the computation of the DMD in order to increase its efficiency; these include the sparsity-promoting DMD [286], the compressive DMD [284] and the DMD with control [283].

The acquisition of the spatiotemporal modes through DMD analyses have been beneficial in the assessment of complex flows, such as swirling jets [287], premixed [288], [289] and partially-premixed flames [290]. Furthermore, the insight obtained from its application varies across different combustion processes [291], [292], namely the analysis of the thermo-acoustics [293], [294], the comparisons against flame transfer functions [295] and combustion instabilities [296]–[301]. Nevertheless, the DMD technique for the assessment of the spatiotemporal coherence in solid-fuel combustors has not yet been reported and thus represents an opportunity to expand the notion of these phenomena.

2.3. Summary

The accurate prediction of the flow field and the distributions of the temperature and species is paramount in the modelling of combustion environments. The combustion of coal particles implies the interaction of a series of complex phenomena whose models require to be carefully adapted and evaluated prior to their implementation. Further, the different scales into which the combustion process takes place requires the adoption of high resolution models that quite often are not feasible to apply for realistic scenarios.

In this chapter, a review of the models employed in the modelling of the coal combustion by means of CFD has been presented. The necessity to expand the RANS calculations, which currently serves as the standard for pilot-scale and industrial applications, into the LES framework for a better representation of

the turbulent motions was identified. The transient nature of the LES, in addition to the high-definition data obtained from these simulations allows us to broaden the understanding of the dynamics of the process. Moreover, the details of the models required to capture the combustion process were introduced, as well as the influence of the altered environment, a characteristic of the CO_2 rich oxyfuel combustion, among them. It was acknowledged that a correct representation of the heat transfer mechanisms is imperative to obtain a precise characterisation of the process. Radiative heat transfer is recognized as the most relevant heat transfer mechanism; hence, the selection of the appropriate model is a key decision in the modelling process. The utilization of global methods, such as the FSCK model, provides independence from the gas composition, thus preventing a necessary adjustment of the model form each computed scenario.

Furthermore, a methodology for the estimation of the temporal, spatial and spatiotemporal coherence of a finite sample of data was reviewed and its pertinence in the assessment of the systematic motion of the flows was acknowledged. The coherent modes obtained from the decomposition of the fluid flow data are a reference of the stability of the flame, which is often used as an indicator of the combustion efficiency. The development of novel combustion technologies, and the changes to the operational conditions associated to it, compel the formulation of robust methodologies for their study. In addition, the ability to compute the statistical behaviour of the combustion process will allows the anticipation of the effect of such technologies in the overall process performance. In the following chapters the assessment of the spatiotemporal coherence in swirled coal flames will be performed, firstly in terms of the experimental data gathered using a flame imaging system, and later by means of CFD modelling. The methodology employed for the CFD calculations is developed and tested on an isothermal swirling jet in order to analyse the characteristics of these structures. Finally, the methodology is employed to the flow developed in a coal combustor in which both the effects of the swirling motion and the chemical reactions are evaluated.

3. Experimental facilities and data collection

3.1. Introduction

This chapter provides a description of the facilities used to acquire the necessary data to perform analyses of the spatiotemporal coherence though an entirely experimental approach and CFD calculations. In Section 3.2, the pilot scale combustion facility used for the assessment of the stability and coherence of coal flames carried out in Chapters 4 and 6 is detailed. In addition, Section 3.3 features the apparatus used to examine the behaviour of an isothermal swirling flow; the data reported from this test is used in Chapter 5.

3.2. 250 kW Combustion Test Facility

The development and evaluation of the methodologies used in Chapter 4 and 6 for the estimation of the stability and spatiotemporal coherence of coal flames were sustained by the data obtained from an experimental campaign. The experimental test rig consists of a 250 kW solid fuel combustor, and it is a UK national facility. The CTF is part of the CCS Research Centre Pilot Advanced Capture Technology (PACT) Facilities, and is located in Sheffield, South Yorkshire, UK.

The core of the CTF is the down fired, multi-fuel, cylindrical furnace. The furnace has the capability to burn pulverised coal and biomass, and operate under either air or oxyfuel environments. The facility incorporates a parallel fuel feeding system for coal and biomass particles that is digitally controlled. In addition, the upper section of the furnace features a detachable fitting, hence providing the flexibility to switch between different types of burners easily. The operation and monitoring of the equipment is continuously performed by a customized supervisory control and data acquisition (SCADA) system.

3.2.1. Coal burner

The PACT furnace was devised as a flexible test array that is capable to working under various operational conditions and for different fuels. The uppermost section was fitted with an easy access flange that couples the furnace to the different interchangeable burners available in a down-firing disposition. The coal burner consists of a scaled-down version of a commercially available third-generation low-NO_x burner of 250 kW; the burner was manufactured by Doosan Babcock Ltd.

The burner is of a staged type with different concentrically arranged annular flow channels. An image of the front of the burner is presented in Figure 3.1. At its centre contains a natural gas inlet paired with an annulus that delivers the necessary air to light an initial flame that is used in the heating of the furnace prior to the solid combustion tests. The fuel-entraining channel is composed of four coal gutters in which only a fraction of the gas required for the combustion reaction is introduced; a bluff body is located at the end of the primary channel in order to promote the anchoring of the flame to the near burner region. The rest of the oxidiser is delivered into the furnace through the secondary and tertiary annular channels. Angular momentum is provided to the flow by means of a series of fixed-blade arrangements located upstream in each of the flow channels. The disposition of the blade arrangements can be seen in the computer aided image shown in Figure 3.1. The blades in the primary channel are placed at a polar angle of 63^{o} and they have equal chord length; afterwards, the swirled primary flow is conducted through four constricted sections that clusters the coal before it finds its way into the combustion chamber. The flow in the secondary and tertiary annuli are swirled in a similar fashion with flat blades disposed at polar angles of 64^{o} and 33^{o}, respectively.

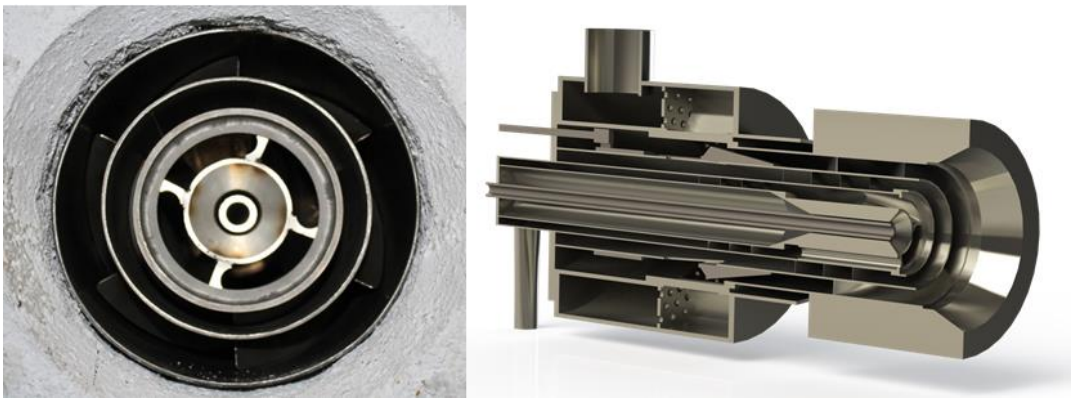

Figure 3.1 Photograph of the front view of the Doosan Babcock 250 kW coal burner (left), and cross-section computer aided drawing of the coal burner (right).

The amount of oxidiser that flows in the secondary and tertiary channels is controlled by a damping mechanism that splits a single air supply; the damper is allocated within a wind-box above the burner concentric registers. The damping mechanism can hold different positions, from diverting the entire flow into a single channel to fully restricting it. The appropriate set-up of the burner through the damper position is of prime concern as it affects the combustion efficiency directly. Several test runs on the rig are necessary to find the more efficient position. The compact size of the burner, in addition to its assembly

philosophy, complicates the access of sampling probes into the wind-box. The quantification of the oxidiser flow in each channel has been estimated after performing CFD calculations based on photographs of the arrangement and metrology of its internal components [65].

3.2.2. Furnace

The furnace at PACT is a down-fired array of cylindrical shape and it is 4 m in height and has a 0.9 m internal diameter. The furnace body assembly comprises eight sections, which are 0.5m in height and are lined with a layer of refractory material of 0.1 m in thickness with the commercially available VecoForm RCF1700. The composition of the refractory material is approximately 80% alumina and 20% silica, and each section was specifically moulded to suit the geometry of each section of the furnace. The refractory of the upper section of the furnace is composed of different materials as shown in Figure 3.2. The central part of the top section was made from the high-density fire resistant Durax 1850 concrete, it has a 185 mm duct in which the end of the burner is fitted; a quarl throat, that is formed by a chamfer of 25^{o} and 50 mm long, was casted at the end of the duct. The enclosing refractory zones at the top section of the furnace were manufactured using Jonlite IC16 and Skamolex Super-Isol.

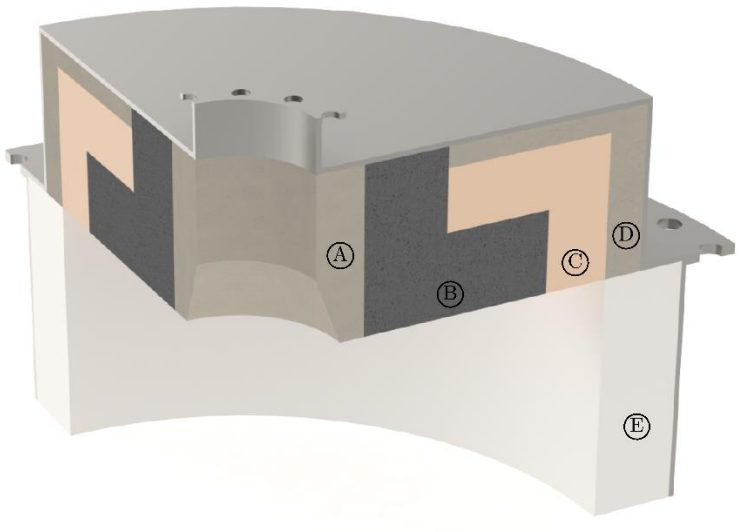

Figure 3.2 Schematic of the cross section of the refractory layer installed in the 250 kW CTF The sections A and B are made from Durax 1850 concrete, and the sections C, D and E of Jonlite IC16, Skamolex Super-Isol and VecoForm RCF1700, respectively.

Several sampling ports are located along the furnace with the vast majority of them residing in the top three sections, where the flame front is contained. The upper six sections and the exhaust pipe of the furnace are cooled by a closed circuit of flowing water. For safety purposes, the water temperatures, and thus the heat transfer from each section are monitored individually. The heat extracted from the furnace through the water is transferred to the atmosphere in a 500 kW forced-convection cooler. The water tray, that is located on the bottom of the furnace, provides flexibility to contain the pressure fluctuations of the combustion process and impede the flue gases from escaping. A centrifugal fan is coupled to the exhaust pipe that is located in the bottom section of the furnace. The furnace operates under a low induced draft to inhibit leakages of the combustion products. The flue gases are conducted through a cyclone separator and a high temperature candle filter, where the flying solid particles are removed. Photographs of the furnace are presented in Figure 3.3.

Figure 3.3 Photographs of the 250 kW furnace, the upper 3 sections are located at the mezzanine level (left) while the bottom 5 sections are on the ground floor of the building(right).

3.2.3. Oxidiser and fuel supply system

The oxidiser stream required for the air combustion reaction is provided in a pressurized state at 7 bar by a reciprocating compressor unit. The compressor unit is coupled to a cooler and an arrangement of coalescing and activated coal filters in order to remove the moisture and oil traces from the compressed gas. The total air flow is split into two pipelines, one being the entraining stream and the second corresponding to the rest of the oxidiser. Each line is fitted with control valves and mass flow meters that are regulated by a set point that is provided via a programmable logic controller (PLC).

The primary line, carrying the entraining stream, is fitted to the coal feeding system to carry the particles into the furnace. The air flow containing the entrained coal particles is directly conducted through the primary channel of the burner. The second pipeline that contains the remaining part of the oxidiser is attached to the wind box of the burner, and this is allocated into the secondary and tertiary channels as per the position of the damping mechanism within the burner.

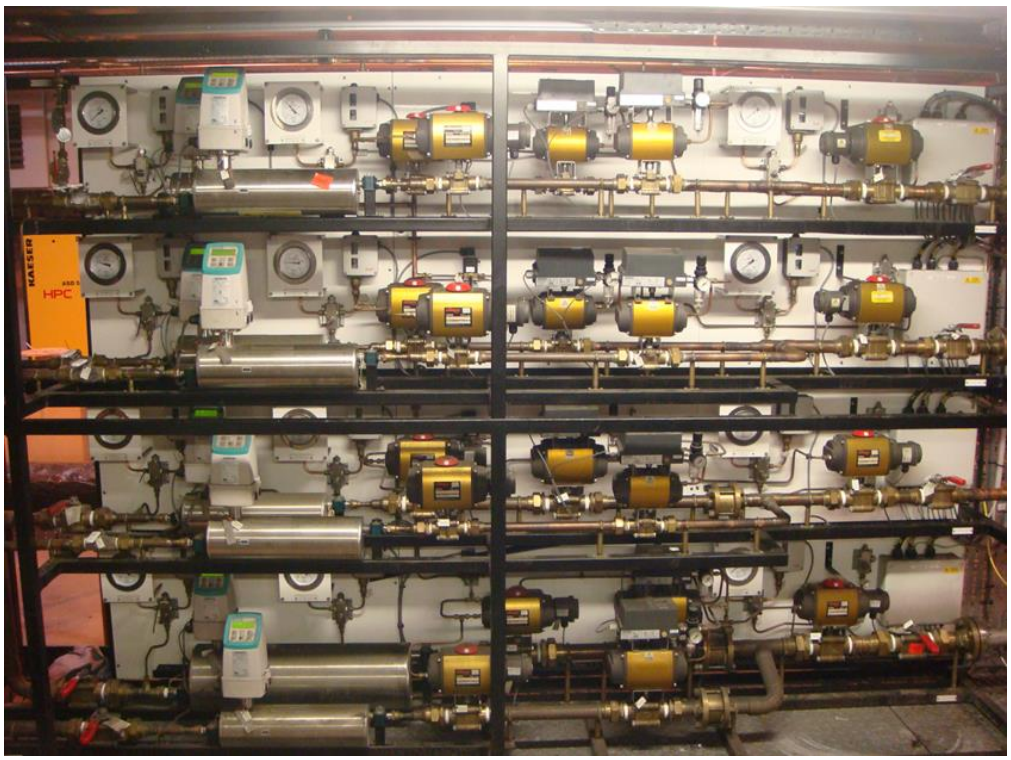

Figure 3.4 Photograph of the oxidiser supply manifold of the 250 kW CTF.

For the oxy-fuel combustion tests, the oxidiser is a gaseous mixture with a pre-established concentrations of O_2 and CO_2. The gases are contained in separate

liquid tanks at 5 bar from which they are conducted through a natural convection evaporator and into a mixing manifold. A photograph of the oxidiser manifold is shown in Figure 3.4. The manifold contains a set of flow control valves that are coupled to independent mass flow meters and O_2 analysers. The output lines of the manifold are jointed to the primary and secondary-tertiary air channels. The junction from the oxy-fuel manifold and the air channel in the primary pipeline is located prior to the coal feeding system, thus replacing the air for the O_2/CO_2 mixture as the entraining fluid.

An electric heater unit is installed on the secondary-tertiary pipeline and this is used to increase the temperature of the gases before entering the burner. The temperature of the gases is set to 523K, a similar value to those obtained in a power plant. As a security measurement, the temperature of the primary stream is that of the surrounding environment, in addition its O_2 concentration for the oxyfuel tests are kept below 21 vol%.

Figure 3.5 Photograph of the mechanical feeder used in the coal delivery system.

A mechanical feeder, as presented in Figure 3.5, is used to ensure that the appropriate amount fuel is carried into the furnace. The feeder consists of a cascade-type hopper array, with the main coal storage on the upper level. A smaller amount of coal is allowed into the second hopper, which is located on

the ground floor, through a rotary valve. The coal contained in the lower hopper is constantly mixed in order to homogenize its density and decrease the risk of agglomeration in the walls. A screw conveyor is located at the bottom of the lower hopper and this is used to transport fuel into a vibrating plate in order to produce a smooth fuel delivery ratio. The screw conveyor is driven by an electric fix-geared motor that is capable of adjusting its angular velocity; the angular velocity is set by an electro mechanic controller. Subsequently, the conveyed fuel is dropped into a junction pipe that is of a conical shape and from where it is carried by the oxidiser into the burner.

The pressure of the fuel feeder system is maintained at low negative values to enhance the displacement of the coal particles. A small amount of the primary oxidiser is redirected through a parallel pipeline into the feeder, where a differential pressure cell is used to control the amount of diverted oxidiser.

The calibration of the fuel feeder system is preformed prior to each test, or whenever relevant changes to the fuel composition takes place, such as for a different fuel batch. Also, several measurements of the fuel displaced at various set points are carried across different short time bursts, ranging from 1 to 5 minutes. A linear regression of the experimental data is used to estimate the required set point for the coal mass flow values that were not tested. The calibration curve that is employed throughout these studies is presented in Figure 3.6.

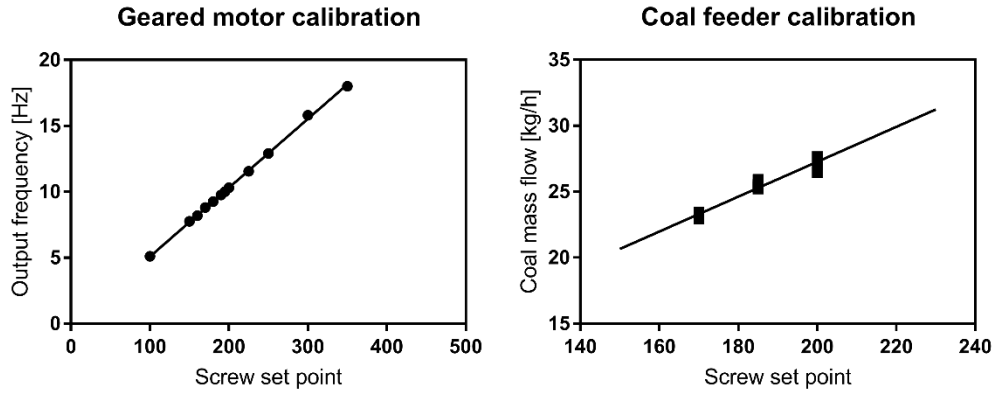

Figure 3.6 Calibration curve for the frequency of the geared motor (left), and for the fuel mass flow (right), of the fuel supply system.

The fuel used for all the experimental campaigns is a South American bituminous coal, which has a high volatile content, and it is commercially branded

as 'El Cerrejon'; the fuel is supplied by the manufacturer as a pulverized powder in bags of 20 kg. The stockpiles of the fuel bags are stored in a low-humidity closed space and the composition and calorific values are obtained for the coal using the relevant British Standard procedures, and these are presented in Table 3.1.

Table 3.1 Properties of the 'El Cerrejon' coal.

'El Cerrejon' coal			
Ultimate analysis (%, DAF)		Proximate analysis (%, as received)	
Sulphur	0.52	Moisture	7.63
Carbon	80.92	Ash	2.90
Hydrogen	5.12	Volatile matter	35.50
Nitrogen	1.65	Fixed carbon (by diff.)	53.98
Oxygen (by diff.)	11.79		
Gross calorific value [MJ/kg]	29.61		
Net calorific value [MJ/kg]	28.41		

The particle size distribution of the coal was obtained after several samples were gathered from different bags and locations of the coal. The particle size trend is approximated by a Rosin-Rammler distribution [302] and it is used as an input for the CFD calculations.

3.2.4. Experimental capabilities

The 250 kW CTF was conceived to be able to perform as many experiments as possible through its probe allocation capabilities and several measurement techniques have been employed to analyse the efficiency of the combustion process. A large number of ports are located along the eight furnace sections; those used for the flame assessment are located in the first three sections of the furnace, where the flame front resides.

3.2.4.1. Gas analysis

The ports used for the gas sampling and heat flux measurements are comprised of 1.5 inch couplers with compression fittings attached that allows the installation of probes of up to 1 inch in diameter. The compression fittings provides a tight seal between the sampling port and the probe, thus restricting air leaking into the furnace.

A water-cooled sampling probe is used to extract gases at different locations in the furnace. The outlet gas composition was always sampled from the exhaust pipe, while various positions were tested in a similar way. The condensates generated within the sampling channel of the probe are removed from the gas using a Dreschel bottle attached to the sampling line that is located immediately after the probe. Additionally, the sampled gas is conducted through a fine particle filter that removes all the carried solids. Finally, the sampled gas enters the analyser array, where the remaining moisture is eliminated and the gas composition assessment is performed.

Figure 3.7 Photograph of the cluster of analysers used for the gas composition assessment on the 250 kW CTF.

The analysers cluster is a MAXSYS 900 series from Signal Group Ltd; it comprises O_2, CO_2, CO, SO_2 and NO_x analysers that work in parallel, a photograph of the analysers cluster is shown in Figure 3.7. In addition to the analysers, a vacuum pump and a cooler unit are mounted on top and bottom of the rack; the vacuum pump provides the suction required to extract the gas sample while the cooler unit is used to fully remove the moisture contained in the sample. The analysers are constantly calibrated throughout the experimental tests, thus ensuring the accuracy of the measurements. Three different calibration procedures are performed; one of them is executed while zero grade N_2 is flowing through the sampling line and this is used to set the zero point value on the analysers. The second calibration uses beta standard gases with a preestablished concentration for the species measured by the analysers, and the

concentration level for the species are situated within the expected range in the experimental campaigns. The calibration to the value of the beta standard value is used to set a second point, namely the span level point. A third calibration is used exclusively for the CO_2 analyser when the oxy-fuel conditions are tested, due to the wider range in the values of species concentrations. The value obtained for a pure CO_2 gas stream is recorded and the measurements obtained during the test are corrected as required.

3.2.4.2. Temperature measurements

The temperature measurements of the gas are approximated by a series of thermocouples along the furnace. A type R thermocouple is located in each of the eight sections of the furnace, and these are encapsulated in a ceramic shield that protects them against radiation-induced damage. Due to the direct line-of-sight between the thermocouples and the flame front, and the proximity of the glowing furnace walls, the measurements are expected to be affected by radiative heat transfer. The temperature values obtained from the furnace thermocouples are used as a reference during the experimental tests; however, they must not be used as the value of the temperature at either the wall or the gaseous flow.

3.2.4.3. Heat flux measurements

The total heat flux at the wall of the furnace was measured by a heat probe which was designed and manufactured by The International Flame Research Foundation. The probe consists of an ellipsoidal cavity that is water-cooled and have an aperture in one end and a thermopile at the other, thus effectively focusing the entering radiation into the measuring sensor. The thermopile consists of a stainless steel plug with thermocouples at each end, and produces an electromotive force directly proportional to the absorbed energy. The surface of the ellipsoid is plated with a gold layer of thickness 0.5 mm in order to minimize the effect of the surface absorption. In addition, a protecting window is mounted in the cavity as a guard for the thermopile and to avoid errors associated to convective heat transfer. Furthermore, a purge flow of nitrogen is used to prevent the entry of combustion gases in to the ellipsoidal cavity.

3.2.4.4. Flame imaging

The furnace of the 250 kW CTF contains several ports that are designed to accommodate different devices for the 2D imaging and 3D tomography reconstruction techniques. The flame imaging system used in this experimental campaign consists of an optical probe fitted with a wide angle telescopic lens and a high-speed camera. The optical probe is cooled with water to protect the

telescopic lens array from the high temperatures of the furnace. A stream of air, that is directly discharged to the telescopic lens, was used to prevent the adhesion of particles that might obstruct the view of the flame front. An additional array of focus and aperture lenses is paired to the telescopic lens to adjust the depth of field as required.

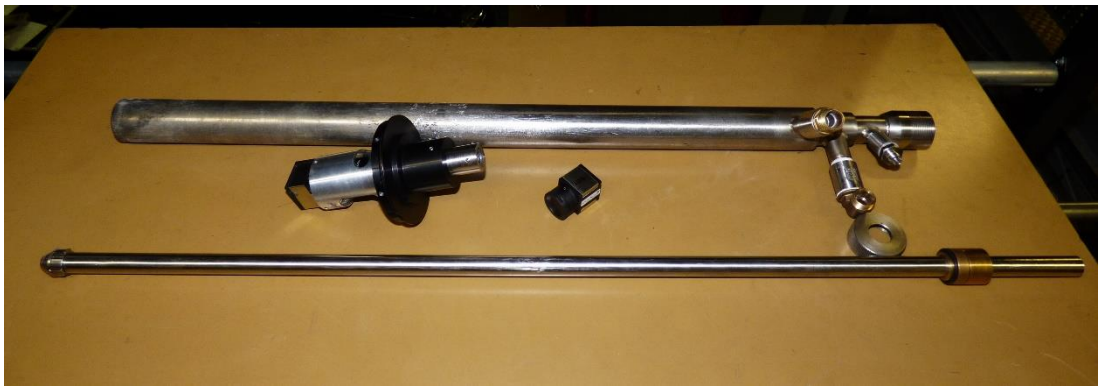

Figure 3.8 Photograph of the flame imaging array used during the experimental campaign. From top to bottom, water-cooled probe, focus and aperture lenses, industrial RGB camera and telescopic lens.

The device used to record videos of the flame is an industrial grade RGB camera, and a photograph of the flame imaging probe is presented in Figure 3.8. The sensor of the camera is of a complementary metal-oxide-semiconductor (CMOS) type, and it is capable to recording videos up to 265 frames per second. The camera sensor is contained within an integrated electronic circuit, and the camera output is coupled to a personal computer through a Universal Serial Bus (USB) 3.0 connector. Live images, as well as recorded videos, from the camera are obtained through a dedicated software.

3.2.5. Conditions analysed

The experimental coal combustion campaign conducted as part of this thesis was performed at 200 kW_{th} of thermal load, and the fuel used during the experiments was 'El Cerrejon' bituminous coal, whose properties can be found in Table 3.1.

Four different cases were tested, being air combustion and three oxyfuel scenarios with overall O_2 concentrations of 24, 27 and 30 vol%. The portion of the oxidant delivered to the furnace was through the primary channel, and it was used as the carrier flow for the coal particles, this was set at 20%. The remaining flow was split into the secondary and tertiary by the damping mechanism in the burner wind box. Different positions of the mechanism were tested prior to the experimental campaign until the optimal ratio was achieved; the position

of the mechanism was then held thereafter. The secondary-tertiary flow was preheated to a temperature of 523 K in both the air and oxyfuel conditions; the oxidiser in the primary channel was retained at 293 K. A summary of the amount of oxidiser used for the experimental campaign is presented in Table 3.2.

Table 3.2 Operating conditions used in the coal combustion experimental campaign.

Coal combustion campaign				
	Primary flow		Secondary-Tertiary flow	
Case	Air [l/min]		Air [l/min]	
Air	825		3250	
	O_2 [l/min]	CO_2 [l/min]	O_2 [l/min]	CO_2 [l/min]
Oxy24	138	523	657	1992
Oxy27	124	464	674	1677
Oxy30	111	419	685	1428

3.3. Isothermal swirling flow apparatus

Turbulent swirling flows are commonly used in combustion applications to enhance the mixing of reactants and to stabilize the resulting flame. The interaction of the swirling jets in a confined space, such as a combustor or a furnace, generates zones where counter current flows occur [32], [36].

The comprehension and control of the swirling flows is a major concern due to its associated practical applications in the combustion industry [303]. The conditions experimented within a combustion chamber, such as high gas temperatures and incident radiation, often interfere with the acquisition of detailed experimental measurements. Non-reactive swirling flows have been historically used to develop and validate suitable models that later are applied to different combustion scenarios [304].

The development of the methodology used for the assessment of the spatio-temporal coherence in swirling flows through Large Eddy Simulations are presented in Chapter 5, and these are based on the experimental report produced by the Lewis Research Center, which is part of the National Aeronautics and Space Administration (NASA) in the United States [305]. The report provides detailed measurements of an isothermal, non-reactive swirling flow. The principal components of the test rig are a water reservoir tank, a metered flow circuit with an inlet plenum, a test section made of glass, a dye injection system

and an argon ion laser. A computer-aided representation of the test rig is shown in Figure 3.9.

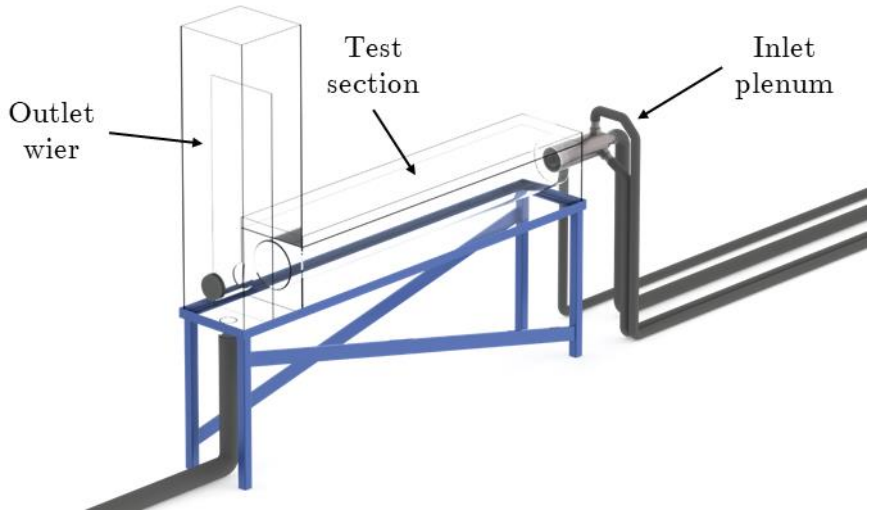

Figure 3.9 A computer-aided representation of the isothermal swirling flow test rig.

3.3.1. Swirling flow duct

The test section of the swirling flow apparatus comprises of a glass tube which is 1 m long and 0.122 m internal diameter in which water at a temperature of 293 K is circulated. The tube was enclosed by a glass box filled of the same fluid that serves as a direction distortion reduction mechanism for the laser beams.

Water enters the test section though a jet tube and a concentric annular duct in which an arrangement of blades provides a swirling component to the flow; the test section outlet is coupled to a vertical chamber that acts as a weir. The weir section is open to the atmosphere, thus allowing to mitigate any over pressurization of the system. The water flow over the weir wall is returned to the water reservoir tank in the closed circuit configuration; for the cases where a dye was injected into the entering water stream, the outflow was discharged to the drain.

3.3.2. Water inlet plenum and swirler arrangement

A water inlet plenum is used to pass the water into the test section of the isothermal swirling flow apparatus, and it is composed of two concentric flow channels. The inner channel is a jet tube of 0.025 m internal diameter; rigid piping of the same internal diameter was used up to 3 m before the plenum in order to ensure a fully developed profile. The outer flow channel is annular

section of 0.059 m and 0.0306 m outer and internal diameter, respectively. The wall that separates both flow channels was provided with a flare angle of 7.5° at the end of the tube. The annular channel of the plenum contains three perforated plates to enhance the uniformity of the flow and a region with a honeycomb structure to remove any swirl prior to the blade arrangement.

A cluster of fixed blades is installed in the annular channel of the water inlet plenum in order to provide swirl to the flow. Several blade profiles and geometric dispositions were tested as part of the rig construction. The design selected produced a 30°mean-angle, and a free-vortex tangential velocity distribution with a uniform axial velocity distribution; it consists of an arrangement of eight turning blades whose trailing edges are located 0.051 m upstream of the test section. A schematic of the blade arrangement is presented in Figure 3.10.

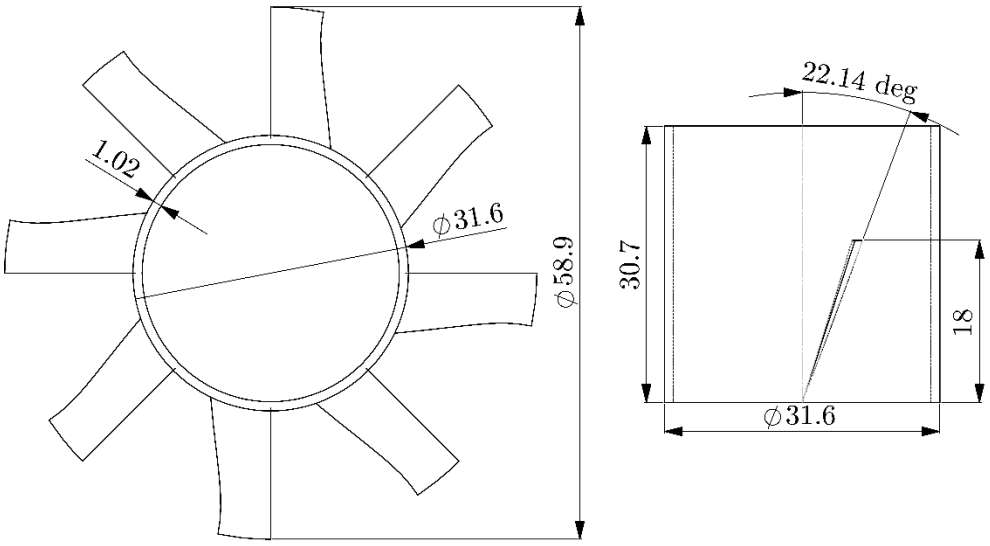

Figure 3.10. Schematic of the design characteristics of the blade arrangement installed in the isothermal swirling flow apparatus, top view (left) and front view (right).

3.3.3. Flow visualization techniques

The main purpose of the study was to acquire and analyse the flow velocity and mass transport rate through non-intrusive techniques within the test section. A combination of laser velocimetry (LV) and laser induced fluorescence (LIF) techniques were employed to obtain instantaneous velocity components and concentration distributions. The turbulent transport rate was determined after two velocity components were obtained simultaneously. As a result, the

data acquired for the concentration and velocity distributions were gathered in at least two non-consecutive test runs.

The flow visualization system was built using a combination of commercially available equipment and in-house made components that were tailored to perform a specific function. The two colour laser lines, blue and green, produced by an Argon ion laser were employed in the LV measurements. The particles that are contained naturally in the tap water were used as seeds that scattered the volume created by the laser beams. A photomultiplier was coupled to the Laser Doppler Velocimetry (LDV) signal processors and these were employed to first modulate the light intensity and then to obtain two velocity components for several data points. The two velocity components for each analysed plane were obtained for a period of time of 0.001 s.

In addition, a tracer dye that consists of a solution of fluorescein disodium salt was injected into the test volume through the inner jet line. The blue line from the Argon ion laser used in the LV measurements was adopted as the fluorescence inducer in the mixed fluid. The filtered signal obtained from a photomultiplier was amplified and converted into voltage and the LV and LIF results were stored as a pair for future assessment of the flow.

3.3.4. Flow conditions reported

The results presented in the report were aimed to be used as a database in the evaluation of the mathematical and computer-based transport models for axisymmetric flows. Steady state flows were obtained after time-independent statistics had been presented in accordance to the nature of the transport models. A qualitative assessment of the steadiness of the flow was performed prior to the laser-based data acquisition period. In parallel, the symmetry of the flow was inspected along the test section in order to minimize geometrically biased results. High-speed photographs were acquired using a shutter speed of 0.001 s for a continuous stream of dye in the inner jet water line and for pulsating dye injection stream into the swirl inlet.

The collection of photographs were used in the analysis of the structures present in the flow. It was found that the flow contained four distinguishable zones comprised by a wake region attached to the bluff body between the inner and annular channels, a noticeable shear layer between the two streams, an outer recirculation zone adjacent to the inner plane and a re-attachment zone further downstream. The inlet conditions used for all the cases evaluated during the

experimental campaign carried out by The Lewis Research Center are presented in Table 3.3.

Table 3.3 Experimental conditions evaluated in the isothermal swirling flow test array.

Experimental campaign of isothermal swirling flows				
	Mean axial velocity [m/s]		Flow rate [gpm]	
Flow condition	Inner jet	Annular jet	Inner jet	Annular jet
1	0.52	1.66	6.2	52.8
2	0.27	1.66	3.2	52.8
3	2.08	1.66	24.6	52.8
4	0.94	1.51	11.1	48.0
5	0.94	2.87	11.1	94.8

Despite testing all the experimental conditions, the detailed data acquired was only reported for the flow condition 1; the CFD computations, in whose the development of the methodology for the assessment of the spatiotemporal coherence was based, are supported by these published results.

3.4. Summary

In this chapter, a review of the experimental facilities used in the in analyses for the forthcoming sections of the thesis was presented. The details of the solid combustion rig, which is part of the PACT facilities in South Yorkshire, UK., were introduced. Special attention was given to the data acquisition capabilities of the furnace, and details of the experimental probes and sampling equipment were provided. The data obtained from the flame imaging system was used to perform the analysis of the flame stability in Chapter 4 while the complementary data gathered from the experimental campaign, such as the temperature distribution, heat flux and chemical species concentrations were employed to validate the CFD model developed in Chapter 6.

Furthermore, a description of the isothermal swirling flow apparatus of the Lewis Research Center, part of the NASA in the United States, was presented. The test rig was the central part of the experimental research in swirling flows carried out by the institution over two decades and which results are published. The constituents of the device were enumerated and further described individually; a layout of the array of fixed blades, the foremost important component of the rig, was produced in order to clarify the swirl generation mechanism.

The results reported from the experimental campaign carried over the apparatus were employed to validate the CFD model and the methodology for the spatiotemporal coherence assessment that was developed in Chapter 5.

4. Spectral and digital imaging analysis of coal flames

The ability in maintaining a stable flame is key in the deployment of novel technologies in combustion, such as oxyfuel techniques. The alterations in the flame characteristics such as colour, shape and brightness are often used as an indicator of its stability [32].

This chapter presents the assessment of the stability of a range of coal flames based on the quantification of its transient nature. A digital imaging approach was used for the different coal flames to obtain transient data that later was used to account for their stability. The instantaneous variations of the flame parameters, such as temperature and luminance, are employed in the evaluation of its fluctuating behaviour through spectral and oscillatory analyses [306]. As a non-intrusive technique, digital imaging provides a useful approach to recover information from the flame without interfering in its natural behaviour.

The experimental set up used through the coal combustion campaign is presented in Section 4.1 followed by the introduction of the methodology employed in the flame stability assessment in Section 4.2. The results obtained from the spectral and oscillatory intensity analyses are reported in Sections 4.3 and 4.4, respectively. Finally, a summary of the results alongside the general conclusions of these studies are discussed in Section 4.5.

4.1. Experimental set-up

Digital imaging techniques have been widely employed in the characterization of the combustion of a range of fuels across different conditions [307]. The utilization of spectral analyses in the assessment of the behaviour of a flame was previously used for both premixed and diffusion gaseous flames [308], [309], and later deployed in the characterization of heavy-oil flames [310]. In addition, spectral analysis has proven to be successfully adapted in the study of coal flames under air [311]–[313] and oxyfuel conditions [40]. As a complement to the CFD computations, spectral analyses have been employed in order to comprehend the underlying mechanisms of the oscillatory behaviour of swirling flows and combustors [314], and to estimate their impact on the stability of the flame in terms of its temporal repeatability [64], [315].

The coal combustion campaign was carried out on the 250 kW solid-fuel combustion test facility of the UK CCS Research Centre located in Sheffield, UK. The experimental rig, described in Section 3.2, was fitted with a scaled-down version of a third-generation low-NOx burner that produces 250 kW, the design and manufacture of the burner was executed by Doosan Babcock Ltd. A thermal load of 200 kW_{th} of a high volatile bituminous coal, commercially branded as 'El Cerrejon', was fired in all cases. The composition and calorific values of the coal are summarized in Table 3.1.

The experimental campaign consisted in one air-fired and three oxyfuel cases under overall concentrations of 24, 27 and 30 vol%. The composition of the combustion environment was adjusted through an O_2/CO_2 mixing skid; the concentration of O_2 in the primary channel was retained at 21 vol% for security purposes. The amount of oxidant delivered to the furnace through the primary channel was 20%, while the remaining fluid was split into the secondary and tertiary streams in the plenum of the burner. The position of the damping mechanism of the burner was set after a series of preliminary tests, in which the aerodynamics of the flame was assessed; the disposition of the damper was then fixed, and held during the experimental campaign, to that in which the optimal burnout was achieved and levels of NO remained low. An electric heater was used to raise the temperature of the secondary-tertiary gas flow to 523 K in all cases; the temperature of the oxidiser flowing in the primary channel was maintained at 293 K to reduce the risk of early ignition. The total gas flows used in the coal combustion experimental campaign are presented in Table 3.2.

A digital imaging system was fitted to a port in the top section of the furnace, thus allowing a direct line of sight to the flame front. The flame imaging system is composed of a water-cooled optical probe that encases a wide-angle telescopic lens. The depth of field is adjusted by an external array of focus lenses and an iris mechanism that regulates the aperture. The perceived light is conducted through the lenses into a complementary metal-oxide-semiconductor (CMOS) sensor of an industrial camera. The light spectrum captured by the camera is divided into three primary channels (red, green and blue) thus producing a colour space in which all the remaining colour can be estimated, a schematic representation of the RGB colour space is presented in Figure 4.1 [316]. The installed camera is of a RGB type and it is built as an integrated circuit into which the CMOS sensor is embedded. The camera is paired to a custom software from where it is possible to record videos and visualize live images. The

software is capable of alter the exposure time and recording speed of the camera sensor, for the experimental campaign the exposure was set at 1.5 ms. The flame imaging system have a maximum recording speed of 265 frames per second however it has been decreased to capture 250 frames per second or less in order to avoid data loss due to Bus bandwidth depletion.

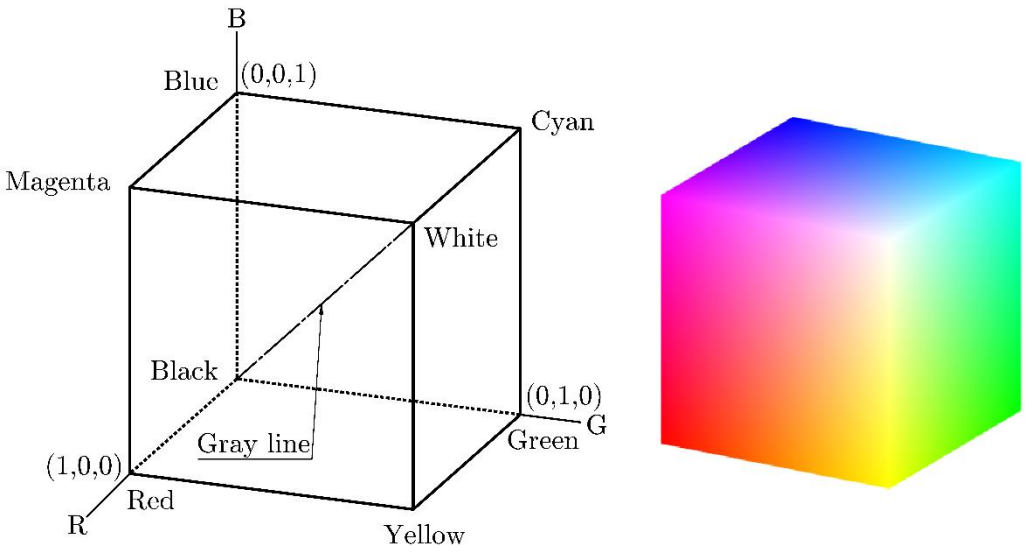

Figure 4.1 A Cartesian representation of the RGB colour space (left) and a three-dimensional colour cube used to capture the light spectrum (right).

A set of 8000 images were extracted from recorded videos for each case, the images comprised a resolution of 320×256 pixels. The stability of the flame was computed for two regions of the flame front, the first corresponding to the maximum captured extension, and the second zone, commonly known as the root region, being the vicinity of the burner tip in which flow mixing and emissions formation phenomena are predominant due to a larger concentration of volatile matter [310]. The transient signals were constructed by post processing the recovered frames using a computational algorithm that is coded specifically for this purpose in MATLAB R2015a.

4.2. Methodology

A series of still images were extracted from videos recorded during the experimental coal combustion campaign. The recording speed of the flame imaging system was set at 200 fps, while the minimum length of each video was 40s. The number of images, or snapshots, used for the stability assessment in each case was fixed at 8000 for the sake of consistency. Each snapshot is composed by a matrix array of size M×N×3, where M and N represents the number of pixels, or the resolution of the image, in width and height, and 3 is the number

of colour channels in which the light spectrum is captured by the CMOS sensor of the camera. Each colour matrix is composed of evenly quantized 24-bit values for each pixel within the recorded area. The colour channel recorded by the camera sensor are red, green and blue.

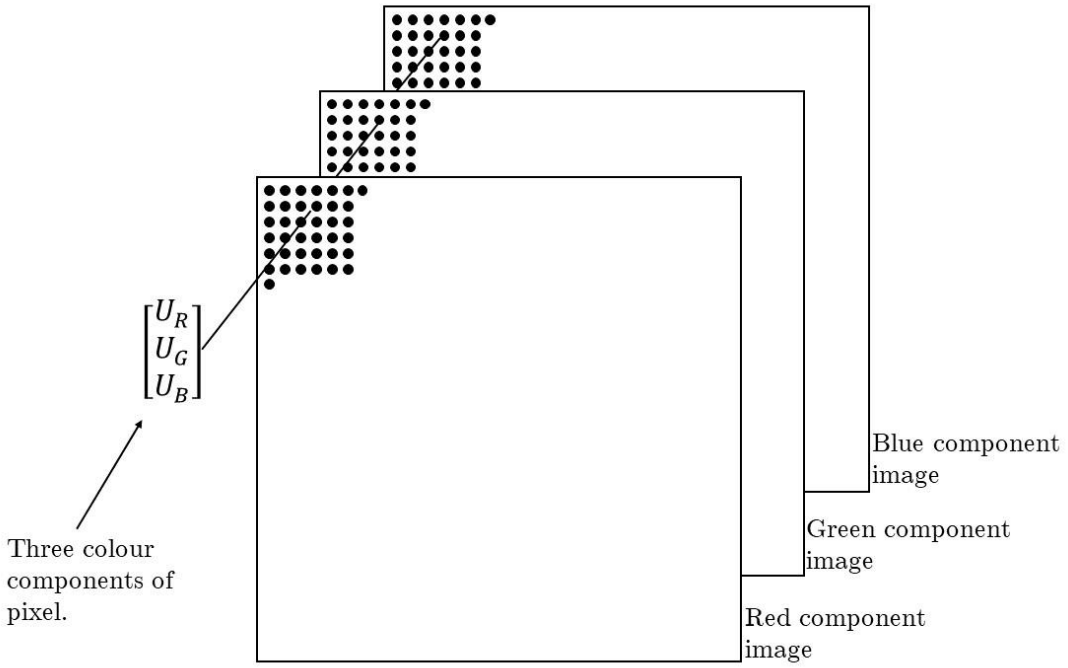

Figure 4.2 Schematic representation of the array of matrices used to represent an image in RGB colour space.

A stability analysis was performed after three complementary flame parameters were recorded. The first parameter used is mainly associated with the larger char particles combusting and corresponds to the flame brightness [317]. The flame brightness is represented by the value of the digital luminance for each snapshot. The second parameter employed is the temperature calculated by the two-colour pyrometer method [318]–[320]. The temperature computed by the two-colour pyrometer method accounts for the volume contained by the flame front and includes the transient effects of both the volatile and char combustion, as well as those derived from its associated highly radiant particulate products, such as soot. Finally, the third flame parameter used in the estimation of its stability corresponds to the entire light spectrum captured by the camera. An overall index is computed after the magnitude of the light fluctuations in the colour hue, intensity and saturation space [321].

The dynamic nature of the flame is captured by the repeatability of its recorded parameters. Spectral analysis are performed over the transient data obtained

from the digital luminance and temperature estimations, thus accounting for the temporal coherence of the flame. In addition, the severity of the oscillations manifested by the flame are accounted by the index calculated after the light spectrum. In conjunction, both the temporal coherence and the severity of the oscillations are employed in the evaluation of the flame stability exhibited in each case.

4.2.1. Digital luminance

The ability to properly characterize the light is paramount in the science of colour and image-based analyses. If the light does not produce any colour, it can only be characterized by its magnitude, or intensity, and this type of light source is known as achromatic. However, colourful light, or chromatic light, resides in a wider range of the electromagnetic spectrum, from 400 to 700 nm, approximately. The quality of the chromatic light source can be represented by its radiance, luminance and brightness. The energy flowing from the light source is accounted by the radiance, while the luminance measures the amount of energy perceived by an observer from a referred light source. The brightness term comprises a subjective connotation as it refers to the way a light source is sensed by an observer, and therefore it is practically impossible to measure [322].

Different mathematical relationships have been developed to calculate the radiance and luminance of light sources, and lately these have been modified to be adopted to the data obtained from digital devices, such as cameras and recorders. The digital luminance perceived by the camera sensor, $\mathcal{L}_D$, was calculated by weighting the quantized values of the colour channels for each pixel location. The weighting relationship coded into the mathematical algorithm is as follows:

$$\mathcal{L}_D = \alpha_R R + \alpha_G G + \alpha_B B \tag{4.1}$$

Where the values R, G, and B corresponds to the pixel-wise value of the quantized light spectrum in the red, green and blue colour channel, respectively. The weighting coefficients for each colour channel were set as per the recommendation of the International Telecommunications Union and have values of $\alpha_R = 0.2989$, $\alpha_G = 0.587$ and $\alpha_B = 0.114$ [323].

4.2.2. The two colour pyrometer

Historically, the emission of light in combustion processes, caused by the thermal decomposition of the fuel constituents, has been used as an indicator of the reaction efficiency. The necessity of an accurate measurement of the radiated heat and temperatures reached within a furnace motivate the development of non-intrusive techniques such as the optical pyrometer [318].

In optical pyrometry, the temperature calculation is based on the magnitude of the radiance on a singular wavelength or across different bands of the light spectrum. In multiphase combustion environments, such as in a coal furnace, the single band optical pyrometer was found to be not suitable due to its inability to account for the temperature of particulate matter [324]. In contrast, the temperature of highly radiative solids produced in the combustion process, such as soot, can be accounted for by expanding the range of the light spectrum in which the radiance is measured. By encompassing the radiance at two different wavelengths, hence the two-colour pyrometer, the prediction of the temperature for the solid particles can be derived through relationships in the intermediate values recorded [318].

The relationship employed for the calculation of the temperature was constructed as a correlation of the quantized values in the red and green channels, and it is presented in as follows [320]:

$$T = \frac{(C_2)\left(\frac{1}{\lambda_G} - \frac{1}{\lambda_R}\right)}{\ln\frac{R}{G} + \ln S + \ln\left(\frac{\lambda_R}{\lambda_G}\right)^5} \tag{4.2}$$

where C_2 corresponds to the second Planck's constant and it has a value of 1.4387×10^{-2} mK. The terms λ_R and λ_G are the peak wavelength values in the light spectrum for the red and green colours, their values are 615 and 540 nm, respectively. Finally, S denotes an experimental-based apparatus that can be obtained as a ratio of the colour bands used in the temperature approximation [320], [325], [326]. The apparatus experimental factor is computed by the following expression:

$$S = (0.3653)\left(\frac{R}{G}\right)^2 - (1.669)\left(\frac{R}{G}\right) + 3.392 \tag{4.3}$$

4.2.3. Temporal coherence

The temporal repeatability of the flame parameters, introduced in Sections 4.2.1 and 4.2.2, was obtained by performing spectral analyses on their respective transient data. The magnitude of the flame parameters obtained for each pixel location within the image were combined into a single term through an arithmetic mean value calculation. The arithmetic mean values for each snapshot are then incorporated to produce a transient digital signal.

The transient signal obtained from the set of snapshots obtained through the digital imaging system is used to construct a spectrum a frequencies in which the signal resides, this procedure is known as spectral analysis. The frequency spectrum alongside the power spectral density, which states the contribution of each of the computed frequency bands, is obtained by performing fast Fourier transforms to the transient signals. The power spectral density, $P(f)$, is given as follows:

$$P(f) = \frac{1}{n_s}\left(FFT_{n_s}(f)\right)^2 \tag{4.4}$$

where $FFT_{n_s}(f)$ represents the fast Fourier transform at a frequency band f, of the transient signal composed by n_s sampled points. The value obtained for the power spectral density value at $f = 0$ Hz has been removed from the frequency spectrum as it is not associated to the dynamics of the flame front [327].

By analysing the spectrum of frequencies constructed from the transient data, the temporal repeatability of the analysed flame parameter can be judged. However, based on the length of the signal and its sampling rate, the spectrum might be an intertwined arrange of the frequencies that, in harmony, represent the dynamic motion of the flame. A characteristic oscillatory frequency is introduced in order to interpret the potentially large amount of data obtained from the spectrum into a single term. The weighting expression used in the estimation of the characteristic oscillatory frequency is given by:

$$F = \frac{\sum_{i=1}^{n_f}[P_i \cdot f_i]}{\sum_{i=1}^{n_f} P_i} \tag{4.5}$$

The characteristic oscillatory frequency F is obtained after the summation of the values of the frequency and power spectral density, P_i and f_i, respectively, of the ith band of the n_f divided spectrum. Therefore, the oscillation frequency obtained represents a characteristic repeatability ratio and can be interpreted as the coherence in time of the flame parameter from which it was estimated.

4.2.4. The oscillation severity index

The assessment of the overall stability of a flame exclusively through the spectral analysis, as described in Section 4.2.3, may be misleading due to its intrinsic formulation. The construction of the spectrum of frequencies relies uniquely in the temporal repeatability, without regarding how severe the oscillations are, hence evidencing the necessity of a complementary indicator in the flame dynamics. An oscillation severity index based on the pixel-wise values obtained from the recorded snapshots of the flame have been introduced [328], and the index is derived to produce a range of values between 0 and 1.

In order to appropriately capture the magnitude of the oscillations in the flame, a better representation of the observed colour is required. The colour emerged from the flame vastly depends on the properties of the fuel, the stoichiometric rate of the reaction and on the adiabatic temperature reached [328]. The RGB colour space stands as a straightforward approach to depict the colour spectrum, and it has proven to be useful in digital image processing, however it oversees the physical interpretation of the colour through the eye. An observer usually defines the colour of an object through its hue, saturation and intensity or brightness, rather than as a percentage of the primary colours composing its shade. The hue can be interpreted as the attribute of the light that represents its pure colour while the saturation measures the extent into which the pure colour has been diluted by white light. The brightness of the colour is a subjective term that comprises, to some extent, of sensorial information from the observer; however, it inherently encloses the achromatic meaning of intensity, a value that can be quantized. Effectively, by converting the colour spectrum into the hue, saturation and intensity (HSI) space, the intensity component, the key in the assessment of the oscillation severity, is isolated from the colour information and obtained as a unique feature of the processed image.

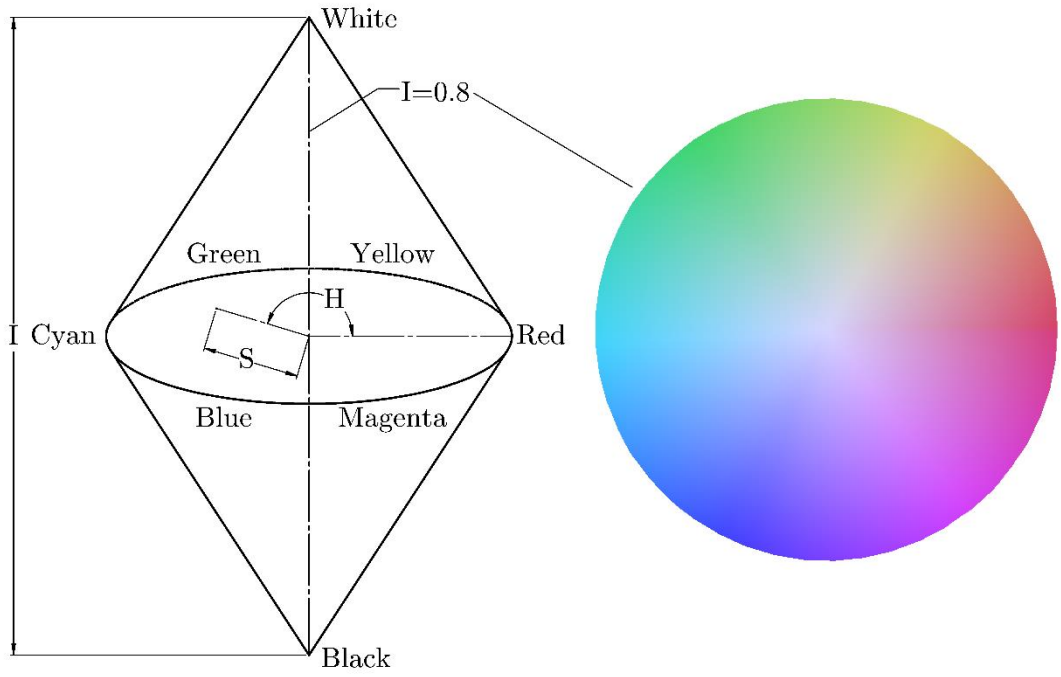

Figure 4.3. Three-dimensional representation of the HSI colour space. The circular colour plane presented is computed at I=0.5.

The HSI system separates the colour information of an image from its intensity information. Colour information is represented by the hue and saturation values, while the intensity, which describes the brightness of an image, is determined by the amount of the light. Hue represents basic colours, and is determined by the dominant wavelength in the spectral distribution of light wavelengths. It is the location of the peak in the spectral distribution. The saturation is a measure of the purity of the colour, and signifies the amount of white light mixed with the hue. It is the height of the peak relative to the entire spectral distribution. A three-dimensional representation of the HSI colour space is presented in Figure 4.3 [316].

The relationships used to convert the values obtained in the RGB colour space into the more comprehensive HSI are introduced as follows [328]:

$$H = \cos^{-1}\left(\frac{\frac{1}{2}[(R-G)+(R-B)]}{[(R-G)^2+(R-B)(G-B)]^{1/2}}\right)\Big/360^\circ \qquad (4.6)$$

$$\text{For } B \leq G$$

$$H = 1 - \cos^{-1}\left(\frac{\frac{1}{2}[(R-G)+(R-B)]}{[(R-G)^2+(R-B)(G-B)]^{1/2}}\right)\Big/360° \quad \text{For } B > G \tag{4.7}$$

$$S = 1 - \frac{3}{R+G+B}\cdot[\min(R,G,B)] \tag{4.8}$$

$$I = \frac{R+G+B}{3} \tag{4.9}$$

The severity in the flame oscillations is estimated after computing the mean value of the hue, saturation and intensity components of the image. In addition, a second term known as the contrast is introduced as a registry of the range width in each of the HSI image components. The mean and contrast values are computed by the following expressions:

$$M_k = \frac{1}{M \times N}\sum_{i=0}^{M-1}\sum_{j=0}^{N-1} U_k(i,j) \tag{4.10}$$

$$C_k = \left(\frac{1}{M \times N}\sum_{i=0}^{M-1}\sum_{j=0}^{N-1}(U_k(i,j)-M_k)^2\right)^{1/2} \tag{4.11}$$

where the subscript k represents each of the image components in the hue, space and intensity colour space and $U_k(i,j)$ is the pixel element located in the ith-jth coordinate of the $M \times N$ image frame. As a complement to the fluctuations in the colour spectrum captured through the HSI components, the area occupied by the flame front is included in the estimation of the oscillation severity index, thus incorporating the potential fluctuations in the shape of the flame. The effective area of the flame is obtained by performing a background removal operation to each of the flame snapshots. The background removal operation takes advantage of the relative large difference in brightness between

the flame front and the darker surroundings. The brighter region in the frame is obtained by converting the coloured image into a monochromatic array through a threshold estimated from the grey-level histogram [329]. The monochromatic image is constructed using the following criteria:

$$U_I(i,j)\begin{cases}1, \text{ if} > \text{threshold}\\ 0, \text{if } \leq \text{threshold}\end{cases} \tag{4.12}$$

The relative area in which the flame front is residing is defined as follows:

$$A_I = \frac{1}{M \times N}\sum_{i=0}^{M-1}\sum_{j=0}^{N-1} U_I(i,j) \tag{4.13}$$

In order to incorporate the transient component into the computation of the oscillation severity index of the flame, the standard deviation across the sampled snapshots for each of the seven parameters previously introduced, σ_{X_i}, is obtained. The oscillation severity index, is obtained by merging the standard deviation and the maximum dynamic values of the flame parameters into a comprehensive term, and it is given by:

$$\delta = \prod_{i=1}^{7}\left(\frac{\phi(X_i) - \sigma_{X_i}}{\phi(X_i)}\right)^{w_i} \tag{4.14}$$

Where, $X_i \in \{M_H, M_S, M_I, C_H, C_S, C_I, A_I\}$ and $\phi(X_i)$ is the dynamic range of the signal produced by each of the flame parameters In this study, $\phi(X_i) = 0.5$ for M_H, M_S, M_I, A_I and $\phi(X_i) = 0.25$ for C_H, C_S, C_I. Finally, w_i corresponds to a weighting factor that is used to stipulate the relevance of each parameter against the remaining ones. The value of w_i was set to 2 for all the parameters after recognizing them as being equally important in combustion studies [328].

The results obtained after the oscillation severity index, in conjunction to the spectrum of frequencies, will serve as the basis in the assessment of the flame stability.

4.3. Spectral analysis

The flame imaging system described in Section 3.2.4.4 was installed in a port located in the top section of the 250 kW CTF furnace at PACT, the remaining port in the furnace were sealed to avoid leakages into the furnace. The water-cooled probe that encloses the telescopic lens of the flame imaging system was inserted into the refractory wall of the furnace until no further obstruction in the view was noticed and a direct line of sight of the flame front was achieved. The depth of field was manually corrected by adjusting the focus and aperture external lenses prior to each recording session, in addition, the exposure time of the sensor was set to 1.5 ms through its proprietary software and this was retained throughout the experimental campaign.

A set of 8000 images was extracted from videos recorded during the experimental test; the recording speed and resolution of the system was established at 200 frames per second and 320×256 pixels, respectively. The cluster of images obtained for each case was post-processed in order to convert the multi-dimensional data into a digital signal that was later the base in which the frequency spectrum was constructed. The post-process operations were carried out in MATLAB R2015a, a multipurpose numerical computing tool, via an algorithm designed for this function.

Two regions of the flame front were analysed, the first corresponds to the whole length of the flame and the second is focused on the near burner region. During the preliminary assessment of the methodology, the signal constructed after the temperature estimation by the two colour pyrometer method exhibited a low oscillatory behaviour, contrary to what is expected for diffusion flames; a detailed inspection revealed a large damping effect in the calculations caused by the hot walls of the furnace that were captured as background. The area of the image used in the calculation of the temperature, and the subsequent signal conversion, was reduced in order to mitigate this effect. The flame area was obtained after the implementation of a global threshold algorithm in a similar fashion to the calculation of the oscillation severity index [329].

The repeatability of the present study was evaluated by comparing the results of a second set of images obtained from different videos of the flame under air, Oxy27 and Oxy30 conditions; the second group of videos were recorded on

different test days to ensure their validity. The results comparison exhibited differences of less than 1% for the whole captured frequency spectrum, while differences in the oscillatory severity index were, on average, 4.4%.

4.3.1. Full flame region

The frames extracted from the videos of the flame were trimmed into a smaller area in order to employ them in the subsequent calculations. Only the region in which the luminous front of the combustion reaction is located and the size of the image used in the estimation of the digital luminance and temperature is 190×235. An original snapshot extracted from the video alongside their correspondent luminance and temperature computed frames are depicted in figure 4.4.

Digital signals for the perceived luminance and temperature flame parameters were constructed as a time series of the singular values generated by each processed frame. The constructed signals were retained unaltered throughout the study due to the lack of preliminary knowledge of their type and the associated impossibility to properly build a filter that will exclusively remove noise. The Fourier transforms performed over the flame parameter signals produced spectrum of frequencies that are sharply arranged in the lower range, thus reassuring the triviality of a filtering operation for these particular cases.

The frequency spectrums were constructed up to the maximum range possible that is bounded by the Nyquist frequency of 100 Hz, however the majority of the relevant frequencies, measured by the magnitude of their power spectral density, were contained below 10 Hz. The constructed frequency spectrums are displayed, in their normalized form, in Figure 4.5; the maximum value for the frequency axis in the plots is 10 Hz for a better appreciation of the relevant bands.

The relevant frequencies contained in the constructed spectrums appear to be more spread for the oxyfuel cases; however, they were clearly contained below 4Hz. Low range relevant frequencies, such as the cluster exhibited for all the coal combustion cases, are associated to slower phenomena, such as the combustion of char particles. In contrast, the oscillatory frequencies of higher values are generally related to faster reaction rates of gaseous combustion [189].

The overall characteristic oscillatory frequency, calculated as a weighted value of the data contained in the whole spectrum, exhibited a narrow difference among all the cases for the luminance approach. The compactness of the values of the weighted frequencies for the luminance approach, as shown in Figure

4.6, suggest that the char burn rate was similar for all the cases; all the weighted oscillatory frequencies ranged between 1.8 and 1.9 Hz.

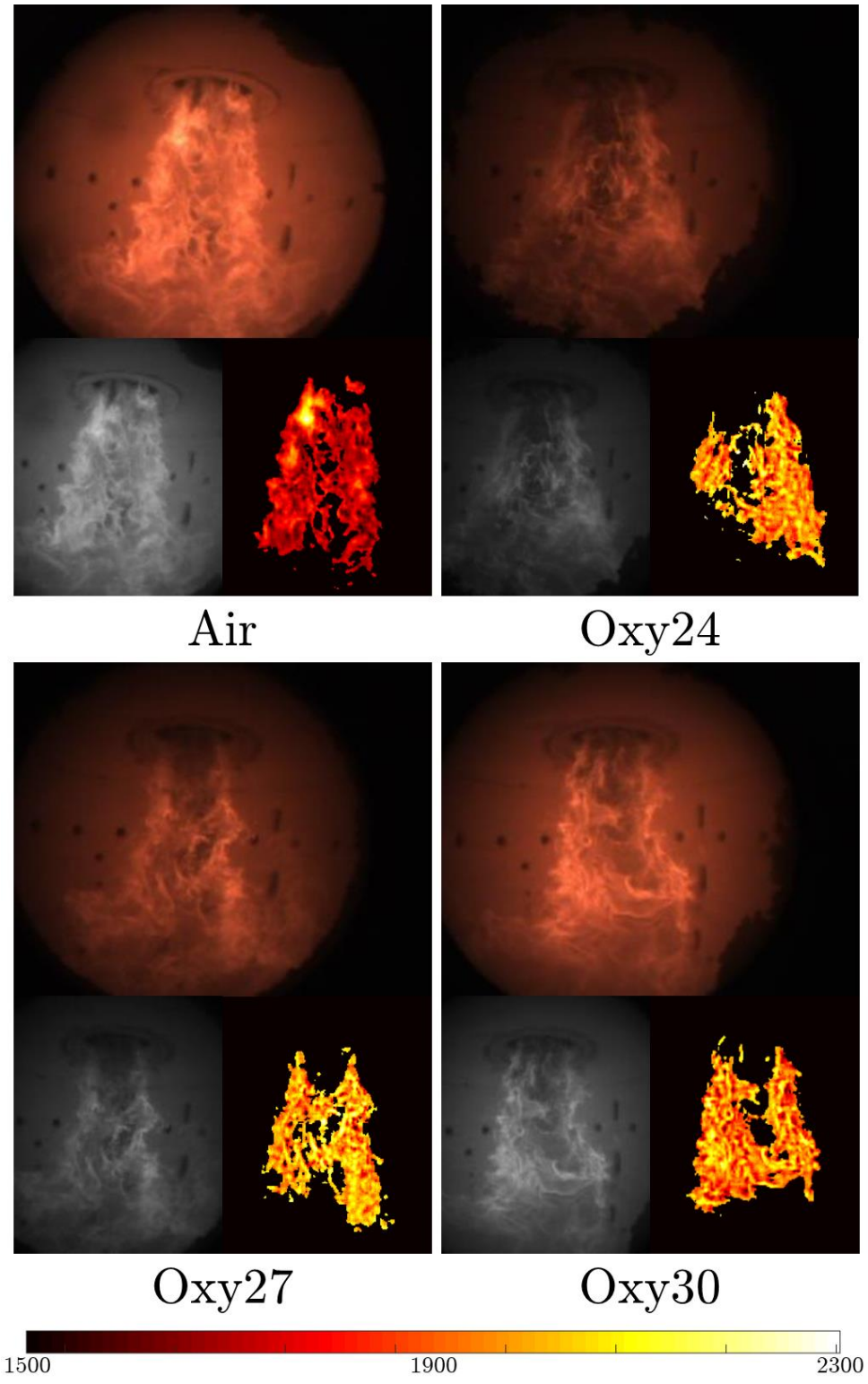

Figure 4.4 Original snapshot recovered from the recorded video (top) and the correspondent processed frames for luminance (low left) and temperature (low right).

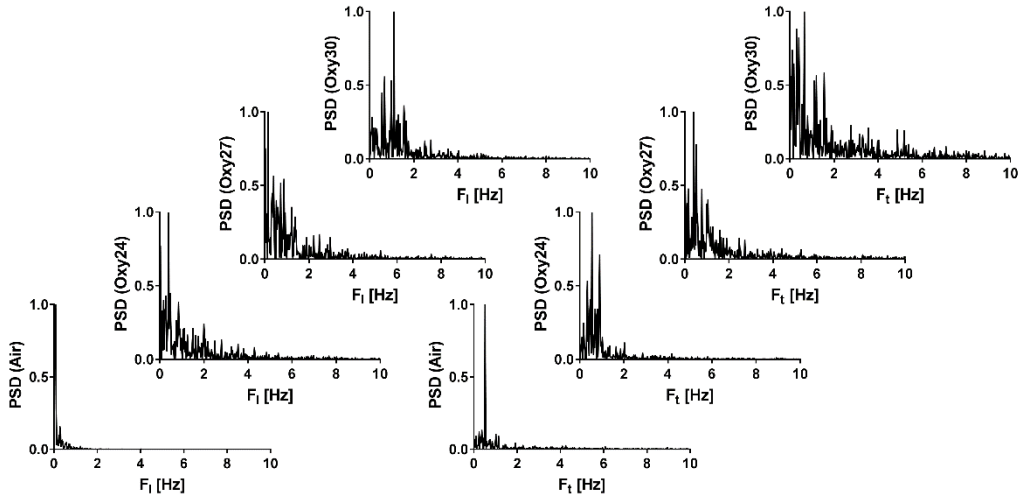

Figure 4.5 Normalized spectrum of frequencies constructed after the digital luminance (left) and temperature parameters computed using the full flame region.

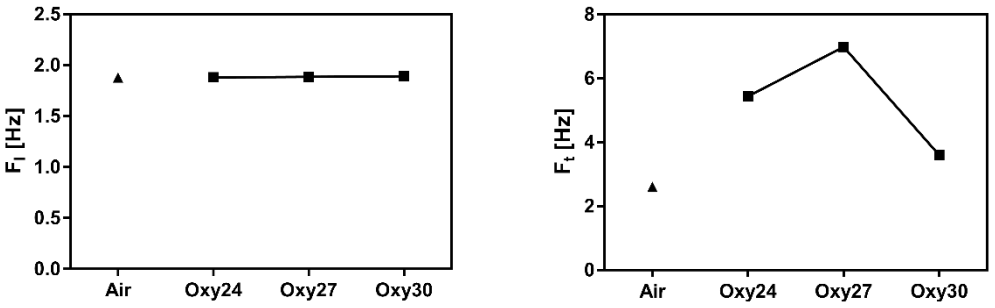

Figure 4.6 Trend of the characteristic oscillation frequencies for the luminance (left) and temperature (right) approach using the full flame region.

In contrast, the values obtained by weighting the frequency spectrums generated by the temperature fluctuations produced a wider range; the characteristic frequencies for the Oxy24 and Oxy30 cases were 2 and 2.6 times higher than that originated from air-fired combustion. The value for the richer oxygen case, Oxy30, displayed a discontinuity in the trend by dropping to a lower value of 3.6 Hz, which is closer than that exhibited by the air case at 2.6 Hz. The discrepancies among the values in the characteristic oscillation frequency of the temperatures may be a direct consequence of both the lower diffusivity of oxygen in a CO_2 rich environment and the lower adiabatic temperatures achieved in the Oxy24 and Oxy27 cases in comparison to that of the air case [330].

4.3.2. Near burner region

The same set of snapshots recovered from the recorded videos of the flame were used for the assessment of the oscillatory behaviour in the region near the burner front. The original frames were cropped into a smaller area than that used in the full flame region; the final snapshots used in the computations were of a resolution of 190×100 pixels. The position of the area used in the analysis was carefully set to entirely accommodate the burner throat. A preliminary assessment of the temperature transient data evidenced that the damping effect of the walls into the oscillatory trends was lower in comparison to the full flame region; nonetheless, the same background removal operation was performed for the group of images in order to avoid biased results. A singular snapshot cropped to the near burner region alongside its luminance and temperature estimations are presented in Figure 4.7.

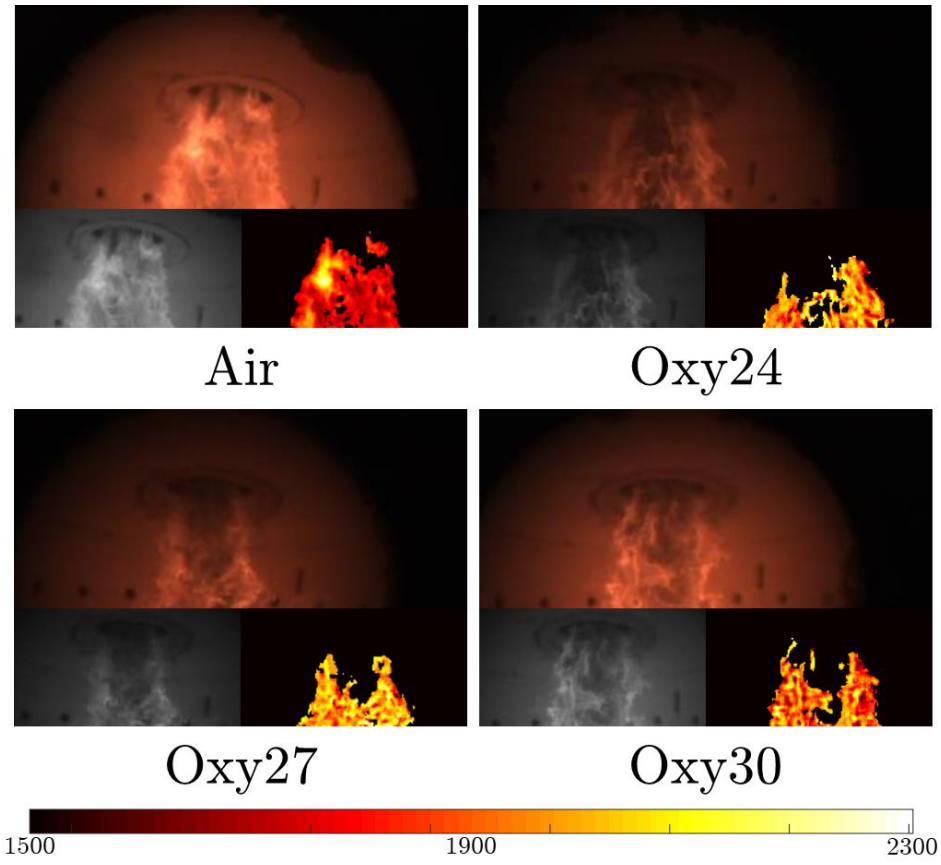

Figure 4.7 Original (top) and processed luminance (left) and temperature (right) snapshots used in the assessment of the characteristic frequency in the near burner region.

The normalized frequency spectrums generated for the flame parameters recorded in the near burner zone showed a similar arrangement as in the full flame

region, with the vast majority of the relevant frequencies clustered in the low range of the spectrum. The frequency spectrums for the luminance and temperature approaches are presented in Figure 4.8.

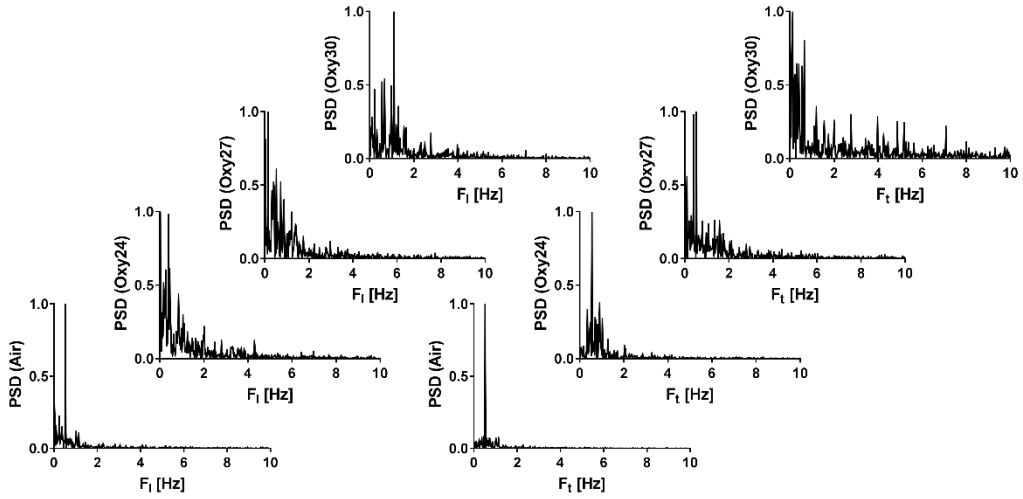

Figure 4.8 Spectrum of frequencies obtained after the luminance (left) and temperature (right) parameters in the near burner region.

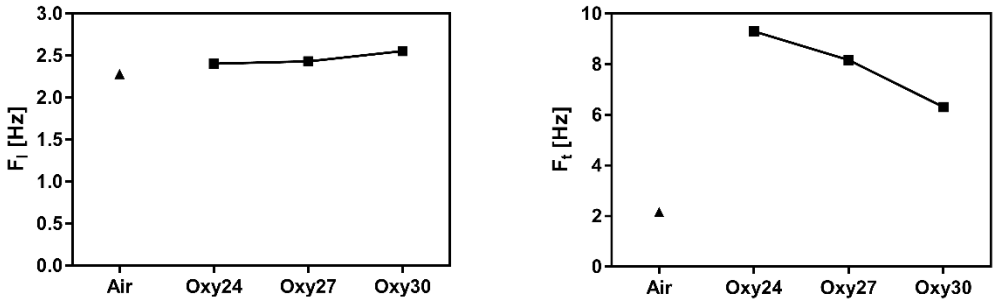

Figure 4.9 Characteristic oscillation frequencies for the digital luminance (left) and temperature (right) of the flame, measured in the near burner region.

Despite the sharpness of the frequency spectra, the weighted values for the characteristic frequencies were larger in comparison to those obtained using the larger area. The characteristic frequencies for the digital luminance signals, presented in Figure 4.9, were grouped between 2.3 and 2.55 Hz, in a similar trend to what the full flame exhibited. In addition, the characteristic frequencies obtained from the temperature estimations appears to be inversely proportional to the oxygen concentration for the oxyfuel cases, this progression

resembles the tendency observed in the analysis for the full flame region. However, the range in the magnitude of the frequencies in the near burner region, as expected for a rich volatile zone, was broader; the air case showed a characteristic frequency of 2.2 Hz, while the Oxy24, Oxy27 and Oxy30 scenarios obtained frequencies of 9.3, 8.2 and 6.3 Hz, respectively.

4.4. Oscillation severity analysis

The oscillation severity index, δ, conceives the stability of a flame as a direct relationship of the oscillation in the colour components. The oscillatory range is accounted for by a numerical relationship between the mean value and the standard deviation of the image; the area occupied by the flame is included into the expression to encompass its spatial variations.

The oscillation severity index is calculated from the same snapshots used in the spectral analysis and that were extracted from the flame videos. A colour space transformation is performed to convert the recorded data in the RGB space into the more comprehensive HSI space. While converting the images into the HSI colour space, the intensity, a value largely associated to luminous phenomena such as combustion, is decoupled from its position within the colour palette, thus facilitating posterior analyses.

The mathematics for the oscillation severity index was constructed to represent the unsettling of the flame through a value within the range between 1 and 0. A value of 1 in the oscillation severity index represents a flame in which all the recorded parameters remained unaltered during the sampled period. In contrast, a flame with an oscillation severity index of 0 portrays the maximum oscillatory behaviour that the flame imaging system is capable of capturing; this lower limit value will require a shift from the maximum to the minimum magnitude on all the flame parameters for each sampled snapshot.

Following its mathematical formulation, it can be established that the oscillation severity index and the stability of the flame are directly proportional; it is important to be noted that the temporal repeatability for the oscillations recorded are not included into the estimation, thus making essential to perform both the oscillation severity and spectral analyses simultaneously.

4.4.1. Full flame region

The set of snapshots used in the spectral analyses were used in the calculation of the oscillation severity indices. The extracted snapshots were trimmed into

a smaller area in order to focus attention on the luminous region; the final size of the images is 190×235 pixels.

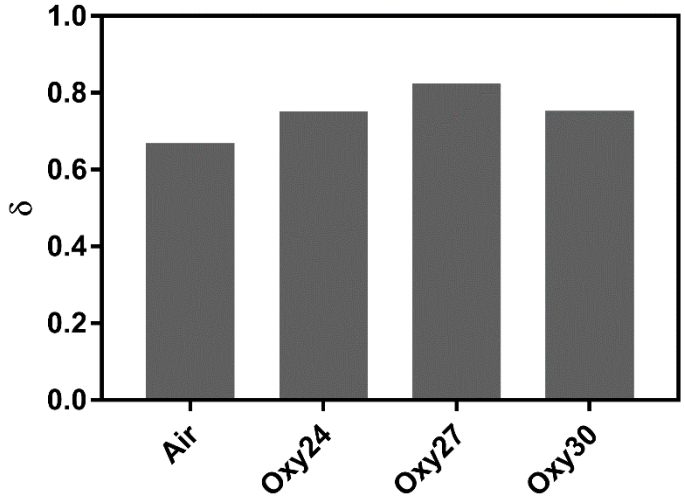

Figure 4.10 Oscillation severity index computed using the full flame region.

The values obtained for the oscillation severity index, as presented in Figure 4.10, shows that the oxyfuel flames appear to produce oscillations of lower severity than their counter part under air-fired conditions. The severity index computed for air combustion is 0.66, whilst the Oxy24 and Oxy30 cases shared a value of 0.75; the oxygen enriched Oxy27 case displayed the more steady behaviour, achieving a value of 0.82 for its oscillation severity. The range of values in which all the cases are contained evidenced that the natural occurring combustion oscillations remained relatively low during the experimental campaign, thus indicating stable flames overall.

4.4.2. Near burner region

The assessment of the oscillation severity in the near burner region was performed using a similar procedure to the spectral analysis approach. The extracted frames were undersized, and the area used in the estimation of the oscillation severity index was positioned to incorporate the tip of the burner.

The magnitude of oscillation severity indices, in accordance to the values obtained for the full flame region, showed a distinguishable increment for the oxyfuel cases. The air case generate an index value of 0.65, while a sustained increment for the index was obtained in direct proportion to the oxygen enrichment level; the oscillation severity indices for the oxyfuel cases were 0.74,

0.80 and 0.81 for the Oxy24, Oxy27 and Oxy30 combustion scenarios, respectively.

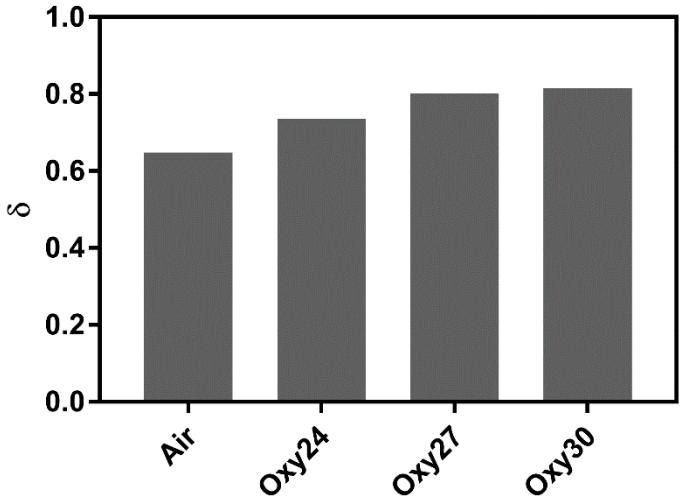

Figure 4.11 Oscillation severity index for the near burner region of the coal flame.

Despite the noticeable changes in their temporal repeatability, evidenced through the characteristic oscillatory frequency, the severity of the oscillations manifests itself steadily across the whole flame front. The insensitivity to the sampled region in the computation of the oscillation severity index, reassures the necessity to generate an inclusive data set from which a better insight into the whole combustion process can be obtained.

4.5. Summary

An assessment of the flame front produced by the combustion of pulverized coal particles in the 250 kW furnace of the PACT facilities was performed after recording information through a digital imaging system. Two different methodologies, namely spectral and oscillation severity analyses, were employed to characterize the dynamic nature of the flame.

The repeatability in time of the flame oscillation was accounted for by the spectral analyses performed to the digital signals generated after the post-processing of the experimental data. Two different flame features were approximated from a finite set of images, the first being the digital luminance and the second the temperature. The frequency spectrums obtained for both flame features displayed a tight array of frequencies in the lower range, with no relevant values beyond 10 Hz. The absence of frequencies in the higher range of the

captured spectrum suggests that the motion of bright particles through the flame front represented a larger contributor to the temporal repeatability rather than the light emitting phenomena associated to the combustion of volatiles. The spectrum of frequencies obtained for the temperature signal were more spread across the range, thus generating higher values for their corresponding weighted characteristic frequency.

The trend obtained for the weighted frequencies evidences that the digital luminance, mainly driven by the char combusting particles, remained uniform for all the cases, thus indicating good char burnout rate. In contrast, the effects of the different combustion environments for the oxyfuel cases produced a noticeable alteration in the weighted values for the oscillatory frequency of the temperature. The oscillations in the temperature frequency exhibited an inverse proportionality to the oxygen concentration of the environment, which appears to be directly related to the adiabatic flame temperature achieved. An equivalent flame temperature and heat transfer profile to those obtained under an air combustion environment will require an oxyfuel recycle rate between 27 and 35%, hence consistent to the results obtained throughout this study.

In addition, the results obtained after the oscillation severity index computation indicated that the oxyfuel environment promotes the stability of the coal flames by decreasing the range of their oscillations. An increasing trend in the steadiness of the flames was depicted in concordance to the oxygen level. The comparison of the results obtained using the full flame and the near burner regions showed that the capture of the oscillation severity index is independent of the sampled region, and therefore a good approach for application in which the flame front can only be partially observed.

The definition of flame stability comprises an ambiguous connotation due to the wide range of variables from the combustion and fluid flow phenomena involved that are inherently dynamic. The convention singular approach in order to quantify the stability of a flame is therefore complicated, and to some extent futile. In contrast, the temporal repeatability and the severity of the flame oscillations can be quantified, and their results employed in a more comprehensive approach towards the interpretation of the stability of the flame.

5. The coherence of an isothermal swirling flow

The effects of swirl in a flow field are vivid and favourable for particular applications. Their utilization and control is crucial in the design stages for the development of innovative technologies across many disciplines. Swirling flows can be encountered in a wide range of phenomena, such as in weather systems, tornadoes, whirlpools and maritime currents, as well as in different practical equipment such as cyclone separators, vortex amplifiers, jet pumps and combustors. In combustion, the effects of the swirling motion are widely used to stabilise the high intensity reaction and as control mechanism for the generation of pollutants [331].

A swirling flow is the result of the application of a spiralling motion, often referred to as swirl or tangential velocity, to the flow by means of swirl vanes, by providing a tangential inlet to the combustion chamber or by using axial-tangential swirl generators [332]. Furthermore, experimental results have shown that the effects of the swirl in the fluid motion are ubiquitous and long-lasting, thus directly influencing the jet growth, entrainment, decay rate and the vortex size and shape [331], [333].

In order to take advantage of the intrinsic benefits of swirling flows, accurate predictions of the flow behaviour must be obtained. Mathematical models have been developed and modified to account for the intertwined arrangement of the flow. As discussed in Chapter 2, a more detailed representation of the fluctuating nature of turbulent flows can be obtained by performing large eddy simulations. However, the amount of data produced by this methodology is generally large and complex to synthesise into practical information of the process. Further processing of the information is often required in order to acquire statistically meaningful values and to successfully characterize the flow.

In the following sections, a methodology for the assessment of the coherence exhibited by an isothermal swirling flow is developed. The particularities and the operating conditions of the experimental rig will be reviewed. Furthermore, the settings employed, as well as the selection of mathematical models used in the numerical simulations, are discussed. Moreover, the methodology for the evaluation of the temporal, spatial and spatiotemporal repeatability of the flow, using one and two-dimensional sampled data, is presented. Finally, a

summary of the results obtained, in addition to the insights provided by them into the flow behaviour and a discussion on the pertinence of the methodology for further swirling flow applications, is provided.

5.1. Case description

The case used for the development of the methodology to perform the assessment of the coherence in a swirling flow corresponds to that reported by the Lewis Research Center, part of the NASA, in the United States [305]. The report comprehends an experimental campaign carried over a test rig that was constructed to evaluate the performance of a swirling jet in an enclosure. The apparatus consisted of a test section made of glass where a combination of laser velocimetry (LV) and laser induced fluorescence (LIF) were employed to obtain the instantaneous velocity components of the water flow and the concentration distribution of a dye. The flow entered the domain through an inlet plenum consisting of two concentric channels. The outer channel is of an annular shape and allocates an arrangement of fixed blades that provides the angular component to the flow. The inner channel is a pipe of a rigid material, long enough to ensure that a fully developed profile is achieved before the mixing with the swirled fluid occurs. A detailed description of the components of the experimental rig, as well as the experimental techniques employed in the data sampling can be found in Chapter 3.

Table 5.1 Characteristics of the flow condition used to develop the methodology for assessment of the coherence in swirling flow.

Flow condition 1					
Mean axial velocity [m/s]		Flow rate [gpm]			
Inner jet	Annular jet	Inner jet	Annular jet	Fluid	Temperature
0.52	1.66	6.2	52.8	Water	293.15 K

The experimental apparatus was designed and manufactured as part of an inclusive project that intended to expand the knowledge of the effects of the swirling motion in combustors. Different swirler geometries and flow conditions were evaluated during the set-up of the device; however, the data collected from these tests are not reported. Nevertheless, the data obtained from a stable operational state, regarded as flow condition 1, was thoroughly documented and it is the condition used for the present CFD study and the subsequent coherence analysis. A summary of the conditions that characterize the flow is presented in Table 5.1.

The selection of an isothermal flow to evaluate the mathematical models and to develop the methodology employed in the coherence assessment in this thesis comply to the similarities in the mixing process between the swirling test apparatus and the coal combustion furnace. Furthermore, the development of zones of recirculating flow in the domain, as documented in the NASA report, is characteristic in combustors of recent generation, thus providing additional similarities between applications. Different test rigs have been modelled and the characteristics of their particular swirling patterns have been reported [334]–[338]. However, many of them are based on unconfined flows thus excluding the effects of the boundary wall in the overall flow structure [339]. The methodology developed in this chapter will be extended to the investigation of a coal combustor, in which the influence of the gaseous and char combustion in the flow distribution will be studied.

5.2. Numerical settings

The domain used in the CFD computations consists of two sections, firstly the main test section, is a cylinder of 122 mm in diameter and a length 1024 mm. In addition, a portion of the inlet plenum is included on the side and it is 51 mm long for the annulus and 169 mm for the jet inlet. A cross section of the simulated geometry is presented in Figure 5.1.

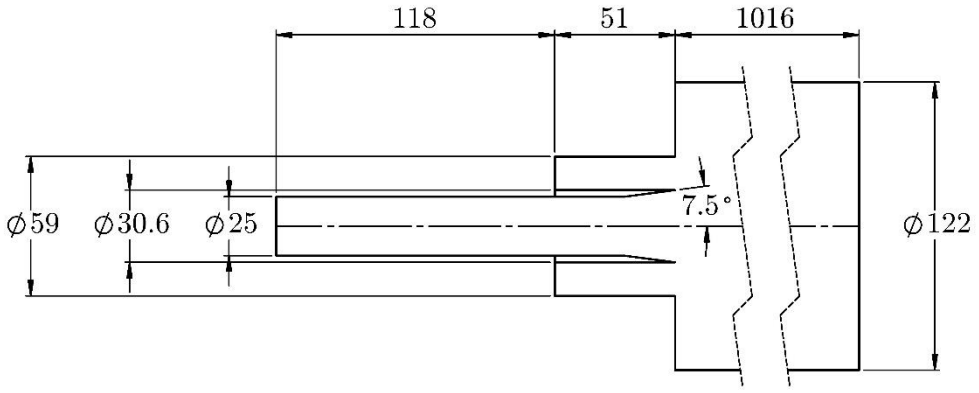

Figure 5.1 Cross section of the isothermal swirling flow apparatus.

The grids employed along this study were constructed using ANSYS ICEM, and consisted of hexahedral elements. The grids were generated by employing the structured blocking technique over the fluid body. Moreover, element refinements were applied near the chamber walls and in the regions of interest

as required. A preliminary study to evaluate the performance of different RANS models was performed over three different two-dimensional grids, the details of the grids are presented in Table 5.2.

Table 5.2 Details of the numerical grids employed in the evaluation of different RANS models for turbulence modelling and in the LES computations.

Numerical grids for RANS and LES calculations					
	Grid 1	Grid 2	Grid 3	Grid 4	Grid5
Grid type	2D	2D	2D	3D	3D
Number of elements	117235	265100	475863	14608800	22195812

The RANS turbulence models tested in the two-dimensional grid are the $k - \epsilon$ [93], the $k - \omega$ [105] and the RSM approach [106]. In addition to the standard versions of these models the renormalization group (RNG) [95] and the realizable [100] variations of the $k - \epsilon$ model, as well as the shear-stress transport (SST) [104] version of the $k - \omega$ were included. The results obtained from these analyses were used to obtain the element size distributions that later were set in the three-dimensional mesh required for the LES simulations.

The three-dimensional mesh consisted of 22195802 hexahedral elements and it was used to perform the LES calculations. The RANS results were compared against those obtained using the two-dimensional grids. Furthermore, the volumetric mesh was refined near the inlet plenum, in order to capture the effects of the recirculating flow. These refinements were made after constantly reviewing the data generated by the RANS models and by assessing the computer resources available for the subsequent LES computations.

A fully developed profile was used as the boundary condition for the jet inlet. The profile was produced by a preliminary simulation that used a translational periodic approach over the smaller domain of the pipe. In addition, the effect of the swirlers was accounted for by a separate simulation in which the blades were incorporated into the domain as surfaces. The results obtained at the inlet surfaces, such as the velocity distributions and the relevant turbulence variables, were incorporated into the three-dimensional simulation of the isothermal chamber as a profile distribution. For the LES simulation, the spectral synthesizer [134] was used to provide perturbations into the inlet flow, furthermore, constant pressure of 0 Pa was used as the outlet condition of the domain.

The CFD simulations were performed using ANSYS Fluent v17.2, which is a commercially available software. The pressure-velocity coupling was carried by the semi-implicit method for the pressure-linked equations (SIMPLE) algorithm [340]. A second-order upwind scheme was used for the spatial discretization of the pressure and momentum in the RANS cases, meanwhile the bounded central differencing scheme was employed in the LES computations. The second-order implicit scheme was used as the transient formulation. The selection of an adequate sub-grid scale (SGS) model is paramount in the prediction of the swirling motion of the flow, therefore, the Smagorinsky-Lilly and the Sigma models were tested in the LES framework in order to compare their performance.

The time-step used for the calculations was set to 1×10^{-4} s and the sampling frequency was fixed at every two time-steps. The total flow time of the simulation was no less than two-seconds for each LES case.

5.3. Velocity field results

The results obtained for the simulation of the flow condition 1 in the isothermal-swirling flows test-rig of the Lewis Research Center are presented in the following sections. The study of the performance of various RANS turbulence models, alongside the assessment of the influence of the grid size, are presented in the first section. Following, the velocity field obtained from the LES calculations is introduced and a direct comparison of the two SGS models is performed. Furthermore, the characterization of the vortex type in the domain is introduced.

Different monitors for a series of field scalars were defined at several locations in the domain and the transient variations of the scalars were recorded at a fixed sampling rate. In addition, vector fields of the velocity at different planar locations were gathered. The transient recorded data was used as input in the analysis of the temporal, spatial and spatiotemporal coherence of the flow that is later presented.

The flow field was reported to be of the vortex breakdown type, with two well-defined recirculation zones and one vortex, one of the recirculating regions is located at the outer zone of the vortex and close to the inlet plenum, and the second recirculation zone is located at the centre of the cylinder and it is enclosed by the vortex. Furthermore, the LIF and the high-speed photography revealed that the principal flow interaction occur at the shear layers between

the swirling and jet inlets and between the swirling and the recirculating outer flow [305].

5.3.1. RANS turbulence models and grid size assessment

The assessment of the performance of different RANS turbulence models was carried out by comparing the results yielded for the flow condition 1 case. Three different meshes, using a two-dimensional space and an axisymmetric formulation, were constructed for this purpose. The results obtained for each mesh are showed in Figures 5.2 to 4. Four locations were used to sample data from the flow and these were located at consecutive axial positions according to what it was documented in the report of the Lewis Research Center. The summary of the positions and the type of monitors employed throughout this study can be found in table 5.3.

Table 5.3 Summary of the monitors employed in the assessment of the coherence in an isothermal swirling flow.

Summary of locations and monitors		
Position	Axial distance [mm]	Monitor types
1	5.1	6 points, 1 line, planar
2	12.7	6 points, 1 line, planar
3	25.4	6 points, 1 line, planar
4	50.8	6 points, 1 line, planar

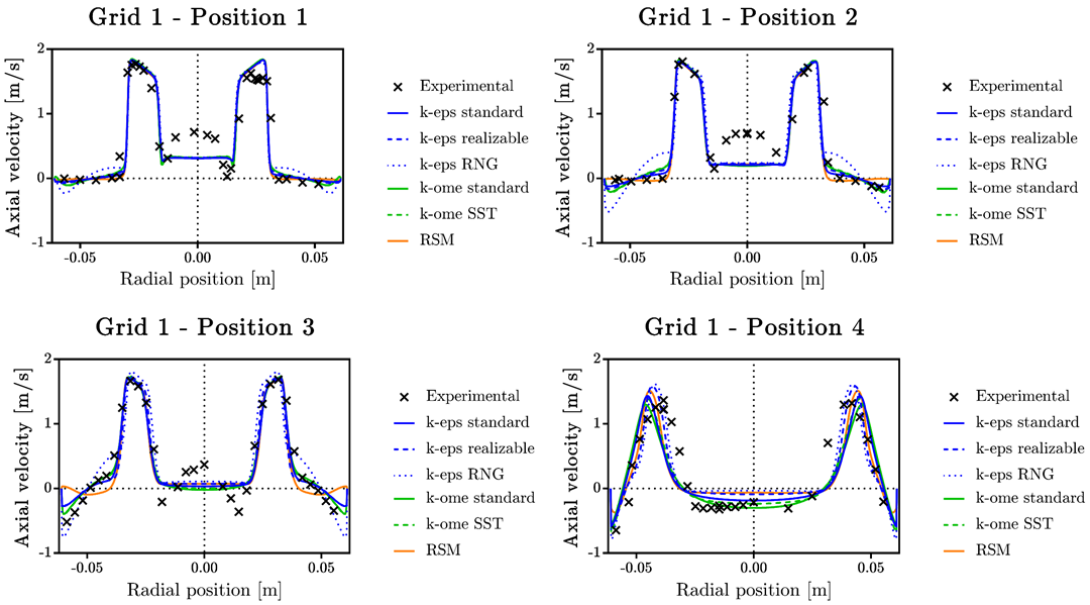

Figure 5.2 Comparison of the axial velocity obtained for different RANS models using the coarse two-dimensional grid (grid 1) at different axial positions.

The results obtained from the coarse grid displayed that the flow coming from the central jet was poorly captured in all cases. In contrast, the maximum axial velocity in the swirling channel and the recirculation zones exhibited a better agreement. Furthermore, the RNG $k - \epsilon$ model showed an over prediction in the magnitude of the velocity and the location of the recirculating zone.

Further refinements were made to grid 1 in the central region in order to improve the representation of the jet inlet, however, no significant changes in the velocity profiles were observed while using the new grid, known as grid 2. The behaviour of the RANS models remained unaltered for the two-equation models, while the RSM approach exhibited small variations for the position 1, as presented in Figure 5.3.

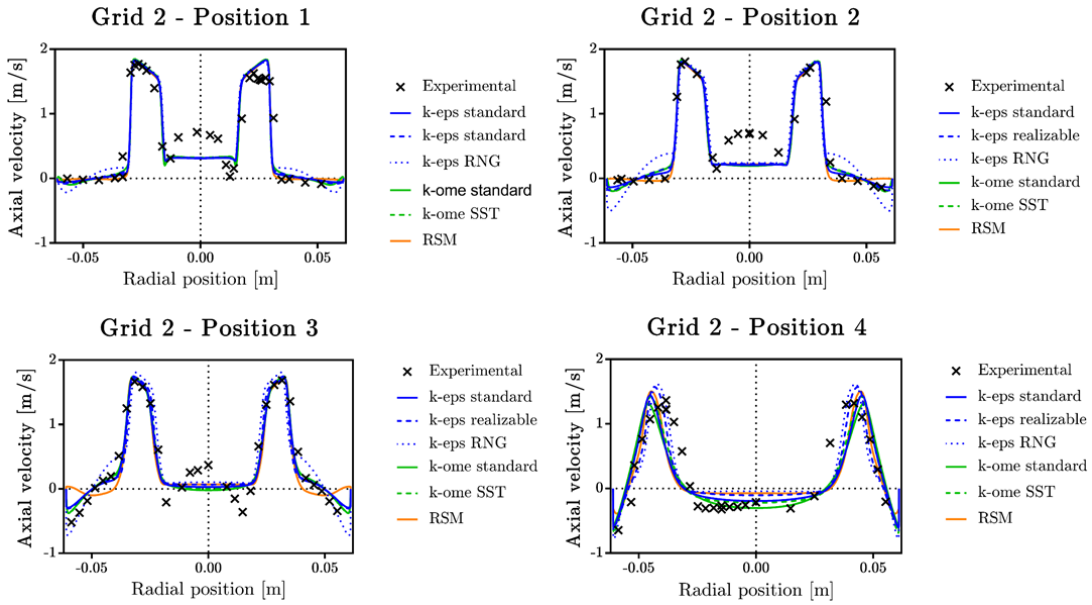

Figure 5.3 Comparison of the axial velocity for the different RANS models on the two –dimensional grid with medium refinement (grid 2).

An additional refinement was performed to the two-dimensional grid, including the central region and the outer recirculation zone, with the resulting grid (grid 3) consisting of 475863 quadrilaterals. Although the element distribution was heavily dense in the near plenum region, no noticeable improvement was observed for the two-equation models whilst the RSM marginally enhanced the velocity magnitude of the outer recirculation region. However, the numerical stability in the solution for the RSM and the standard $k - \omega$ model was evidently compromised, thus requiring a decrease in the under relaxation factors for the momentum and continuity equations and, as a consequence, necessitating additional iterations to achieve a satisfactory convergence criterion.

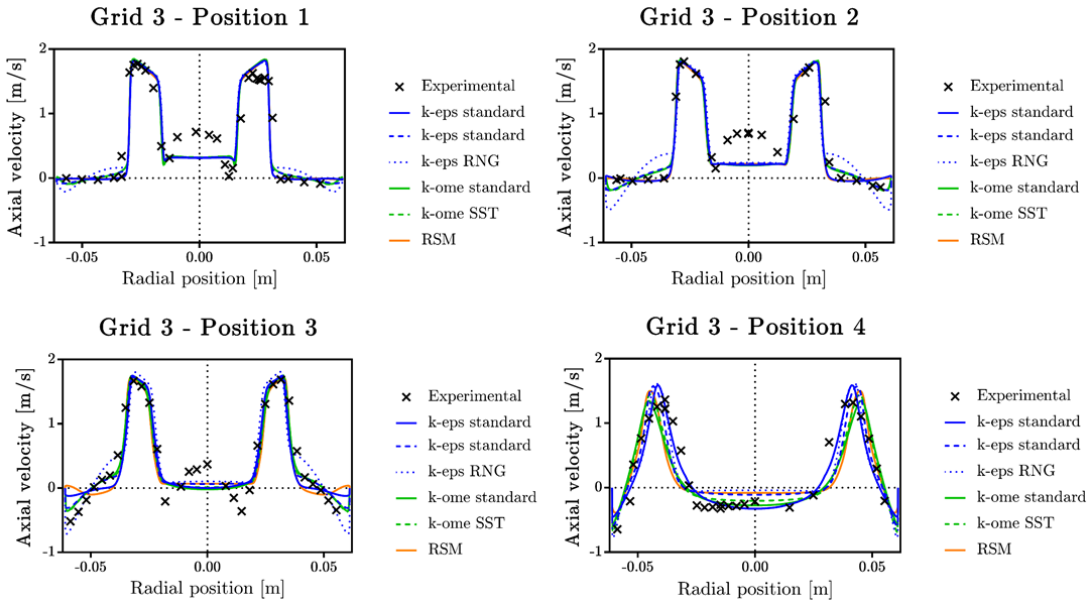

Figure 5.4 Comparison of the axial velocity produced by different RANS models on the most refined two-dimensional grid (grid 3).

The overall performance of the two-equation models, and their respective modified versions, was similar in all of the two-dimensional grids considered. However, the realizable $k-\epsilon$ model and the $k-\omega$ SST appeared to be the more robust models, thus producing more stable processes than the other models. In contrast, the RSM was shown to be prone to become numerically stiff and exhibited a large dependence on the grid size and distributions. Furthermore, the RNG $k-\epsilon$ model was unable to accurately predict the recirculation in the outer side of the vortex despite the refinements made to the grid. Finally, all the RANS models failed to capture the distribution of the jet inlet into the domain, however the predictions of the velocity field improves as the mixing between the two inlet flows occur downstream.

A three-dimensional mesh was generated using the structured blocking technique in ANSYS ICEM. The initial block was fitted to the fluid domain by including O-grids as required and collapsing the edges that capture the sharp chamfer in the jet-swirling flow intersection. The resulting mesh was comprised of 14608800 hexahedrons whose distribution across the domain followed the criterion of the grid 2. The three-dimensional mesh allowed us to supress the effects of the axisymmetric flow assumption, thus accounting for a more realistic approach to the turbulent motion. The boundary conditions for the inlets were set by employing profiles of the superficial velocity distribution and the relevant turbulence quantities. The profile for the swirling flow was obtained by performing a CFD analysis of the annular channel in which the fixed blades

of the swirler were included as two-side surfaces. The jet inlet was established through a fully developed profiled obtained by performing a transitional periodic simulation of the pipe.

The realizable $\kappa - \epsilon$ model was selected to test the mesh pertinence for LES calculations as it was shown to be the most stable among the two-equation formulations. Furthermore, an evaluation of the Scalable and Menter-Lechner functions [94] for the near wall treatment was performed, and the results for this comparison are presented in Figure 5.5.

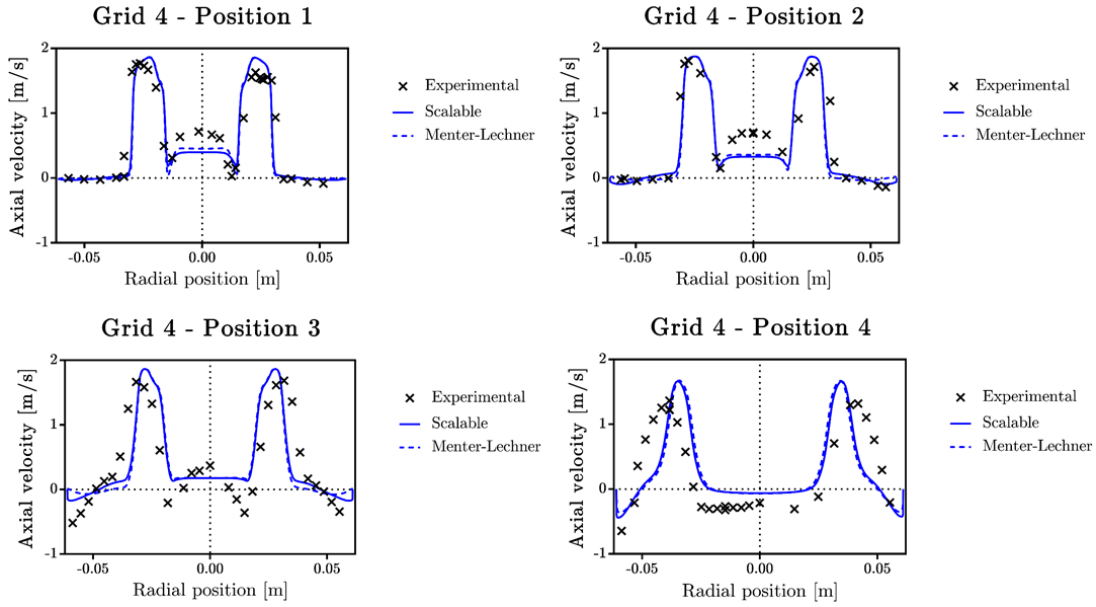

Figure 5.5 Comparison of the axial velocity at different axial positions for the evaluation of the near-wall treatment functions on the three-dimensional mesh.

The three-dimensional simulations showed that the Menter-Lechner functions generated slightly higher values for the maximum velocity of the central jet for positions 1 and 2. However, no differences were observed at different radial positions and for locations 3 and 4. The pertinence of the mesh to fully resolve the large eddies was assessed by the mathematical expression $\mathcal{L}_{grid}/(\mathcal{L}/12)$ [81] which was previously introduced in Equation 2.60. The value of $\mathcal{L} = \kappa^{1.5}/\epsilon$, was evaluated using the results obtained from the RANS simulation. It was found, that despite the majority of the elements in the grid comply with the criterion introduced before, in some regions of the mesh were still too coarse. A series of successive refinements to the mesh were carried out taking into account the grid size and the projected computation time. The final mesh contains 22195812 hexahedrons and it is denominated as grid 5 henceforth. Larger meshes were generated, but they were difficult to manipulate and the

computational resources required for the solution of the CFD simulation escalated rapidly, thus reducing the feasibility of the study.

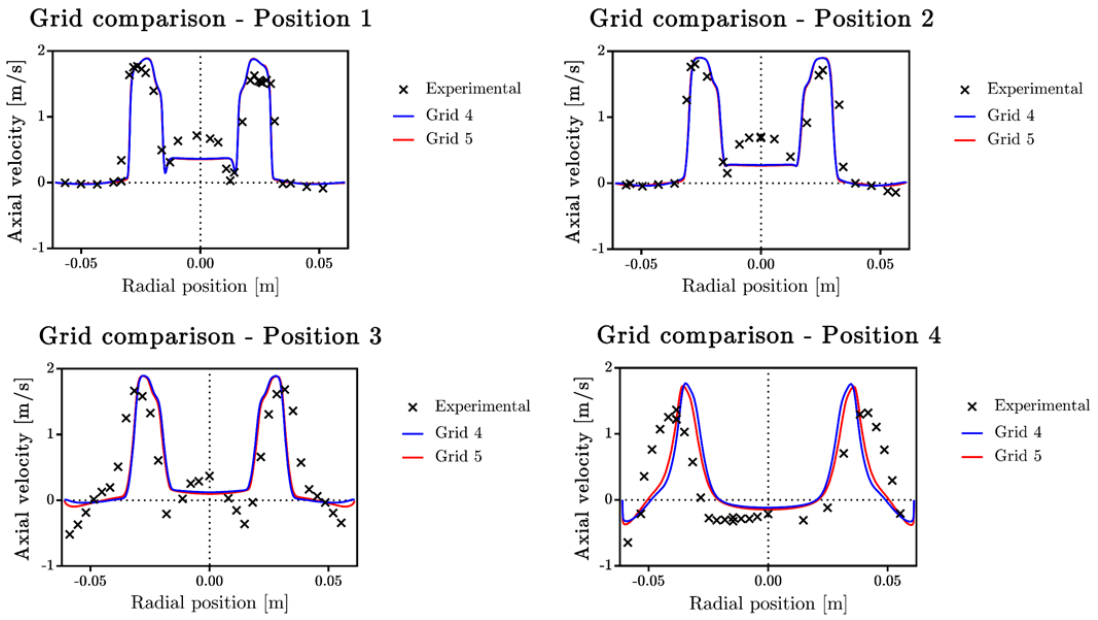

Figure 5.6 Axial velocity a various positions used to evaluate the effect of the refinement of the three-dimensional grids in the RANS computations.

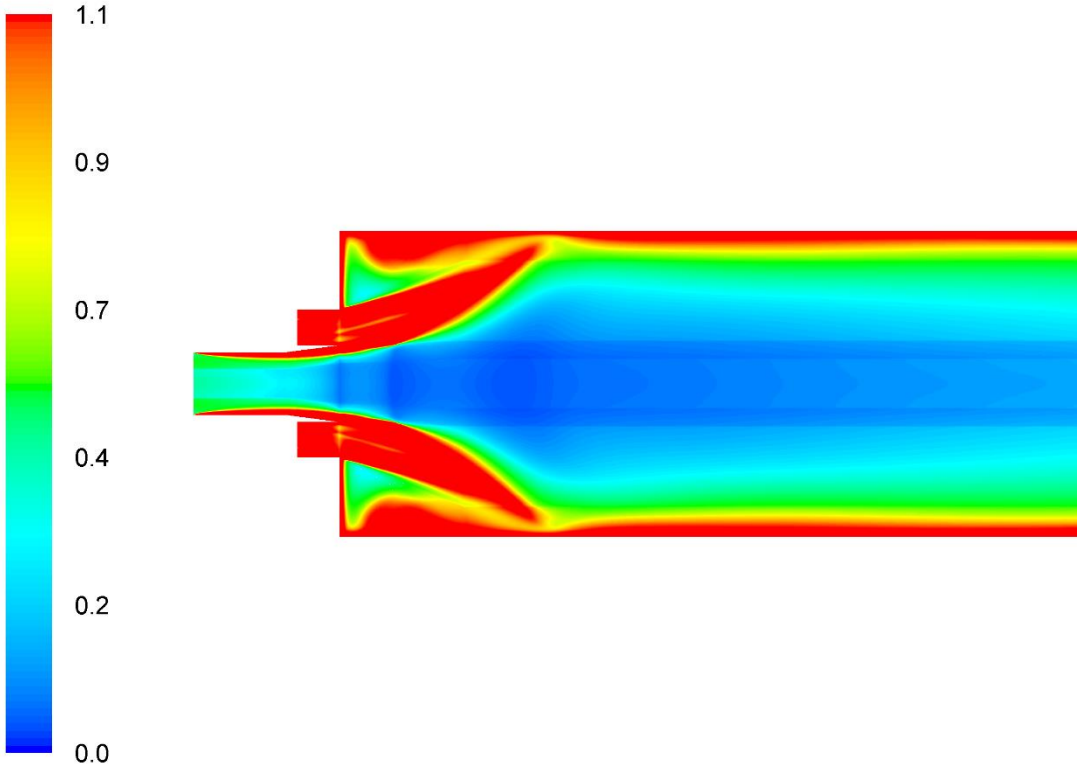

Figure 5.7 Assessment of the mesh suitablity for LES based on the quality criterion, the areas coloured in red need further refinement.

The performance of the three-dimensional grids, namely grid 4 and grid 5, was compared by carrying out CFD simulations with the same numerical settings. The realizable $k - \epsilon$ model, coupled with the Menter-Lechner wall functions, was selected for the comparison and the results are presented in Figure 5.6.

The results of the axial velocities showed that the capture of the region near the inlet plenum, comprising positions 1 and 2, suffered no noticeable improvement and the enhancement in the prediction of the outer recirculation zones in the positions 3 and 4 is marginal. However, the pertinence of the mesh for LES simulations was considerably improved; the distribution of the quality criterion on the domain is showed in Figure 5.7. Despite the effort in the mesh refinement, there are regions that remain too coarse to successfully resolve the turbulent kinetics and, therefore, further mesh refinement might be required if sufficient computational resources are available for future calculations.

5.3.2. Transient velocity distributions and vortex identification

The effects of the sub-grid modelling are crucial in the accurate prediction of the velocity field in LES [341]. The accuracy, cost of use and the range applicability are often regarded as the criteria for the selection of the appropriate SGS model [81], [128]. In addition to the complexity of the swirling phenomena, the influence of the walls on the overall flow evolution must be included. Two different SGS models, namely the Smagorinsky-Lilly [116] and the Sigma model [122], have been tested for the same flow conditions. The Smagorinsky-Lilly model is a popular choice for SGS modelling due to its numerical robustness. However, the turbulence in the near-wall region is acknowledged to be over predicted, thus suggesting the inability to properly capture wall-bounded flows [120]. In contrast, the Sigma model stems from the Wall-Adapting Local Eddy Viscosity (WALE) model [121], which included a correction for the solution of the turbulence near the wall. The sigma model is based on the eigen-decomposition of the velocity gradient tensor and it has been shown to outperform both the Smagorinsky-Lilly and WALE models [123]. The details for the formulation of the SGS stress tensor in both models can be further reviewed in Chapter 2.

The results of the comparison among the SGS models are presented in Figure 5.8, and the profile obtained in the RANS calculation is included to illustrate the advantages of the LES over the steady state approach. The variables used for the comparison are the mean values of the scalars obtained after sampling each variable for a period of time. The results exhibited a better capture of the central region of the domain, where the jet inlet is located. Furthermore, the representation of the shear layer generated where the jet and the swirling fluid

are combined was enhanced in the LES cases, as can be noted in the plots for the positions 1, 2 and 3. Downstream, as the intensity of the swirl decreases, and as the mix of the inlet streams occur, the differences in the results are educed. The location of the outer recirculation zone was miscalculated in all cases, hence the inaccurate trend observed in the position 3. Nevertheless, the magnitude of the recirculating velocity was successfully predicted downstream in position 4. Finally, the mixing process of the streams appears to be under predicted when employing the Sigma model, hence the slightly higher value of the velocity in the central region at the position 4, which is a remnant of the central jet.

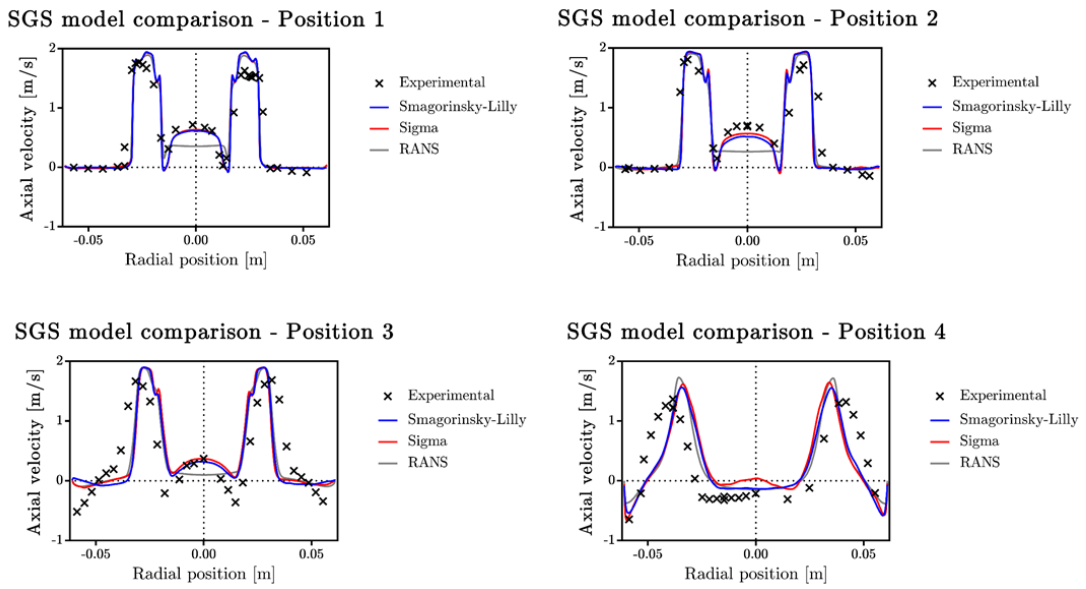

Figure 5.8 Comparison of the axial velocities obtained for different SGS models and for the RANS approach.

In addition to the comparison in the velocity distribution, a series of contours are introduced. The contours depicted in Figure 5.9 correspond to the distribution of the axial velocity in a cross-sectional plane. The contours evidenced the improvement in the representation of the central jet while implementing the LES approach, as it is noticeable that the jet penetrates the central recirculation zone and the RANS approach fails to capture this behaviour. Furthermore, the extension of the central recirculation zone is similar in all cases, but a narrower region is predicted on the RANS approach. Moreover, the swirling jet exhibited a sudden decay in the magnitude of the axial velocity for the LES cases, thus allowing a disruption in the vortex structure; the swirling jet in the RANS case showed, in contrast, to be a constant entity until eventually hitting the wall of the chamber. The shape of the shear layer in the outer recirculation

zone is slightly different for the LES cases with a small crest being present for both SGS models, while in the RANS contour of the interface is smoother. The outlet exhibited backflow at its centre which may be due to the associated boundary condition selected.

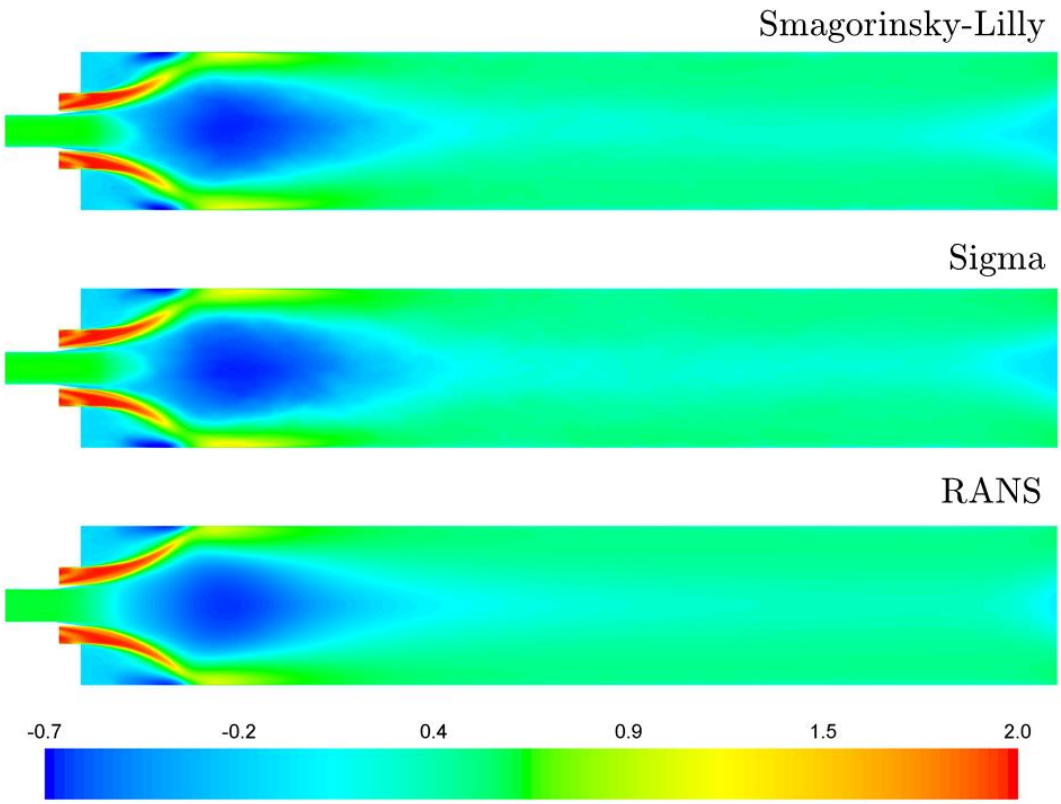

Figure 5.9 Distribution for the axial velocity [m/s] on the cross-sectional plane of the test section.

In addition, contours plots at the four different axial positions are presented in Figure 5.10. It should be noted that the positive values obtained for the axial velocity in the RANS approach are higher than those generated by the LES calculations. In addition, the profile of velocities that is generated by the arrangement of swirling blades is well retained in the LES computations whilst in the RANS case it become more diffused. Furthermore, the separation of the inlet streams at the axis is well maintained in the LES, as shown for the positions 1 and 2, but it is non-existent in the RANS results. Moreover, the range of velocities in the LES case using the Sigma SGS model is wider and the diameter of the recirculation zone predicted by the Sigma model is smaller than that obtained from the Smagorinsky formulation and the RANS approach, as evidenced in the contours for positions 3 and 4. Further, the high-speed ring, depicted in the contour for the position 4, suggests that it is comprised of several spots of rapidly moving fluid that might be related to the

turbulent coherent structures, such as the vortex breakdown phenomena. In contrast, the RANS approach produced a smoother ring body, with a more evenly distributed velocity.

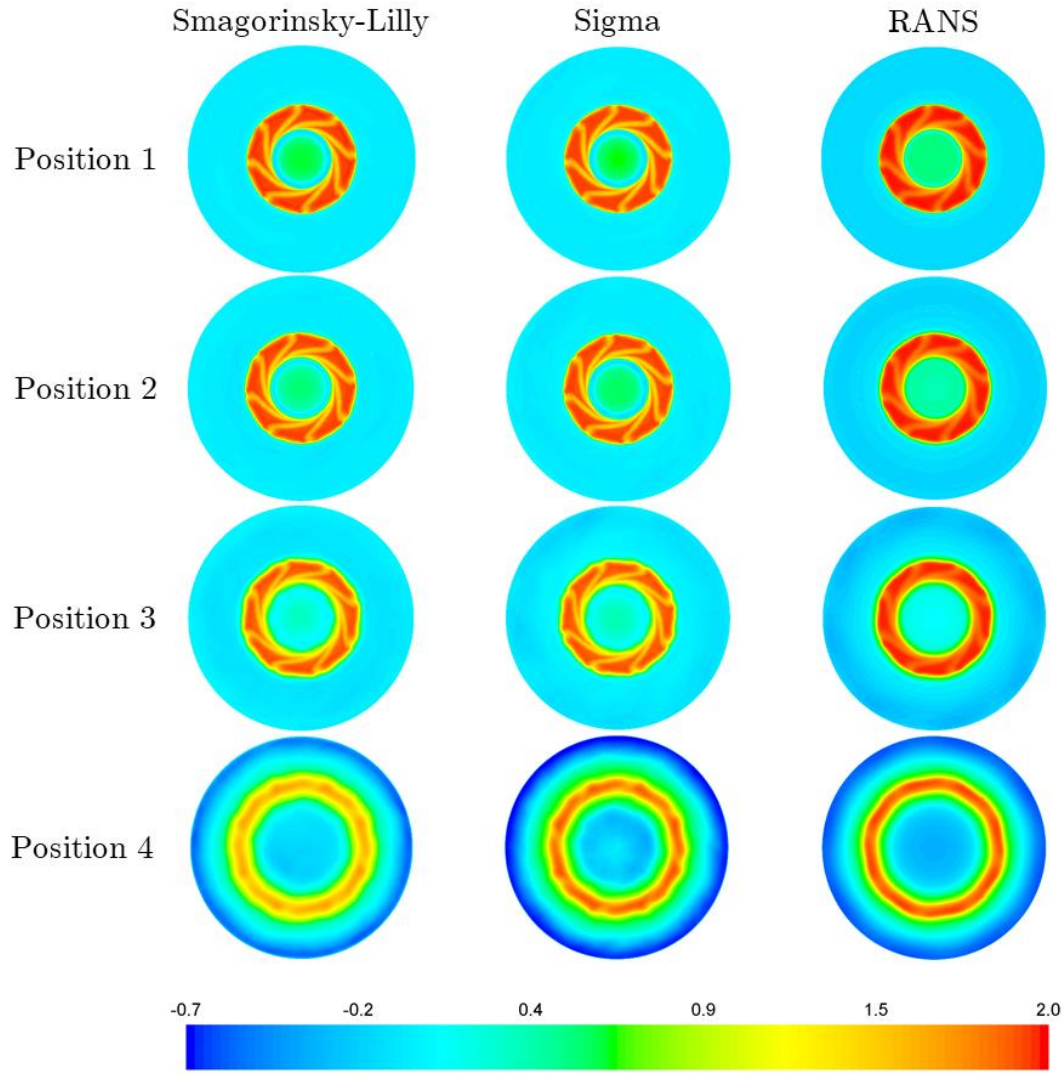

Figure 5.10 Plots of the axial velocity distribution [m/s] at different positions along the axis.

The plots and contours previously analysed provide a representation of the velocity distribution in the domain but they fail to fully identify and characterize the vortex generated. The appearance of vortices is often assumed to be inherent in the turbulent motions of the fluid, nonetheless a universal consensus in the definition of a vortex is still debatable [79]. Furthermore, the spatially coherent, temporally evolving structures that arise in turbulent shear flows dominate the dynamics of the flow, hence making the appropriate identification of the vortices a crucial factor in the analysis of swirling flows. Dif-

ferent requirements have been set in order to determine the presence of a vortex core, a region in which fluid particles move around, but having net vorticity and a geometry that is Galilean invariant are often employed in vortex analyses. Three different vortex identification schemes have been used in this study, and they are the vorticity magnitude, the Q-criterion and the Lambda-2 criterion [342], [343]. A series of plots of the isosurfaces generated for each vortex identification scheme are presented in Figure 5.11. The isosurface for the vorticity magnitude corresponds to the 10% of the maximum value, while the isosurfaces of the Q-criterion and Lambda-2 criterion were obtained at 15% of the maximum value for the Smagorinsky model and 20% the Sigma model.

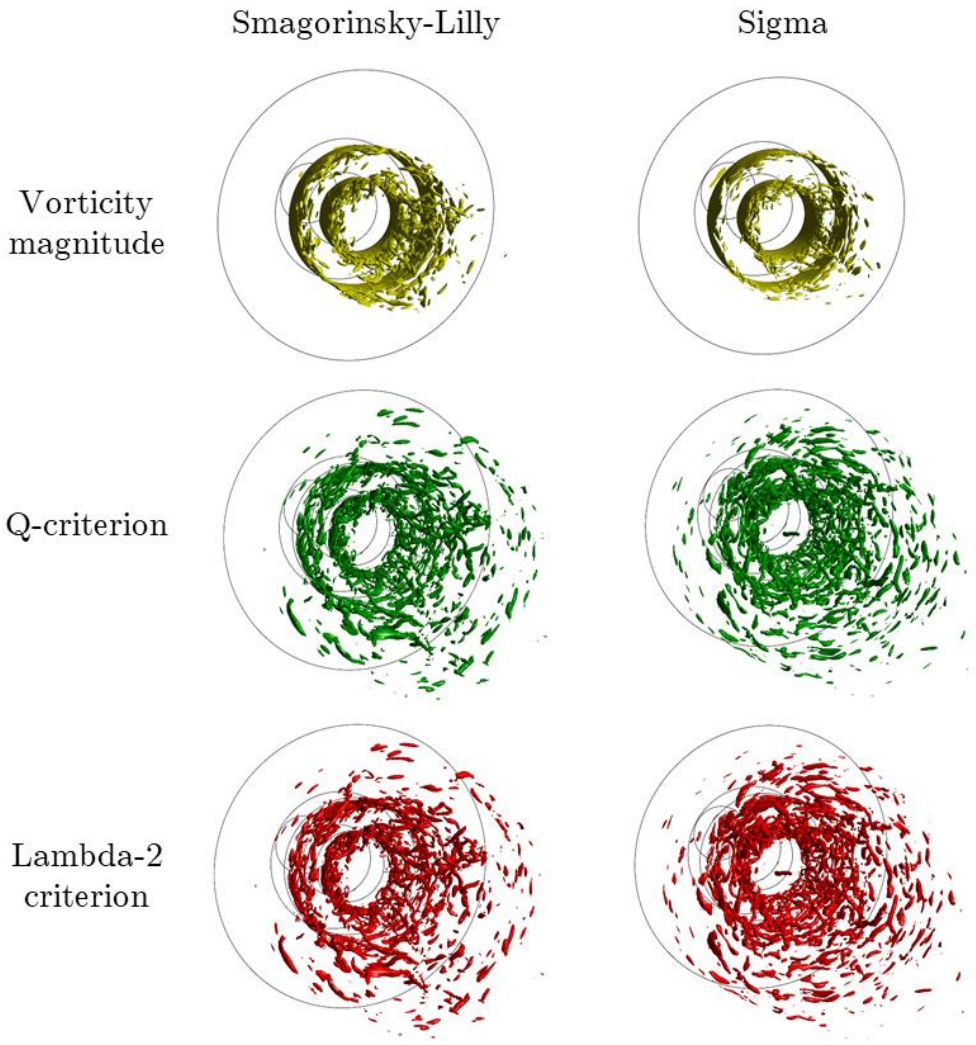

Figure 5.11 Isosurface for the vorticity magnitude, Q criterion and Lambda-2 criterion used to identify the type of vortical arrangement.

The tangle of vortices depicted in the isosurfaces suggest that there is no major vortex structure, instead smaller vortex filaments coexist within the swirling

flow as they move through the domain. In addition, it appears that some of the structures eventually collide, and consequently form larger vortices. Furthermore, the trail of vortices are mostly contained in the shear layers, which agrees with the findings of the experimental campaign. The high density of the water, in addition to its viscosity value, appears to influence the orderly disposition of the vortices and the lack of a singular major turbulent structure, which is often characteristic in applications involving air as the working fluid. Nonetheless, the assessment of the vortical structures indicate a high degree of uniformity and therefore coherence in the fluid flow.

5.3.3. Temporal coherence analysis

The evaluation of the temporal repeatability provides an insight into the dynamics of the flow, and it is a paramount attribute in their utilisation across different industrial applications. The transient behaviour on a swirling flow that exhibit a discernible sequence of oscillations in its velocity components can be predicted, and therefore improves the possibility to control it. Swirling flows that are able to produce a distinguishable oscillatory behaviour are the pinnacle in the stabilisation techniques for the flame in combustion applications. The transport phenomena is greatly enhanced by the swirling motion, however transient instabilities that might arise, or be exacerbated, from the erratic behaviour of the flow are regarded as the principal cause for disruption in the process [332]. Therefore, it is necessary to determine the degree of repeatability of the flow variables in order to successfully take advantage of the benefits of the swirl.

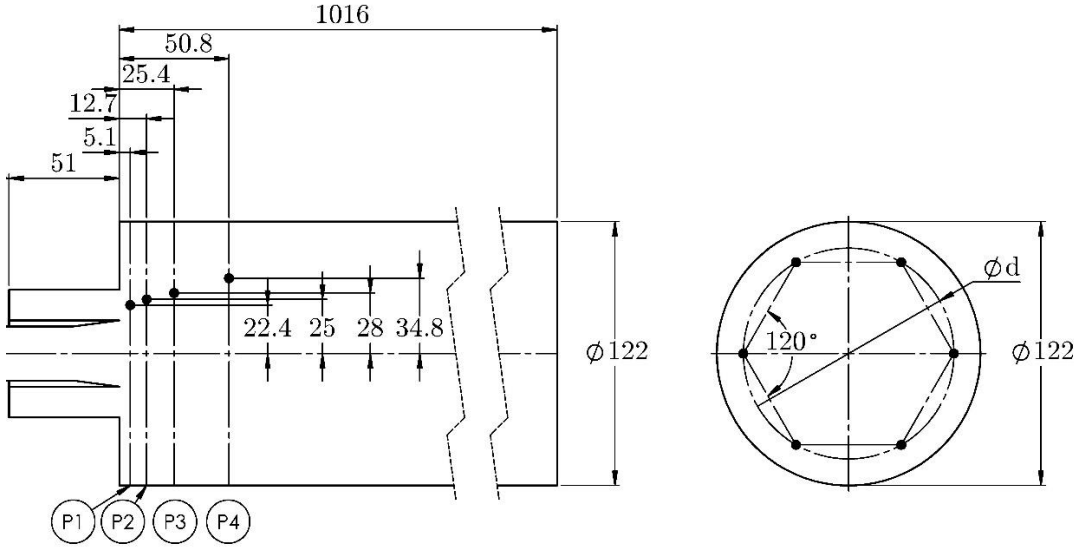

Figure 5.12 Location of the different monitor points (depicted as black dots) used in the analysis of the temporal coherence.

For the assessment of the temporal coherence of the flow, 24 monitor points were placed in the domain, six of them were located at each axial position as stated in Table 5.3. The coplanar points were distributed so they form a perfect hexagon, furthermore the diameter d of the circle that circumscribes the hexagon was adjusted for each axial position in order to locate the monitors within the swirling vortex. The value for the axial velocity was recorded simultaneously at all locations and the spectral analysis of the signals was performed [344]. In addition, the cross-correlation for the signals is presented as an indicator of the influence from one point to the other and as an indicator of the degree of interdependence [345]. Moreover, the analysis is performed using the results produced by the Smagorinsky-Lilly and the Sigma model, thus providing an additional comparison of the performance of each SGS model.

The instantaneous value for the axial velocity was recorded at a sample rate of 2×10^{-4} s, which is every two time-steps during the LES calculation. The signals consist of a total of 780 records, which is the maximum value of time-steps accomplished for the Sigma model using a single batch job in the high performance computing facility used for this study. The signal obtained from the Smagorinsky–Lilly model was shortened for consistency to the Sigma model. Furthermore, the values of the PSD and the cross-correlation have been normalised to enable a direct comparison between the points and the frequency plot has been clipped at 500 Hz to facilitate its reading despite that the spectrum was calculated up to the Nyquist threshold of 2.5 kHz.

5.3.3.1. Axial position 1

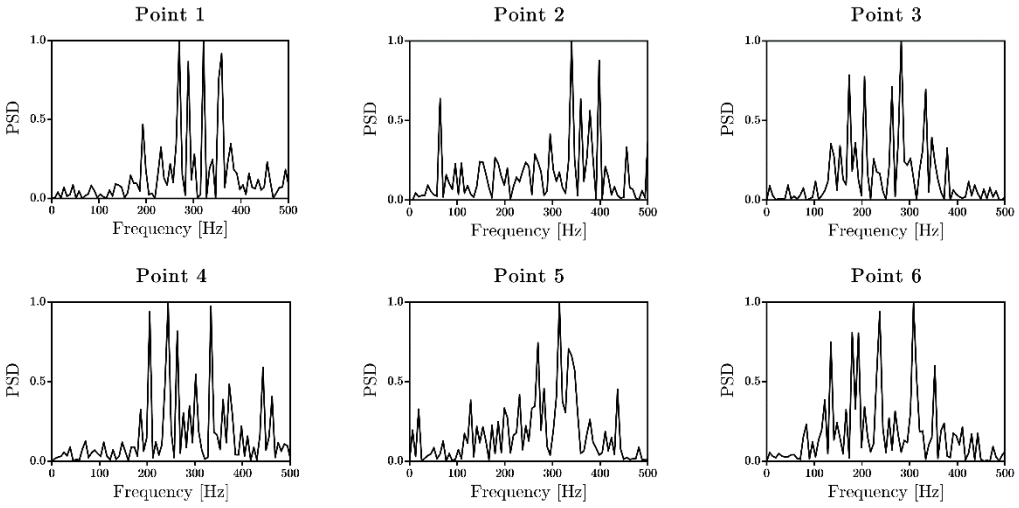

Figure 5.13 Spectrum of frequencies obtained for the monitors at position 1 using the Smagorinsky-Lilly SGS model.

The spectrum of frequencies obtained from the Smagorinsky-Lilly model showed up to five noticeable frequencies that are scattered between 0 and 500 Hz, as presented in Figure 5.13. This arrangement of frequencies suggest that at this axial position, the variations in the flow velocity superimposed by the perturbation algorithm at the inlet boundary have not been diffused and are still noticeable. The weighted value for the oscillatory frequencies averaged 287.8 Hz, however the large number of relevant frequencies prevent the assumption of this value as the overall temporal frequency.

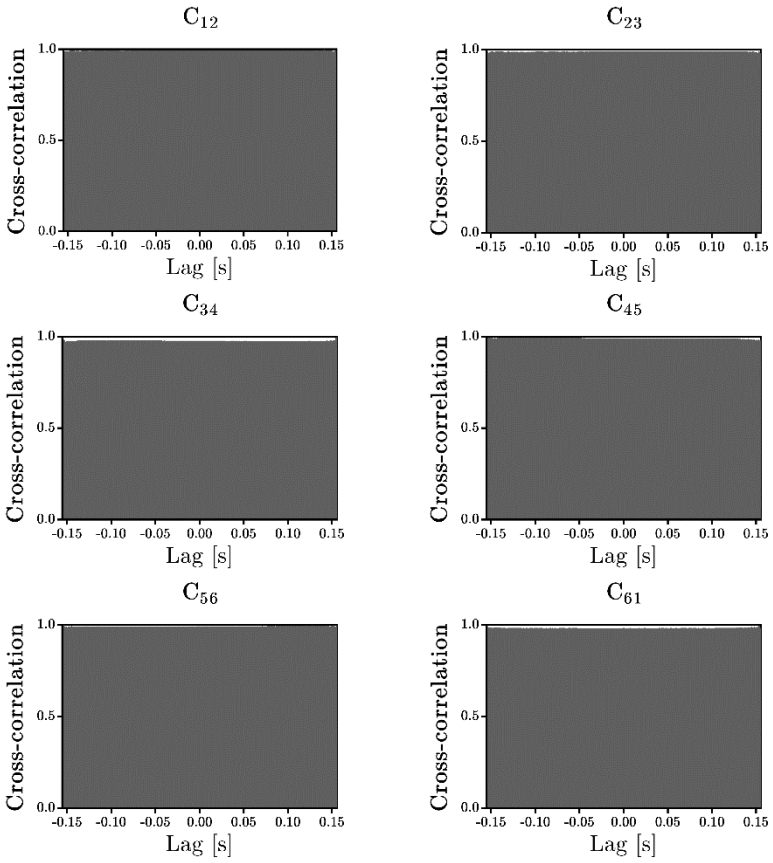

Figure 5.14 Cross-correlations of the signals recorded at consecutive points at position 1 using the Smagorinsky-Lilly model.

The plots for the cross-correlation between signals are ranged from 0 to 1 where 1 corresponds to the highest correlation possible, with the x axis being the time, thus illustrating the lag between recorded signals. The cross-correlations for the Smagorinsky-Lilly model, as displayed in Figure 5.14, exhibits a high degree of inter dependence, with almost no lag perceived and this represents that, despite the unsettled spectrum of frequencies, the flow field produced by the Smagorinsky-Lilly model appears to be moving coherently.

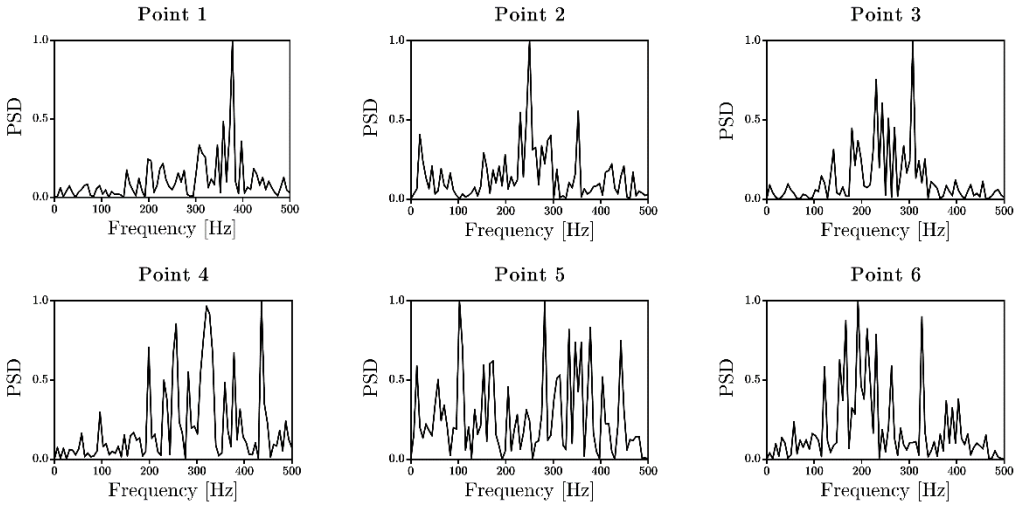

Figure 5.15 Frequency spectrums produced by the Sigma model for the different points located at position 1.

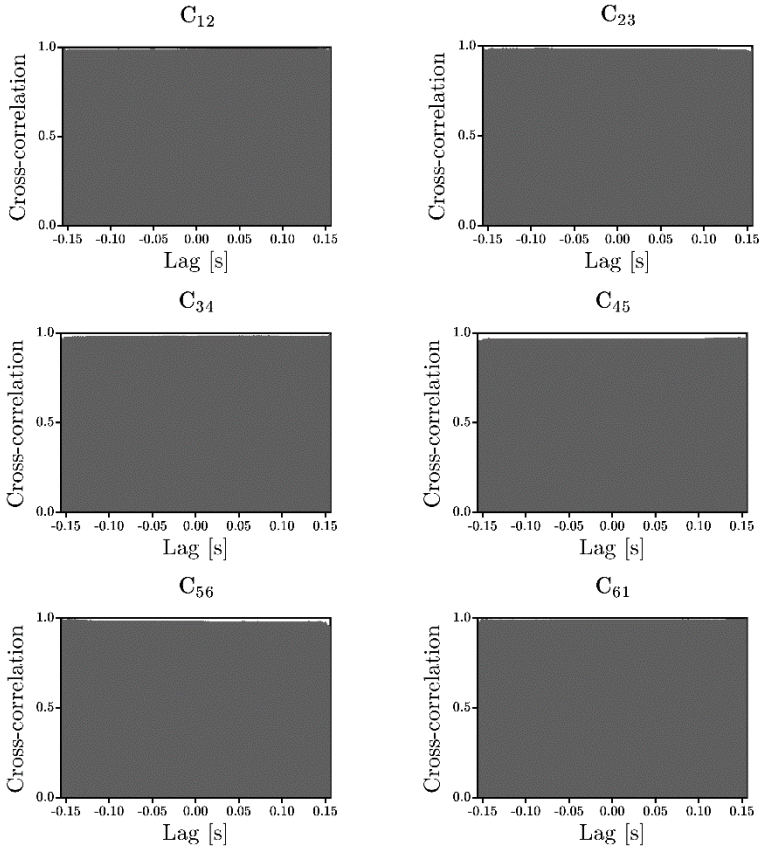

Figure 5.16 Plots of the cross-correlation for the temporal signals obtained using the Sigma model across the different points at position 1.

The frequency spectrum produced by the Sigma model was sharper for a couple of locations, with well defined principal frequency components around the 250

Hz frequency band. The velocity fluctuations that are enforced at the inlet influence the distribution of frequencies across the spectrum in a similar manner that what it was observed for the results of the Smagorinsky-Lilly model. Furthermore, the plots for the cross-correlation function of the point-wise signals exhibit the highest degree of interdependence with virtually no lag detected among the dataset. This shows that the signals recorded at that position are almost identical despite the perturbations perceived in the frequency spectrums.

5.3.3.2. Axial position 2

The results obtained for the second axial position, located 12.7 mm downstream of the inlet plenum in the axial direction, shows that the number of relevant frequency bands in the spectrum obtained using the results produced by the Smagorinsky-Lilly model decreased. Despite the lower number of relevant frequencies, the spectrum still shows a high level of disturbances across the lower frequency range, as can be observed in Figure 5.17. The overall weighted frequency of oscillation was estimated at 218.4 Hz, which is a narrower range than that obtained for position 1.

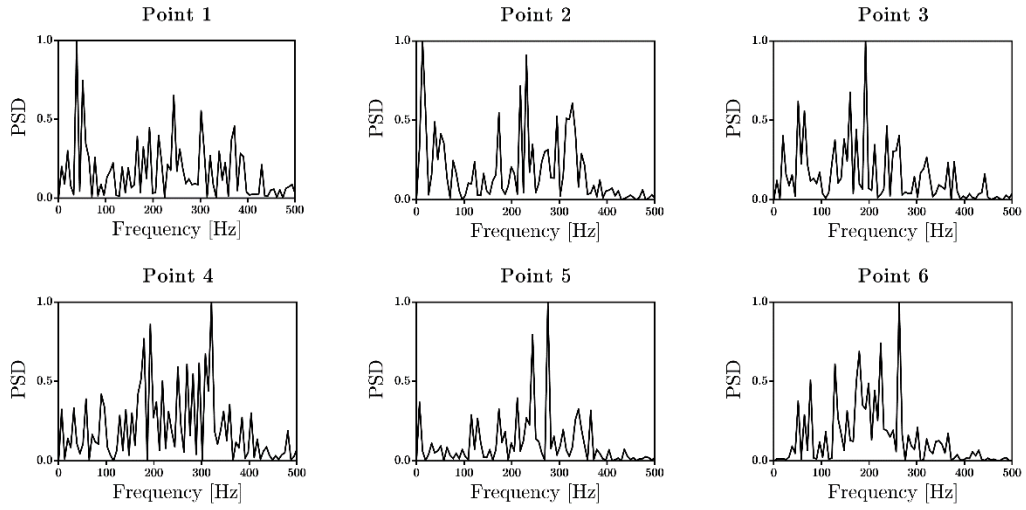

Figure 5.17 Frequency spectrums obtained at different point in the position 2 using the results produced by the Smagorinsky-Lilly SGS model.

In addition, the level of interdependence among the recorded signals remained strong for all the cases, with a value for the normalised cross-correlation being higher than 0.9 and it remained nearly constant throughout the length of the signals. The correlation between points 2 and 3 appeared to be the lowest for this location, however they remain strongly coherent, as shown in Figure 5.18.

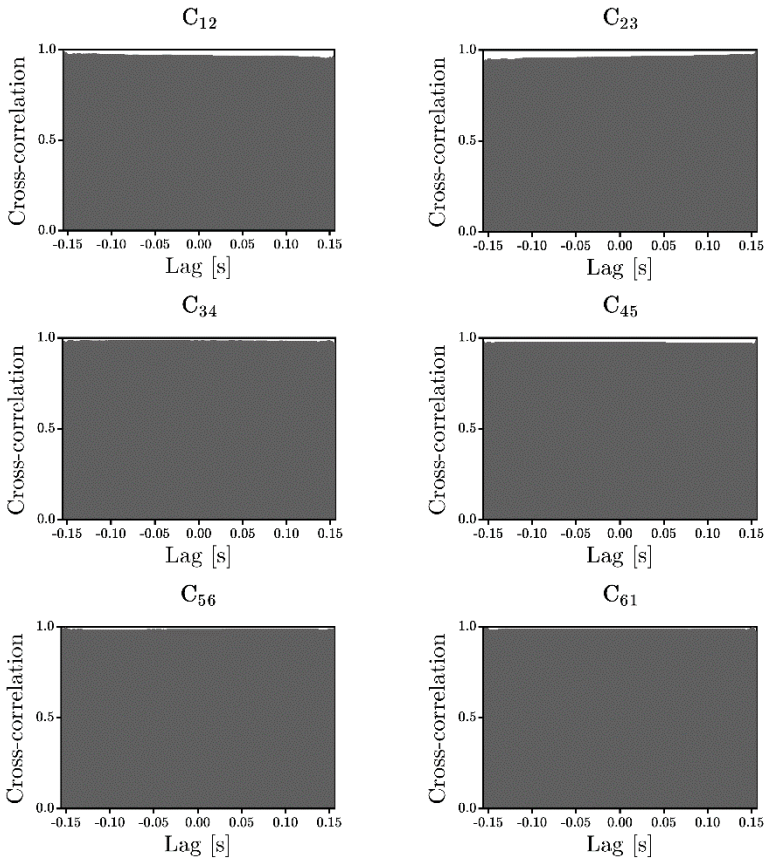

Figure 5.18 Value for the cross-correlation of the signals produced at different points located at the axial position 2, and the Smagorinsky-Lilly SGS model was employed for this case.

The frequency spectrums obtained from the LES using the Sigma SGS model, introduced in Figure 5.19, shows the influence of the velocity fluctuations produced at the inlet. A noteworthy frequency spectrum was produced for point 2, in which a single frequency band was found perceived as relevant. A later inspection to the transient signal evidenced that this was caused by a sudden changes in the value of the velocity rather than a sustained change in their trend. Furthermore, relevant frequency bands appeared in the low range of the spectrum, thus evidencing the influence of the mixing in the overall flow distribution.

The cross-correlations of the point-wise signals produced by the LES that employs the Sigma model, as presented in Figure 5.20, exhibited the same tendency as those calculated for the axial position 1, with an almost perfect correlation among all of them. Despite the emergence of new structures with a lower oscillatory rate, as confirmed by the spectral trends, it appears that those

inhomogeneities are well distributed in the domain so the overall temporal coherence of the flow does not suffer a significant alteration.

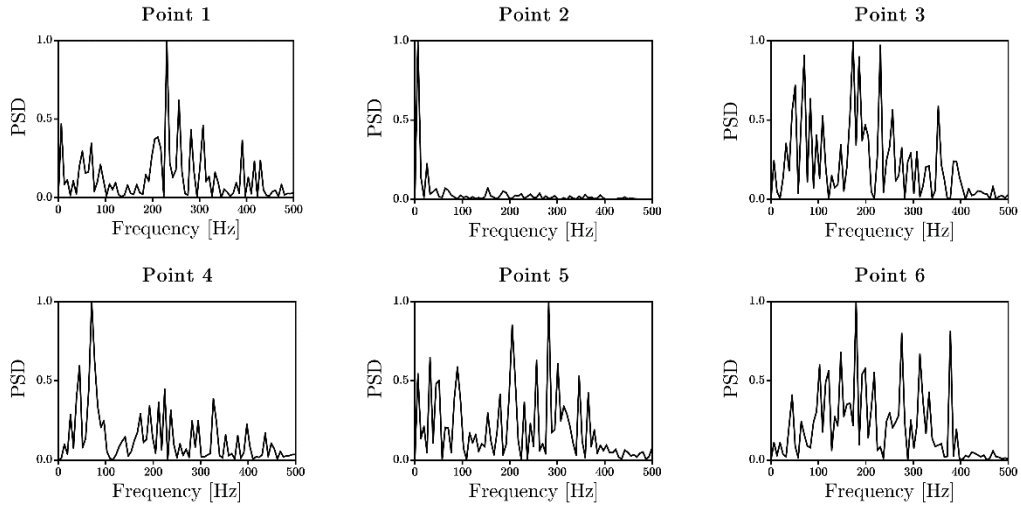

Figure 5.19 Frequency spectrums for the signals produced by the LES simulation using the Sigma SGS model. The signals were sampled at the axial position 2.

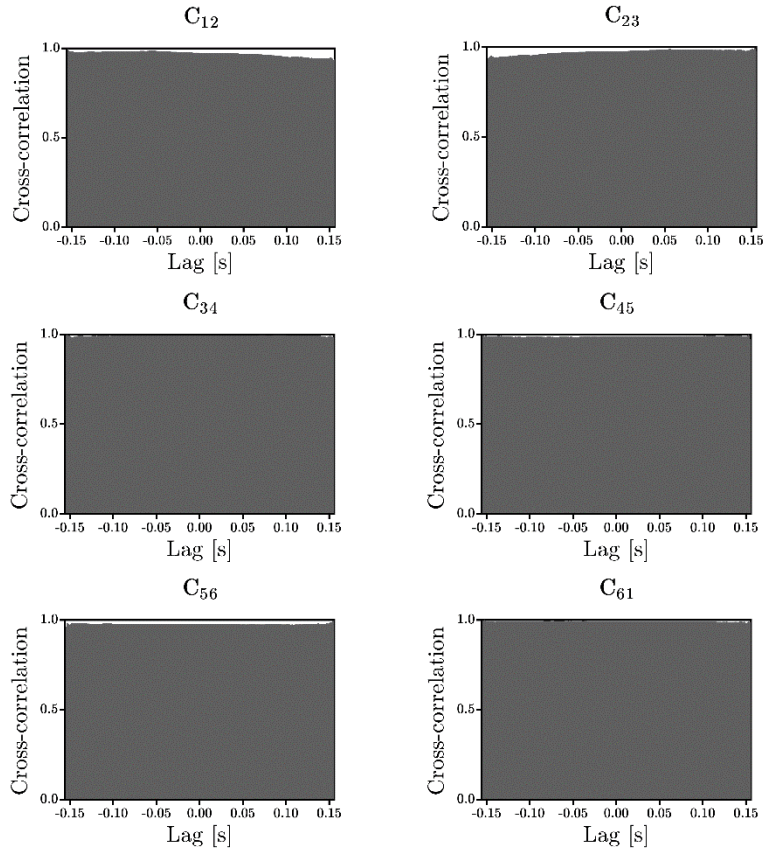

Figure 5.20 Plot of the cross-correlations of the different transient signals obtained at the axial position 2 by the LES computation that employs the Sigma SGS model.

5.3.3.3. Axial position 3

As the fluid travels through the domain, the overall transient behaviour equalise and a better arrangement in the flow can be perceived. The frequency spectrums calculated after the transient oscillations in the axial velocity for the LES case that utilise the Smagorinsky-Lilly formulation for the SGS stresses appeared to be less noisy and considerably better defined, as shown in Figure 5.21. The majority of the trends obtained show that only a few frequency bands can be considered as being relevant across the captured spectrum, and most notably the bands around 70 Hz. The overall value for the weighted frequency of the spectrums was observed to have a narrow range across the measured points and it was estimated at 82 Hz. The random fluctuations in the flow imposed at the boundary condition that ended up producing the spurious frequencies measured in the spectrums for the point at the positions 1 and 2 have been dissipated by this point, and the frequencies captured in this analysis appeared to be have a better physical meaning.

The correlation among the signals, depicted in Figure 5.22, did not suffer remarkable alterations in comparison to those estimated for the two previous locations. The signals at this position exhibit a strong interdependence and the value for the cross-correlation is almost constant for the entire possible lag at all locations.

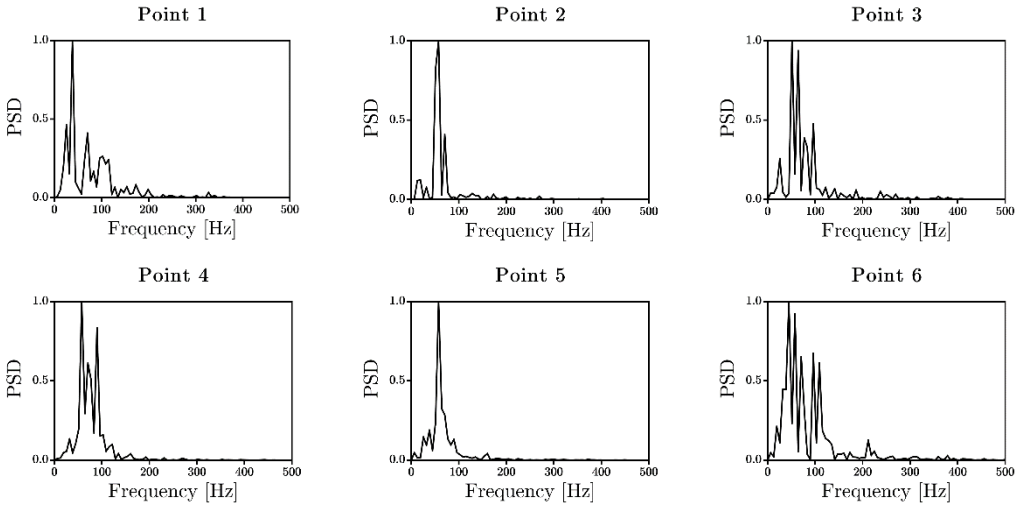

Figure 5.21 Distribution of frequencies obtained after the analysis of the transient signals recorded at different points at the axial position 3 employing the Smagorinsky-Lilly SGS model.

The spectrum of frequencies obtained by processing the temporal data generated by the Sigma model within the LES framework, presented in Figure 5.23,

displayed a similar behaviour to those produced by the Smagorinsky-Lilly approach. The accord in the frequencies indicate that the larger contributions to the structure of the fluid flow can be distinguished, and these are contained in the low range part of the spectrum. The overall value for the weighted frequency was calculated at 85 Hz, thus agreeing well with the estimate of the Smagorinsky-Lilly approach.

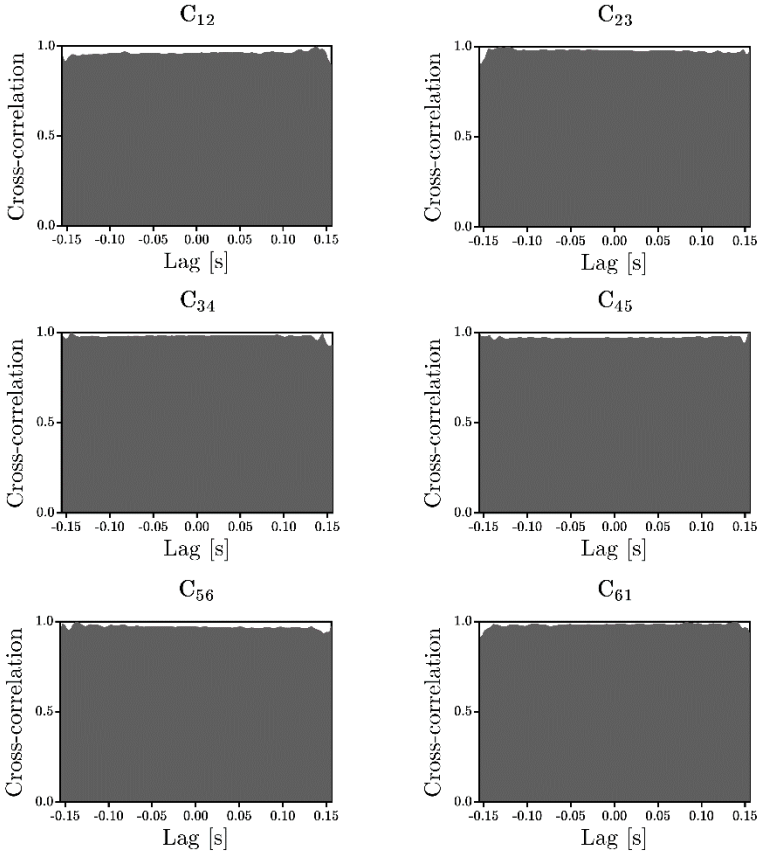

Figure 5.22 Ratio of the interdependence among the locations computed as the cross-correlation of the transient signals. The results were obtained using the Smagorinsky-Lilly approach.

The set of monitor points placed at the axial position 3, as in the previous positions, exhibited a high degree of correlation. However, slight misalignments in the frequencies of the points 2, 4 and 1 were observed across the whole signal length. The presence of misalignments in the cross-correlation plots may be evidence of the presence of turbulent structures if the shifting of the signals is found to be repetitive. Nevertheless, the lack of additional deviations in the trends for the correlations imply that misalignment in the signals was an isolated event, or probably a remnant of the flow oscillations enforced at the inlet. Despite the minor shifting in the signals, as showed by some discrepancies in

the frequency spectrums, the swirling flow has retained its shape until this position and is manifesting to be coherent.

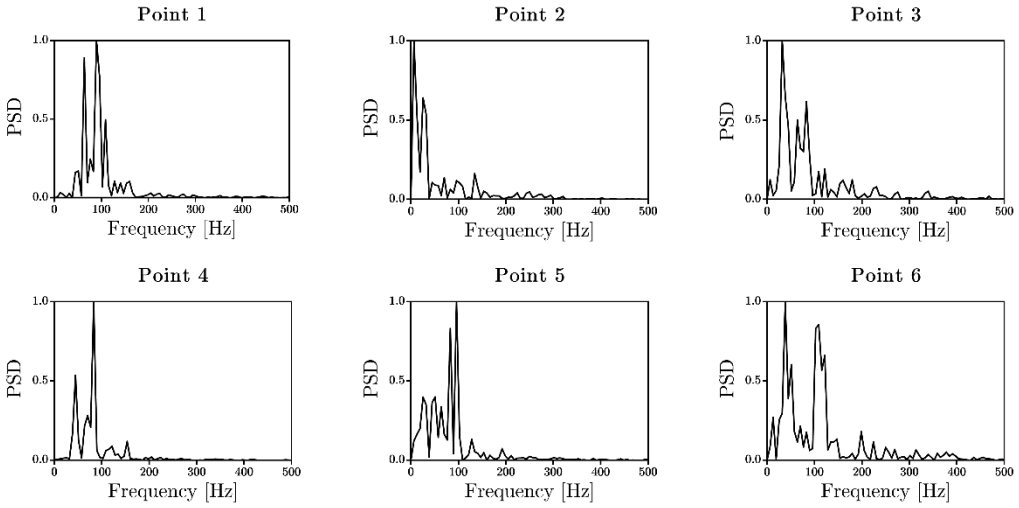

Figure 5.23 Frequency spectrums for the points located at position 3, computed using the Sigma model.

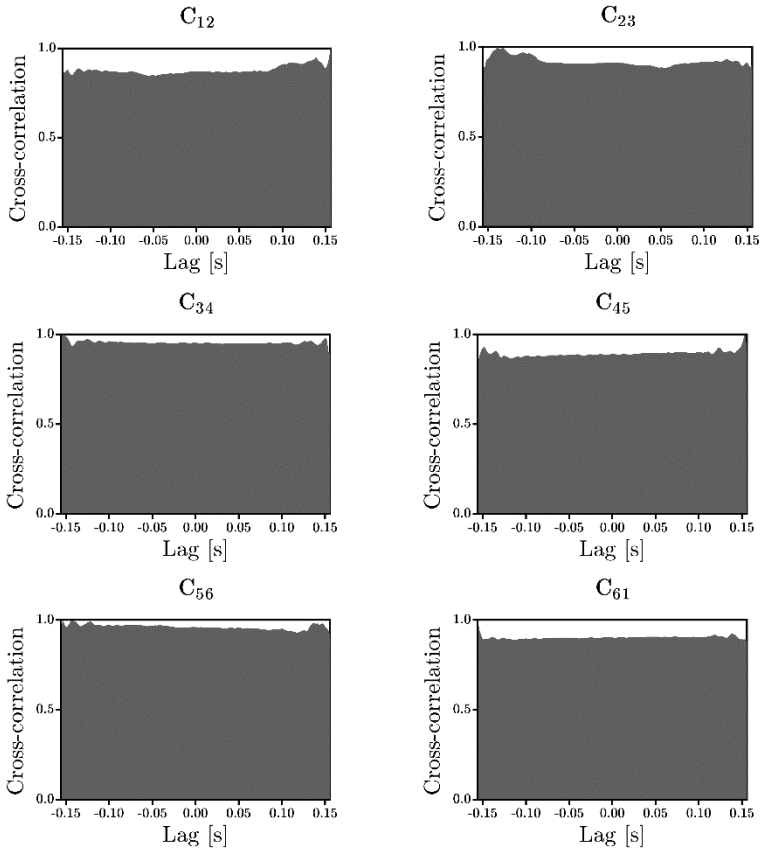

Figure 5.24 Cross-correlation of the transient signals recorded at different points located on axial position 3 while employing the Sigma model.

5.3.3.4. Axial position 4

The results obtained for the furthest axial location showed the same progression as at position 3. The relevant group of frequencies are disposed to coalesce in the low range of the spectrum while the high frequency oscillations tend to dissipate into the flow, thus decreasing their contribution into the flow field dynamic behaviour.

The frequency spectrums calculated for the signals at position 4 by performing LES that employs the Smagorinsky-Lilly model are presented in Figure 5.25. While the number of high contributing bands in the spectrum decrease, the weighted value of the frequency becomes more relevant in the characterisation of the flow. The average weighted value for the spectrums obtained by the LES transient data employing the Smagorinsky-Lilly model is 74 Hz. This indicates that as the swirling stream expands in the test chamber, and mixes with the central jet, the flow homogenises and decreases its oscillatory rate.

The correlation for the temporal signals, however, is shown to be less than in the previous positions, as introduced in Figure 5.25. A large misalignment was obtained for the correlations involving point 1, namely C_{12} and C_{61}, and since the value of the shift appears as the highest measured so far, and it this evidenced at two locations, the appearance of a fluid structure is implied. A similar trend, but of a lower intensity is advised for the correlations C_{34} and C_{45}, which suggests that an additional inconsistency of the flow was captured at point 4.

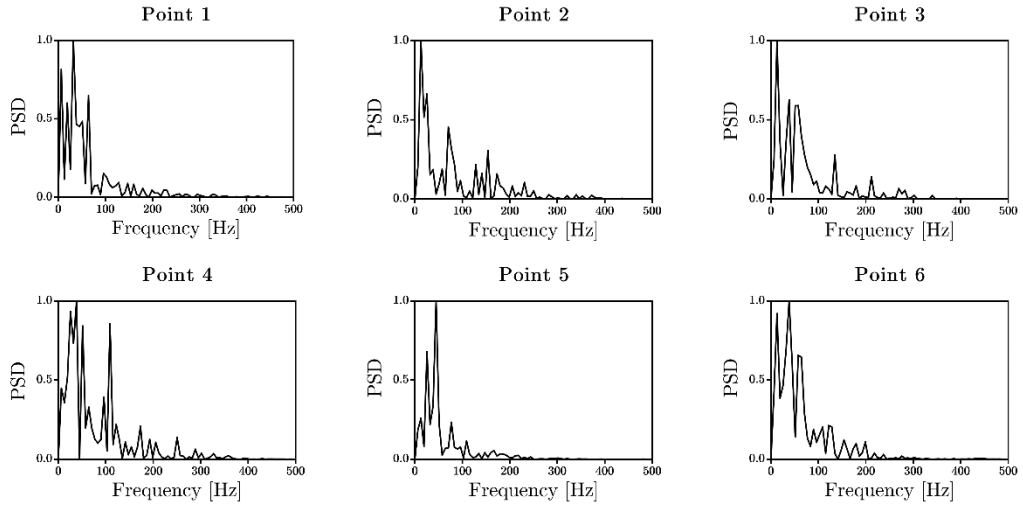

Figure 5.25 Frequency spectrums calculated after the transient data that was produced by the LES computations using the Smagorinsky-Lilly model, and these were recorded at the axial position 4.

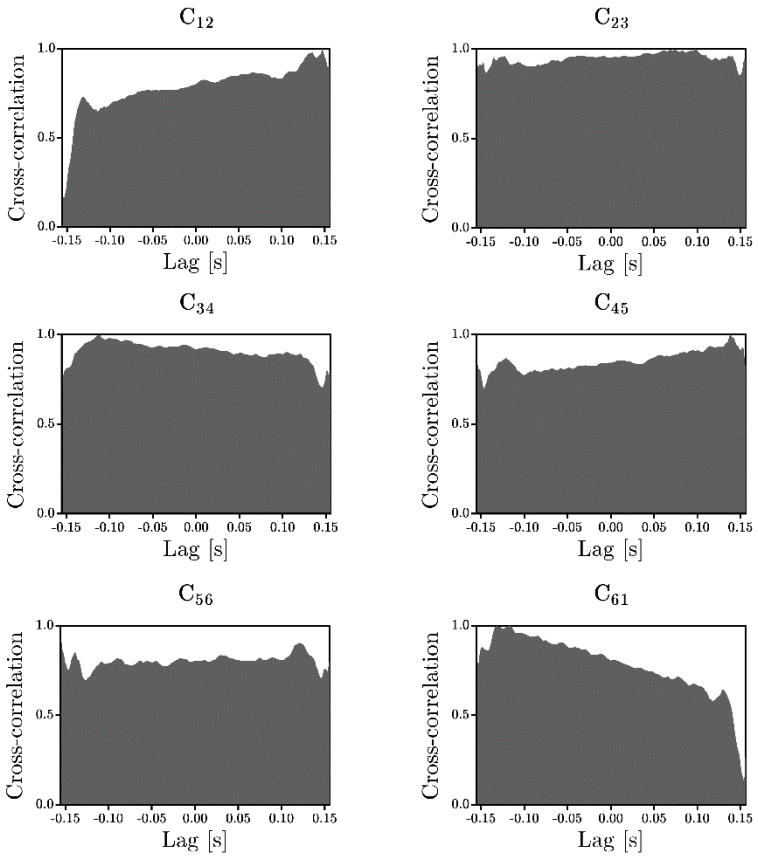

Figure 5.26 Cross-correlations of the transient signals sampled at position 4. The LES calculations involved the Smagorinsky-Lilly SGS model.

Furthermore, the frequency spectrums generated by the LES calculations that comprised the Sigma model showed a decrease in the number of relevant frequency bands with their aggregation occurring further down in the spectrum range, as shown in Figure 5.27. The average weighted frequency was estimated at 73 Hz, hence comparing well with the estimates computed for the Smagorinsky-Lilly results.

The results obtained for the cross-correlations manifested that none of the signals are perfectly aligned. Moreover, the misalignments in the temporal data occur across the entire length of the signal and remain relatively constant, as shown in Figure 5.28. Furthermore, the levels of the correlation for the temporal signals produced by the Sigma model were higher that its counterpart using the Smagorninsky-Lilly approach. This suggests that, despite the existence of the flow anomalies, these are more scattered and less energetic. Nevertheless, the degree of correlation obtained for the points at this position suggest that the flow retains its arrangement and that after diffusing the fluctuations set at the inlet, its coherence is more noticeable.

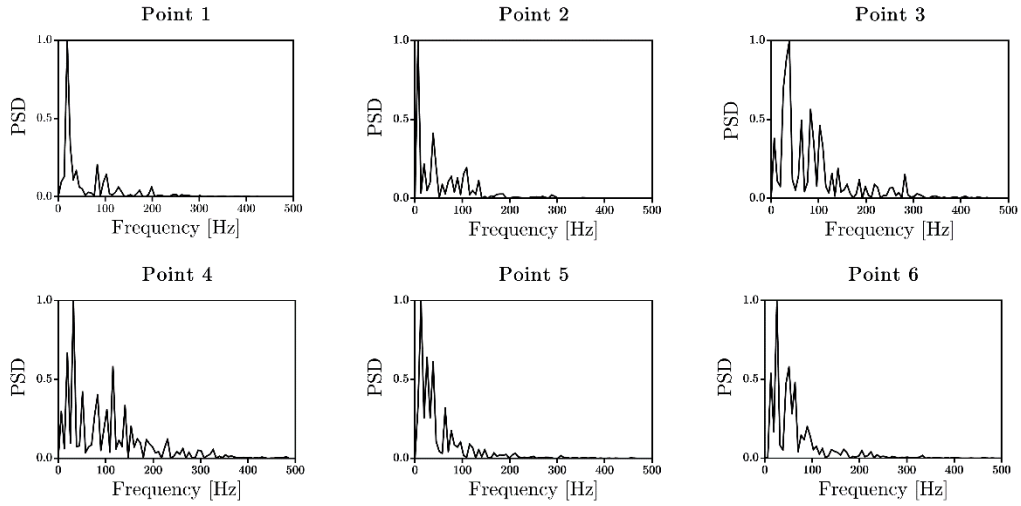

Figure 5.27 Frequency spectrums obtained for LES using the Sigma model. The transient signals were obtained at the axial position 4.

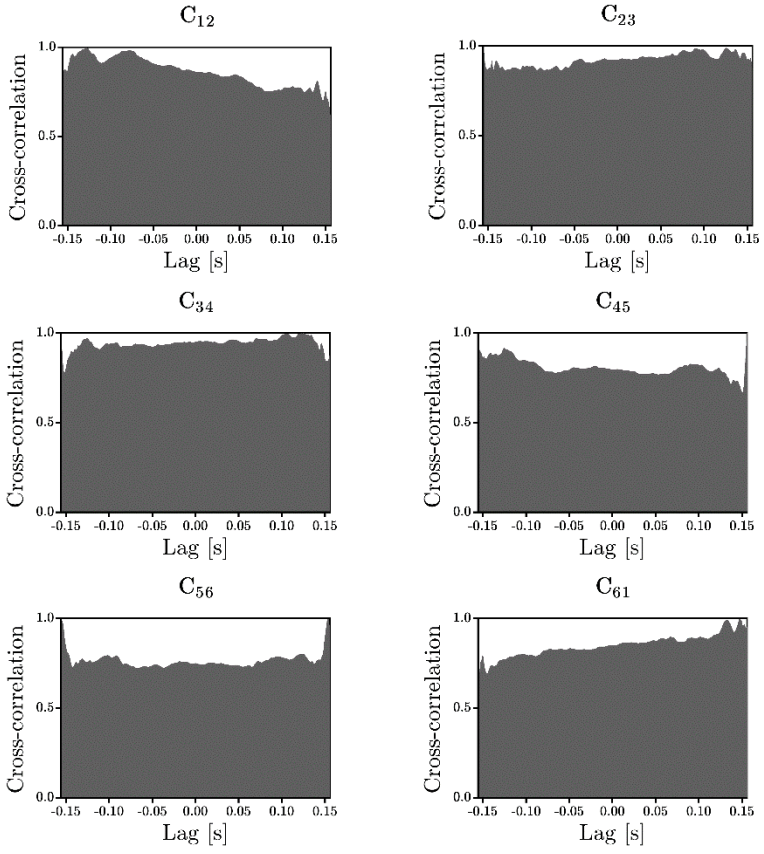

Figure 5.28 Cross correlations for the temporal signals at position 4. The signals were generated by LES incorporating the Sigma SGS model.

5.3.4. Spatial coherence analysis

The analysis of transient data by means of the frequency spectrum, as introduced in the previous section, provides a representation of the dynamics of the flow. However, since it relies on the temporal information recorded at a particular location, its validity across the whole domain is questionable. The inclusion of additional monitor points, and the calculation of the cross-correlation function for each pair, improves the characterisation of the flow, but the amount of data that has to be analysed sharply escalates and becomes unpractical. Furthermore, the resolution on the data obtained experimentally and numerically have increased recently, thus compelling the development of methodologies for the evaluation of large data sets.

The proper orthogonal decomposition (POD) is a methodology that allows the extraction of the dominant features and trends from a finite set of data. These predominant structures influence the overall dynamics of the fluid flow and are directly related to the spatial coherence of the system. In the POD analyses, the flow field, and any other scalar considered, is decomposed into a sum of weighted basis functions, known as modes. The decomposition of the flow field in the POD is a linear procedure and, therefore, the modes obtained are equally linear even if the input data and the nature of the system to characterise is dynamic [346].

A POD analysis, based on the snapshots method [254], was performed over the flow field captured at different flow times in a LES computation. Each snapshot consisted of the instantaneous values of the velocity field obtained for all the coplanar grid points located at a given position in the domain. The positions used for this study were the same as those employed in the spectral analysis and these are presented in Table 5.3. Moreover, the number of snapshots have been selected, for the sake of consistency, so they correspond to the number of sampled entries and to the period of time obtained in the transient signals. Each snapshot was obtained in the shape of a matrix of size $M \times N \times 3$, where M and N are the number of grid points in the X and Y directions in the Cartesian coordinate system, and 3 corresponds to the velocity components, namely u, v and w, for the three Cartesian directions. The axial component of the velocity, which is aligned to the Z direction was included in the POD analysis in order to acknowledge its contribution to the development of the dominant structures in the flow. However, the results are presented in the form of a vector field in a planar basis. In addition to the computation of the principal modes, the average value for the velocity obtained from the set of

snapshots is presented alongside a plot for the contribution of each mode into the overall energy of the system. In addition, the energy values of the POD modes have been normalised based on the maximum energy obtained in the system, and the order of the modes has been re-arranged in a decreasing order accordingly to the contained energy. The POD analysis produced a number of nodes equal to the number of samples but only the first six modes are presented in order to facilitate the inspection of the flow structures captured by the methodology.

5.3.4.1. Axial position 1

The POD analysis performed to the snapshots obtained from LES simulations using the Smagorinsky-Lilly model showed that for the position 1, the majority of the energy is contained in the first 10 modes, as shown in Figure 5.29. In addition, the vector plot for the mean velocity values exhibit a good agreement with the contour plots obtained for a longer sampled period. Furthermore, the velocity distribution of the inlet boundary condition is noticeable in the arrangement of the vectors, and a high velocity region is perceived in the shear layer when the swirling streams and the central jet coincide. Moreover, the assessment of the POD modes, as presented in Figure 5.30, revealed that the relevant structures reside in the shear layers and these appear in an orderly fashion in the outer region of the swirling jet. Some recirculating patterns can be recognised in the internal shear layer which might arise from the interaction and the discrepancy in the velocities between the two inlet streams. Similar patterns appeared in the outer shear layer for the POD mode 4 and onwards, but they are not as clearly defined as in the interior region.

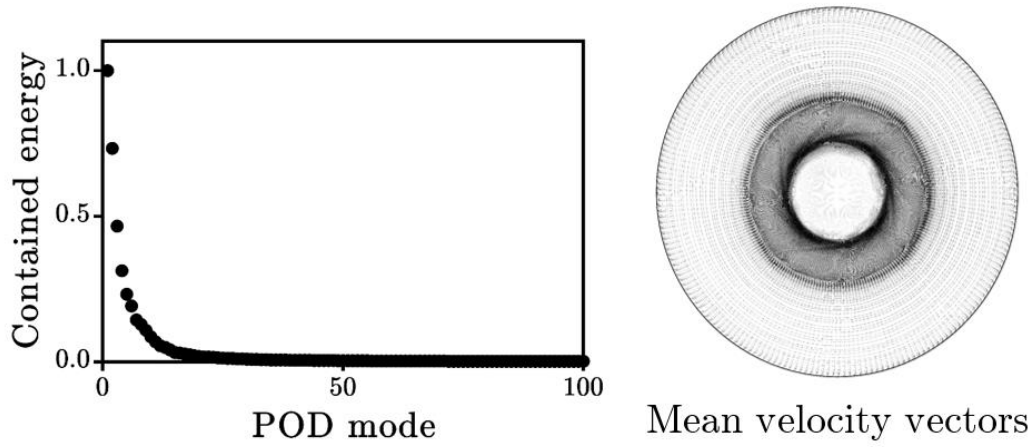

Figure 5.29 Distribution of the energy contained per POD mode (left) and vector plot of the mean velocity components obtained by the LES that incorporates the Smagorinsky-Lilly SGS model (right).

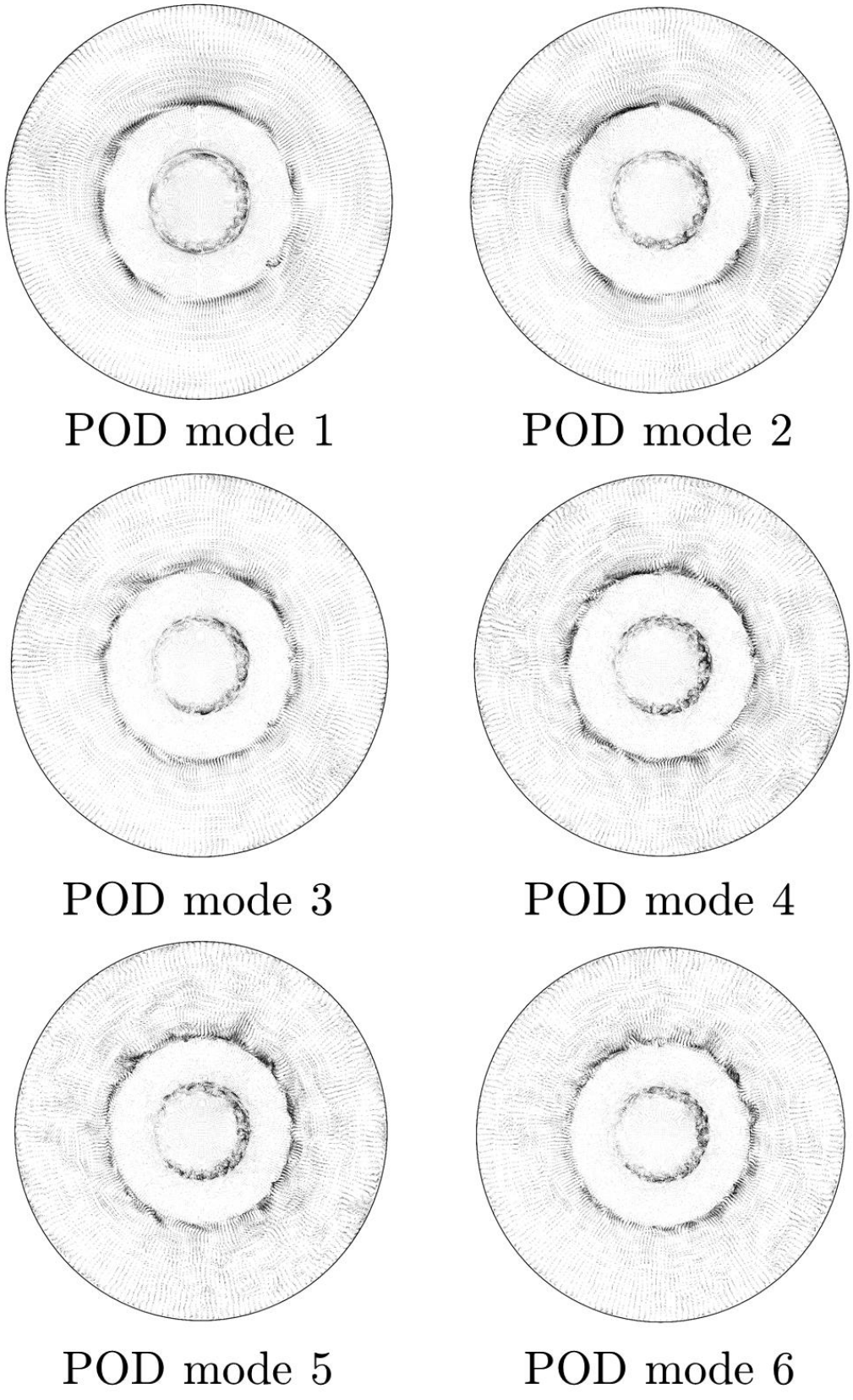

Figure 5.30 POD modes obtained for transient snapshots produced by the LES using the Smagorinsky-Lilly model for the SGS tensor at the axial position 1.

The vector plot for the mean velocity values obtained after the results yielded by the LES that employs the Sigma SGS model show a similar flow distribution to that obtained using the Smagorinsky-Lilly approach, as noted in Figure 5.31. However, the width of the internal shear layer produced by the Sigma SGS model is narrower and some locations within the central jet containing higher velocities appeared to be moving towards the internal flow interface. The appearance of these high-velocity locations suggest that the Sigma model prompts the mixing of the streams earlier than when using the Smagorinsky-Lilly model. In addition, the distribution of the contained energy across the POD modes exhibited the same pattern as in the processing of the results yielded by the Smagorinsky-Lilly model, as can be noted in Figure 5.31, with the dominant structures of the flow being well contained in the first few POD modes.

The inspection of the POD modes obtained for the transient data generated by the LES with the Sigma model shows that, as in the previous SGS model, the principal structures of the flow are contained in the shear layers, as shown in Figure 5.32. However, the direction of the vectors at the interface suggest that the spiralling motion is retained and that the flow moves more orderly in the axial direction. As a consequence of this flow disposition, less recirculating zones are captured by the POD methodology. The recirculating zones perceived in the domain are mostly contained in the POD mode 4 and larger, and they appeared to be evenly distributed between the two shear layers. However, their size and intensity are lower than those observed in the results produced by the Smagorinsky-Lilly model.

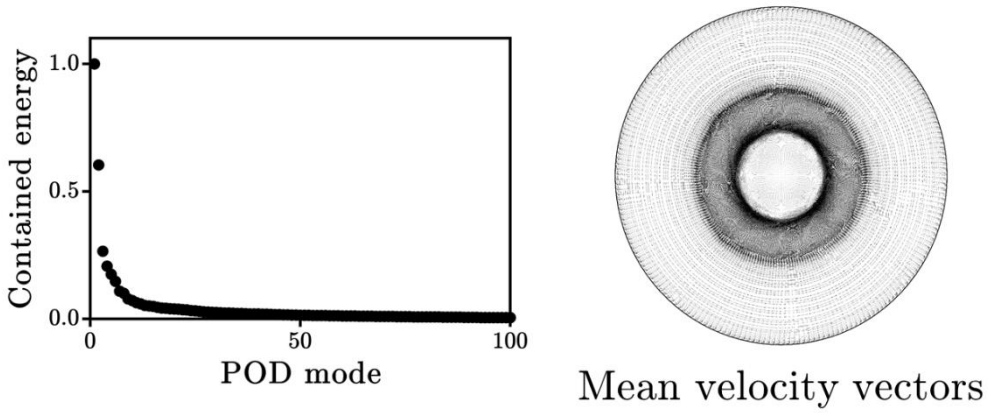

Figure 5.31 Plot of the distribution of the energy of the system in the POD modes (left) and the vector field of the mean velocities produced by the Sigma model in the LES framework at the axial position 1 (right).

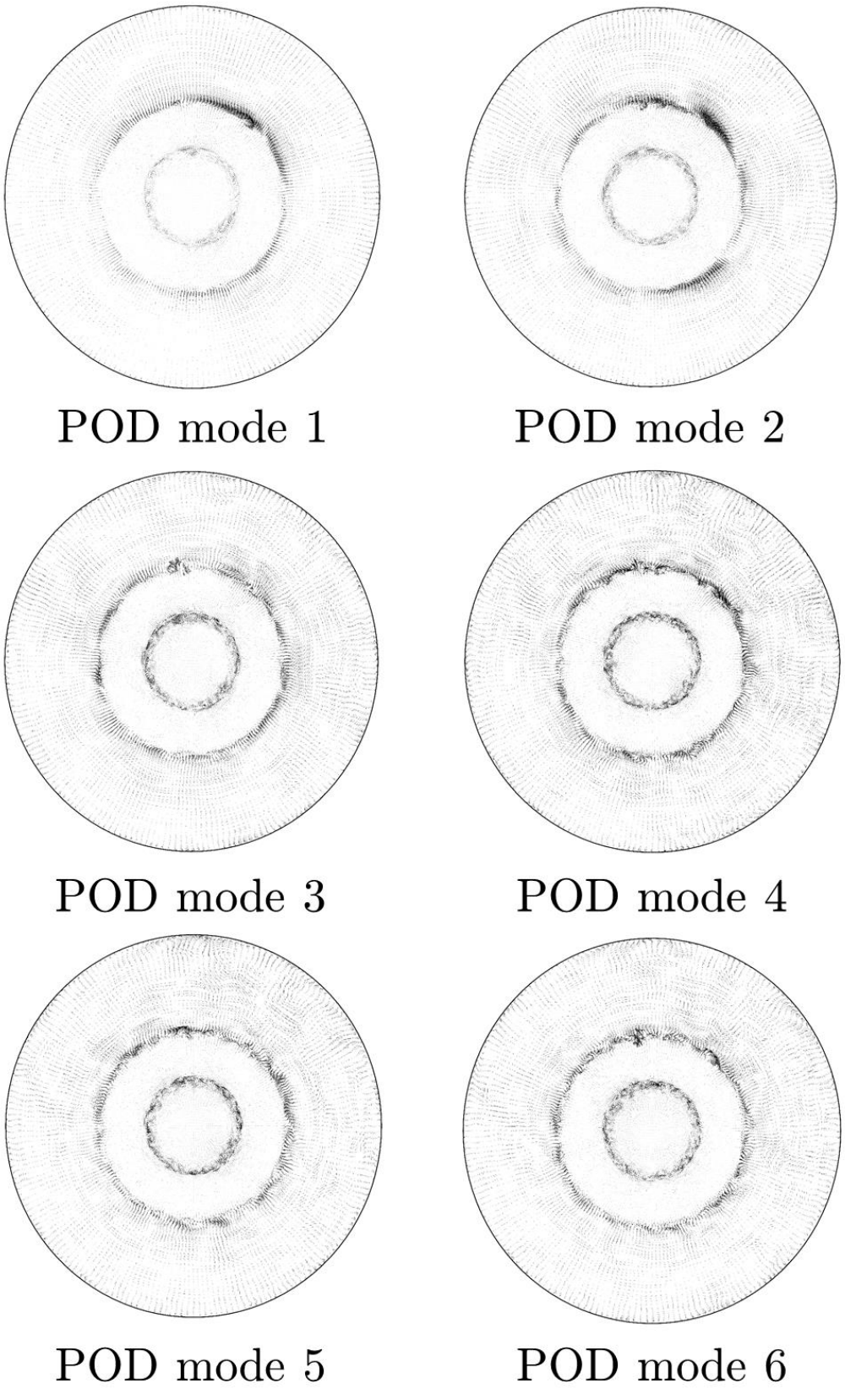

Figure 5.32 POD modes for the set of snapshots produced for the axial position 1 by the LES with Sigma model for the SGS effects.

5.3.4.2. Axial position 2

The POD analysis performed to the transient snapshots obtained from the LES calculation that employs the Smagorinsky-Lilly model showed that for the second axial position, the amount of energy contained by each mode is smaller than what was observed for the position 1. The decrease in the contained energy, as shown in Figure 5.33, implies the necessity to incorporate a larger number of modes for the full characterisation of the flow. In addition, the dominant structures captured for each mode by the POD, despite being well defined, will not be as influential in the overall fluid flow as those depicted for the flow position 1. Furthermore, the vector plot for the mean velocity components, introduced in Figure 5.33, shows the effect of the mixing that occurs as the flow travels through the domain. The flow pattern imposed at the inlet boundary is more dispersed and the internal shear layer produced a widening in space.

The examination of the POD modes computed for the position 2 shows the appearance of oscillatory structures in the central shear layer, as presented in Figure 5.34. These recirculating zones exhibit consistency in their shape and their occurrence is observed for all the computed POD modes. Further, the relevant structures that are present in the outer shear layer appeared to be directly aligned to the direction of the swirling jet, thus accounting mostly to the swirl motion of the fluid body rather than to the mixing phenomena in the shear layer. Moreover, a small amount of momentum transfers between the shear layers is observed by the small number of vectors being displaced mostly from the internal to the outer region.

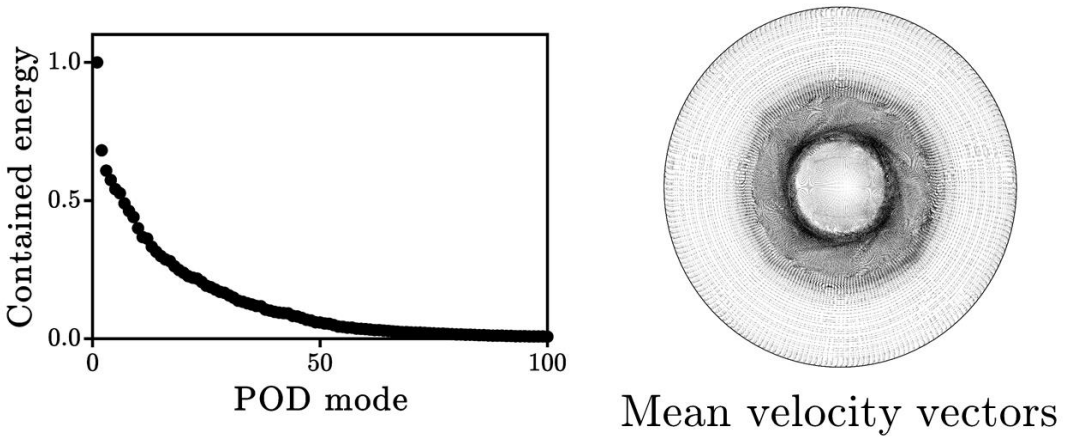

Figure 5.33 The contained energy across the POD modes produced by analysing the transient data of the LES with Smagorinsky-Lilly formulation for the SGS effects (left). Vector plot of the mean velocity components for the same study (right).

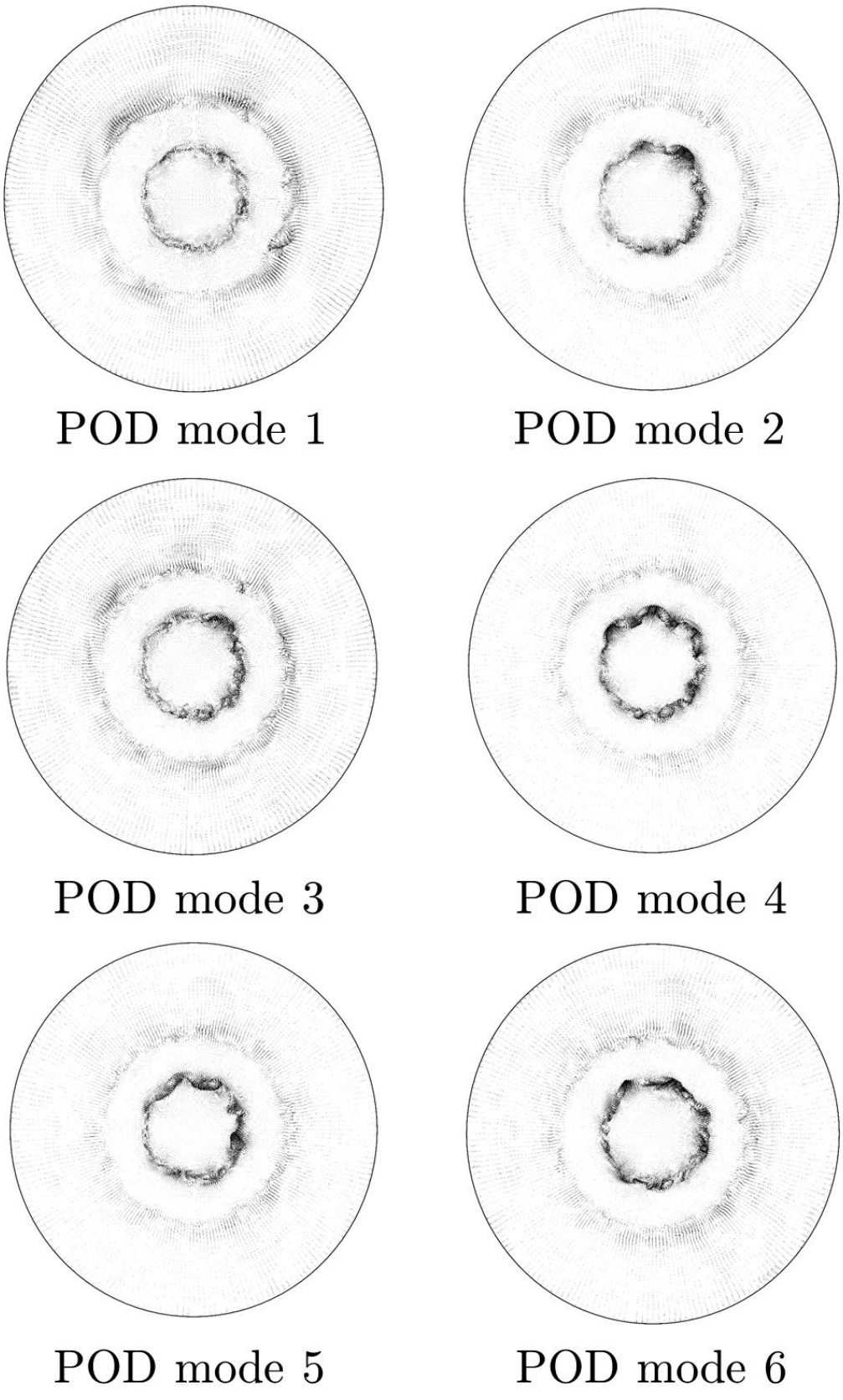

Figure 5.34 POD modes computed for the LES that employs the Smagorinsky-Lilly SGS model at the axial position 2.

In contrast, more energy of the system was contained in the first POD modes produced while using the transient data generated by the Sigma model for the SGS effects in a LES, as shown in Figure 5.35. The prevailing structures observed in the first POD modes are, therefore, more relevant to the flow structure which can be estimated by employing a combination of fewer modes than what was required for the results of the LES that uses the Smagorinsky-Lilly SGS model. Nevertheless, the comparison of the vector plots for the mean values of the velocity field for both SGS models showed no noticeable differences for the majority of the domain, except for that space occupied by the central jet inlet. No traces of large fluid displacement was perceived for the Sigma model results, showed in Figure 5.35, however in the Smagorinsky-Lilly predictions this behaviour was evident for some of the region of the central jet.

The analysis of the POD modes, presented in Figure 5.36, showed that the structures contained in the outer shear layer are of the recirculating type, especially for modes 6 and onwards and this differs from what was encountered for the data produced by the Smagorinsky-Lilly model. In addition, the most energetic structures appeared to be scattered along the exterior fluid interface. Furthermore, the structures found in the internal shear layer were found to be smaller in comparison to those predicted in Figure 5.34. However, these turbulent structures are predicted to be tightly clustered and contained in a well-defined region. Some vectors, in accordance to the analogous analysis for the Smagorinsky-Lilly SGS model, were found to indicate the transfer of momentum among the fluid shear layers.

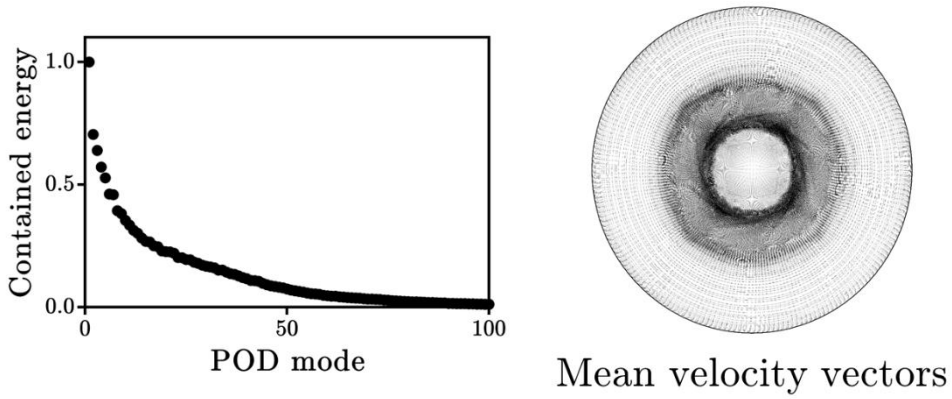

Figure 5.35 Plot of the distribution of energy in the POD modes computed for the results of the LES with the Sigma model for the SGS stresses (left), and vector plot of the mean velocity field at the axial position 2 (right).

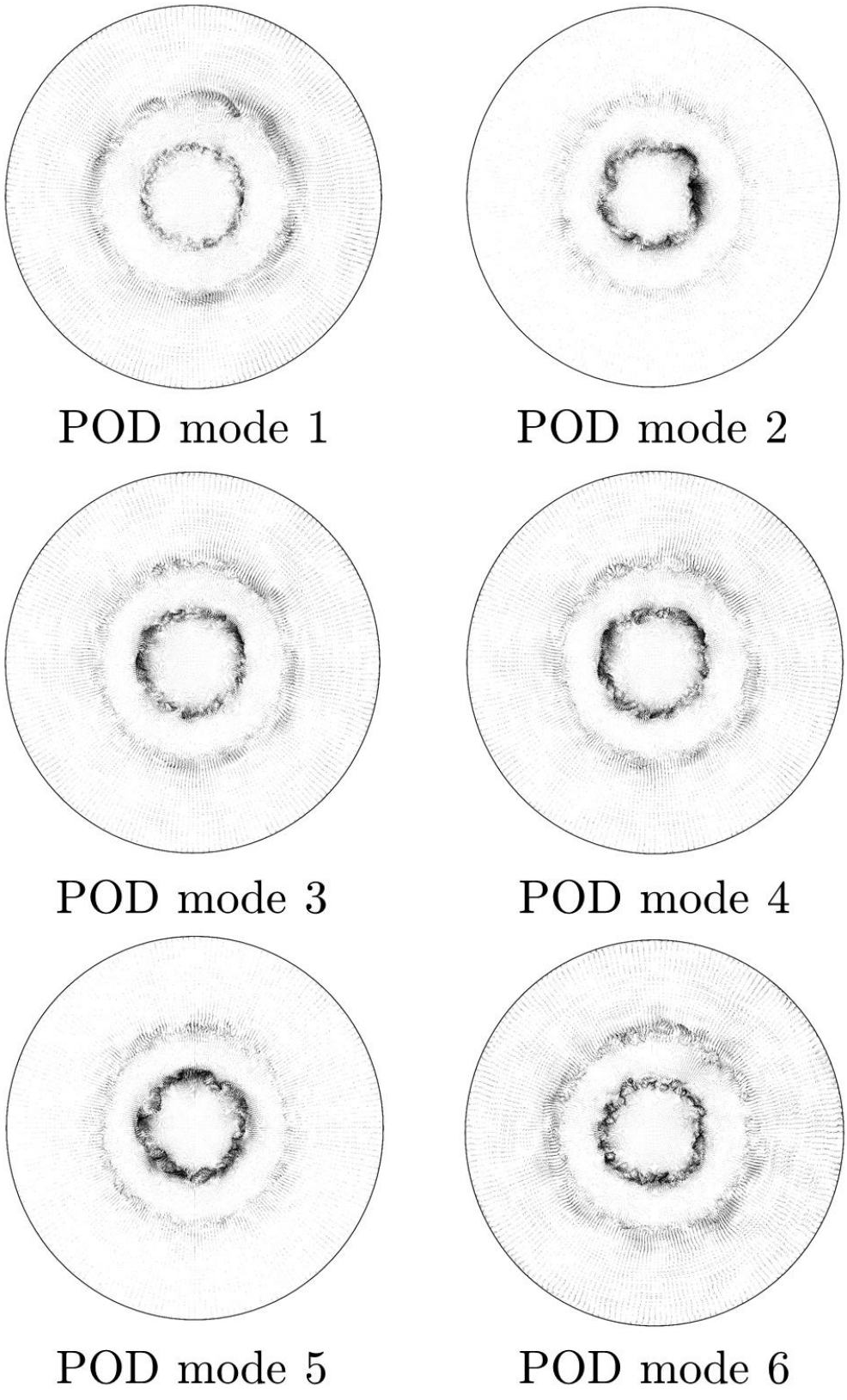

Figure 5.36 POD modes calculated for the data sampled at the axial position 2 and that is produced by the LES using the Sigma approach for the SGS effects.

5.3.4.3. Axial position 3

The distribution of energy across the POD modes, shown in Figure 5.37, present a similar trend for the results produced by the Smagorinsky-Lilly model at the axial position 2. The number of modes containing a significant share of the energy of the system is the larger value in this study, thus suggesting position 3 as being the most unstable position in the analysis. Moreover, the vector plot of the mean values of the fluid velocity, introduced in Figure 5.37, shows the mixing process that occurred in the flow. Furthermore, a detailed inspection to the distribution of the vectors, and their directions, demonstrate that the flow is arranged around the centre of the chamber and that it is spinning around it, thus indicating that the swirl motion is the overall form of the displacement in the flow.

The analysis of the POD modes produced for the results generated by the Smagorinsky-Lilly model revealed the presence of several dominant structures in both shear layers, as shown in Figure 5.38. Furthermore, the majority of the relevant turbulent structures exhibited recirculation and appeared to be overlapping. Moreover, the cohesion of the dominant structures are adequately defined, as may be observed in the POD mode 4. The structures in the outer shear layer are less energetic but, likewise of those on position 2, they are of a recirculating type. However, the cohesion in the outer structures is weak, thus appearing as a cluster of contiguous, self-contained structures. The effect of the transfer of momentum between the interfaces is noteworthy, as indicated by many vectors in the in-between region of the shear layers.

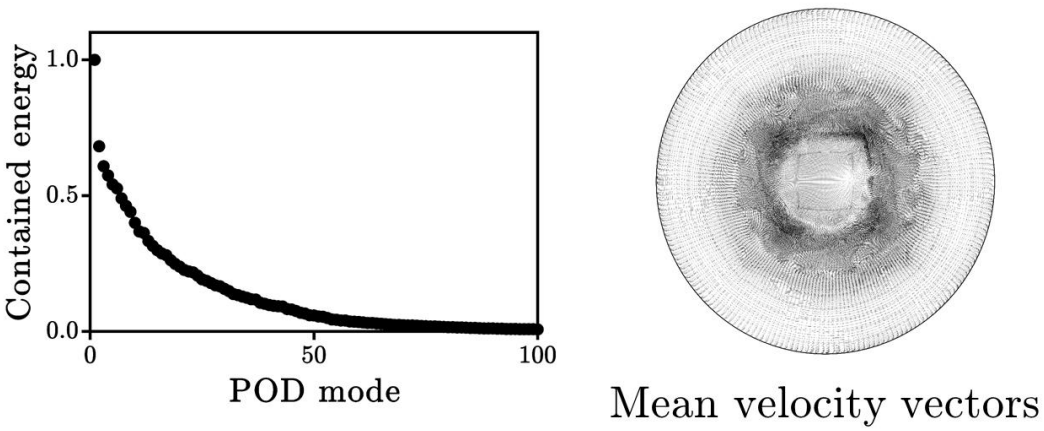

Figure 5.37 Plot of the distribution of energy in the POD modes calculated for the axial position 3 using results of the LES with the Smagorinsky-Lilly SGS model (left) and the vector plot of the mean velocity (right).

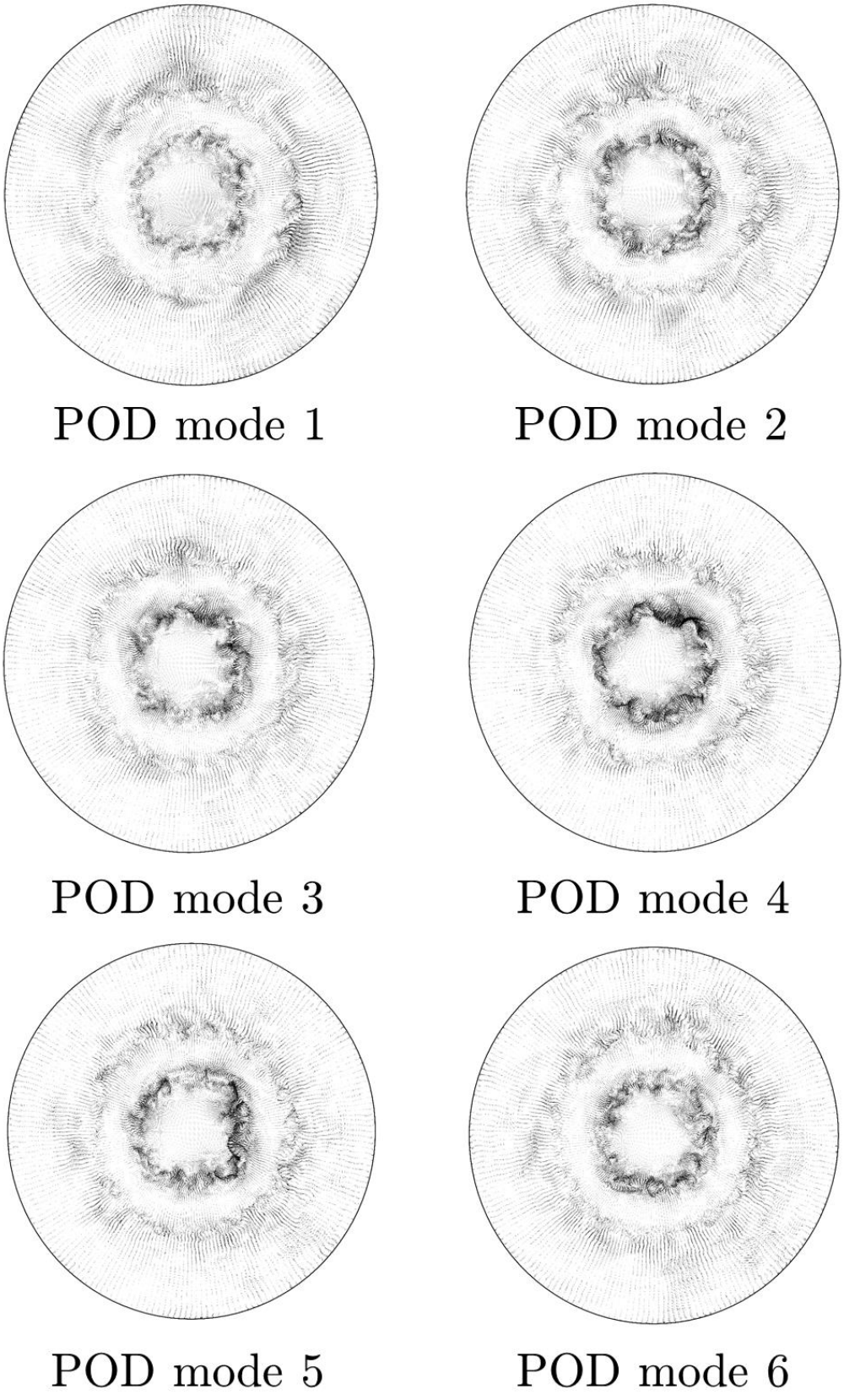

Figure 5.38 POD modes for the LES results, at the axial position 3, employing the Smagorinsky-Lilly model.

The POD results produced for the LES that employs the Sigma SGS model showed a distribution for the energy in the modes similar to that obtained by the Smagorinsky-Lilly model, as presented in Figure 5.39. However, the number of POD modes containing a relevant amount of the energy appeared to be slightly higher. Nevertheless, a comparison of the energy distribution in the POD modes across different axial positions confirms position 3 as being unsteady, thus spreading the dominant structures of the flow across a wider number of modes. In addition, the vector plot of the mean velocity, displayed a more organised distribution of the flow, with the influence on the flow disposition coming from the inlet boundary still being perceived. In addition, the effects of the mesh resolution was perceptible in the appearance of high velocity regions in the corners of the O-grids created as part of the meshing strategy for the results of the SGS models.

The analysis of the POD modes of the LES data indicates that, as in the results for the Smagorinsky-Lilly model, the predominant structures exhibit recirculation, as shown by Figure 5.40. Furthermore, the size of the turbulent structures predicted by the POD analysis are smaller than for the Smagorinsky-Lilly model, however, they are evenly distributed over the shear layer. In addition, the attachment of the turbulent structures is less evident for this set of POD modes, thus producing a series of segregated structures that are intertwined. Some structures, especially in the internal shear layers, contain more energy than the rest, thus suggesting an uneven distribution of the flow. Moreover, the interaction between the shear layers appear to be substantial, with a large number of aligned vectors, as can be noted in the POD modes 1 to 3, that shows this effect.

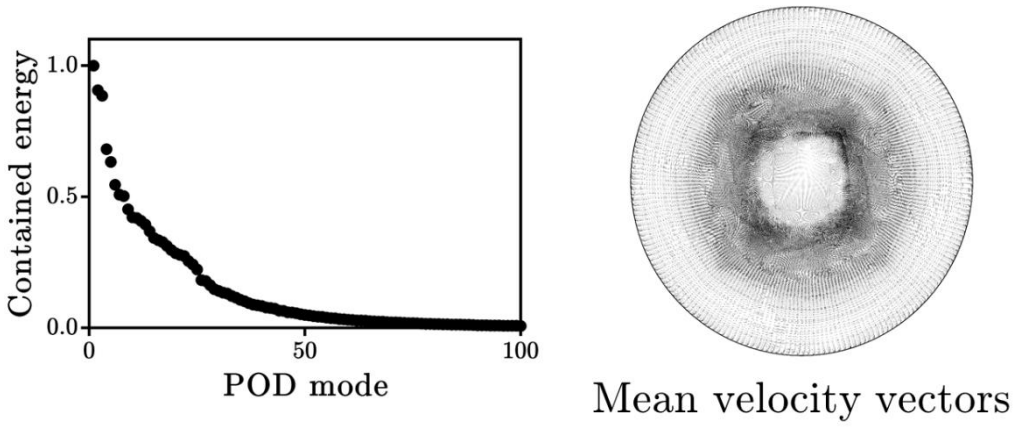

Figure 5.39 Energy distribution in the POD modes (left) and vector plot of the mean velocity obtained from the LES with the Sigma model for the position 3.

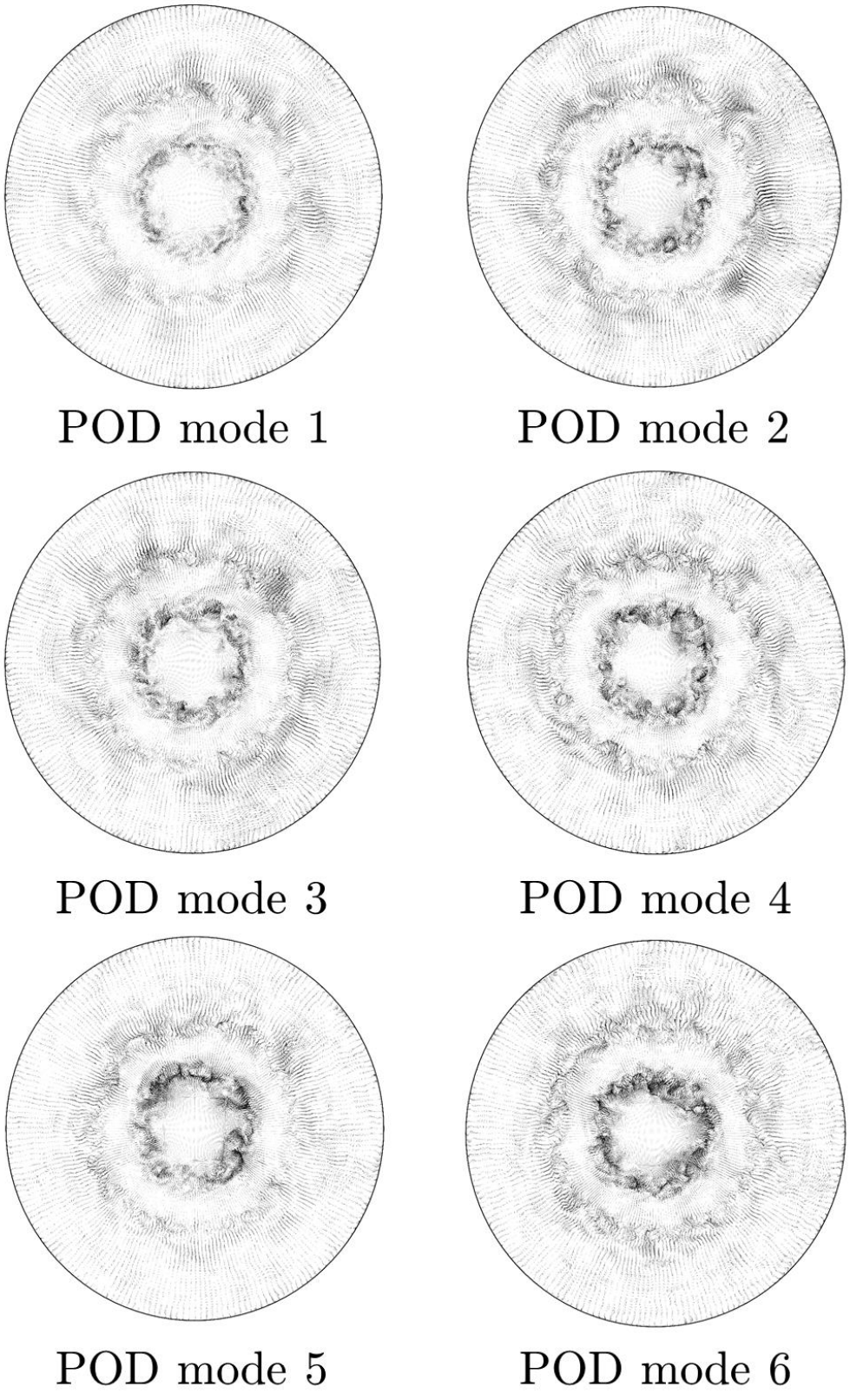

Figure 5.40 POD modes for the transient results obtained for the Sigma SGS model at the axial position 3.

5.3.4.4. Axial position 4

The results of the POD analysis performed to the transient data generated by the Smagorinsky-Lilly model on the LES showed, for position 4, a decrease in the number of modes containing a large share of the energy of the system in comparison the prediction for the positions 2 and 3. The difference among the contained energy is considerably smaller at this position in the domain and this indicates that for the first modes, their contribution to the overall fluid flow is similar, as shown in Figure 5.41. Furthermore, the mean velocity field, depicted by the vector plot presented in Figure 5.41, is more evenly distributed and a clear arrangement around the geometric centre, a characteristic of the swirling motion, can be noted. In addition, the mesh influence in the results was more prominent at the vertices of the blocks onto which the fluid body geometry was mapped. A cluster of vectors with high velocity were found at the vertices of the O-grids pointing in the same direction as those nearby, thus suggesting that the clustering effects observed in the vector plot was due to the element and the size distributions in the mesh.

The POD modes generated for the LES results that employs the Smagorinsky-Lilly approach for the SGS stresses showed that at position 4, no distinguishable predominant pattern can be recognised; instead, an aggregation of scattered smaller structures is predicted. Recirculating regions were found across the entire region studied, with no discernible difference in the amount of energy contained by them. In addition, a high intensity small region is produced in the POD modes that, as in the mean velocity vector plot, appears to be related to the distribution of the elements in the mesh.

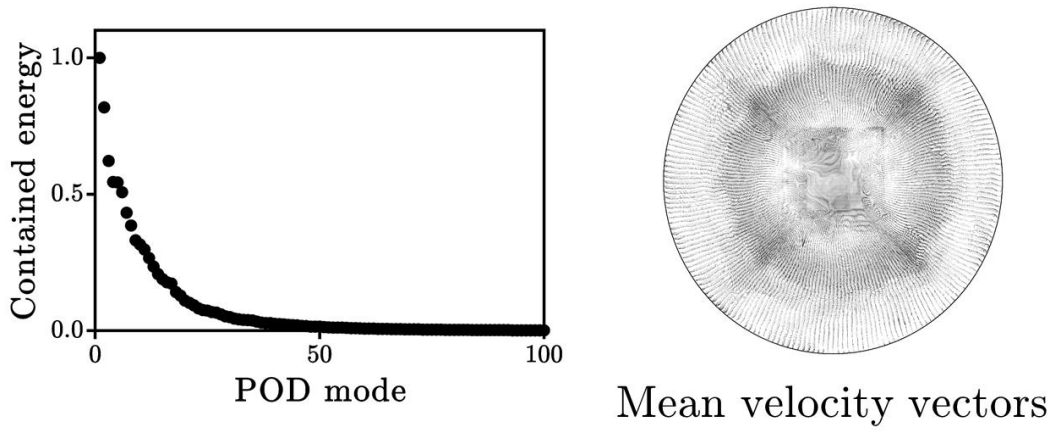

Figure 5.41 Plot of the distribution of the energy in the POD modes (left) and mean velocity vector plot (right) computed for the results produced by the LES with the Smagorinsky-Lilly SGS model at position 4.

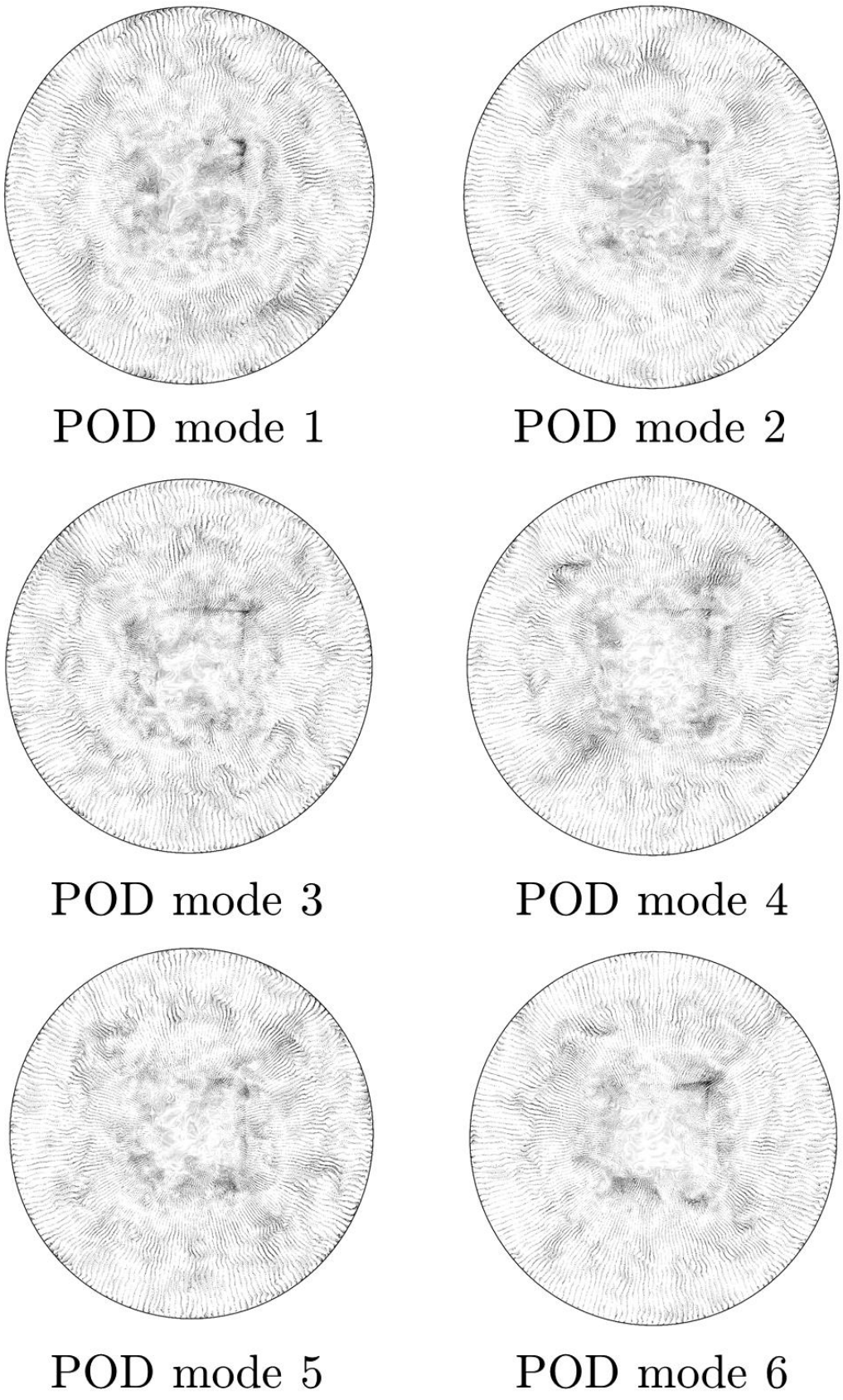

Figure 5.42 POD modes obtained for the data produced by the LES using the Smagorinsky-Lilly model, at position 4.

The distribution of energy in the modes generated by the POD of the data generated by the LES that employs the Sigma model exhibited a sharp reduction in the number of relevant modes for the characterisation of the fluid flow at the axial position 4, in comparison to the trend at position 3. However, as in the analogue analysis for the results of the Smagorinsky-Lilly approach, the smoother arrangement of the flow field caused by the mixing phenomena results in smaller differences in the amount of energy contained by each POD mode, as shown in Figure 5.43. Furthermore, the effect of the mixing in the flow can be noticed by the vector field of the mean velocity, as presented in Figure 5.43. The flow is displayed in an even distribution that contains a swirling pattern that is easily recognisable. In addition, the effect of the size and distribution of the elements in the grid was less evident than in the results for the Smagorinsky-Lilly model, with some vectors grouped around one of the vertices of the meshing blocks. Moreover, the vectors suggest that the central jet is mixed into the swirling stream, hence diminishing the separation length that was perceived in the previous positions.

The analysis of the POD modes computed for the Sigma model in the LES framework showed a randomised flow with flow structures dispersed in the domain, as shown in Figure 5.44, and this agrees well with the predictions for the Smagorinsky-Lilly model. Some structures contain recirculation patterns and they are mostly contained in the inner part of the domain, thus suggesting that they are remnants of the internal shear layer. In contrast, the structures located in the outer region, and close to the wall showed the swirling motion of the flow, despite its more chaotic arrangement.

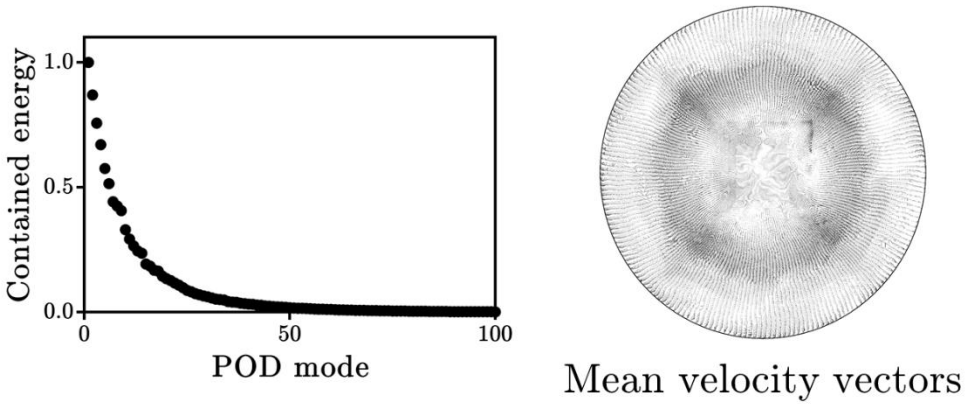

Figure 5.43 Plot of the distribution of energy across the POD modes (left) and vector plot for the mean velocity components computed for the transient data generated by the LES with the Sigma model to compute the SGS stresses at position 4.

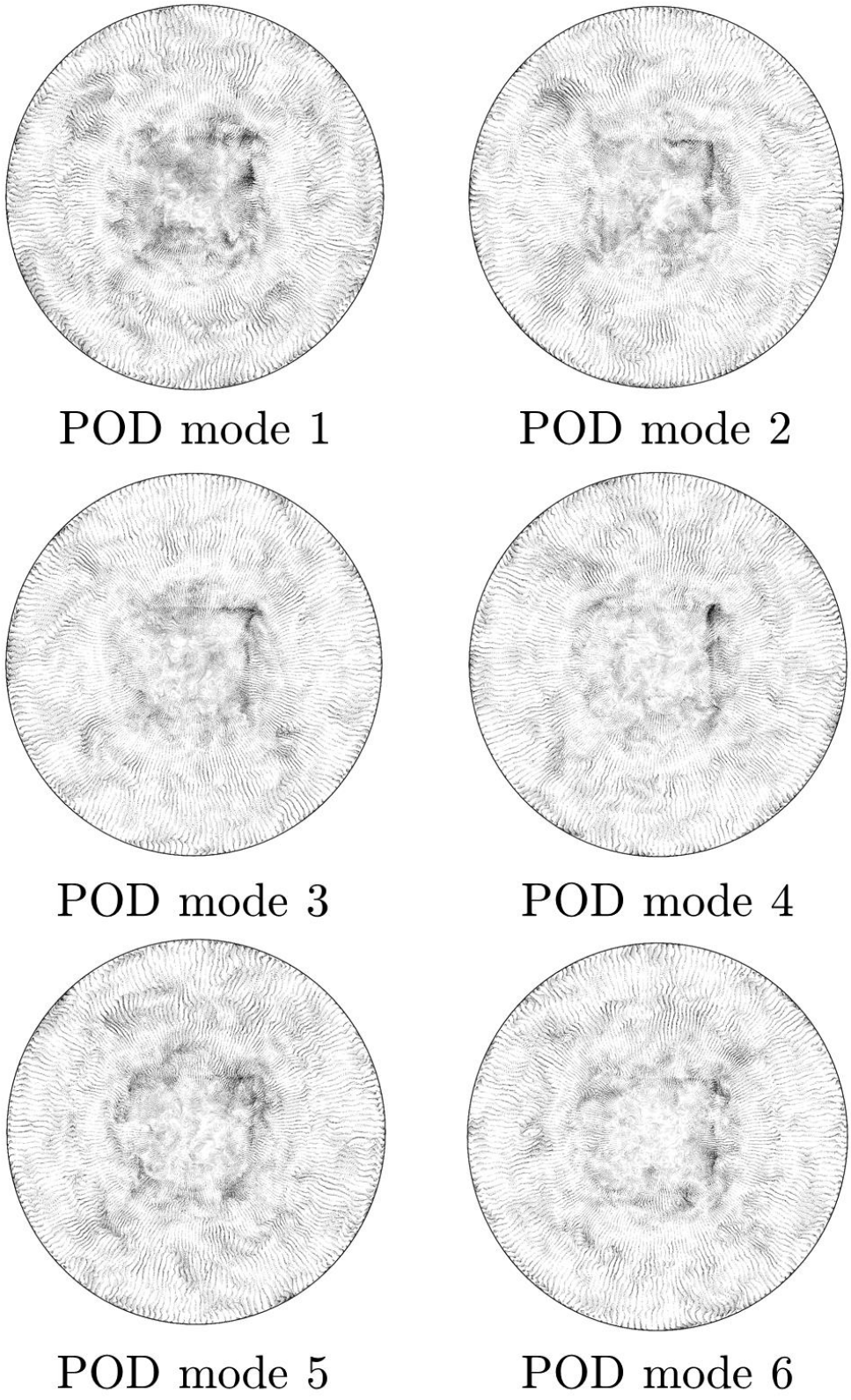

Figure 5.44 POD modes computed at position 4 for LES results that were used in the Sigma model for the SGS stresses.

5.3.5. Spatiotemporal coherence analysis

In the analysis of fluid flows, the acquisition of the underlying mechanisms that influence the motion of the fluid is paramount. In many cases, the physical features exhibited by a certain type of flow, such as swirling streams, can be encountered across a variety of applications, thus suggesting that the derived predominant structures are part of the dynamic nature of the flow. Different mathematical procedures have been developed in order to successfully describe the characteristics and behaviour of the turbulent structures. These methodologies are often developed as low-dimensional approaches in order to describe what in principle is a highly complex phenomenon into a more comprehensive description that can be easily employed for further studies or technological developments [346].

In the previous section, the characteristics of a swirling flow were assessed by performing a POD to the transient data obtained from LES calculations. The POD modes obtained provide a representation of the spatial distribution of the flow structures and they are often used to gain insights into the coherence of the flow. However, the POD methodology have acknowledged drawbacks, such as the usage of an arbitrary criteria for the number of modes to compute, and the suppression of the high-order correlations in its calculation. More importantly, is the disregard of the temporal component of the analysis which produced POD modes that are composed from an accord of structures with different associated frequencies [347].

The dynamic mode decomposition (DMD) is a mathematical model used for the analysis of dynamics systems that relies on a set of data sampled over a period of time [281]. The DMD utilises the temporal data from the sample, thus producing dynamic modes that are associated to a singular frequency value. The dominant structures depicted by the DMD modes are coherent, both in time and in space. In this section, a DMD analysis over the same data set employed for the POD study is performed. The three velocity components, assuming a Cartesian coordinate system, were employed to construct each snapshot of the flow, thus assuming a multivariable DMD methodology for this study [291], the results however, are presented in the form of vector plots for better representation of the relevant flow structures. In order to improve the confidence in the results yielded by the DMD, the pertinence of the data sample for analysis was assessed by confirming that the spectrum of frequencies obtained was evenly distributed over the complex plane [348], [349]. In addition, the produced DMD modes were re-ordered so that they better represent their

physical relevance over the flow field structure. A matrix constructed after the growth/decay rate for each DMD mode was used as an index to sort the modes [286]. The DMD analysis was performed for the numerical data obtained at the four axial positions introduced in Table 5.3. The results of the DMD analysis are presented in the forthcoming sections, and these include a plot of the normalised power contained in each DMD mode and a vector plot of the DMD mode obtained at a frequency 0 Hz, and this represents the steady state flow. Furthermore, a graphic representation of the first six DMD modes are presented.

5.3.5.1. Axial position 1

The DMD calculated for the results obtained from the LES with the Smagorinsky-Lilly SGS model produced a frequency spectrum in which only a few modes appeared to be the most relevant, as shown in Figure 5.45. In addition, the DMD mode obtained for the frequency band 0 Hz presented a good agreement with the results of the POD analysis, with a noticeable influence of the velocity inlet profile. The overall arrangement of the flow exhibits a strong rotational motion around the geometric axis, which is a distinctive feature of swirling flows.

The analysis of the DMD modes showed a large difference in the frequency of the leading and the subsequent DMD modes, as show in Figure 5.46. The leading DMD mode, however, is chaotic in its arrangement and appears to be related to the perturbations imposed at the inlet boundary condition. In contrast, the successive modes contain a combination of recirculating and well defined swirling regions that are mostly located in the shear layers.

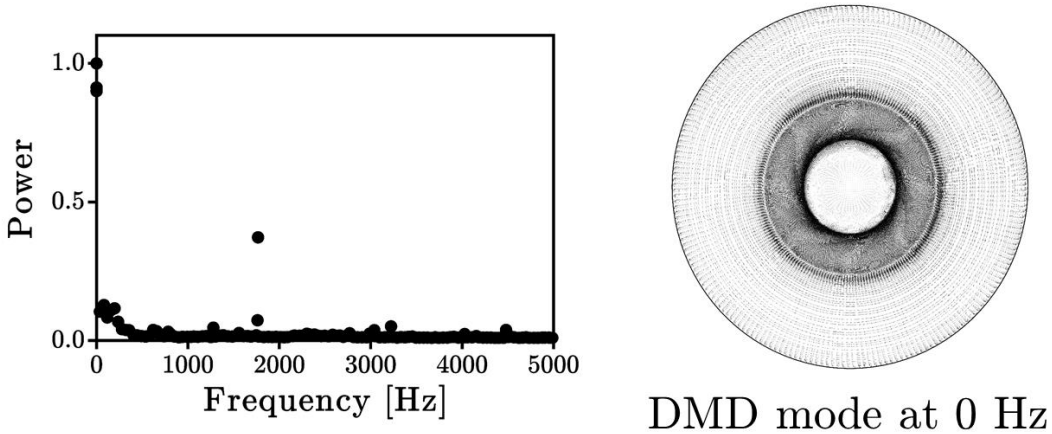

Figure 5.45 Frequency spectrum (left) and steady state DMD mode (right) calculated at position 1 for the LES data that was employed in the Smagorinsky-Lilly SGS model.

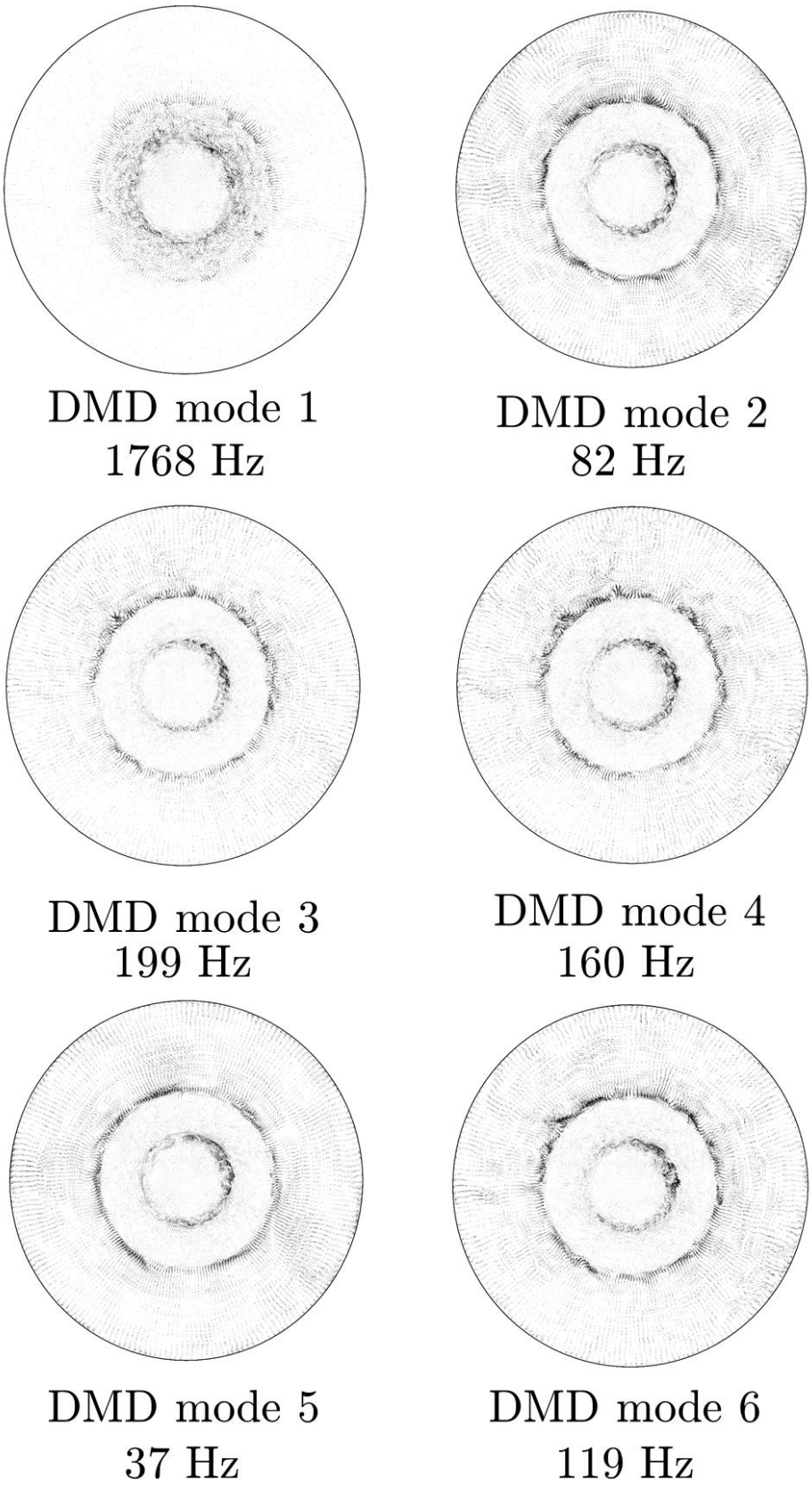

Figure 5.46 DMD modes for the axial position 1 calculated for the data obtained by performing LES with the Smagorinsky-Lilly approach as the SGS model.

The relevant DMD modes produced for the transient data obtained from the LES that employs the Sigma formulation for the SGS stresses are well distinguished in the spectrum, as shown in Figure 5.47. However, the remaining DMD modes contain similar amount of energy, and thus coincide in their contribution to the flow arrangement. In addition, the DMD mode obtained for the steady state of the system showed the same trend as in the previous analyses, with a good arrangement of the flow around the geometric centre. The region occupied by the inlet jets still exhibit the flow disposition set at the inlet boundary and, therefore, is not as well organised as in the outer region.

The DMD modes generated for the Sigma SGS mode case showed that the dominant structures are located in the shear layers, as presented in Figure 5.48. The first two DMD modes are highly fluctuating with oscillations up to a hundred times faster than the successive modes. Nevertheless, the influence of the flow structures depicted in these high-frequency DMD modes appear to be restricted to a smaller region of the domain. In contrast, the consecutive DMD modes expand their effects into a broader region that contains the outer region of the flow and both shear layers. Furthermore, some regions in the domain exhibited recirculation and are more noticeable in the DMD mode 5. The recirculating structures were predicted to be located in the shear layers, however, they only appeared as a discontinuity in the more organised swirling motion, thus suggesting that their contribution to the flow arrangement is relatively low. Some variations in the intensity for the vectors can be noticed in the outer region, however, their direction appeared to be unaltered.

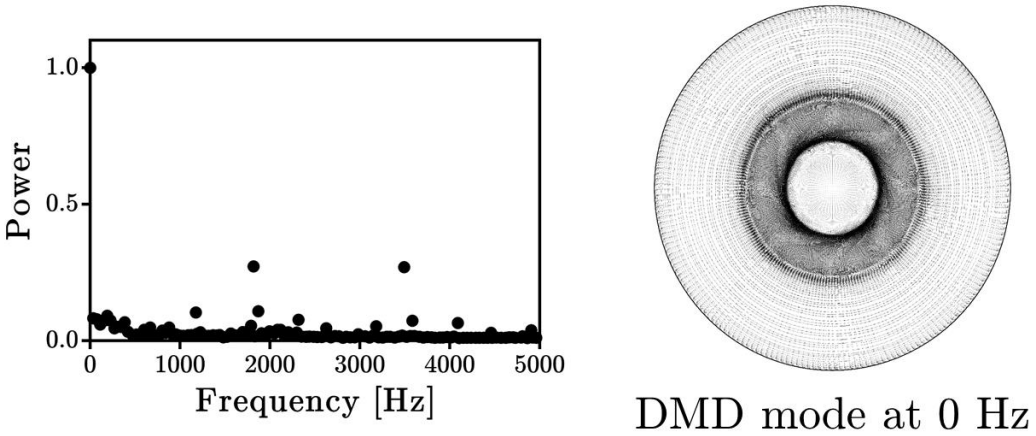

Figure 5.47 Spectrum of frequencies and their association to the DMD modes computed for the LES with the Sigma SGS model (left), and the steady state DMD mode at the axial position 1 (right).

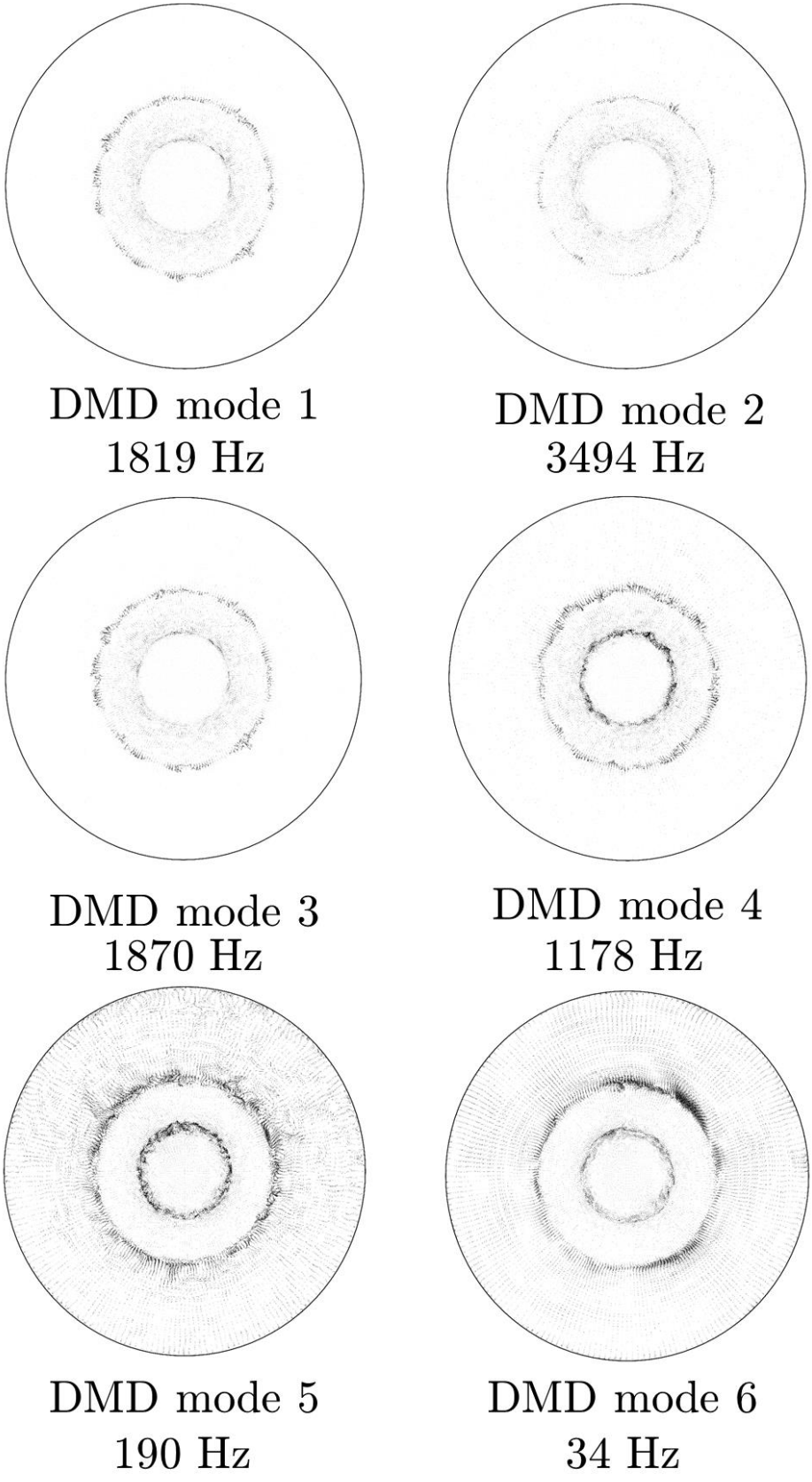

Figure 5.48 DMD modes calculated from the results of the LES with the Sigma SGS model and the transient data was obtained at the axial position 1.

5.3.5.2. Axial position 2

The DMD performed for the results obtained at the axial position 2 showed a more unsettled flow, with the DMD modes exhibiting high values for the normalised power in the system scatter across the whole spectrum of frequencies, as can be seen in Figure 5.49. Nevertheless, the steady state DMD mode, shown in Figure 5.49, presents a good flow distribution and it is in agreement with the results produced from the methodologies previously described. However, slight discrepancies can be observed in the internal shear layer in comparison to the POD estimate, as this region appeared to be wider and containing some vectors that resemble the disposition of the swirling vanes. Nonetheless, the overall swirling structure of the flow, present in all the previous analyses, is still prominent.

An inspection of the DMD modes obtained for the data generated by the CFD computations using the Smagorinsky-Lilly SGS model, introduced in Figure 5.50, showed that two different types of structures are dominant at this location in the domain. The most noteworthy flow structures are contained in the shear layers, as is evident for the representations of the DMD modes 1, 3 and 4. However, it can be observed that some additional entities are contained within the swirling jet and these are associated with the higher frequency values. The high-frequency DMD modes appeared as a chaotic arrangement of vectors that only become arranged in the internal shear layer. In contrast, the structures developed in the DMD modes that have lower associated frequency present a recirculation pattern and are more distinguishable.

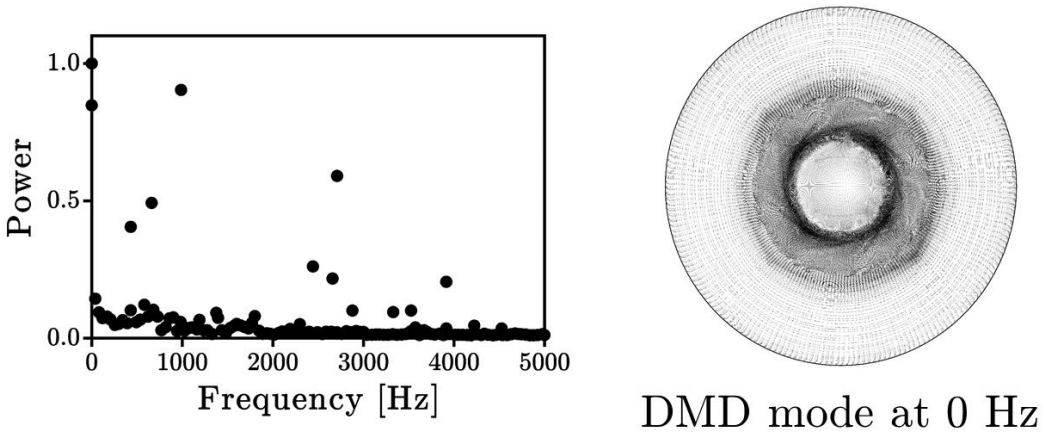

Figure 5.49 Frequency spectrum of the DMD modes computed for the transient data gathered at the axial position 2 for the LES with the Smagorinsky-Lilly model (left) and the steady state DMD mode (right).

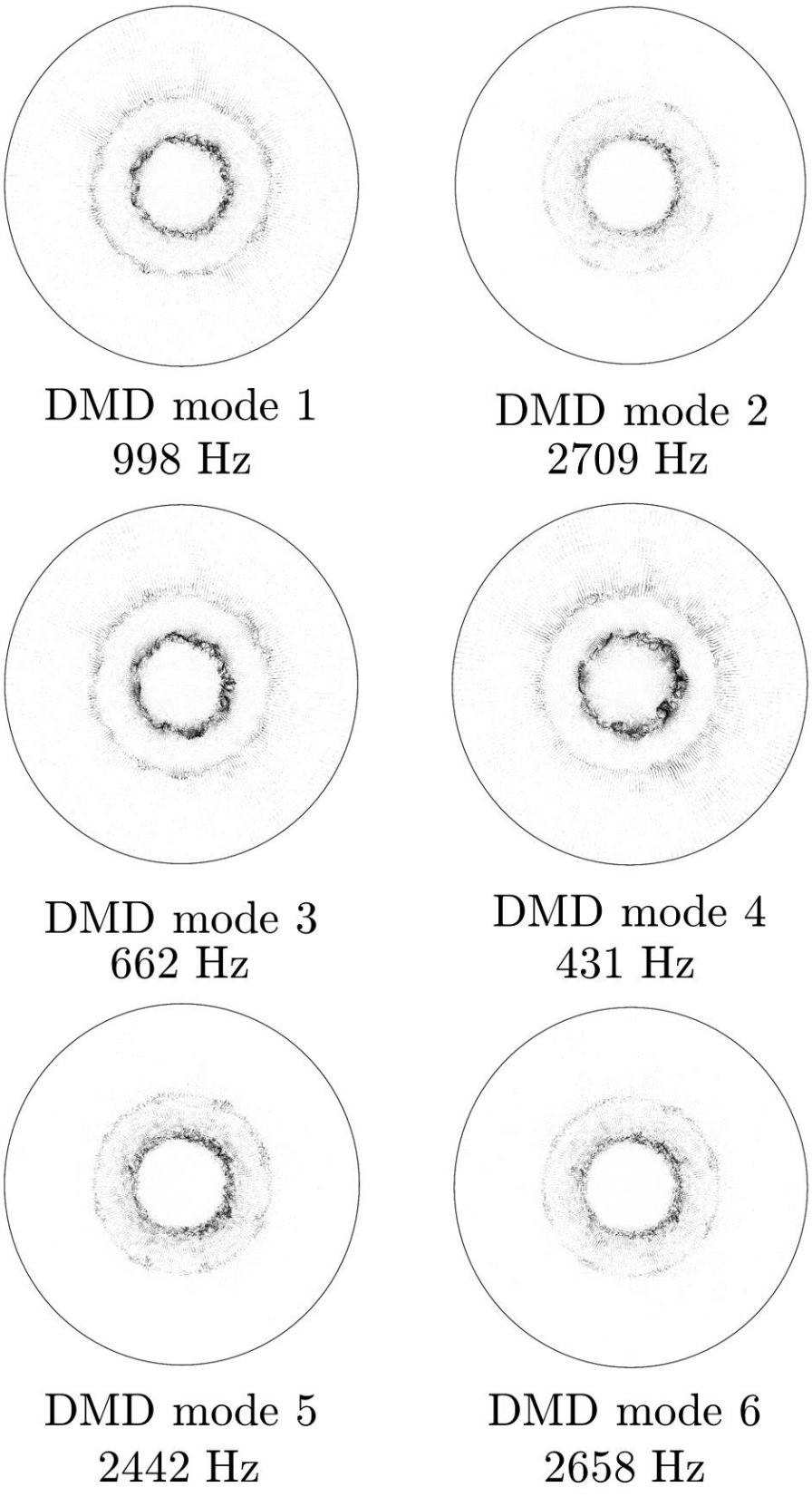

Figure 5.50 The DMD modes for the transient data at the axial position 2 that was obtained from a LES using the Smagorinsky-Lilly SGS model

In contrast, the spectrum of frequencies obtained for the DMD modes computed after the LES results that used the Sigma approach, presented in Figure 5.51, is sharper than that generated for the Smagorinsky-Lilly model and resembles the corresponding calculation at the axial position 1. The frequency associated with the relevant DMD modes of the Sigma approach is lower in general that that exhibited for the DMD modes in the Smagorinsky-Lilly case. The steady state DMD mode showed a good agreement to its counterpart in the POD analysis; however, some recirculating structures arose from the interaction between the central jet and the swirling stream. In addition, some high velocity spots appeared in the outer shear layer, indicating some discontinuities in the overall arrangement of the swirl.

The assessment of the DMD modes, produced by the transient results of the LES using the Sigma SGS model, showed that the dominant structures prevail in the shear layers. The region of influence for each DMD mode appears to decrease as the value of the associated frequency increases. Moreover, the high-frequency structures appear as being more ordered than those observed in the results of the Smagorinsky-Lilly model. In addition, the flow structures in the DMD modes with lower frequency displayed a predisposition to recirculate, thus suggesting that for this flow arrangement only the slower DMD modes will produce lingering flow structures. Furthermore, the turbulent structures captured by the DMD modes in the low frequency range of the spectrum are presented to be cohesive and well distributed over the shear layer circumference.

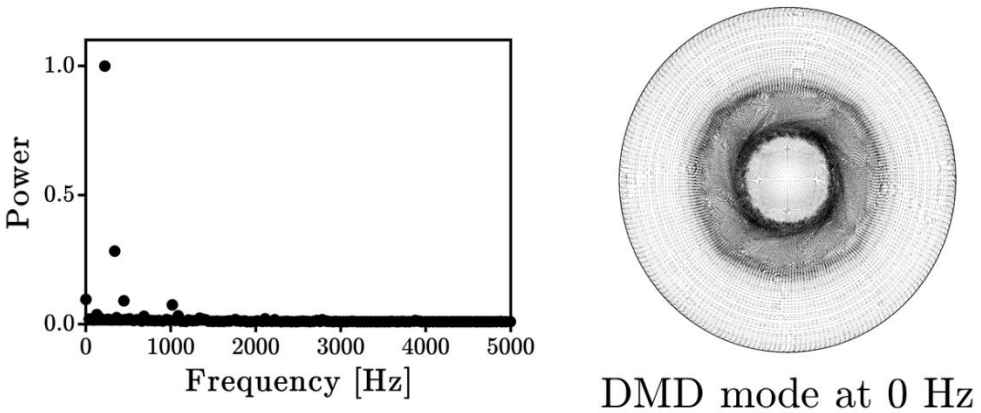

Figure 5.51 Frequency spectrum for the DMD modes (left) and the steady state DMD mode (right) calculated for the LES using the Sigma SGS model at the axial position 2.

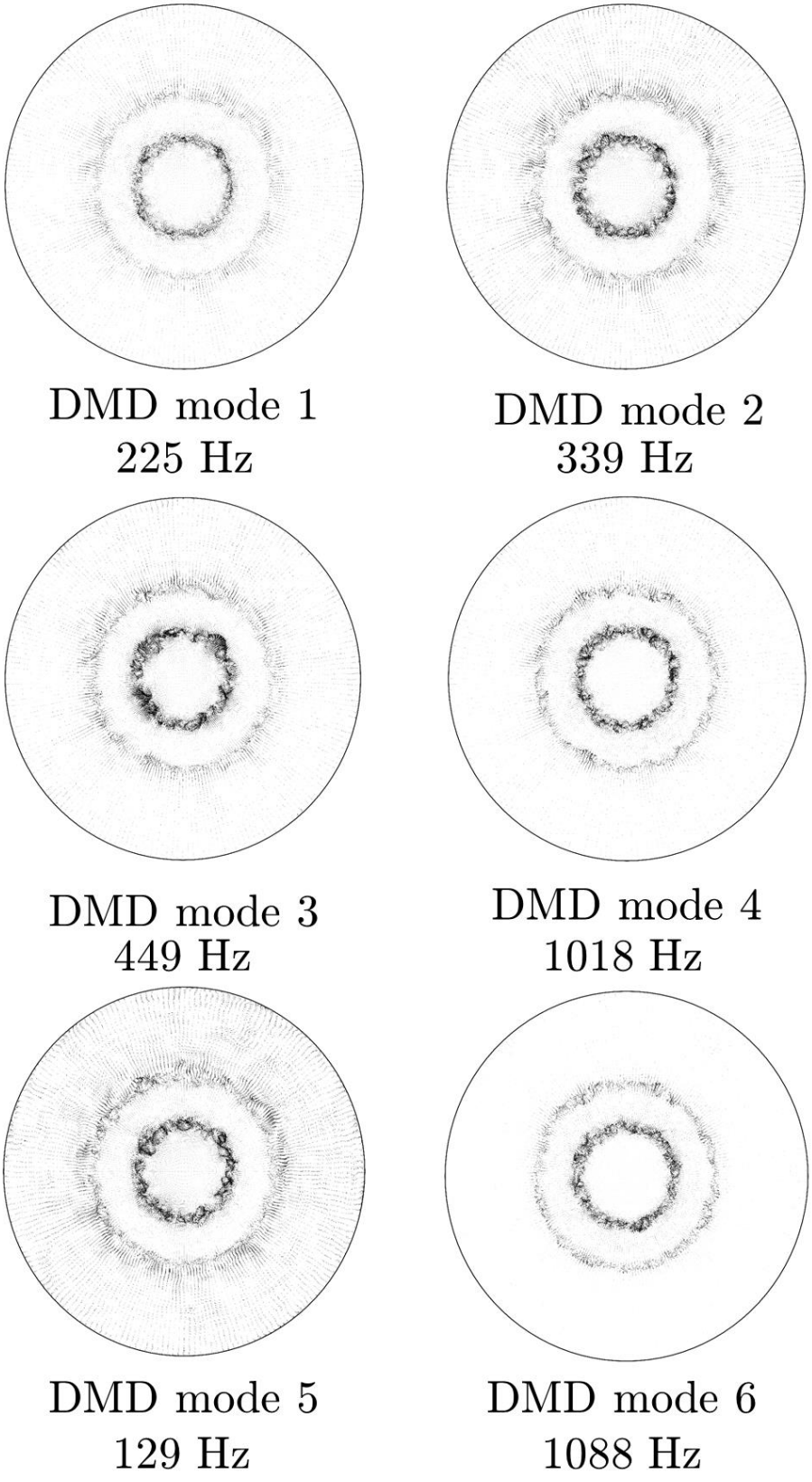

Figure 5.52 The DMD modes produced for the transient data at the axial position 2, generated by a LES with the Sigma approach as the SGS model.

5.3.5.3. Axial position 3

The results of the DMD analysis for the data obtained at the axial position 3 shows the same tendency as at the previous location with a wider range for the spectrum of frequencies occupied by the relevant DMD modes of the LES results that used the Smagorinsky-Lilly SGS model, as shown in Figure 5.53. The steady state DMD mode showed that, in general, the flow is well arranged and it is rotating around the normal vector of sampled plane. However, the circumference of the shear layers are less well-defined and some wrinkles in the interface are observable, thus indicating that the strength of the swirl diminishes for the increasing downstream positions.

The DMD modes calculated for the results produced by the Smagorinsky-Lilly case showed that for those of a high frequency, 2 kHz and upwards, the region of influence in the domain is well contained in the shear layers, whilst the DMD modes with lower frequency affect the whole domain. In addition the vectors obtained for the DMD modes with high oscillations, namely modes 1, 4 and 5, are disorganised and do not possess a noticeable pattern. In contrast, the dominant structures illustrated by the low-frequency modes emerged as being more coherent with a clear recirculation defined in their paths and a large cohesion among them. Moreover, despite the slower relevant turbulent structures being distributed across the domain, there appears to be no changes in the overall swirling motion of the fluid. This is evident in the direction of the vectors located in the outer region of the swirling jet and between the shear layers.

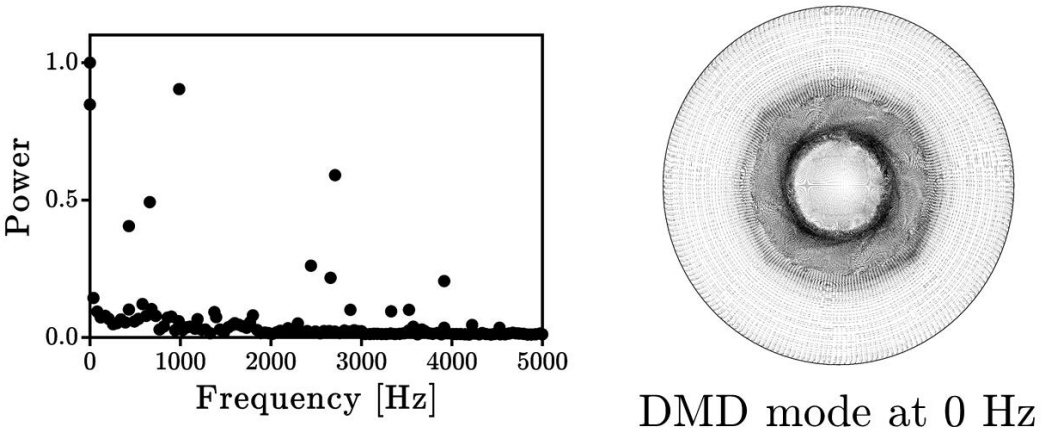

Figure 5.53 Normalised power contained by the DMD modes (left) and the DMD mode at 0 Hz produced for the transient data produced by the LES with the Smagorinsky-Lilly SGS model at position 3.

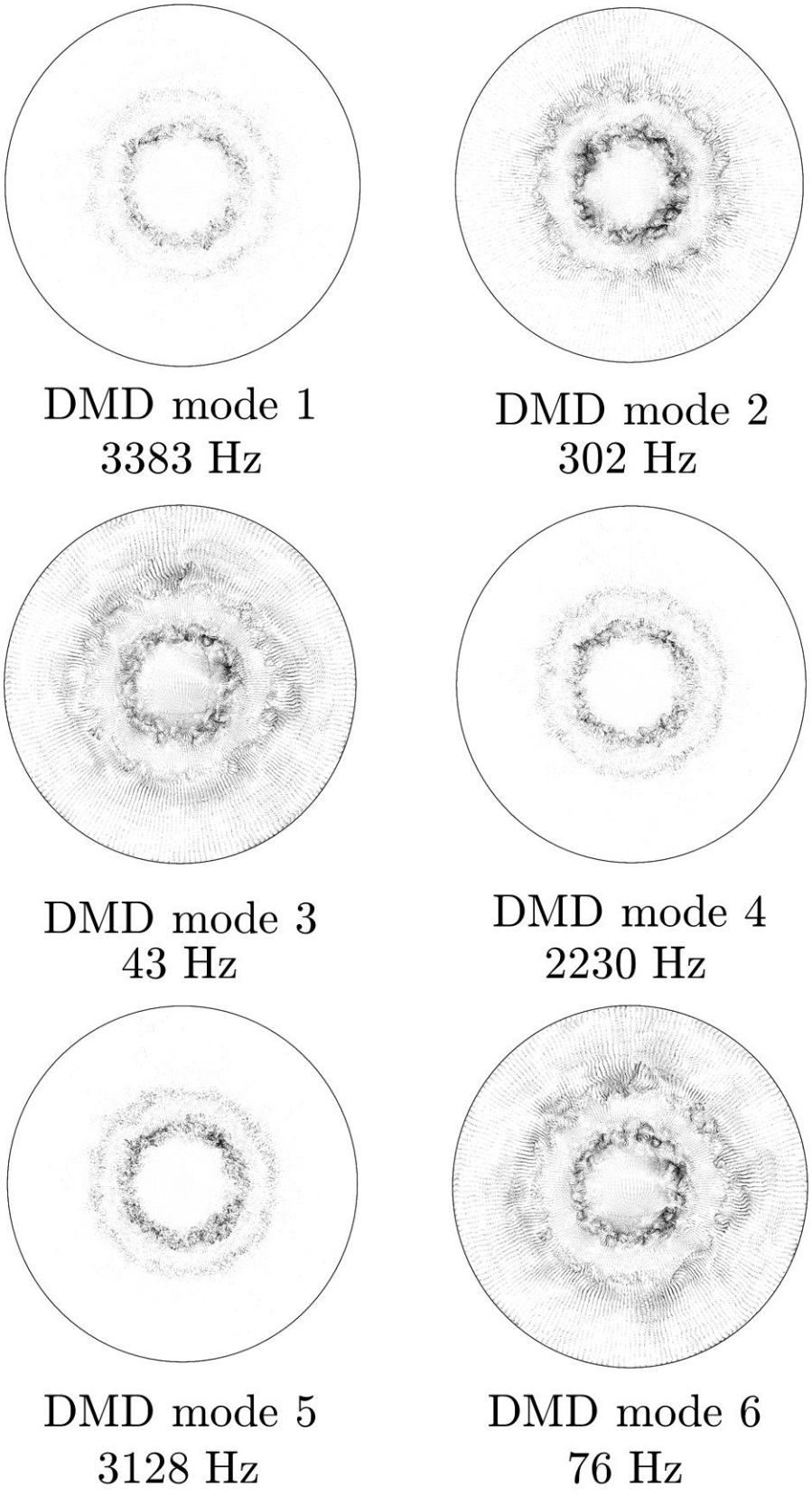

Figure 5.54 The DMD modes obtained for the LES data for the Smagorinsky-Lilly case at position 3.

The distribution of the power in the DMD modes computed employing the data from the LES with the Sigma SGS model showed that, as in the results for the Smagorinsky-Lilly case, the relevant DMD modes are dispersed across the spectrum of frequencies, as shown in Figure 5.55. However, the magnitude of the frequencies associated to the leading DMD modes are lower for this data set. In addition, the steady state DMD mode revealed that the stratification of the swirling motion, as observed in the previous DMD analysis, is not retained at this axial position. Furthermore, the effect of the surface wrinkling in the inner shear layer is more evident for this case, with recirculating zones predicted at the outer flow interface and within the central inlet jet. In addition, the surface wrinkling in the outer shear layer illustrates that the interface is not well defined and in some regions not even distinguishable.

As in the previous case, the DMD modes for the Sigma SGS model, introduced in Figure 5.56, exhibit a large difference in the region onto which the relevant structures influence the flow structure. It has been found that, for this study, the magnitude of the associated frequency is inversely proportional to the region of influence of the flow structures. Therefore, the DMD modes with the highest associated frequencies are predominant for the shear layer regions, where small, rapid structures take place. In contrast, the slower DMD modes contained larger structures with well defined paths that lingered in the flow domain for a longer period of time. The relevant structures predicted out of the shear layers were only captured by the low-frequency DMD modes and they appeared to be arranged around the spiralling motion of the flow, with a few recirculating regions of low intensity.

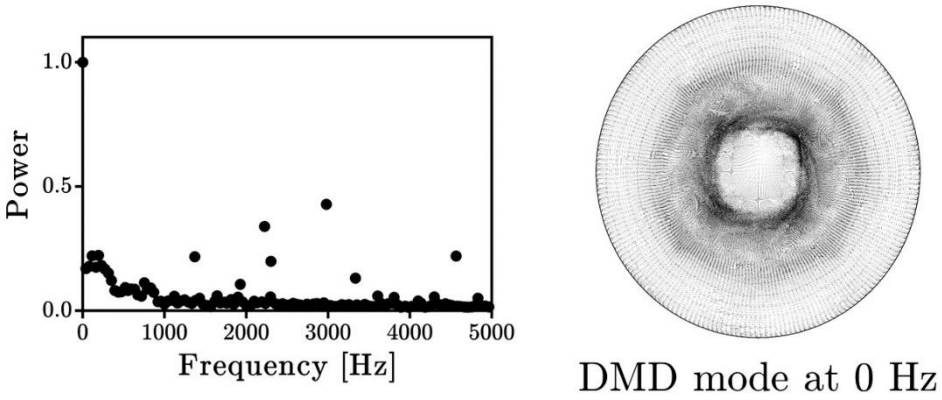

Figure 5.55 Distribution of the power in the DMD modes (left) and the steady state DMD mode (right) for the data produced by the LES with the Sigma SGS model at the axial position 3.

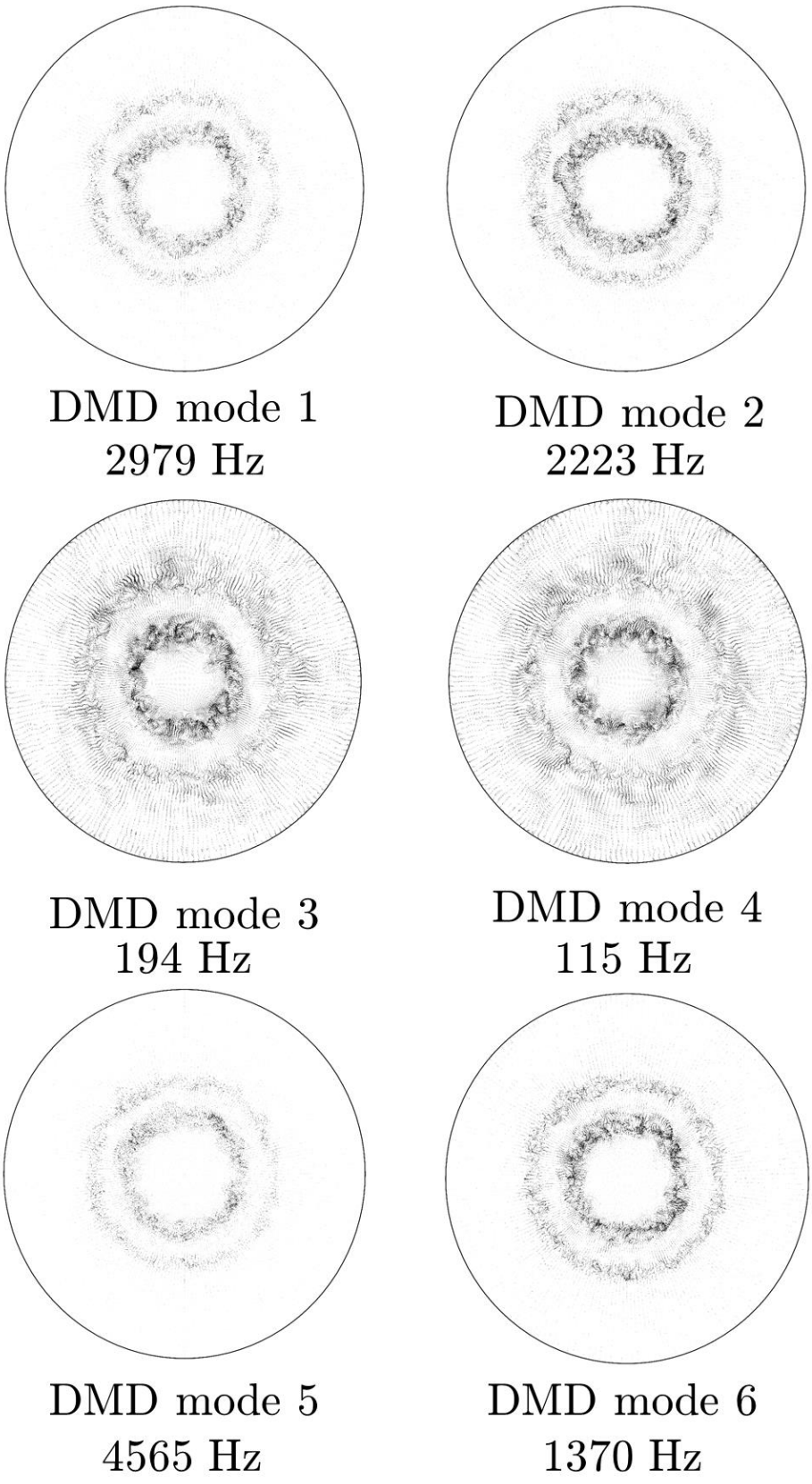

Figure 5.56 The DMD modes computed for the LES data for the Sigma case at the axial position 3.

5.3.5.4. Axial position 4

The spectrum of frequencies associated to the DMD modes, presented in Figure 5.57, showed that there is a sharp decrease in the magnitude of the DMD frequencies for the axial position 4. The distribution of the relevant DMD modes in the spectrum shows a tendency to remain in the low-range, in agreement to the general behaviour of swirling flows captured by low-resolution studies, such as the spectral analysis for point-based temporal signals. Furthermore, the steady state of the flow captured by the DMD mode with an associated frequency of 0 Hz, introduced in Figure 5.57, evidenced the mixing occurred in the flow, where the flow interfaces nearly vanished. Moreover, the overall flow arrangement suggests that the rotating component is preserved, but the emergence of recirculating zones across the domain is noticeable. The recirculating zones captured for the steady state appears to disrupt the flow motion at their particular location and, as consequence, the stratification of the flow structure is lost.

The analysis of the DMD modes, as shown in Figure 5.58, showed that recirculating structures were captured for the majority of them. The flow structures obtained suggest that as the mixing occurs, the shear layers that enclose the swirling stream disappears and the flow disturbances are no longer contained. A remnant of the shear layer is still observed in the DMD modes 1, 3 and 5, however the arrangement of the vectors suggest that the interaction with the outer region, where the rotating motion of the flow is still observed, is more prominent. The structures depicted by the DMD mode 2, a high-frequency mode, are part of the swirling jet and they do not form a recognisable pattern.

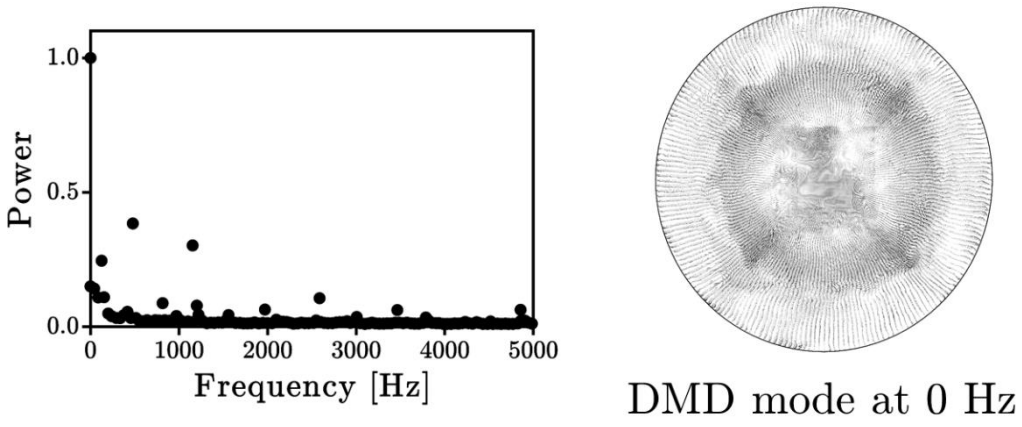

Figure 5.57 Frequency spectrum of the DMD modes (left) and the steady stated DMD mode (right) calculated at position 4 for the LES results with the Smagorinsky-Lilly approach to model the SGS stresses.

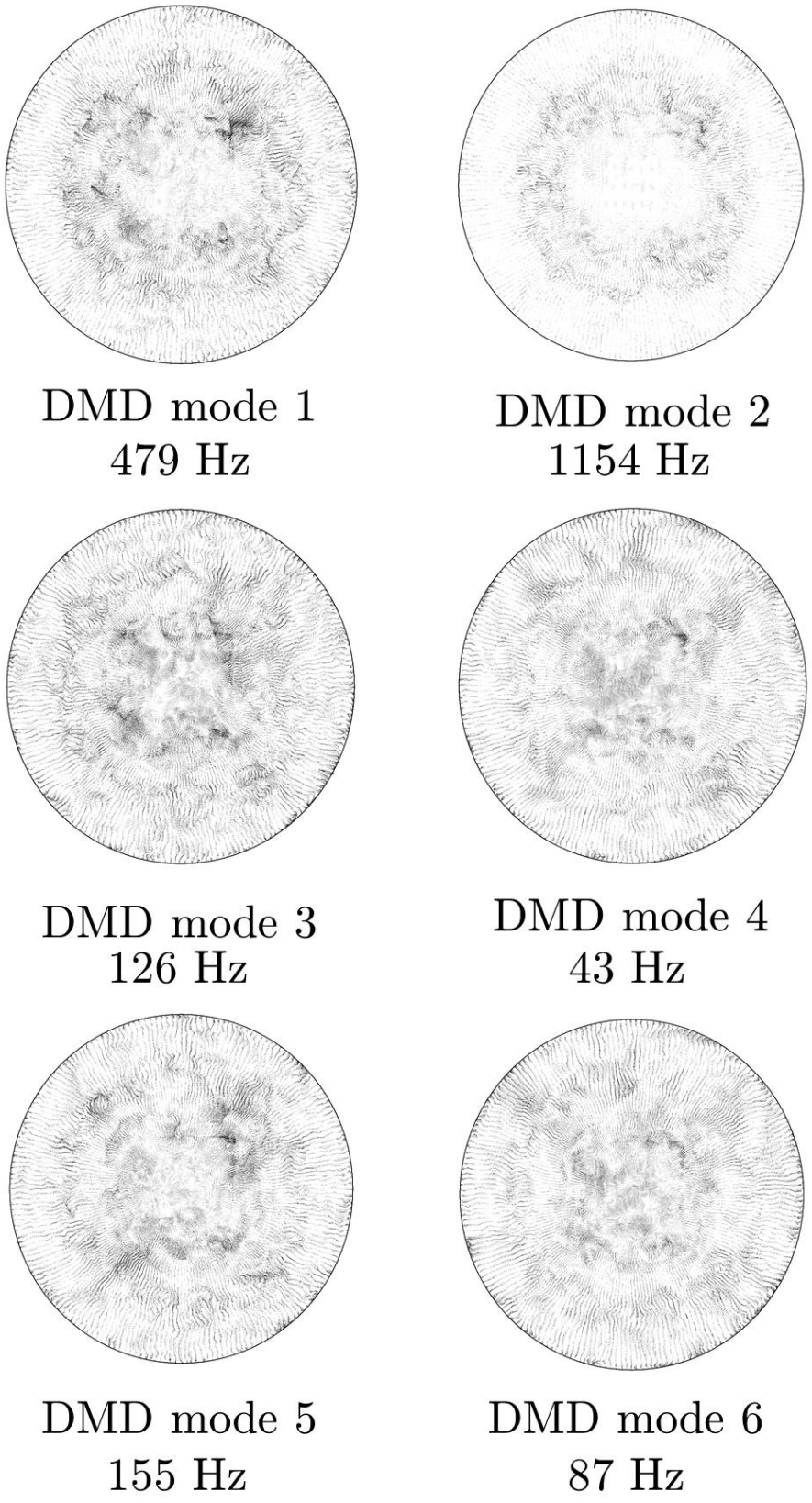

Figure 5.58 The DMD modes for the transient data at the axial position 4 produced by the LES with the Smagorinsky-Lilly SGS model.

The distribution of the DMD modes over the spectrum of frequencies, introduced in Figure 5.59, appears to be sharper in comparison to those obtained for the previous axial positions, thus showing the same trend as in the Smagorinsky-Lilly case. In addition, the amount of power contained in the DMD modes indicate that the predominant flow structures influence, in an almost identical proportion, the distribution of the flow. The steady state DMD mode, presented in Figure 5.59, exhibited a well distributed flow with a circulating pattern tightened around the geometric centre, thus contrasting with the more chaotic arrangement of the Smagorinsky-Lilly case. Small regions of recirculating flow were observed in the steady state vector plot but they are small and do not inflict a substantial disturbance to the overall flow distribution.

The flow structures characterised in the DMD modes for the data of the LES with the Sigma formulation for the SGS modelling are, in general, of a recirculating type and they can be encountered dispersed across the entire domain. However, the interface produced by the shear layers is more noticeable than in the DMD modes of the Smagorinsky-Lilly data, thus suggesting than the Sigma SGS model is more capable to retain the coherence of the flow. In addition, the size of the flow structures remains consistent across the DMD modes and, despite being presented as less energetic than those captured at position 3, they possess cohesion. The overall swirling motion of the flow was evidenced for the majority of the DMD modes regardless of the number of recirculating structures. However, for the DMD modes 4 and 6, the effect of the structures in the flow arrangement was sufficiently large that forced the fluid to move into different regions in the domain, thus enhancing the mixing phenomena.

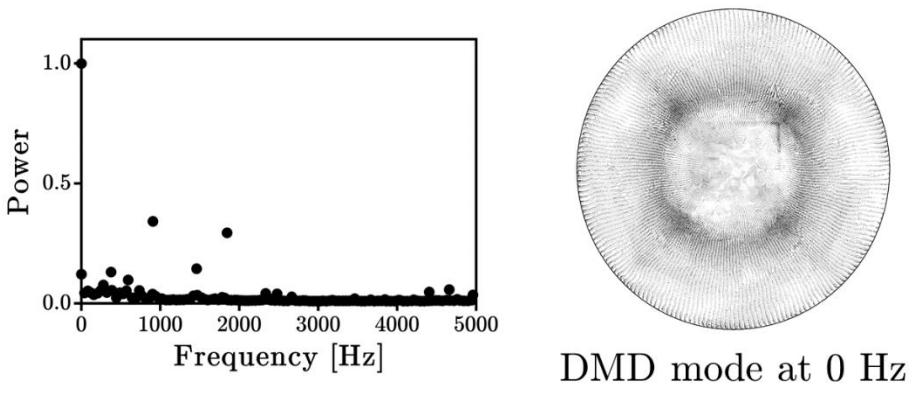

Figure 5.59 Distribution of the power in the DMD modes (left) and the DMD mode at 0Hz computed for the results at position 4 using the Sigma SGS model for the LES computations.

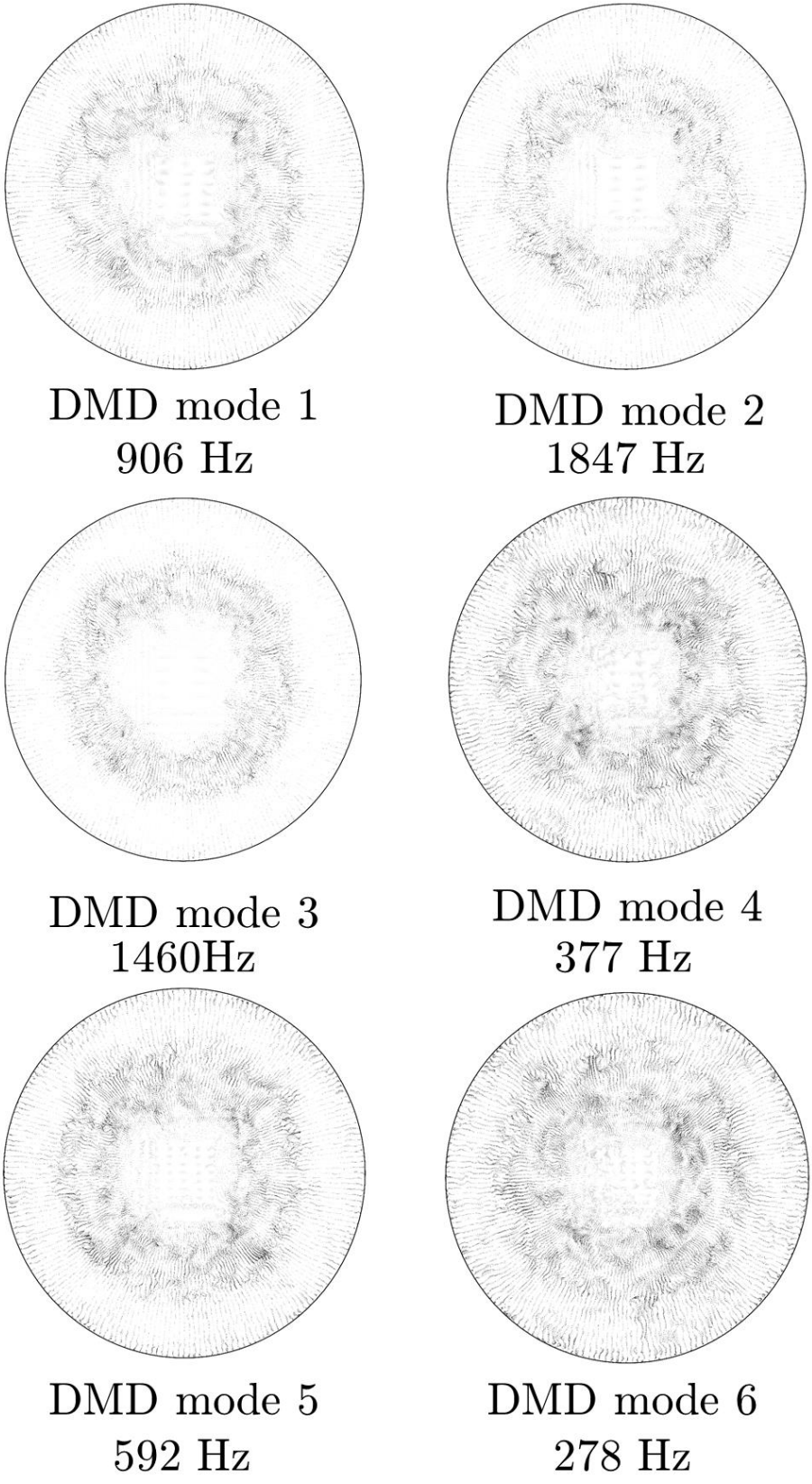

Figure 5.60 The DMD modes computed for the data generated by the LES with the Sigma SGS model at position 4.

5.4. Summary

In this chapter, an assessment of the coherence in time and space of a swirling flow was performed. Three different methodologies, which account for a different definition of coherence, were employed for this purpose, namely the spectral analysis, the proper orthogonal decomposition and the dynamic mode decomposition. The temporal coherence was accounted for by performing spectral analyses over the transient data generated at a prescribed point in the domain. Secondly, the spatial coherence of the flow was analysed by implementing the POD methodology over a transient dataset that consisted of the instantaneous values at a planar location. Finally, the DMD approach was used to analyse the spatiotemporal coherence of the flow by employing the same two-dimensional data.

The transient data was obtained from a computational fluid dynamics study of the test rig constructed by the Lewis Research Center in the United States, in which large eddy simulations were performed. As part of the CFD analysis, the performance of different turbulence models for different types of meshes was investigated. It was found that for the RANS computations, both for the two- and three-dimensional meshes, the realizable $k - \epsilon$ model outperformed the other turbulence models. The numerical stability of the realizable $k - \epsilon$ model for this study was noteworthy, and the accuracy of the results produced by this approach were consistent to those obtained for the distinct RANS models. In addition, the efficiency of two different wall functions, namely the scalable and the Menter-Lechner formulations, required to fully resolve the boundary layer in the near-wall region, were tested and the results showed no noticeable advantage in the accuracy of the results. However, the Menter-Lechner formulation is independent of the y^+ value in the study and, therefore, provides more flexibility for their application.

The mesh required for the LES was constructed based on the results generated by the RANS approach. A quality criterion for the pertinence of the mesh for a LES was used and its results were employed as the basis to perform the refinements to the element size and distribution. Several refinements were made to the initial mesh until it was no longer feasible. Two different approaches for the sub-grid scale effects, the Smagorinsky-Lilly and the Sigma model, were employed in order to evaluate their performance for wall-bounded flows. The results produced by the LES improved the prediction of the flow distributions produced by the RANS approach, especially in the region where a recirculating flow occur. In addition, the velocity magnitude of the central

jet was better captured by the LES and the agreement with the experimental data was enhanced. Moreover, slight differences were observed for the LES results at the first two axial positions, where the effect of the distribution of the flow imposed by the inlet boundary condition is evident. However, further downstream, the Sigma model produced results for the velocity distribution of wider range. In addition, a qualitative characterisation of the flow structures was made by employing isosurfaces of three well-known principles, namely the vorticity magnitude, the Q-criterion and the Lambda-2 criterion. The turbulent structures depicted by the isosurfaces were intertwined filaments that move through the domain in a swirling motion and eventually collide to form larger structures and these are mostly contained in the shear layers generated by the interaction of the swirling stream and the central jet and the swirling stream and the outer recirculating zone.

The spectral analysis was performed over a set of signals generated by the instantaneous fluctuations of the axial velocity component at the different prescribed points. The frequency spectrums produced represent the oscillation in time of the velocity and, hence are a direct quantification of the temporal coherence. It was found that significant differences occur between the two SGS models at the first two axial positions, where the Smagorinsky-Lilly model appear to be highly influenced by the flow perturbation mechanism employed at the inlet boundary condition. This effect might be mitigated by applying a filter to the signal, however the lack of a-priori knowledge of the output frequency spectrum compels caution for it implementation. Nevertheless, as the inlet streams mix in the domain, the spurious frequency components diminish and the overall prediction of the swirling motion equalises to a range of 70 to 80 Hz measured at the third and fourth axial positions.

The spatial coherence analysis was carried out by POD of a dataset consisting of two-dimensional transient representations of the flow obtained at the same axial positions. The planar representations, known as snapshots, of the flow consisted in the velocity components at each vertex location of the mesh. Despite being a planar representation of the flow, the axial velocity component that is aligned to the normal direction was included in order to acknowledge its influence on the overall flow distribution. The POD modes obtained from the analysis showed that the most relevant flow structures are contained in the shear layers for the first three axial positions, while in the results computed for the fourth axial position, the turbulent structures are scattered in the domain. The structures obtained by the POD analysis for the first two positions

appeared to be smaller, more energetic and consistent with the swirling motion of the flow. The structures predicted for the subsequent positions exhibited recirculation and occupy a broader region in the domain.

One of the main drawbacks of the POD analysis is the lack of temporal information regarding the turbulent structures predicted. In the DMD, the computed modes are enforced in order to remain coherent both in time and in space, thus allowing a better characterisation of the structures generated in the flow. In this multivariable DMD analysis, the same data as that used for the POD was employed for the sake of consistency. It was found that the results obtained showed good agreement with both of the previous methodologies introduced, with the relevant flow structures well contained in the shear layers and exhibiting a decay in their oscillatory rate as they mix. However, the differences in the resolution of the data employed in each approach produce discrepancies, most notably in the acquisition of the high-frequency modes relying on smaller locations of the domain that are easy to miss in a point-wise approach. Moreover, the POD and the DMD approach produced similar results, and the turbulent structures contained in the flow field in this study are of a recirculating nature and they are mostly located in the shear layers. In addition, it can be perceived that the flow distribution remained consistent until position 3, and that afterwards the mixing effects in the flow induce a disarrangement. Furthermore, it was found that the high-intensity oscillations are mostly contained within the shear layers, and due to its large frequency values their physical origin and relevance to the overall flow structure is debatable.

In conclusion, the benefits of the LES over the steady state RANS in the study of swirling flow were observed. The transient, high-definition results produced by the LES can be successfully employed in the assessment of the coherence in the flow. Further, a full characterisation of the flow must include an assessment of the temporal and spatial repeatability, and this can be obtained by performing a DMD over the transient data. Finally, the LES appear to be susceptible to the influence of the perturbation algorithm used at the boundary condition and, therefore require caution while selecting the location and type of the sampling mechanisms to be employed. In addition, the Sigma model produced consistent results across the domain and appeared to be more suitable to retain the coherent structures generated in the domain.

6. The coherence of the flow in a coal combustor

The aerodynamic profile encountered in swirling jets is the result of a combination of the characteristic rotating motion of the flow and the free turbulence phenomena inherent to jet and wake flows. The presence of a swirl component in the flow produces gradients in the pressure field for the axial and radial directions which eventually influence the structure of the flow [36], [332]. The intensity of the swirl is paramount in the development of the flow structure. For a sufficiently strong swirl intensity, the opposing pressure gradient developed along the axial direction cannot be overcome by the kinetic energy contained in the fluid particles and a recirculating flow, enclosed between two stagnation points, is developed. The recirculating zones in combustors often materializes as toroidal bodies within the domain; these flow structures carry heat and active chemical species back into the vicinity of the burner, thus acting as an stabilisation mechanism while enhancing the ignition of the mixture entering the domain [350]. The parameters of the flame produced in a swirled combustor, such as its size, intensity and stability, are directly dependent of the type and size of the vortex generated. Furthermore, the utilisation of swirling flows if often preferred over bluff body wakes as a stabilisation mechanism, as they do not contain a surface exposed to the effects of the combustion environment and particle deposits [36].

The alteration of the combustion environment in oxyfuel conditions will modify the stability of the system. The differences between the conventional air-fired conditions and the oxyfuel environment rely on the composition and inlet flows required in the oxidiser stream. Moreover, the effect of the CO_2 rich environment has been acknowledged to lower the adiabatic flame temperature and the flame propagation speed and delay the ignition of the coal particles [351]. Therefore, the sustentation of a stable flame across the different combustion regimes is of a primary concern in the design and evaluation of novel combustion technologies. The predominant feature in the development and deployment of oxyfuel systems is to reassure that the mixing of the oxygen into the stream is produced efficiently. Furthermore, the preservation of the flow structure play an important role in the reduction of pollutant formation, and it is strongly encouraged in the aerodynamics philosophy of staged combustors of recent development. In addition, contemporary combustion systems are de-

signed to dampen the generation of large turbulent structures that are responsible to induce noxious fluctuations to the flow and to reduce the life cycle of the peripheral equipment.

The adoption of CFD analyses have been recognised as a crucial step in the design cycle and retrofit studies for the implementation of oxyfuel systems in power plants. In addition, the results that produced these analyses allow an accurate prediction of the combustor behaviour under different scenarios and the evaluation of different alternatives for the increasing of the efficiency in the system [25], [28], [330]. The mathematical models required to perform CFD simulations of coal combustion, introduced in Chapter 2, are complex, hence their implementation for practical applications is not straightforward. The implementation of LES in the coal combustion framework compels a substantial increment in the computational power required to fully resolve the effects of the phenomenon at the spatial and temporal scales required by the LES. Moreover, the spatiotemporal coherence have been employed in the analysis of different types of combustion processes [288]–[292], and for the analysis of the thermo-acoustics [293], [294], comparisons against flame transfer functions [295] and for the evaluation of combustion instabilities [296]–[301].

The following sections introduce a comparison of the coherence of the flow produced in coal combustor for air and oxyfuel conditions. The characteristics of the test facility are presented, and the operating conditions employed in the study are further introduced. In addition, the numerical settings and the mathematical models selected for the simulations are discussed. Furthermore, the results obtained for the steady state solution of three different reactive cases under different combustion conditions are analysed and the assessment of the aerodynamic profile in the combustor is performed. Moreover, the spatiotemporal coherence of the combustor is analysed by applying the methodology developed in Chapter 5 to the LES results obtained for the isothermal flow developed under air conditions and the correspondent oxyfuel state. Finally, a summary of the findings of this study and a discussion of the insights obtained for the combustor dynamics and their utilisation in the accurate judgement of the flame stability are presented.

6.1. Case description

The cases studied in this chapter were part of an experimental campaign undertaken at the solid-fuel combustion test facility of the Pilot Advanced Cap-

ture Technology (PACT) Facilities, located in Sheffield, UK. The test rig consists of a down-fired cylindrical furnace that allocates a scaled version of commercial coal burner. The coal burner has a staged design with three inlets in the form of concentric annular channels, it produces 250 kW and it was manufactured by Doosan Babcock Ltd. The fuel is entrained through the primary channel, which is the inner most annulus, by a fraction of the gas required for the reaction; four gutters are placed within the channel and a bluff body is attached to the end of the primary channel in order to promote the anchoring of the flame. The remaining oxidiser is provided by the flow in the secondary and tertiary channels. The swirl component in the flow is provided by a series of blade arrangements located in each of the flow channels. The blades in the primary channel were fixed at a polar angle of 63° while those located in the secondary and tertiary channels were placed at polar angles of 64° and 33°, respectively. Furthermore, the oxidiser stream for the secondary and tertiary channels is conducted through an electrical heater unit in order to reach the operational temperature. Further details on the furnace composition, operating philosophy, and the technicalities of the equipment employed to sample data during the experimental campaign have been reviewed in Chapter 3.

Table 6.1 Combustion conditions used in the analysis of the coherence in a coal combustor.

Air combustion						
Mean axial velocity [m/s]			Gas composition		Temperature [K]	
Pri	Sec	Ter	Pri	Sec/Ter	Pri	Sec/Ter
5.41	7.71	6.94	Air	Air	297.15	524.65
Oxy27						
Mean axial velocity [m/s]			Gas composition [mass, %]		Temperature [K]	
Pri	Se	Ter	Pri	Sec/Ter	Pri	Sec/Ter
3.75	5.38	4.85	O_2/CO_2 13.75	O_2/CO_2 23.09	294.15	517.15
Oxy30						
Mean axial velocity [m/s]			Gas composition [mass, %]		Temperature [K]	
Pri	Sec	Ter	Pri	Sec/Ter	Pri	Sec/Ter
3.38	4.83	4.35	O_2/CO_2 13.84	O_2/CO_2 26.44	301.15	526.15

Three different combustion scenarios were simulated, and the steady state results for the reactive cases were compared in order to evaluate how the aerodynamics in the combustor is affected by the oxyfuel conditions. Furthermore, the predictions for the composition of the combustion gases were employed to validate the pertinence of the selected models in the simulation of the combustion reaction [56]. A summary of the characteristic conditions for each of the cases tested is presented in Table 6.1.

The utilization of the methodology developed for the assessment of the coherence in swirling flows, as developed in Chapter 5, allows the characterisation of the dynamics of the flow and will provide insights into the response of the combustor to the oxyfuel environment. The alteration in the conditions, from water in the case analysed in Chapter 5, to a gaseous working fluid in these studies, and the physical properties associated to it, will influence the turbulent structures generation mechanisms. In addition, the dampening of the turbulent structures, as noticed in the chamber analysed in Chapter 5, may be significantly compromised, as the difference in the density and viscosity between the working fluids suggest less cohesion among the structures and more susceptibility to break away from the general flow distribution.

6.2. Numerical settings

The domain used for the CFD calculations in this chapter is a version of the geometry of the solid-fuel test furnace at the PACT facilities that was digitally cleaned in order to remove spurious solids, generated from the tolerances used in the computer-aided assembly, and sharp edges. The diameter of the furnace is 900 mm and its length is 4 m, it contains a quarl section of diameter 230 mm at the top, which is used to fix the burner in position. The oxidiser inlet channels have an annular geometry of widths 10.1, 12.9 and 18.9 mm for the primary, secondary and tertiary channels, respectively. The gutters contained in the primary channel were retained in the geometry in order to incorporate their effect on the flow distribution prior to the combustion chamber. In addition, a refractory plate is placed at the bottom of the furnace in order to increment the radiative heat transfer, thus leaving a circular section of diameter 150 mm, where the outlet of the furnace is assumed to be located. A schematic of the furnace geometry, including a detail view of the secondary and tertiary inlets, is presented in Figure 6.1.

The numerical grid for the three-dimensional geometry consisted of hexahedral elements, and it was constructed using ANSYS ICEM. A structured blocking technique was employed to capture the geometry, in which several O grids and

block splitting operations were necessary. The gutters contained in the primary channel required further modifications to the original block structure, which eventually lead to the rotation of the geometry in order to retain the orthogonality of the blocking array. The grid was refined in the near burner region and close to the walls, and it consisted in 4331721 elements. Further refinements to the mesh were made, however these proved to be difficult to manipulate in the context of the reactive cases and therefore were no longer used.

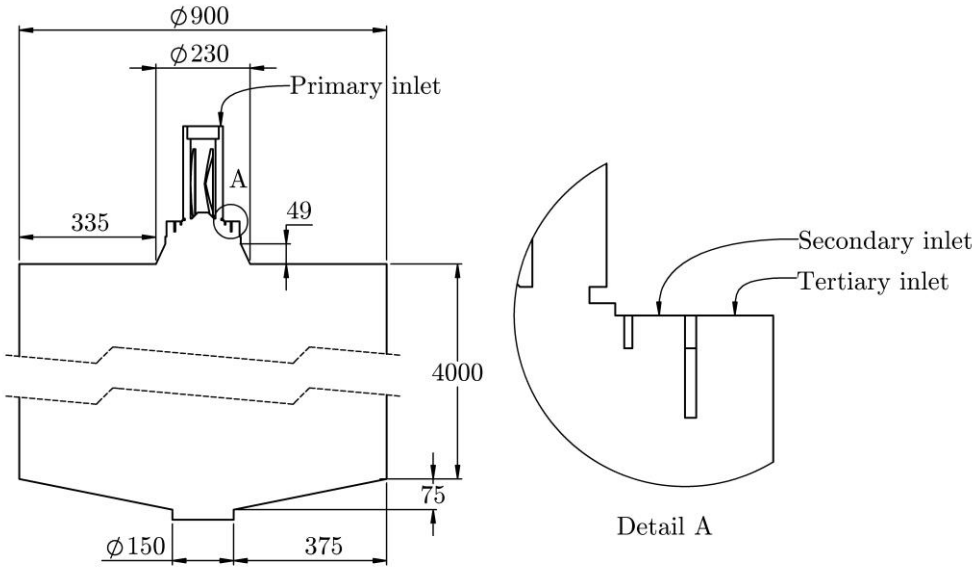

Figure 6.1 Schematic of the solid-fuel furnace of the PACT facilities.

The reactive cases evaluated in this chapter employed a RANS approach for the contributions turbulent motions which, in agreement to the findings of Chapter 5, the realizable $k - \epsilon$ model [100] was employed. The Menter-Lechner wall functions [94] were enabled for the RANS computations as its independence from the y^+ values improves its flexibility across different mesh sizes. In addition, the Sigma model [122] was employed for the subsequent LES isothermal studies, as its performance for wall-bounded applications appeared to be enhanced in comparison to the other SGS models.

The trajectory of the coal particles were calculated using a Lagrangian reference frame which included the gravitational effects [44]. The effect in the particle dispersion due to the fluctuating velocity, caused by turbulence, was incorporated to the particle tracking through the discrete random walk model [140], [352]. A single kinetic rate was employed to account for the release of volatile matter from the coal particle [155]. The parameters for the Arrhenius equation employed in the devolatilisation were carefully set to represent the

pyrolysis of the 'El Cerrejon' coal and these have been successfully employed in similar CFD studies [68], [353].

Table 6.2 Modelling parameters employed in the CFD studies of the flow in a coal combustor.

CFD modelling parameters	
Physics	Model parameters
Turbulence	RANS: Realizable $k-\epsilon$ model with the Menter-Lechner wall functions. LES: Sigma model for the SGS stresses.
Devolatilisation	Single rate with $A = 14841\ \mathrm{s}^{-1}$ and $E_a = 35.3\ \mathrm{MJ/kmol}$
Gaseous combustion	Eddy dissipation model with a two-step reaction mechanism $\mathrm{C}_a\mathrm{H}_b\mathrm{O}_c\mathrm{N}_d\mathrm{S}_e + \alpha\mathrm{O}_2 \rightarrow \beta\mathrm{CO} + \gamma\mathrm{H}_2\mathrm{O} + \zeta\mathrm{N}_2 + \xi\mathrm{SO}_2$ $\mathrm{CO} + \frac{1}{2}\mathrm{O}_2 \rightarrow \mathrm{CO}_2$
Char combustion	Intrinsic model with $A = 4e^{-4}\ \mathrm{s}^{-1}$ and $E_a = 66\ \mathrm{MJ/kmol}$ $\mathrm{C_S} + \frac{1}{2}\mathrm{O}_2 \rightarrow \mathrm{CO}$
Radiation	Finite volume method of the discrete ordinates model with angular discretisation of 3×3. Absorption coefficient given by the FSCK model.
Particle tracking	Euler-Lagrange approach with the discrete random walk model for turbulent fluctuations.

The combustion of volatiles was computed by the eddy-dissipation model (ED) [166], which assumes that the reaction rate is controlled entirely by the turbulent mixing. The mixing rate parameters required for the ED model were set to the values recommended for confined swirling flames [61]. The released vol-

atiles were simulated as a single chemical compound whose properties are derived from the proximate and ultimate analyses of the coal and are presented in Table 3.1. A constant fuel mass flow of 25.7 kg/h was assumed for all the cases investigated. The volatiles are further oxidised assuming a two-step reaction mechanism. The combustion of the char particles that remain after the release of volatiles was modelled by the intrinsic char combustion model assuming previously tested values for its parameters [56], [68]. The radiative heat transfer was solved using the finite volume method variation of the discrete ordinates model with an angular discretisation of 3×3 [198]. The absorption coefficient for the gaseous phase was calculated by the full-spectrum correlated k-distribution (FSCK) model which was incorporated into the analysis as a user defined function [68], [221]. The prediction of soot, and its associated interaction in the heat transfer, was not incorporated into these computations, since previous analyses have shown marginal differences in the results [65], [68] while including the Brown and Fletcher model [354]. Further models have been developed in order to obtain an accurate representation of the soot generation in the combustors however, due to the complexity of the phenomenon, further validation is required in more realistic scenarios [355]. A summary of the models employed in the CFD studies is presented in Table 6.2.

Fully developed profiles for the axial velocity, assuming the 1/7 power law, and the appropriate tangential velocity were employed as the boundary condition for all the inlets of the burner. A zero diffusion flux for all the field variables, with a mass balance correction, was set at the domain outlet. The walls of the furnace were included in the computation as two solid bodies, where the upper body represents the first two sections of the furnace in which the thermal conductivity of 0.92 W/m-K is assumed. The additional solid characterises the remaining six sections of the furnace and the refractory panel installed at the outlet, which takes a value of 0.27 W/m-K for the thermal conductivity. A constant temperature of 300 K was set for the outer surface of the solid bodies, thus assuming thermal equilibrium with the cooling water that circulates in each section of the furnace. The walls at the top of the furnace and those contained in the quarl region were assumed to be adiabatic. In addition, the emissivity for all the walls was set at a constant value of 0.8.

6.3. Steady state reactive flow results

The results obtained for the steady state of the reactive flow in the CFD simulations of the PACT coal combustor are presented in this Section. The CFD

calculations were obtained using a RANS approach for the turbulence modelling and the combustion models introduced in Section 6.2. Furthermore, the predicted species concentrations are compared against experimental data obtained during a test campaign [56]. Different numerical grids have been developed for this particular geometry, with a number of elements ranging from 600000 to 1500000 elements on a quarter of the domain [56], [65]. The implementation of a symmetry boundary condition is not valid in the LES framework, as the turbulent motion is three-dimensional by nature. A three-dimensional mesh consisting in 4331721 hexahedrons was constructed taking into account the element size and distributions employed in similar CFD analyses [68], [315]. Further refinements were made to the mesh; however, the resulting grids contained a number of elements large enough that they were difficult to employ in the computations. In addition, the computer resources available for the calculation of combusting environments were not able to produce the numerical results under a reasonable amount of time.

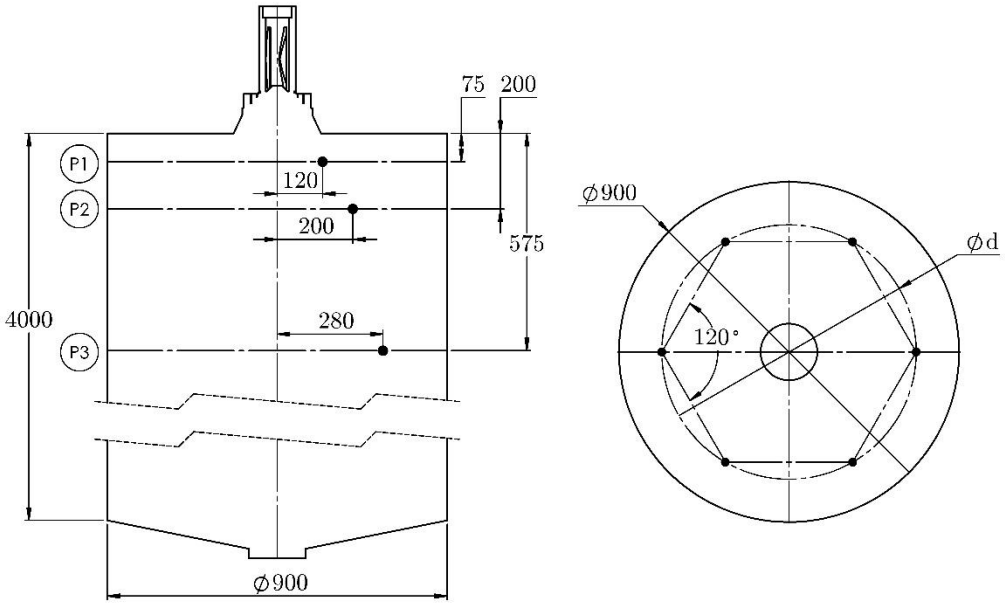

Figure 6.2 Location of the different axial positions and monitor points (represented as black dots) used in the analysis of the temporal coherence in a coal combustor.

The results from the combustion simulations have been evaluated at three different axial positions selected from the domain, being located at 75, 200 and 575 mm measured from the top wall of the combustion chamber. A schematic of the location of the monitors employed in this study is presented in Figure 6.2. Various monitor types have been set at these locations in order to record

the transient behaviour of the flow, and these were used to acquire the data employed in the different analyses performed in this chapter.

The prediction of the distribution of species in the combustion gases showed that the oxygen concentration is well predicted in all of the combustion scenarios at the axial position 1, as shown in Figure 6.3. The location and size of the swirling jet is well defined and the maximum value for the mole fraction was achieved. The prediction for the carbon dioxide concentration was found to be good for the air-fired case, while for the oxyfuel cases a noticeable underprediction was observed. In addition, the carbon monoxide, mostly contained in the internal recirculation zone, was overpredicted for the Oxy30 case, which suggest that the oxyfuel environment delayed the oxidation of CO into CO_2 at the axial position 1.

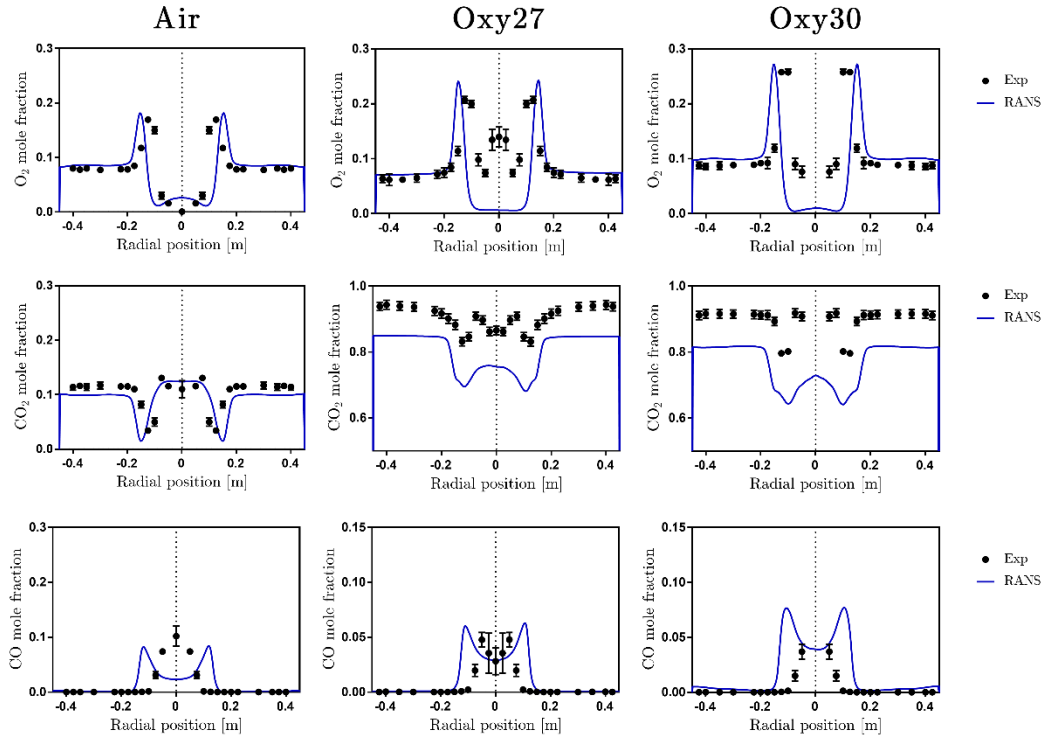

Figure 6.3 Comparison of the predicted gas composition at the axial position 1 against the values measured during the experimental campaign.

Further downstream, at the axial position 2, the prediction of the oxygen concentration was good for the Oxy27 case, as shown in Figure 6.4 . The air-fired and the Oxy30 cases showed a misrepresentation for the location of the maximum oxygen concentration, thus suggesting that the main vortex generated in the flow is captured as a wider structure in comparison to that observed in the experimental results. In addition, the concentrations for the carbon dioxide in

the furnace were better predicted in all cases in comparison to the results obtained at the axial position 1. Nevertheless, the oxyfuel scenarios still under predicted the concentrations measured experimentally, and miscalculations for the position of the low CO_2 regions, in agreement with the predictions of the oxygen concentration, were observed. Furthermore, the mole fraction of CO was found to be lower than the value measured in the experiments for all the cases investigated. The lower values obtained for the carbon monoxide and the carbon dioxide, especially within the central recirculation zone, suggest that the effects of the CO related phenomena, such as the char gasification reaction and the dissociation of the CO_2, that were not included in this analysis may influence in this estimation [56].

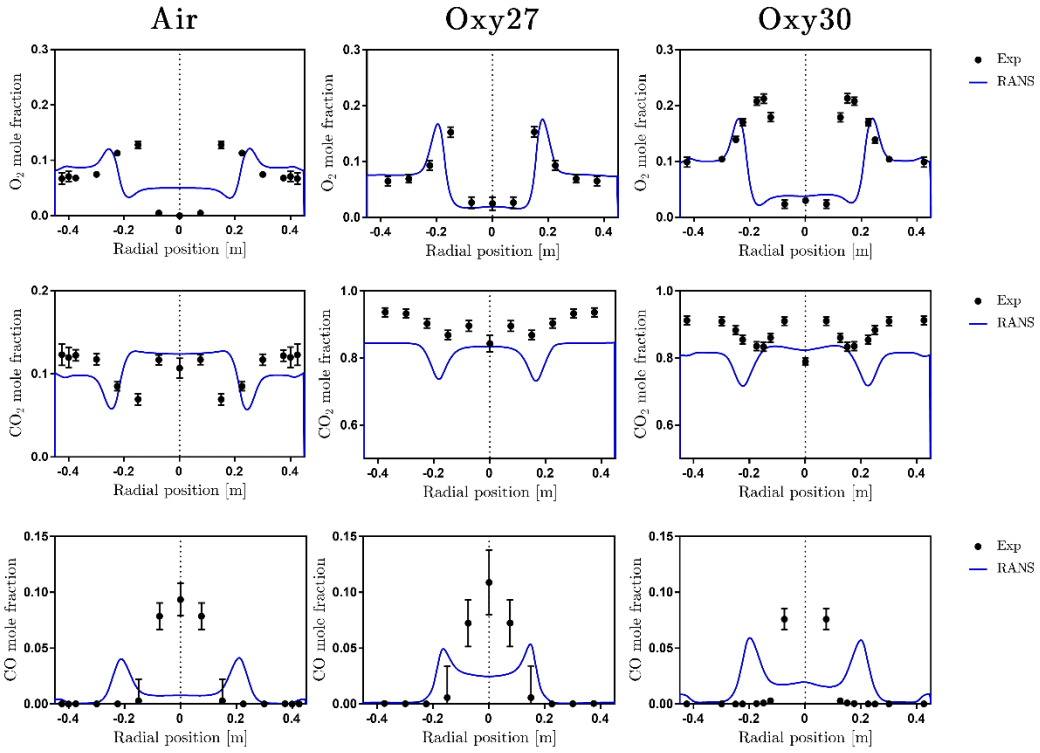

Figure 6.4 Comparison of the gas composition predicted by the RANS computations against the experimental values at the axial position 2.

The results generated for the axial position 3, presented in Figure 6.5, showed that the main vortical entity is vanished for the air-fired and the Oxy30 cases. The profile for the oxygen concentration in the Oxy27 case showed a remnant of the central recirculation zone, thus indicating that the flame in this case is longer than in the other cases analysed. Moreover, the concentration profiles predicted in the CFD calculations for the CO_2 and the CO are lower than the

values measured in the experimental campaign and they appear to be mostly flattened. It appears that the overall mixing of the flow is overpredicted when employing the RANS methodology, thus showing similar behaviour to what was observed for the isothermal swirling flow apparatus in Chapter 5.

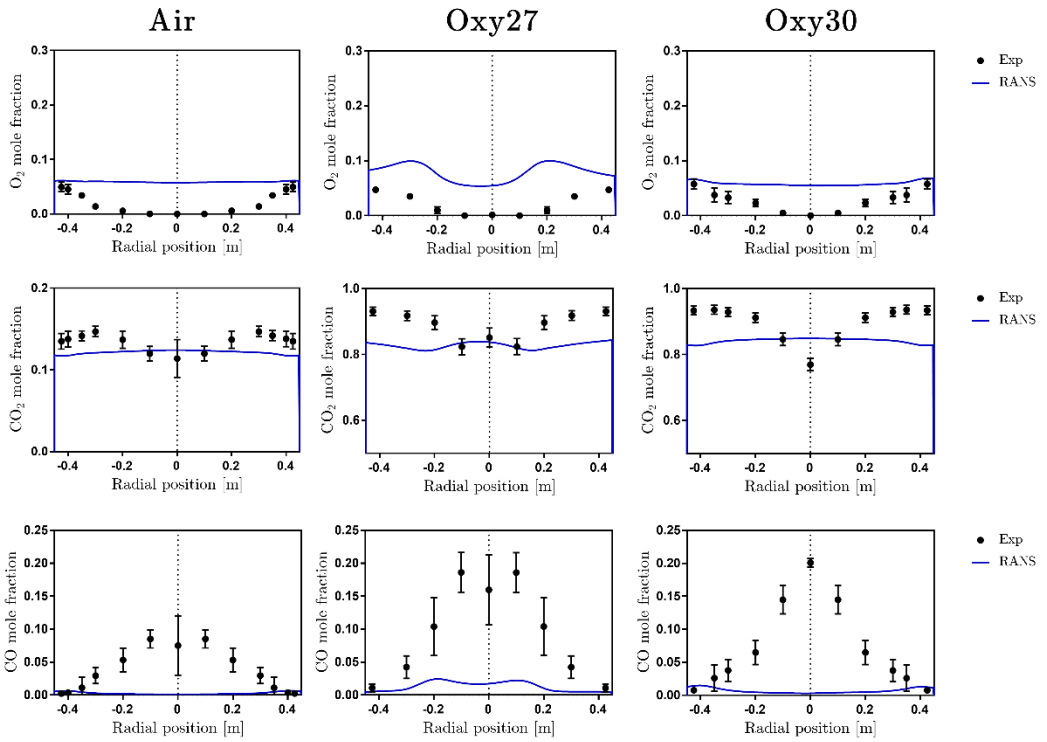

Figure 6.5 Comparison of the distribution of species predicted by the RANS computations of the coal combustor against the experimental measurements obtained at the axial position 3.

The temperature distribution, introduced in Figure 6.6, shows that the flame shape is similar for the air-fired and the Oxy30 cases, where the main vortex generated by the swirling streams from the burner appears to be wider and two separate hot regions are distinguished in the internal shear layer of the vortex. In contrast, the central recirculation zone is shortened for the Oxy27 case and the swirling streams showed to be lightly separated. Furthermore, the tighter central recirculation zone in the Oxy27 case, appears to influence the flame shape, as this appears to be clustered in the central region of the furnace. The contour plots for the axial velocity, presented in Figure 6.6, shows the same trend as in the temperature predictions, with the air and the Oxy30 cases producing similar distributions. However, the range of velocities was larger for the air case both for the inlet streams and for the recirculation zones. The outer recirculation zone in the Oxy27 case was estimated to be longer, with a lower value for its maximum recirculating velocity.

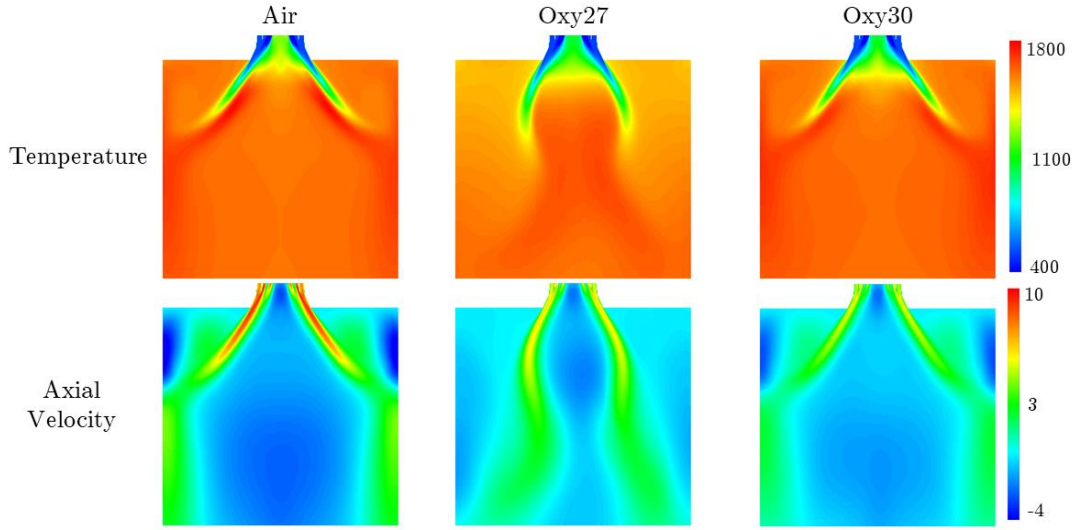

Figure 6.6 Contours of the temperature [K] and axial velocity [m/s] distributions predicted by steady state CFD computations for the coal combustion under air and oxyfuel conditions.

The CFD results produced for steady-state of the reactive flow shows that the overall flow and temperature distributions under air combustion found their equivalent for the oxyfuel environment in the Oxy30 case and this agrees with the findings of the flame imaging campaign discussed in Chapter 4. In contrast, the behaviour exhibited by the Oxy27 case suggest that the flame aerodynamics was compromised for this condition and thus the shape of the recirculation zones suffered changes. In addition, the numerical stability of the solution for the Oxy27 case is lower, as the number of iterations required to achieve convergence was three times larger than those required for the remaining cases. Nevertheless, the difference in the species concentrations shows similar trends for both oxyfuel scenarios, thus suggesting the effect of the modified velocity profile in the coal combustion rate was relatively low.

The purpose of this chapter is to assess the stability of the coal combustor in terms of the spatiotemporal coherence of the flow produced, and to evaluate the effects of the oxyfuel conditions into the flow distribution. For this reason, the air combustion case and the Oxy27 case have been selected to compute LES of their flow conditions, as it is in this oxyfuel case where the most significant changes in the aerodynamics were observed. The LES in the reactive cases require the inclusion of more realistic physics into the particle tracking model. The discrete random walk approach, which produces a satisfactory turbulent dispersion of the particles in the RANS calculations, increases signifi-

cantly the computational power required for the analysis, thus making its implementation not practical. A transient approach for the particle tracking is desirable, as the particle velocity and position directly depends on the flow field. However, in order to increase the accuracy of the particle motion, the effect of the additional forces, such as the drag, lift and thermophoretic force, in the particle paths and distributions must be evaluated and, if required, included in the corresponding model. Furthermore, the algorithm employed in the CFD for the injection of the particles into the domain is often based on the distribution of the elements in the mesh and does not contain temporal variations in the mass flow and particle size distribution. The LES for the reactive cases were set as part of this study, however they showed to be complicate to manage and, due to the size of the domain and the complexity of the physics involved, exhibited large computation times for the high-performance computing facilities available. Different methodologies, in addition to computational subroutines, were developed and tested in order to reduce the computational costs of the reactive LES. Nevertheless, the reductions achieved in the computing time were still insufficient to produce the results under a reasonable amount of time. Therefore, the assessment of the spatiotemporal coherence of the combustor was performed using the results from the isothermal LES of the fluid, in which the inlet mass flow for each case was retained, but the temperature was assumed to be 300 K. The effect of the flame in the overall flow distribution is discussed in the next section.

6.4. Transient results

The analysis of the coherence in a coal combustor requires the acquisition of transient data, and for this purpose, LES have been performed for the air and Oxy27 flow conditions. The Sigma model [122] was employed for the calculation of the SGS stresses, as it allows a better prediction for the development of the flow structures, as observed in Chapter 5. The spectral synthesizer [134] with 250 Fourier modes was employed as a perturbation mechanism for the inlet flow in both cases. A fixed time-step of 5×10^{-4} s was employed for the LES, and the frequency of sampling was every two time steps. The total time of the simulation was at least 12 seconds, and the data employed in the analysis of the spatiotemporal coherence contained the results of 1 second of the flow.

The variations in the field scalars were recorded through a series of monitors of different types that were located at different positions in the domain, as shown in Figure 6.2. The monitor points were placed so they are contained in the vortex observed in the steady state of the air-fired case. These monitors

registered the oscillations in the axial velocity, thus producing temporal signals that later were used as input in the evaluation of the temporal coherence in the flow. In addition, transient snapshots of the flow were generated at the same axial positions as the point monitors for consistency in the analyses. In addition, the cross-section plane of the domain was used to record the velocity vectors in order to analyse the development and displacement of the flow structures in the axial direction. The snapshots recorded consisted in the three velocity components, assuming the Cartesian coordinate system, and the vorticity magnitude. The addition of the vorticity magnitude in the snapshots was intended in order to incorporate the rotational tendency of the continuum, and the associated effects of this motion into the flow structures, into the estimation of the coherence. Moreover, the qualitative assessment of the flow arrangement was performed by employing the three-dimensional results of the calculations.

The flow field depicted by the flame imaging showed that the vortex structure remains strong in the upper part of the furnace and that the flame produced is well anchored to the burner tip. Furthermore, no evident signs of large flow instabilities, such as a single precessing vortex core or the vortex breakdown, were noticed, instead a continuous region of symmetrical spiralling fluid was observed.

6.4.1. Aerodynamics and vortex identification

The profiles for the axial velocities, introduced in Figure 6.7, shows that the flow produced similar distributions in all cases in the near burner region, with the major differences being the values for the flow velocity in the recirculating regions. Further downstream at the axial position 2, the effect of the flame was noticeable as the reactive cases produced wider swirling streams. Moreover, the oxy fuel environment produced an elongation of the vortex, while in the isothermal case this effect was marginal. In addition, the profile obtained for the third axial position showed that, in the LES the mixing of the flow is faster than in the RANS cases. Furthermore, the presence of the flame and it associated phenomena, such as the variations in the fluid density, will influence the extension of the main vortex array. However, despite the differences observed between the aerodynamics of the reactive and the isothermal cases downstream of the combustor, the upper region of the furnace produced similar distributions. The stability of the flame rely directly on the capability to produce a flow arrangement that is capable of sustaining and promoting the combustion reaction, phenomena that occurs in the vicinity of the burner, thus making the

study of the coherence in the flow arrangement, even under isothermal conditions, paramount to guarantee an efficient operation of the system.

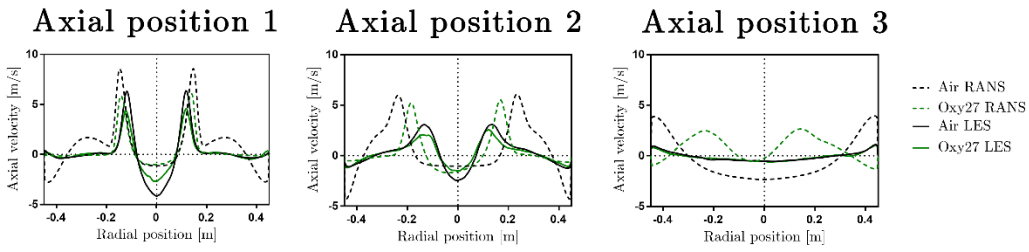

Figure 6.7 Comparison of the axial velocity distribution for the reactive RANS calculations and the isothermal LES.

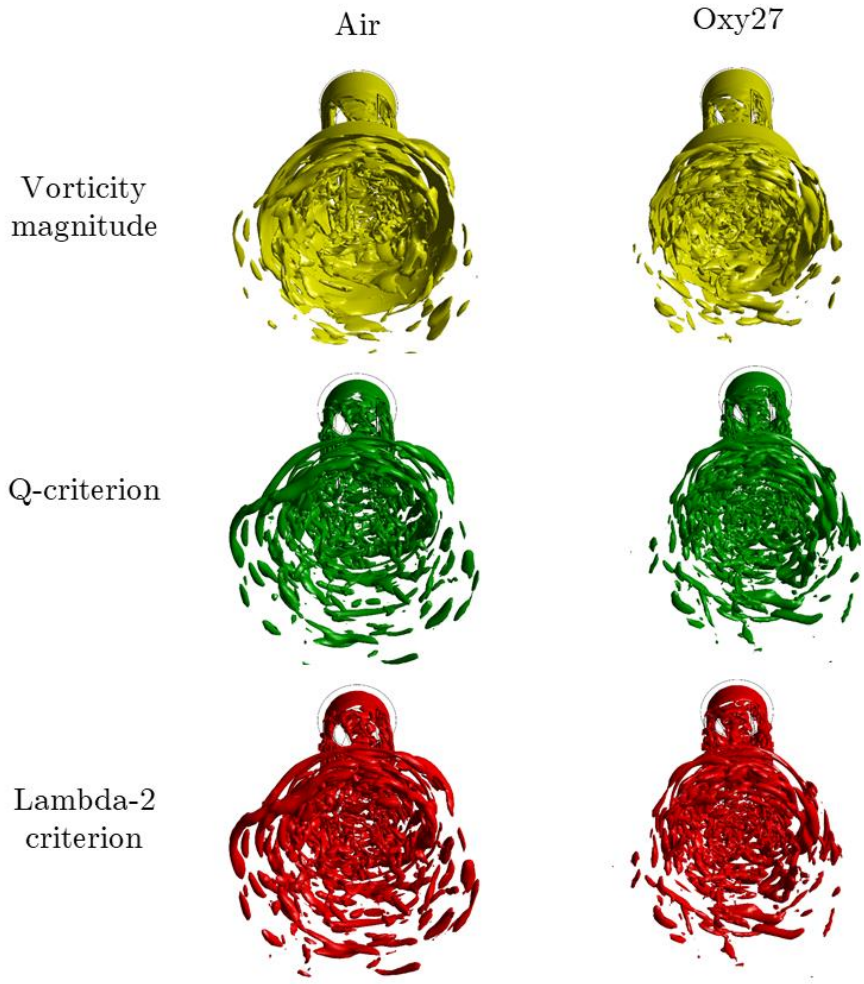

Figure 6.8 Isosurfacces for the vorticity magnitude, Q criterion and Lambda-2 criterion employed as vortex core detection mechanisms in the flow of a coal combustor.

In addition to the velocity distributions previously introduced, the presence of the turbulent structures have been assessed. The difference in the working fluid and size of the domain suggest that, despite being a swirling flow, the flow structures will differ from those observed in Chapter 5. The presence of vorticity and a Galilean invariant geometry have been assumed to be determinant in the detection of a vortex core region [342], [343]. For this purpose, three different numerical approaches, which are based on these flow characteristics, have been employed. The vortex detection schemes employed are the vorticity magnitude, the Q-criterion and the Lambda-2 criterion [342], [343]. A series of isosurfaces were plot using a constant value for each of the vortex detection criteria and these are shown in Figure 6.8. Different values for these criteria were tested in order to produce a clear representation of the developed structures in the region close to the burner and the 10% of the maximum value for the vorticity and 15% of the maximum value for the Q and Lambda-2 criteria were found to be adequate, and therefore were used in this study.

The structures found that the flow shows to be more cohesive than those observed for the swirling flow apparatus analysed in Chapter 5. The size of the structures appear to be larger as they move away from the axis of the furnace. In addition, a good arrangement around the axis was observed for all the structures, thus indicating the swirling nature of the flow. Furthermore, a cluster of small structures in the shape of filaments was produced inside the quarl, and these appear to collide and eventually grow into the bigger structures captured downstream. The effect of mixing in the quarl produce the appearance of a single layer of structures, which contrast with the vortex dynamics studied in Chapter 5. Nevertheless, the dampening effect in the large structures is evident, as these were not noticeable in the vortex core detection mechanisms employed. The qualitative assessment of the flow structure indicates that the flow is well arranged in the near-burner region and, as it progresses downstream, later becomes more unsettled. The appearance of large structures in the flow may induce instability to the process. However, since they are discontinuous and appeared to be scattered in the domain where their influence in the anchoring of the flame and the ignition of the coal particles, processes that occur near the burner, is expected to remain low.

6.4.2. Temporal coherence analysis

Swirling flows are used in combustors to increase the mixing rate of the reactants and to promote stability in the flame. The characterisation of the turbulent structures contained in a swirling flow is paramount to anticipate possible

sources of instability in the system [74]. However, the lack of temporal information, associated to the qualitative methodologies employed in the previous section, complicates the analysis of the vortex dynamics and impede an accurate prediction of their transient behaviour.

In this section, the temporal coherence of the flow produced in the coal combustor for the air-fired and Oxy27 inlet conditions is assessed. The instantaneous variations of the axial velocity were recorded at 18 monitor points that were placed in the furnace domain. The monitor points were divided into groups of six and each group was located at different axial positions. The axial positions employed in this analysis are 75, 200 and 575 mm from the top wall of the furnace. Each set of monitor points were evenly distributed in the planar location, thus forming a perfect hexagon. The circumscribing circle of the hexagon have a diameter d, which was modified for each position so the monitors are located within the swirling stream predicted by the previous RANS calculations.

The instantaneous value for the axial velocity was recorded simultaneously at all monitor points using a sample speed of 1×10^{-3} s, which is every two timesteps of the LES computation. The length of the transient records was set to 1000 samples, thus corresponding to 1 s of the flow time. Spectral analyses were performed to the transient signals in order to obtain the spectrum frequencies that describes the temporal repeatability of the flow oscillations [344]. Furthermore, cross-correlations of the signals at consecutive points were calculated as a representation for the similarity exhibited by the velocity trends and their interdependence in time. The values for the PSD and the cross-correlation coefficient were normalised in order to allow direct comparisons among the results obtained at different locations. The plots of the frequency spectrums are presented up to a frequency of 500 Hz for a better interpretation. However, the spectral analysis calculations were made for the full spectrum which contains a Nyquist frequency of 1 kHz. In addition, the cross-correlations were calculated using the total length of the signal without a prescribed overlapping limit, thus producing values for a maximum lag of $\pm$ 1 s.

6.4.2.1. Axial position 1

The spectrum of frequencies obtained for the air conditions, presented in Figure 6.9, shows that the most relevant oscillations occur at the low end of the spectrum. The principal frequency band were contained below the 50 Hz mark for all of the monitors, with additional frequency components scattered below 100

Hz. The values for the weighted frequency were averaged at 54 Hz, with a standard deviation of 4 Hz. The narrow range in the values of the weighted frequency suggests that the flow contains a characteristic oscillation at this position. Furthermore, the perturbation algorithm employed at the inlet may influence the appearance of several relevant frequencies in the low range of the spectrum. However, the severity of their effect was considerably lower than what it was observed for the axial positions closer to the origin of the vortex discussed in Chapter 5.

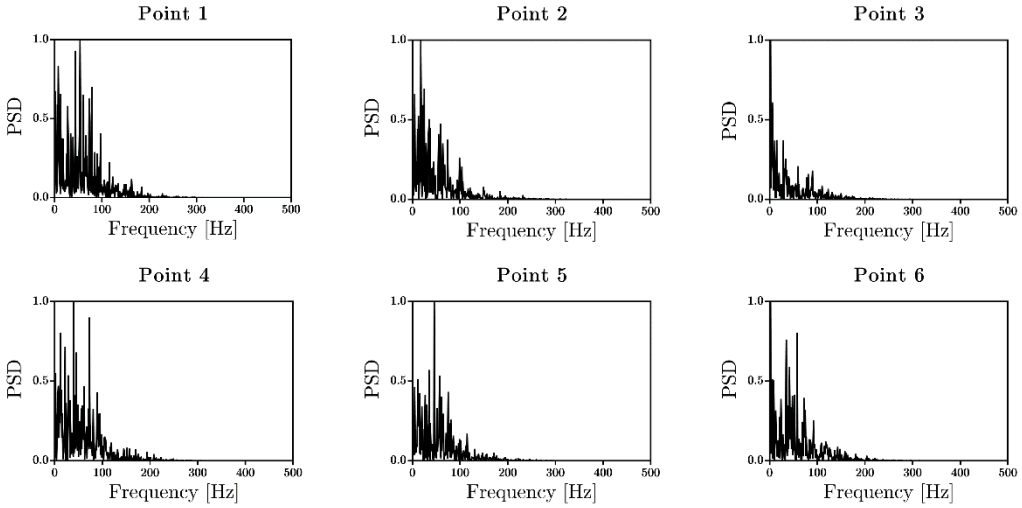

Figure 6.9 Frequency spectrums obtained for the transient data recorded at the axial position 1 using the air conditions.

The cross-correlations calculated for the air flow condition shows that, despite the similitudes in the frequency spectrums, the velocity oscillations perceived at the monitor points are misaligned. In addition, it was observed that the cross-correlations involving point 6 contained the lower level of the arrangement, as they are found to be out of synchrony with its neighbouring monitors, as shown in Figure 6.10. The large discrepancies in the cross-correlation may be evidence of the displacement of the large flow structures observed in the detection of the vortex core. The remaining points appear to have more interdependence, however the arrangement of the flow is depicted as being chaotic.

The spectral analysis for the transient data of the Oxy27 flow conditions produced cleaner frequency spectrums, with the majority of the relevant frequency bands clustered in the low frequency range, as shown in Figure 6.11. Furthermore, the weighted frequencies averaged 43 Hz and contained a standard deviation of 2 Hz, thus suggesting slower flow oscillations in comparison to the measurements for the air condition.

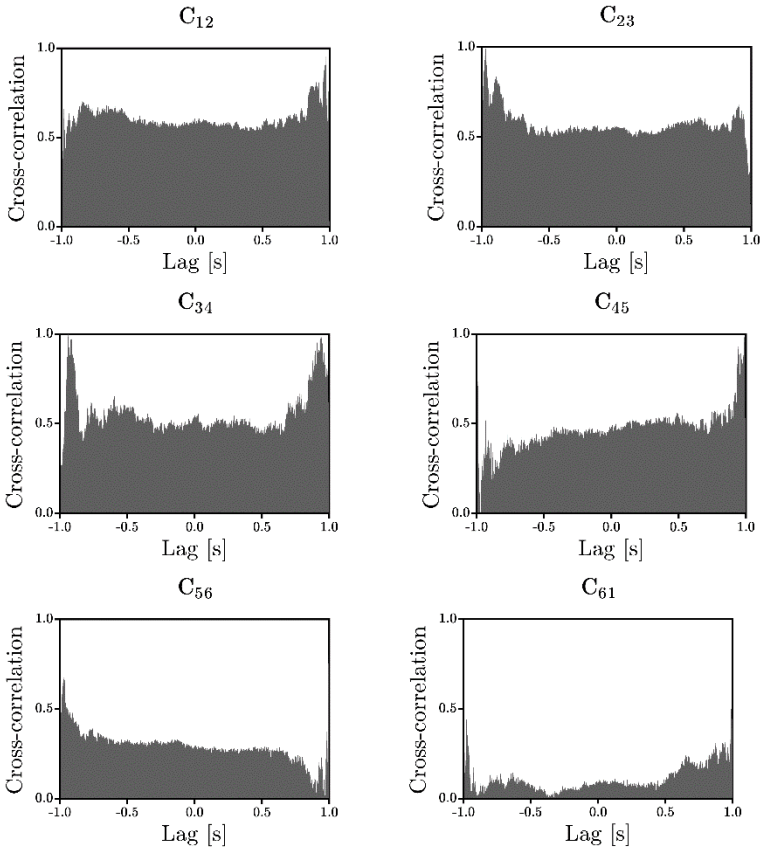

Figure 6.10 Cross-correlations for the transient signals generated by the fluctuations of the axial velocity for the air case at the axial position 1.

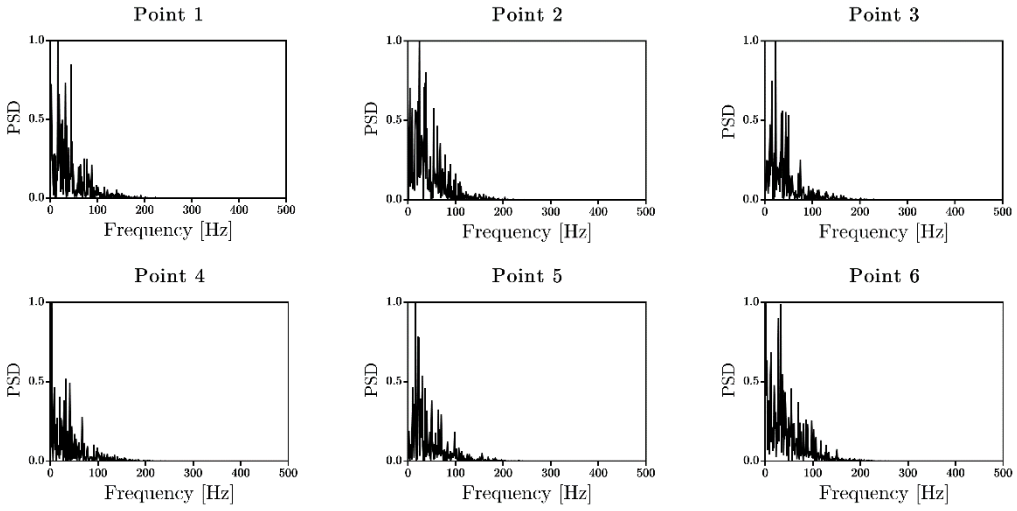

Figure 6.11 Spectrum of frequencies produced by the velocity fluctuations observed for the Oxy27 case at the axial position 1.

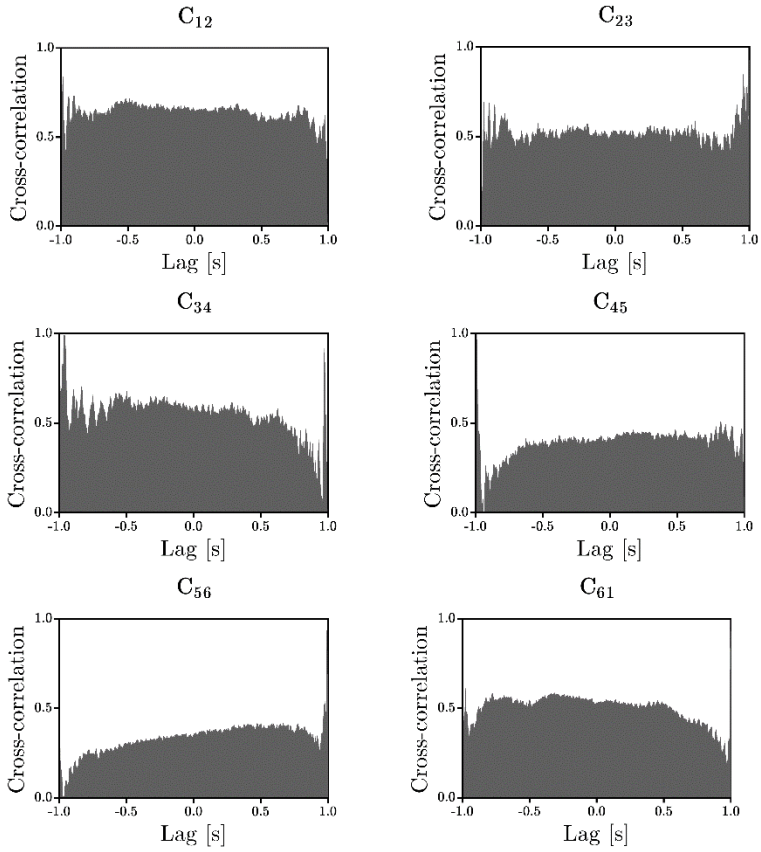

Figure 6.12 Cross-correlations for the transient signals obtained for the Oxy27 flow conditions at the axial position 1.

The cross-correlations obtained for the signals produced by the axial velocity fluctuations at the axial position 1, presented in Figure 6.12, shows that large misalignments occur for the locations in the vicinity of point 6. In contrast, the flow appeared to be more arranged for the point 2 and its neighbouring locations, thus producing lager values for the correlation across the entire lag range. The remaining monitor points produced transient signals whose misalignments remained relatively constant across the calculated lag. The presence of regions of higher and low correlation at the same axial location may be a consequence of the emergence of coherent structures at these locations, or due to the production of an asymmetrical flow distribution. Nevertheless, the overall transient behaviour of the flow suggests that, despite the existence of misalignments in the flow oscillations, a temporal repeatability is discernible and therefore the flow arrangement can be considered to be coherent. The generation of a temporal coherent flow, especially in the near-burner region is paramount to ensure the stability of the flame, and for the conditions analysed it can be concluded that for the combustor analysed this condition was enhanced.

6.4.2.2. Axial position 2

The spectrums of frequencies computed for the velocity fluctuations captured by the monitor points at the axial position 2 in the air case showed less relevant frequency bands, thus exhibiting sharper trends. The weighted oscillations frequencies averaged a value of 17 Hz and a standard deviation of 3 Hz. The frequency spectrum computed for point 6, presented in Figure 6.13, shows a slightly large number of relevant frequencies, however these were found to be lower than the predominant band, thus suggesting that the inlet perturbations did not contribute to them.

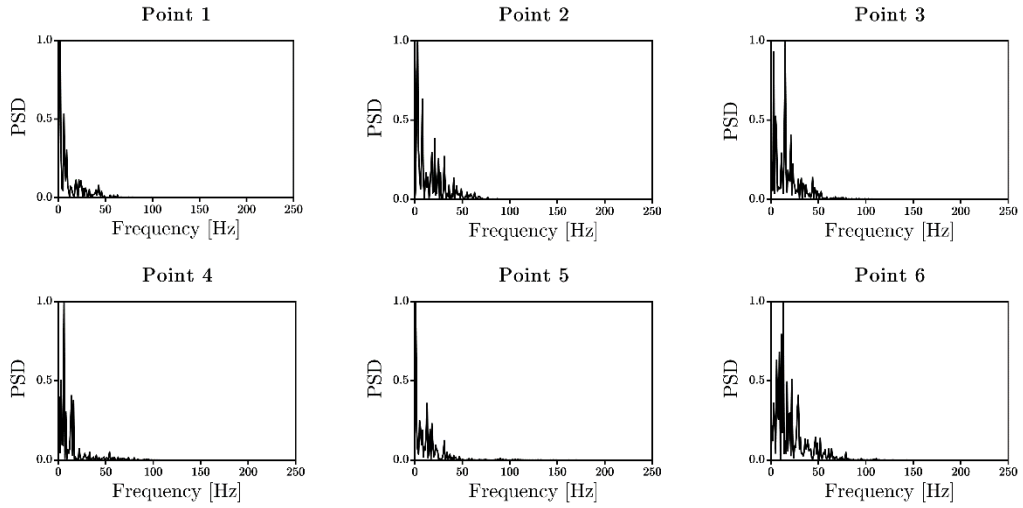

Figure 6.13 Frequency spectrums obtained for the axial velocity fluctuations in the air conditions recorded at the axial position 2.

The level of interdependence in the flow, computed by the cross-correlations of the signals produced by the LES of the air case, appears to increase at this position 2, as shown in Figure 6.14. The trend shows that the region comprising points 6, 1 and 2 have the largest coherence at this location. In contrast, the correlations involving point 4 are found to be less strong for the majority of the computed signal shift. Despite the higher value for the cross-correlations, the flow arrangement is still perceived as being disorganised, as no noticeable pattern is recognised.

The frequency spectrums obtained for the Oxy27 flow conditions at the second axial positon, presented in Figure 6.15, shows a trend similar to the air case, with a sharper spectrum and lower number of relevant frequency bands. The average weighted frequency was 13 Hz and the standard deviation was calculated at 2 Hz, values that are in agreement with the results at the axial position 1 and shows a lower oscillation frequency for the Oxy27 case.

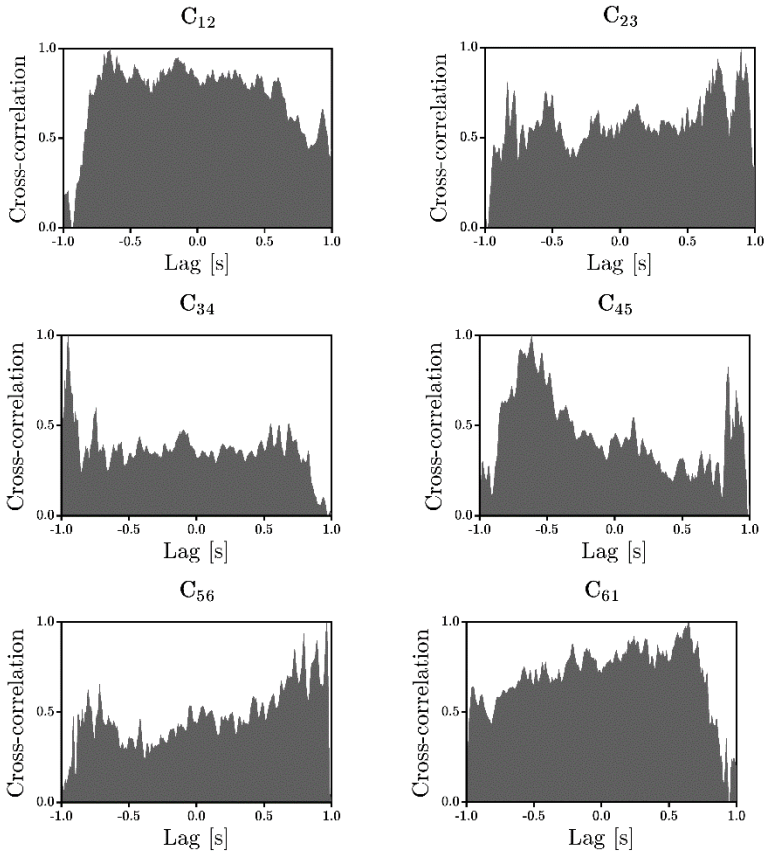

Figure 6.14 Cross-correlations computed for the transient variations in the axial velocity obtained for the air case at the axial position 2.

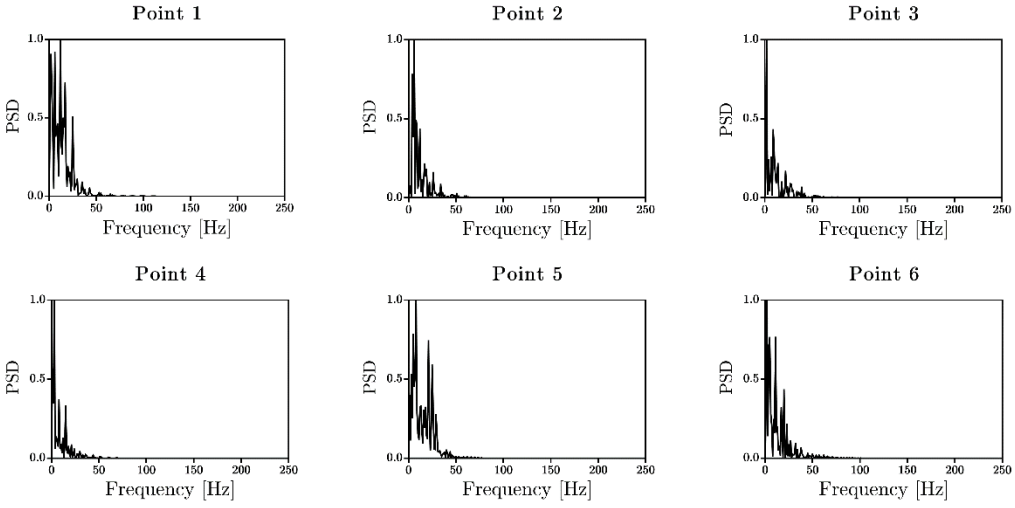

Figure 6.15 Spectrum of frequencies obtained for the transient data produced by the monitor points at the axial position 2 in the Oxy 27 case.

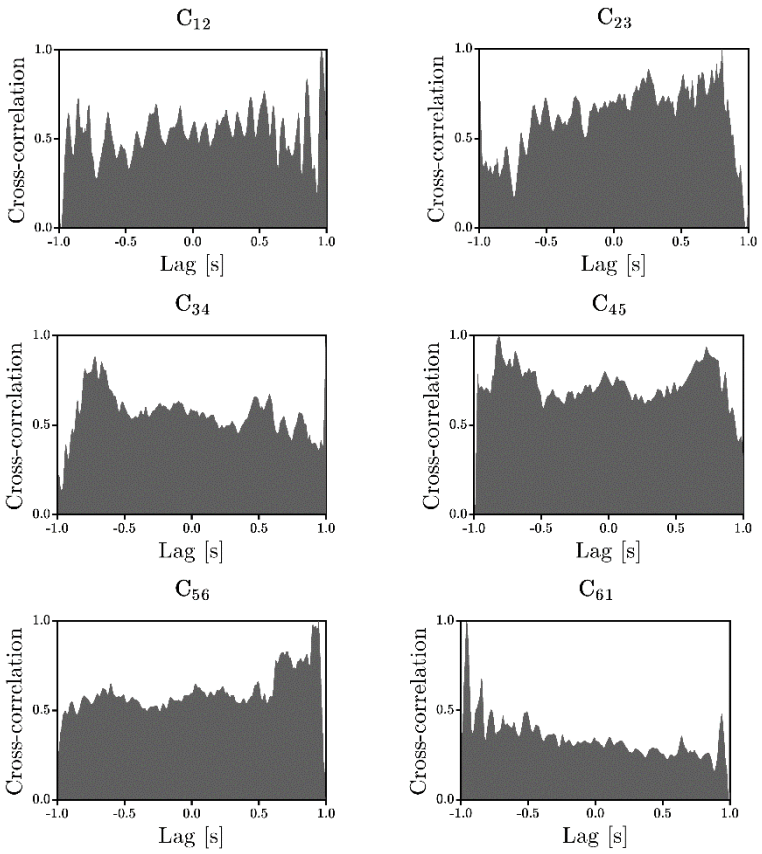

Figure 6.16 Cross-correlations calculated for the transient signals gathered at the axial position 2 in the LES for the flow in the coal combustor under Oxy27 conditions.

The cross-correlations computed for the Oxy27 shows that the monitor point 1 produced the largest misalignments at the axial position 2. The remaining monitors produced cross-correlations of opposite trends, most notably for C_{23}, C_{34} and C_{56}, thus suggesting periodicity in the signals. The presence of periodicity in the transient signals, as shown in Figure 6.16, suggests that the turbulent structures that produce the fluctuations in the axial velocity contain rotation around the geometric centre of the furnace.

6.4.2.3. Axial position 3

The oscillatory frequencies produced by the transient signals of the axial velocity in the air case at the axial position 3, presented in Figure 6.17, shows a noticeable reduction in the number of relevant bands. A single predominant frequency was observed for all the monitor points, and this agrees with the findings of Chapters 4 and 5, where a single frequency was found to be associated to the motion of the fully developed swirling flow. The weighted frequencies obtained for the air conditions at this position averaged 5 Hz and the standard deviation was estimated at 0.7 Hz, thus suggesting that the flow

oscillation is clearly distinguished at this value. Furthermore, the maximum contribution to the PSD in the frequency spectrum was produced in the bands 1 to 3 Hz, a range that is conformal to the values obtained for the oscillations in the perceived luminance and temperature obtained for the flame imaging campaign in Chapter 4.

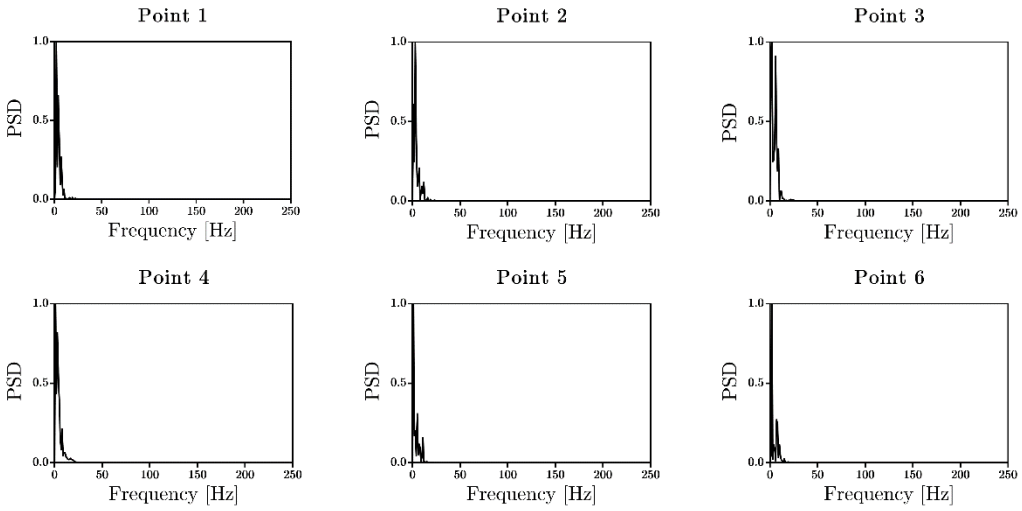

Figure 6.17 Frequency spectrums obtained for the fluctuations of the axial velocity for the air case at the axial position 3.

The results obtained for the cross-correlations of the transient signals of the velocity fluctuations for the air case show, for the axial position 3, that one third of the domain exhibits a large degree of interdependence, while the remaining space appears to be disorganised. The region in-between points 3, 4 and 5 show good correlation in their oscillations, with the misalignments occurring at the sides of the lag axis, as shown in Figure 6.18. The difference observed in the trends for the cross-correlation suggests the appearance of coherent structures in the flow and that these are only contained in a prescribed region of the domain.

The frequency spectrums calculated for the Oxy27 case shows a singular dominant frequency for all the monitor points, with no additional contributions to the PSD from frequencies beyond 15 Hz. The average oscillation frequency was calculated at 4 Hz and the standard deviation was estimated at merely 1 Hz. The prediction of a tight range of oscillation frequencies suggest that as the flow mixing occurs, the oscillations in the main vortex of the flow equilibrate, thus producing sharp frequency spectrums, which improves their pertinence in the characterisation of the temporal repeatability in the flow.

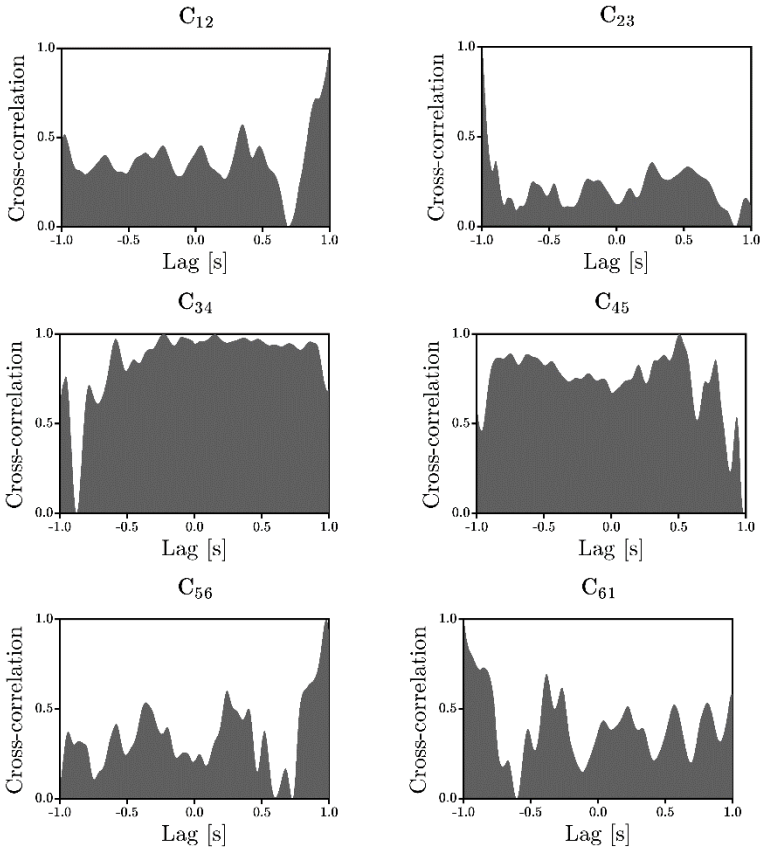

Figure 6.18 Cross-correlations calculated for the transient oscillations in the axial velocity computed for the air case at the axial position 3.

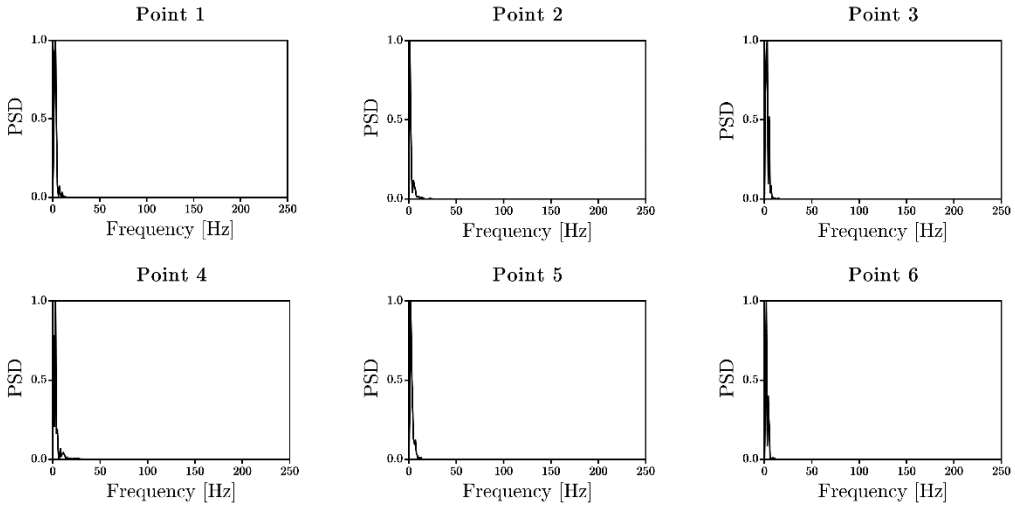

Figure 6.19 Frequency spectrum produced by the transient fluctuations of the axial velocity produced by the LES of the Oxy27 flow conditions and measured at the axial position 3.

The plot for the cross-correlations computed for the temporal signals produced by the variations in the axial velocity show fluctuating trends for all of the monitor points, as shown in Figure 6.20. Furthermore, the oscillations in the signal correlations appear to be repeating themselves at lags of 0.5 s approximately. The appearance of oscillating trends in the cross-correlations suggest that the presence of coherent structures are causing the velocity fluctuations at different monitor points as they rotate around the centre of the furnace. In addition, the range perceived in the cross-correlation plots show that the flow structure is well defined, with no spurious axial velocity fluctuations that could modify the trend observed.

The results produced by the spectral analysis of the transient signals collected from the domain show that the flow is more unsettled for the first axial position, where several frequency bands contributed to the PSD. However, as the flow mixes, a distinguishable frequency of oscillations is perceived for all points, thus representing its temporal coherence.

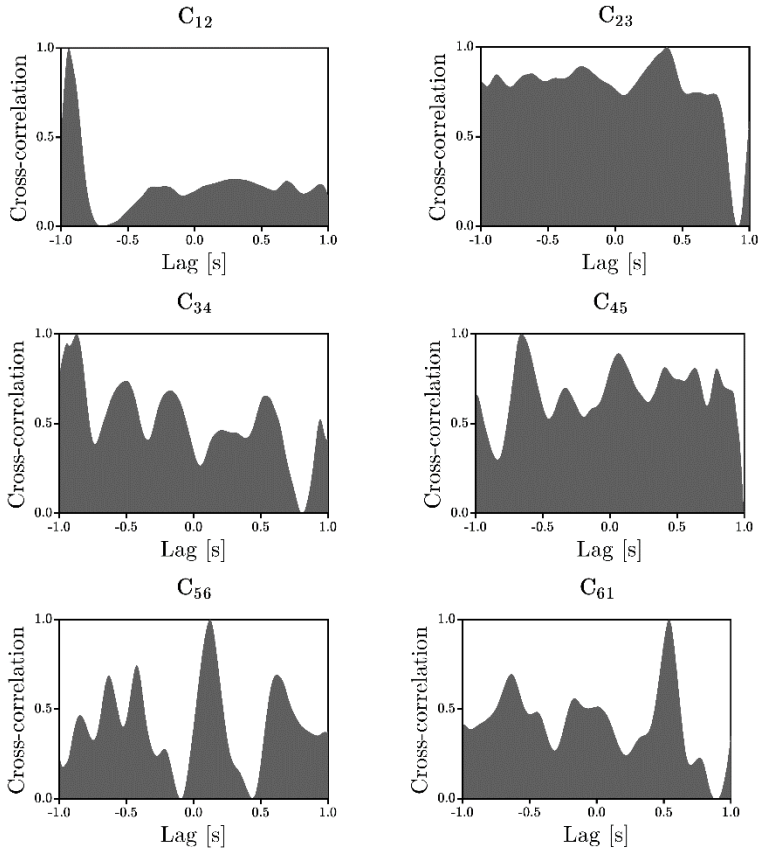

Figure 6.20 The cross-correlations calculated for the transient signals of the axial velocity fluctuations at the axial position 3 in the coal combustor under the Oxy27 conditions.

6.4.3. Spatial coherence analysis

The assessment of the flow dynamics requires a characterisation of the type of flow structures present if the domain, their temporal repeatability and their disposition in space. The POD is a methodology that decompose transient, high-resolution, data obtained from the experiments or produced numerically into a sum of weighted basis functions known as the POD modes. The POD is a linear procedure, thus producing equally linear modes for the assessment of the flow. The linearization of the input data allows the characterisation of the flow field dynamics as an aggregate of the computed POD modes [346], [356]. The predominant flow structures contained in the POD modes are a direct representation of the spatial coherence of the flow and, therefore, a direct representation of the flow arrangement.

A POD analysis was performed on the transient data obtained from the LES of the flow field in the coal combustor. The method of snapshots [254] for the POD was employed, thus requiring the acquisition of the temporal data in the form of matrices. Each snapshot was constructed using the instantaneous values of the flow scalars that were recorded using the coplanar vertices of the mesh at the same axial positions used in the spectral analyses. The snapshots consist of a matrix of size M×N×4, where M and N correspond to the number of locations sampled in the X and Y directions in the Cartesian coordinate system, and 4 represents the number of scalars sampled from the flow. For this analysis, the velocity components in the Cartesian system, namely u, v and w, and the vorticity magnitude where recorded. The inclusion of the axial velocity component, which is aligned in the normal direction of the snapshot, allows the incorporation of the effects of the recirculating regions of the flow into the POD computation. In addition, the vorticity magnitude was added to the sampled scalars in order to include a measure for the local rotation of the flow particles, a quantity that is inherent in the vortex motion of any coherent structure [331]. Nevertheless, the results of the POD analysis are presented in this analysis as vector plots at the prescribed axial positions for a better visualisation of the flow structures. The value for the total energy associated to the POD modes was normalised, and the modes were sorted in a decreasing order in order to assign the first position to the most energetic POD mode. The first six modes for the flow under air and Oxy27 conditions are presented for each axial position. In addition, the POD modes produced at the midplane of the furnace are introduced in order to analyse the dynamics of the flow structures in the axial direction.

6.4.3.1. Axial position 1

The POD modes produced for the data obtained under air conditions at the axial position 1 shows small differences in the amount of energy contained among them. Furthermore, an increase in the number of POD modes required to characterise the flow, as shown in Figure 6.21, was observed. The vector plot produced for the mean velocity value shows a strong swirl motion arranged around the axis of the furnace. The effect of the mesh resolution is observed in the results as a small, dense region of vectors was produced. This mesh-dependant region, however, contains elements that are perfectly aligned with the flow structure. The presence of noticeable shear layers at the interface of the swirling stream and the recirculating zones, as obtained for the swirling flow in Chapter 5, was not observed for this case. In addition, the effects in the flow distribution produced by the different inlet channels of the burner appear to be dispersed, as the flow distribution does not contain any signs of staging.

The analysis of the POD modes produced for the LES results of the air case show that, at the axial position 1, the majority of the structures in the flow are located in the central region of the flow, as shown in Figure 6.22. The predominant structures observed at the POD modes contained recirculation and these are found to be closely distributed in the central region of the domain. Furthermore, the interaction of the recirculating relevant structures produce high-velocity regions in the fluid, which crosses the geometric centre of the furnace in many directions and eventually sustains the overall swirling arrangement of the flow.

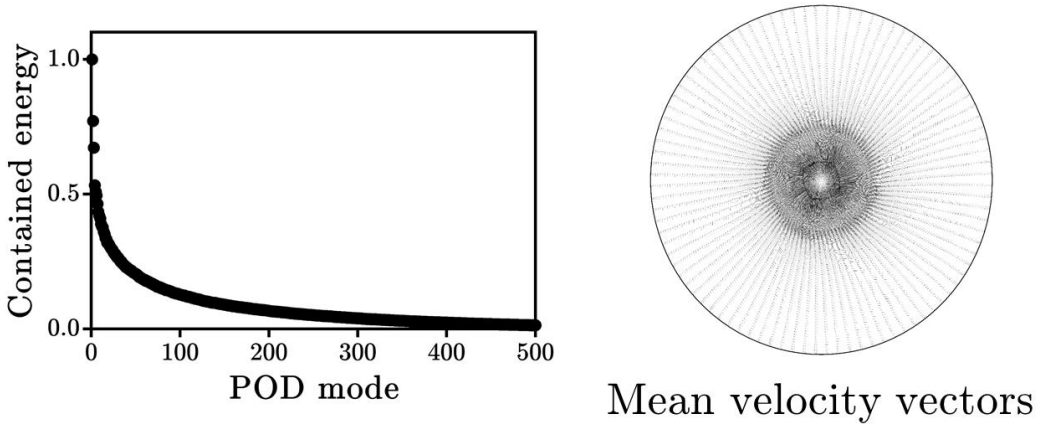

Figure 6.21 Distribution of the energy contained in the POD modes (left) and the vector plot for the mean velocities obtained by the LES for the air conditions at the axial position 1.

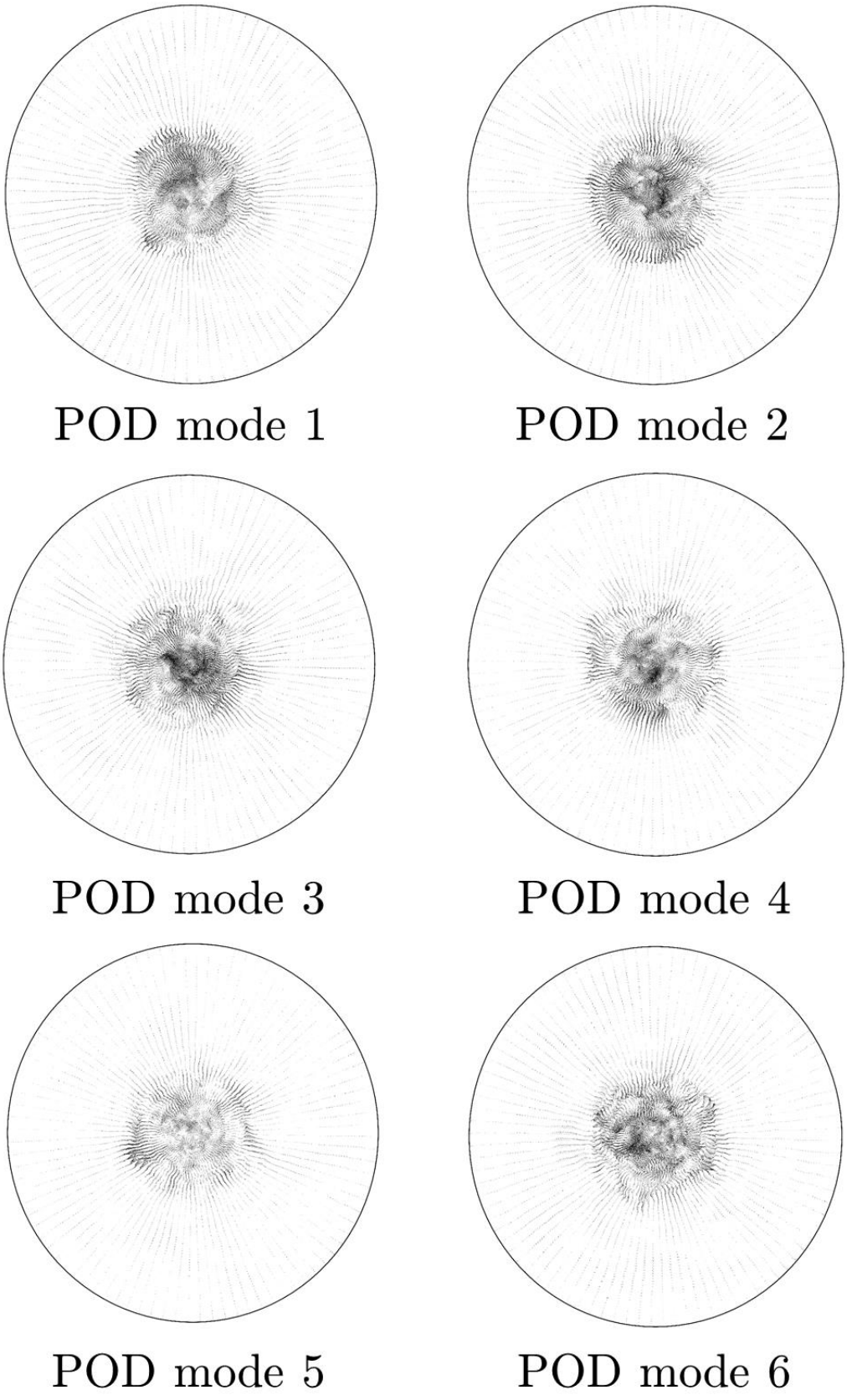

Figure 6.22 POD modes computed for the snapshots produced by the LES for the air case at the axial position 1.

The POD modes calculated for the set of snapshots captured in the LES for the coal combustor under the Oxy27 conditions shows an increase in the contained energy in the first mode, in comparison to the results for the air conditions, as shown in Figure 6.23. The subsequent POD modes are observed to contain lower values of the energy, thus describing them as being similar in their effect on the overall flow distribution. Furthermore, the vector plot of the mean velocity, presented in Figure 6.23, shows a strong swirling arrangement in the flow with a singular centre of rotation being observed. The effect of the mesh resolution produces a small region with a large number of vectors, a pattern that is similar to that obtained for the results of the air case. In addition, the shape of the main swirling structure, depicted as the shaded region, was smaller than in the air case, thus suggesting that the main vortex is narrower.

The assessment of the POD modes obtained from the LES results for the Oxy27 conditions show that the main turbulent structures are contained at the centre of the domain, as shown in figure 6.23. In addition, the coherent structures captured by the POD are shown to contain recirculation. Nevertheless, the number and the intensity of the coherent structures that appear in the POD modes are shown to be lower for the Oxy27 case, in comparison to the flow arrangement obtained for the air conditions. However, their size and distribution appears to be similar to what was observed in the air case. Furthermore, a region of high-intensity and aligned vectors containing the direction of the swirl appears to enclose the recirculating structures in the Oxy27 case, thus suggesting the presence of a shear layer at the interface between the outer recirculating zone and the main vortex structure.

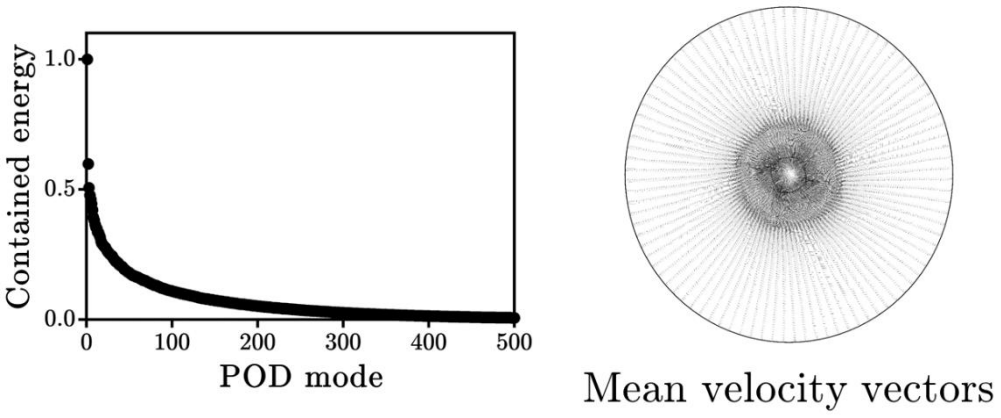

Figure 6.23 Energy distribution in the POD modes (left) and vector plot of the mean velocity (right) computed for the results at the axial position 1 produced by the LES of the Oxy27 flow conditions in the coal combustor.

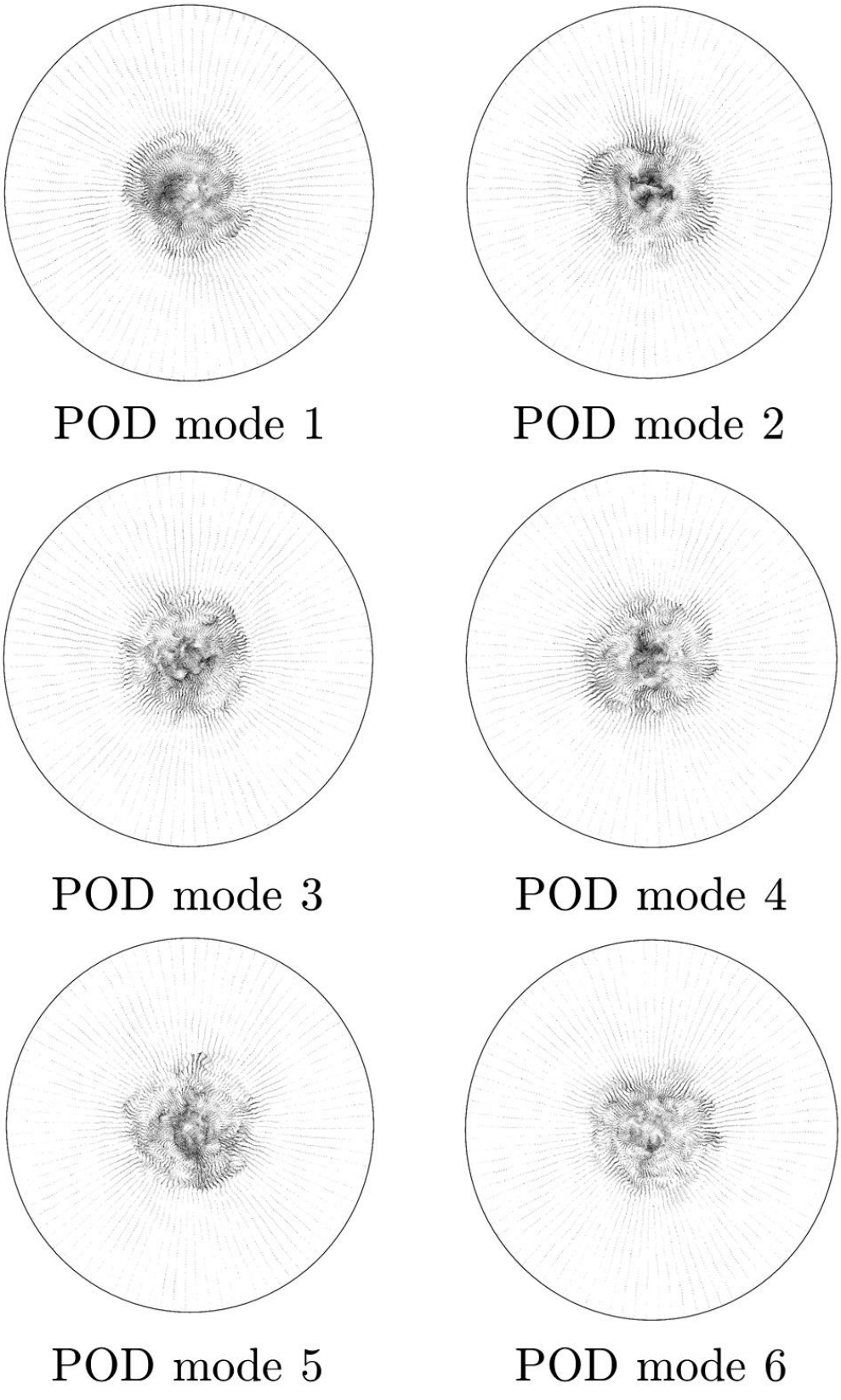

Figure 6.24 POD modes computed for the results obtained at the axial position1 of the LES of the coal combustor under Oxy27 conditions.

6.4.3.2. Axial position 2

The POD analysis performed on the results of the LES for the air condition show an increase in the energy contained in the leading modes computed. The first three POD modes appear as more relevant than the successive modes of oscillation, thus accounting for the disposition of the most relevant flow structures in the domain, as shown in Figure 6.25. The vector plot for the mean velocity values shows that the arrangement of the flow around the furnace axis, a characteristic of the swirling flows, is the predominant flow structure, as shown in Figure 6.25. Furthermore, four regions containing large velocity values, which appear to be located in the same disposition as the coal gutters installed in the primary channel of the burner, were perceived.

The examination of the POD modes obtained for the transient data of the air case, presented in Figure 6.26, shows the appearance of larger coherent structures of a recirculating type that contains an opposing rotation direction. These opposing turbulent structures were more evident for the POD modes 1 and 3, and they are an indicator of precessing vortex core structures [357], [358]. The structures observed in the flow produced by the coal combustor under air conditions are helical filaments that, despite exhibiting precession, are not attached to the burner tip, thus are loosely travelling within the swirling jet. The large filaments occurring in the flow are observed in the isosurfaces produced for the vortex core detection mechanisms in Figure 6.7. However, the presence of a flow arrangement in which two helices are produced simultaneously and strongly interact was not obtained.

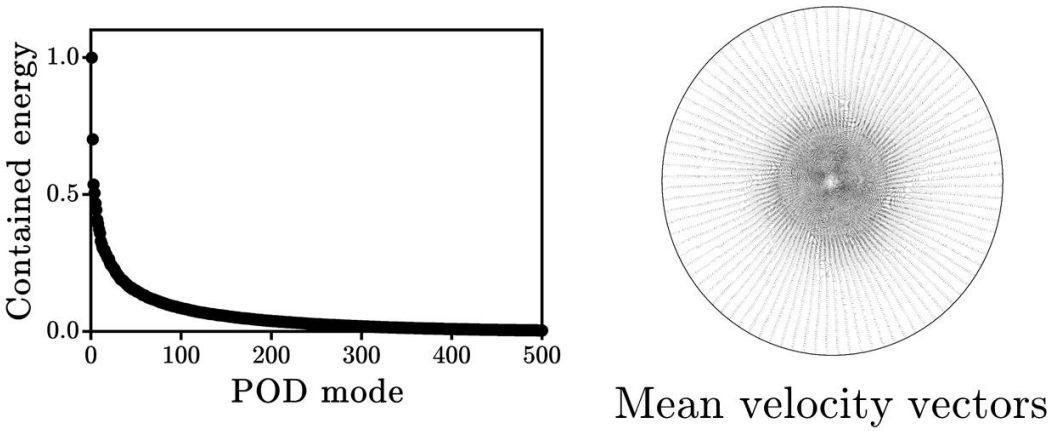

Figure 6.25 Distribution of the energy contained in the POD modes computed for the LES results for the air case at the axial position 2 (left) and the vector plot of the mean velocity values at the same location (right).

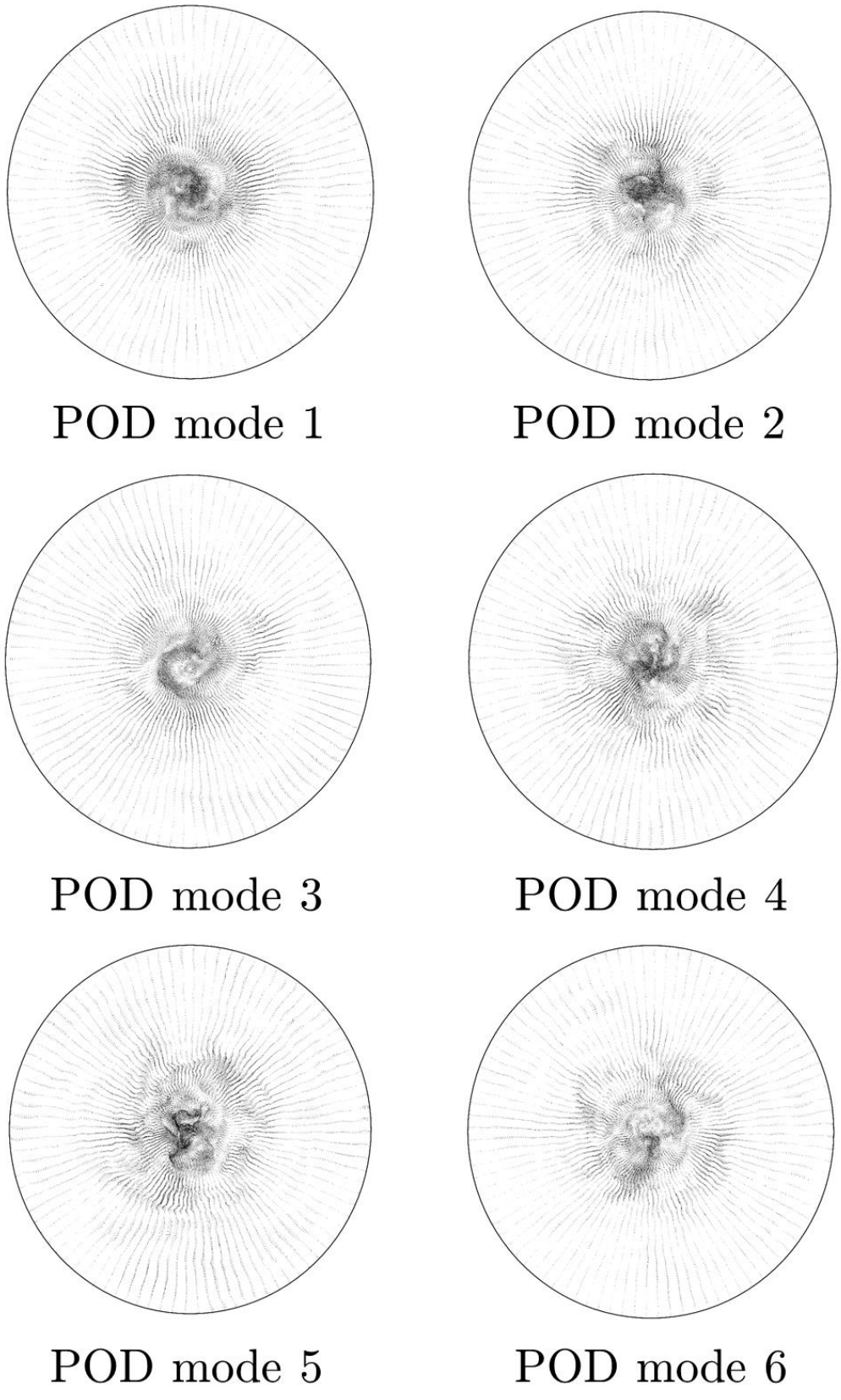

Figure 6.26 POD modes produced for the transient data of the air case at the axial position 2.

The distribution of the energy of the system in the POD modes computed for the snapshots obtained at the axial position 2 of the Oxy27 case shows a decrease in the number of modes that are considered to be relevant. Furthermore, the difference between the energy in the first and the consecutive POD modes was shortened, hence making the subsequent POD modes more relevant in the spatial coherence of the flow. The plot produced for the vector of the main velocity values, presented in Figure 6.27, shows that the swirling motion dominates the flow arrangement. A single centre of rotation was observed for this plot, however the distribution of the vectors near this point shows some minor disruptions in their structures. In addition, the effects of the flow distribution imposed by the gutters installed in the primary flow channel of the burner, as observed in the results for the air case, was not noticeable in the flow under the Oxy27 conditions.

The assessment of the flow distribution produced in the POD modes for the Oxy27 case showed the presence of recirculating turbulent structures, as shown in Figure 6.28. These vortices were observed in the central region of the domain and their intensity was noticed to be higher than for the case under air conditions. In addition, the turbulent structures showed recirculation in opposing directions within the domain, thus producing fluid interfaces where the velocity of the flow is high. The level of vorticity exhibited by the rotating structures was high, as they contained a well-defined centre of rotation. However, they cohesion and their effect on the flow arrangement remains low, as they are depicted in the form of independent structures rather than forming larger vortices, which eventually could compromise the stability of the flow.

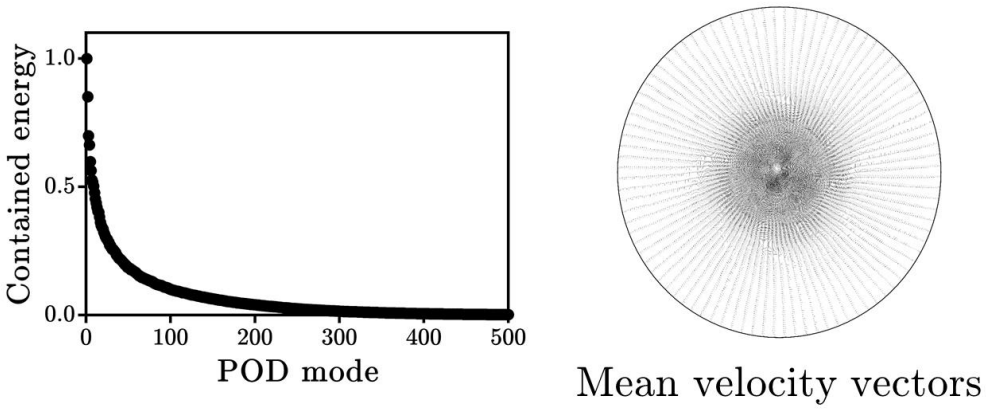

Figure 6.27 Distribution of the energy contained in the POD modes calculated for the results at the axial position 2, produced by the LES for the coal combustor under the Oxy27 flow condition.

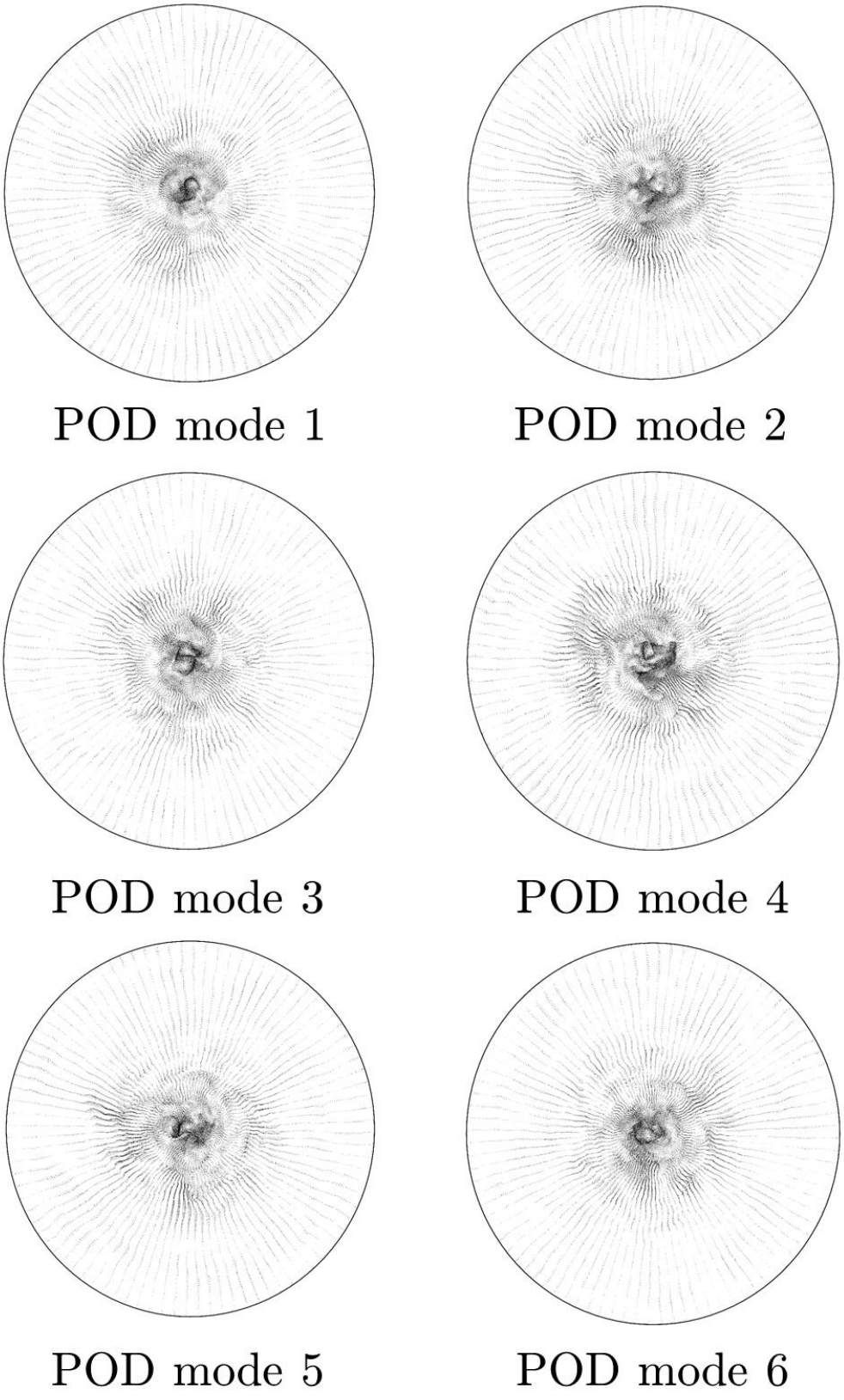

Figure 6.28 POD modes computed for the snapshots captured at the axial position 2 of the coal combustor under the Oxy27 flow conditions.

6.4.3.3. Axial position 3

The results of the POD preformed on the data generated by the LES for the air condition in the coal combustor at the axial position 3 shows, a decay in the number of modes containing a significant part of the energy in the system in comparison to the trends observed for the axial positions 1 and 2. The energy contained in the first five POD modes is significantly larger than the subsequent states, thus increasing their relevance into the flow arrangement, as shown in Figure 6.29. The flow distribution produced by the vector plot of the mean values of the velocity field is tightened around the axis of the furnace, with no traces of disturbances in the arrangement of the vectors.

The assessment of the POD modes produced for the LES of the coal combustor under air conditions, see Figure 6.30, shows flow structures of similar nature to those observed at the axial position 2. The flow structure captured in the POD mode 1, shows a recirculating region close to the geometric centre of the radial cross-section and a series of less energetic swirls that are located around it. The flow distribution for the POD modes 2, 3 and 4 produce a flow arrangement similar to that exhibited at the axial position 2, with two main turbulent structures that recirculate in opposing directions. Furthermore, a region of high velocity was encountered at the centre of the domain, and this is a consequence of the interaction between the two main structures predicted. The flow distribution captured in the POD modes 5 and 6 contains a larger number of turbulent structures with a predominant vortex at the centre of the plot, while the remaining vortical entities are scattered throughout the entire domain of the flow.

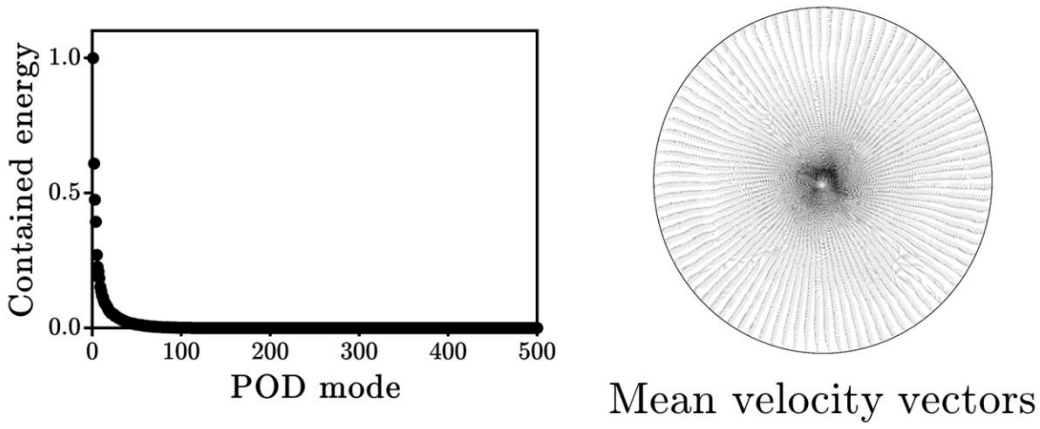

Figure 6.29 Distribution of the energy in the POD modes calculated for the LES results for the air conditions (left) and the vector plot for the mean velocity components obtained at the axial position 3 (right).

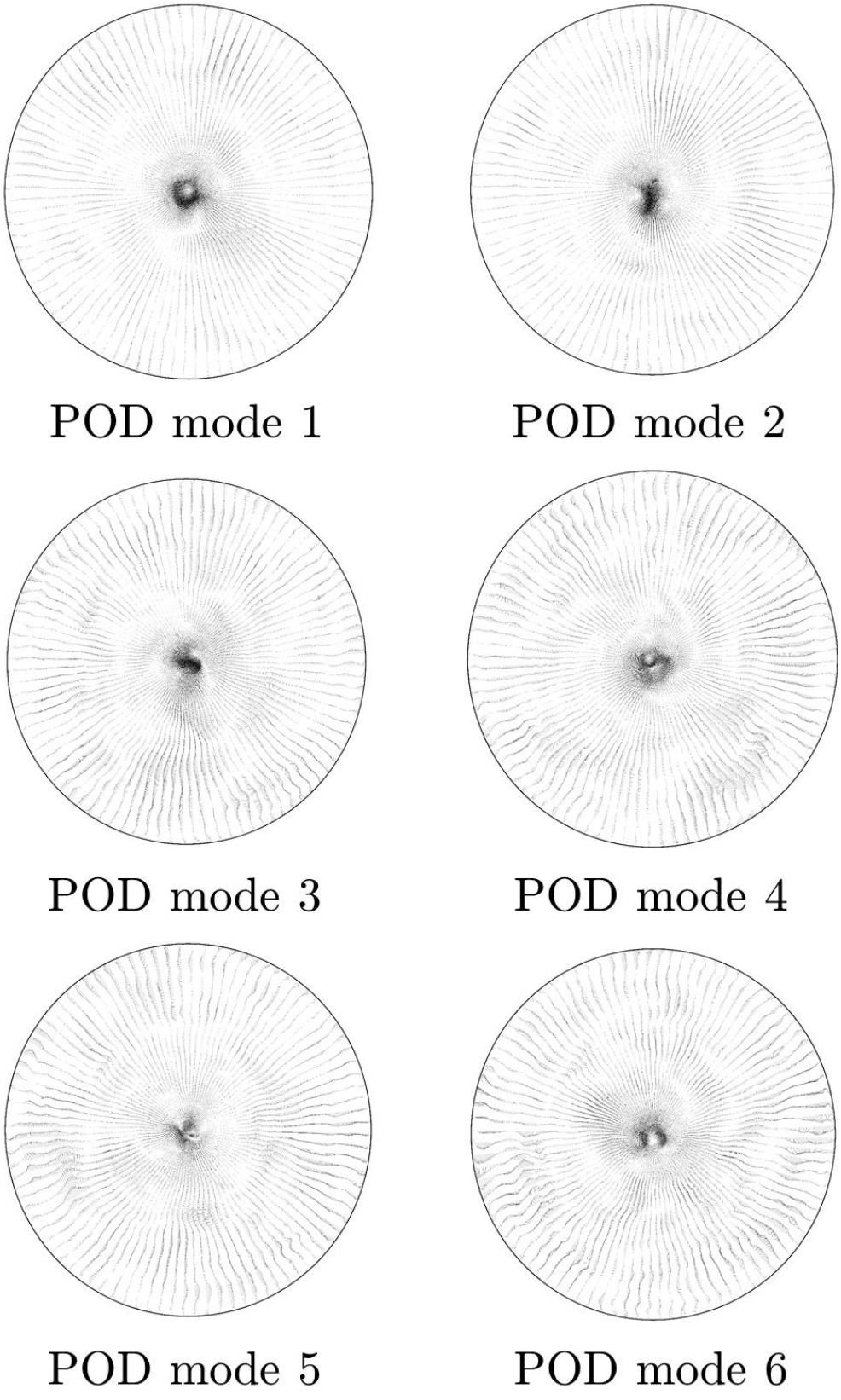

Figure 6.30 Modes produced by the POD of the LES data generated for the air flow conditions in the coal combustor at the axial position 3.

The distribution of the energy contained in the POD modes, presented in Figure 6.31, shows a sharp decrease in the number of relevant modes. In addition, the energy contained in the POD modes show that the impact of the structures captured in them increase their relevance in the flow distribution. In addition, the vector plot obtained for the mean velocity values show an equalised flow distribution with a clear rotational component around a prescribed centre. However, the location of the centre appears to be placed in an offset position from the geometric centre, thus suggesting that the flow was asymmetric for the flow time sampled. The presence of asymmetry in the transient calculations may suggest an additional rotational motion of the fluid, which in this case implies that the main swirling vortex is under precession.

The assessment of the POD modes produced for the transient results of the coal combustor under the Oxy27 flow conditions shows that, at the axial position 3, the coherent structures exhibit recirculation. In addition, the number of recirculating vortices was increased from what was observed at the previous axial positions, thus suggesting the appearance of more structures in the domain. In addition, some of the turbulent structures were show scatter in the periphery, hence indicating that during the flow mixing these structures are not contained. The interaction of the flow structures in the POD modes is well defined with up to four vortices showed at the central region of the furnace. Furthermore, in some regions of the domain, most notably in the POD modes 3 and 4, the structures appear to undergo a double helix arrangement, with the remaining structures accompanying their motion.

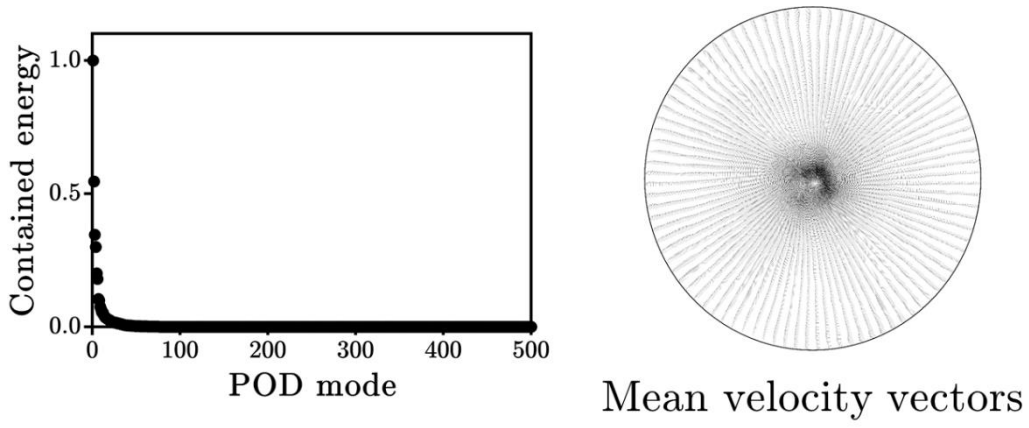

Figure 6.31 Distribution of the energy contained in the POD modes (left) and vector plot for the mean velocities (right) calculated for the snapshots captured at the axial position 3 in the LES for the coal combustor under the Oxy27 flow conditions.

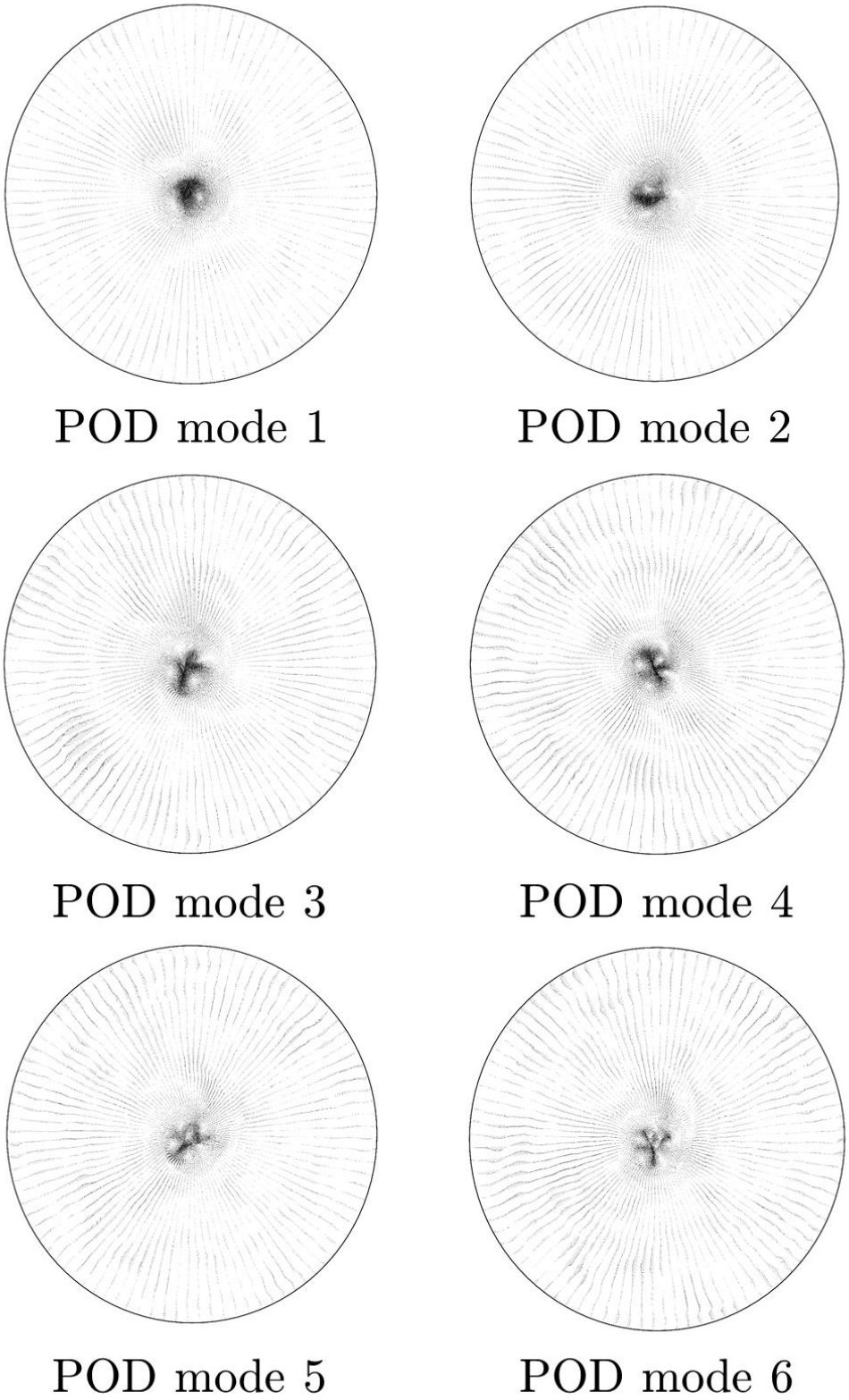

Figure 6.32 POD modes calculated for the transient data-set obtained at the axial position 3 on the coal combustor under the Oxy27 flow conditions.

6.4.3.4. Midplane

In addition to the POD modes produced at different axial locations, snapshots of the flow at the cross-section of the furnace were recorded. The distribution of the energy in the POD modes appear in pairs and this is an indication of the presence of vortical structures under precession [265], [359]. Furthermore, the trend of the energy distribution shows that the first 5 pairs of POD modes are more relevant than the rest, thus producing the sharp decrease in the contained energy presented in Figure 6.33. In addition, the vector plot for the mean velocity values shows good agreement with the velocity distributions previously introduced. The flow arrangement shows a single main vortex that is more defined in the quarl section. As the fluid travels into the combustion chamber, the arrangement in the flow becomes less defined until it vanishes. A noticeable shear layer is observed for the internal flow interface between the main swirling stream and the central recirculation zone. In contrast, the shear layer for the outer recirculation is not well defined for the majority of the domain, hence representing a weak interaction of the fluid at that interface.

The analysis of the POD modes for the air case at the cross-section plane shows that the predominant turbulent structures contains recirculation and are attached to the flame-holder of the burner, as shown in Figure 6.34. The cohesion of these structures are large enough than some of them appear to reach the combustion chamber. A noticeable arrangement of precessing vortex cores was observed in the POD modes 5 and 6, however these are contained within the quarl, thus reducing their impact on the overall flow stability.

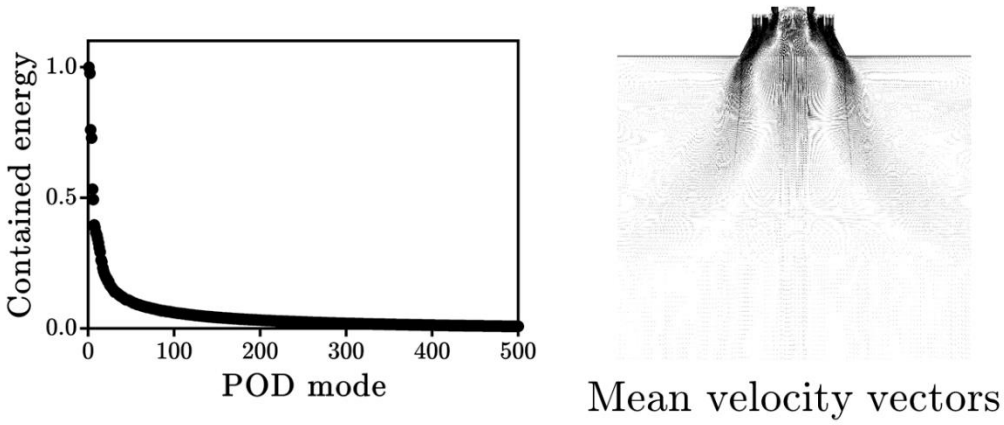

Figure 6.33 Energy distribution in the POD modes computed from the LES results for the air conditions at the cross-section of the furnace (left) and a vector plot of the mean velocity values (right).

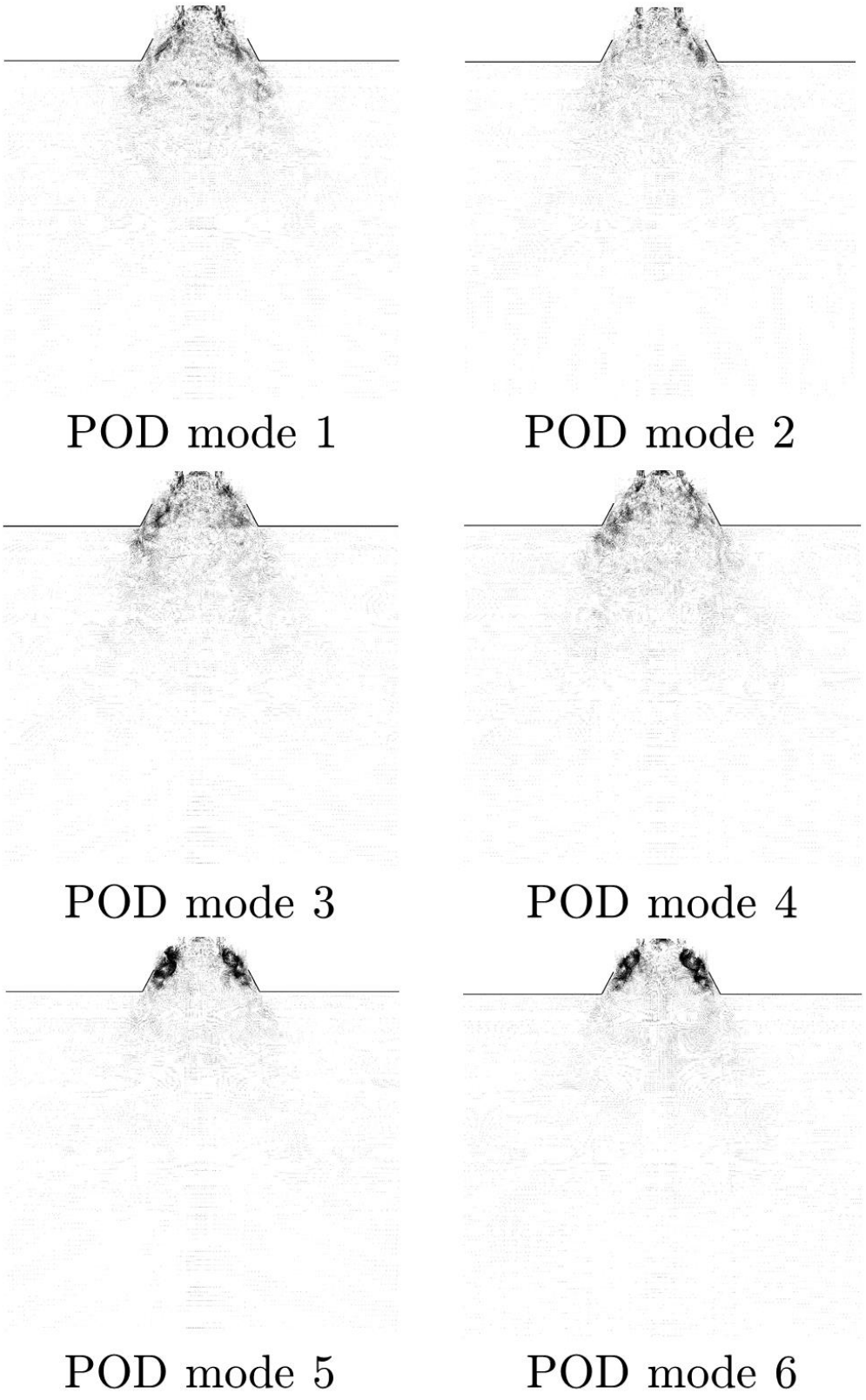

Figure 6.34 POD modes computed for the transient results obtained at the cross-sectional plane for the air conditions in the coal combustor.

The trend produced for the energy contained in the POD modes that are computed for the cross-section of the coal combustor under the Oxy27 flow conditions, are presented in Figure 6.35. These show a different distribution to that obtained for the air case, with only one pair of modes being observed. In addition, the energy of the system is seen to be more spread across the POD modes, thus requiring a larger number of POD modes to accurately characterise the spatial coherence of the flow. The vector plot obtained for the mean velocities, introduced in Figure 6.35, show that the aerodynamic profile under the oxyfuel scenario does not suffer noticeable alterations in comparison to its counterpart for the air conditions. A well defined swirling vortex emerges from the quarl and becomes less intense as it enters the combustion chamber. The internal shear layer is well defined, thus allowing the observation of the shape and extension of the central recirculating zone, which for the Oxy27 case appears to be narrower.

The assessment of the POD modes produced for the Oxy27 conditions allows the observation of the trailing vortices that emerge from the flame holder and extend outside the quarl, as shown in Figure 6.35. The turbulent structures captured in the POD modes show recirculation in the axial direction. Furthermore, an indication of the precessing vortex cores is produced by the POD modes 4 and 5, where a pair of recirculating structures appears to be governing the flow arrangement. However, these structures are contained within the quarl, and, due to their lack of cohesion, their influence in the flow distribution appears to be dissipated further downstream.

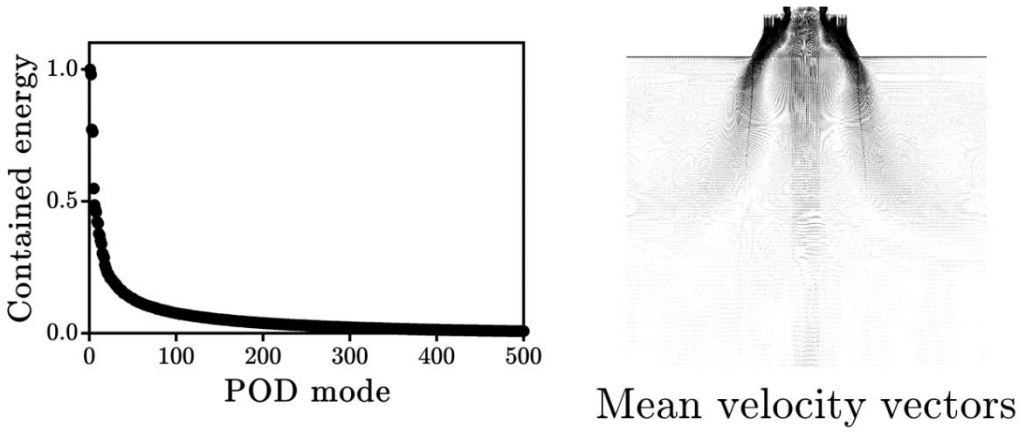

Figure 6.35 Distribution of energy in the POD modes calculated for the results at the cross-section plane in the simulation for the Oxy27 flow conditions in the coal combustor (left) and mean velocity vectors (right) for the same transient data.

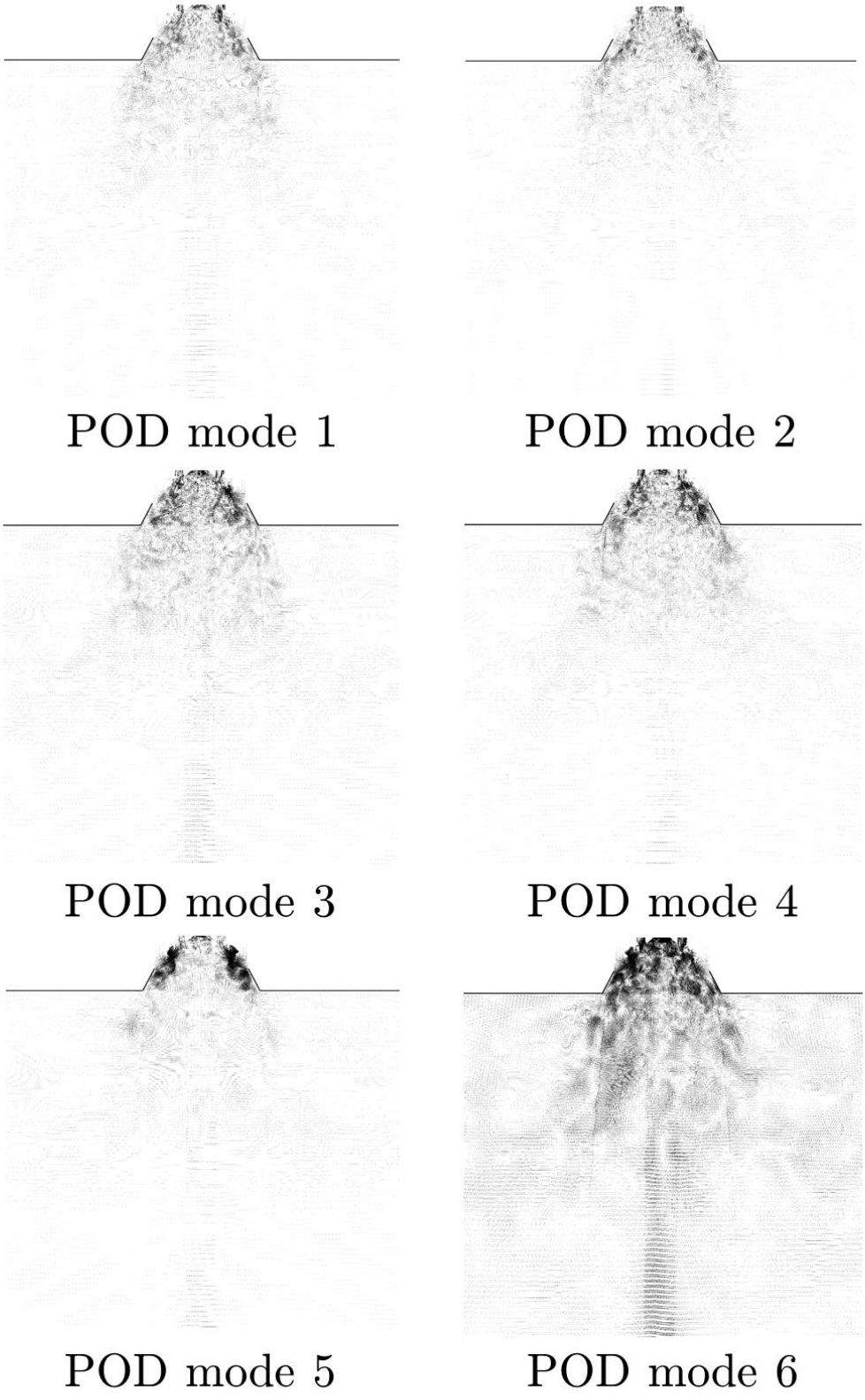

Figure 6.36 POD modes calculated using the transient data recorded at the cross-section of the coal combustor in a LES of the Oxy27 flow conditions.

6.4.4. Spatiotemporal coherence analysis

The flame produced by the combustion reaction propagates against the flow of the reactants, thus being sensible to the alterations in the flow rate, air/fuel ratio and the amount of swirl provided by the burner [36]. A flame is considered to be stable if, for a range in the aforementioned burner parameters, quenching or flashback is not present. In turbulent combustion, the flame front suffers indentations as a consequence of the flow velocity fluctuations and due to the presence of turbulent coherent structures. The disruptions in the flame front, if large enough, are associated to an increase in the production of pollutants, poor combustion efficiency and flame instability. Different techniques, such as the implementation of bluff bodies and swirl vanes in the burner, have been developed in order to enhance the stability of the process. When bluff bodies are installed perpendicular to the flow direction, an adverse pressure gradient is produced downstream and a recirculating vortex system arises in the wake of the bluff body. Furthermore, the addition of a swirl component to the flow velocity improves the generation of recirculating zones, which appear as being broader and more intense. The hot products of the reaction penetrates the recirculating vortex and are transported back to the near-burner region where they are mixed with the fresh oxidiser stream, thus improving the probability of ignition [36], [332], [350].

The assessment of the coherence of turbulent structures contained in the flame front and attached to the bluff body is paramount for the prediction of the stability of the flame. In the previous section, the spatial coherence of the flow structures was analysed by performing the POD to the temporal data obtained from the LES of the coal combustor for the air and Oxy27 flow conditions. Despite obtaining a good characterisation of the flow arrangement, the lack of temporal data associated with them impedes an accurate prediction of their motion. In this section, the dynamics of the system is studied by the calculation of the DMD of the same dataset employed in the POD analysis. A multivariable DMD methodology [291] was employed to obtain the relevant dynamic modes that describe the flow. The DMD modes produced for this study were sorted using the growth/decay rate exhibited, thus allowing us to weigh their contribution into the state of the flow. The pertinence of the sample length was assessed by confirming that the frequencies associated to the computed DMD modes were well distributed over the complex plane [348], [349]. The results for the DMD of the transient data contain a plot for the distribution of the power in the computed modes, and a vector plot for the DMD mode containing an associated frequency of 0 Hz, which accounts for the steady state of

the flow. Furthermore, graphical representations for the first six DMD modes, and their associate oscillation frequencies, have been presented.

6.4.4.1. Axial position 1

The spectrum of frequencies obtained for the LES results of the coal combustor under air flow conditions shows that the first six DMD modes appear to be more relevant than the rest, as shown in Figure 6.37. Furthermore, the steady state of the flow, depicted in the DMD mode at 0 Hz, shows slight differences to the vector plot for the mean velocity values introduced in the Section 6.4.3.1. In the DMD mode, a noticeable shear layer for the interface of the swirling jet and the outer recirculation zone is observed. In addition, a region of high intensity is observed within the swirling jet, and this appears to be related to the geometric disposition of the primary flow channel of the burner.

The analysis of the DMD modes produced for the LES results for the air conditions, presented in Figure 6.38, shows a tangle of vortical entities coexisting in the central region of the furnace. The DMD modes associated to the lower quarter of the frequency spectrum appears to influence a larger region of the domain, while the DMD modes with faster oscillatory rates are more contained. The coherent structures captured by the DMD modes shows to have recirculation, and in many cases an opposing rotation direction. The interaction between the swirls produced regions of high velocity in the flow, appearing as shaded zones in Figure 6.38. Furthermore, the number of entities depicted at this axial position suggests that they are small and are tightly clustered. Nevertheless, the overall flow distribution exhibits an arrangement around the axis of the furnace, and it is more evident in the outer region of the swirl jet.

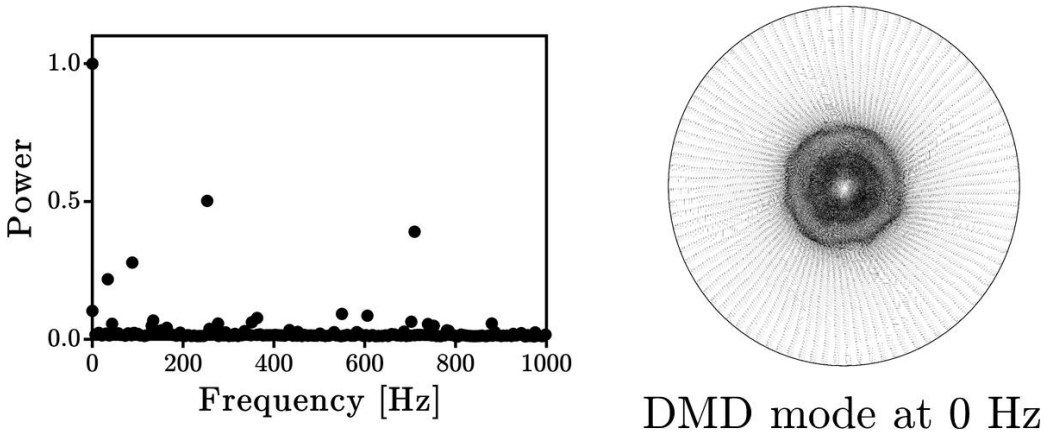

Figure 6.37 Frequency spectrum for the power contained in the DMD modes (left) and steady state DMD mode obtained for the LES for the air flow conditions.

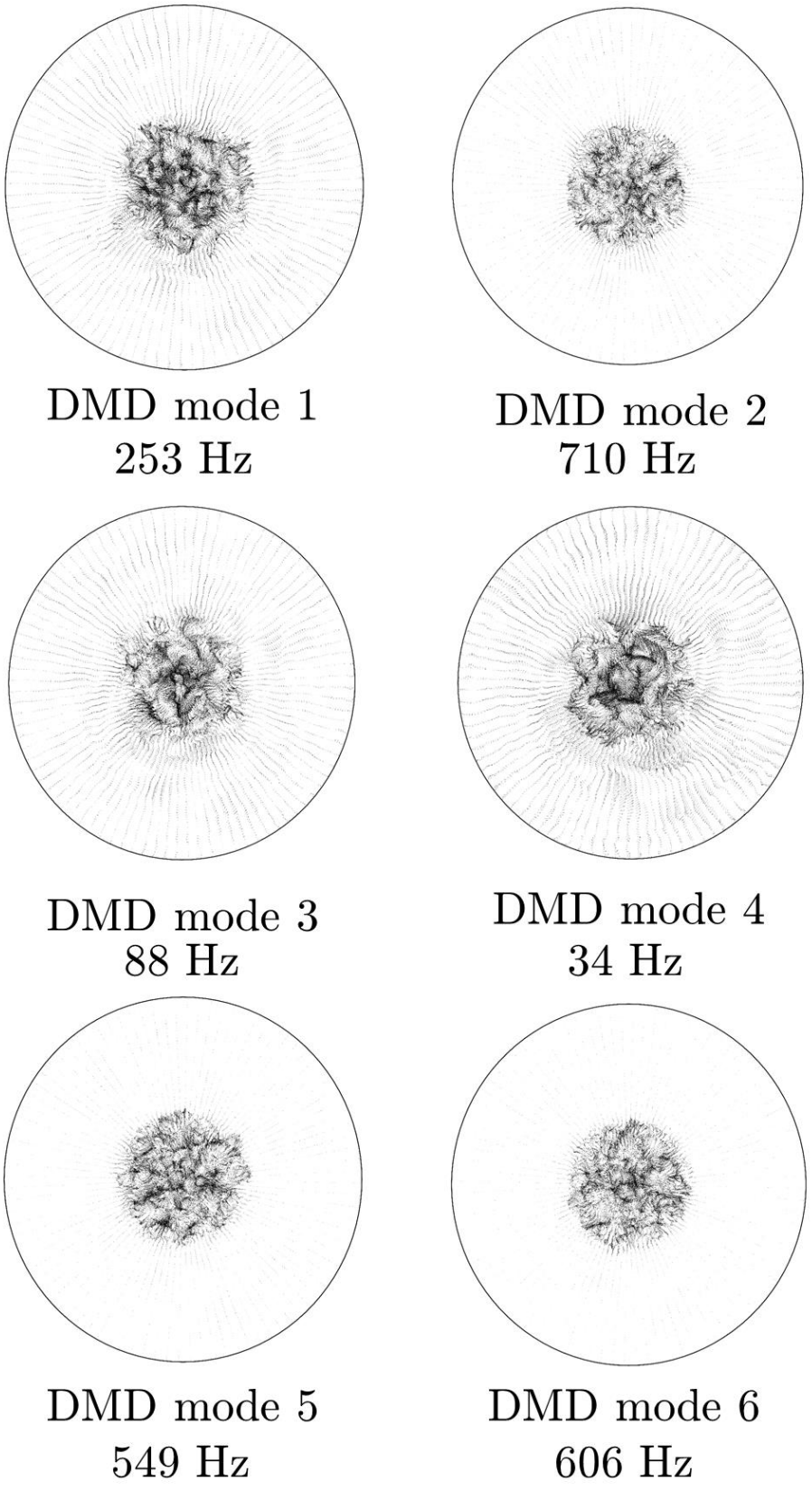

Figure 6.38 The DMD modes obtained for the transient data generated for the air case at the axial position 1.

The spectrum of frequencies produced by the DMD modes obtained for the Oxy27 flow conditions, introduced in Figure 6.39, shows a larger number of relevant dynamic modes than in the air case analysis. Furthermore, the most relevant DMD modes appear to contain higher oscillating frequencies associated with them. Furthermore, the steady state of the flow, as captured by the DMD mode with an associated frequency of oscillation 0 Hz shows a good agreement with the prediction using the POD methodology. However, the effect of the flow distribution generated by the primary channels of the burner, which contains four gutters, is more noticeable. The flow arrangement produces a region in the central region of the domain where the intensity of the vectors suggest the influence of the flow staging produced by the burner. In addition, two shear layers are observed for the interfaces between the swirling jet and the recirculating zones. Despite the appearance of disturbances in the flow, the overall flow arrangement retains the characteristic rotation about the axis of the confined swirling jets.

The analysis of the most relevant DMD modes produced for the Oxy27 flow conditions in the coal combustor, presented in Figure 6.40, shows that a tangle of vortices is produced in the central region of the domain and that they do not expand their region of influence beyond that zone. In addition, the structures with higher frequencies of oscillation exhibit a chaotic distribution and produce erratic patterns in the flow. In contrast, the structures presents more cohesion and appears to produce discernible patterns for the lower frequencies, such as in the DMD modes 2 and 5.

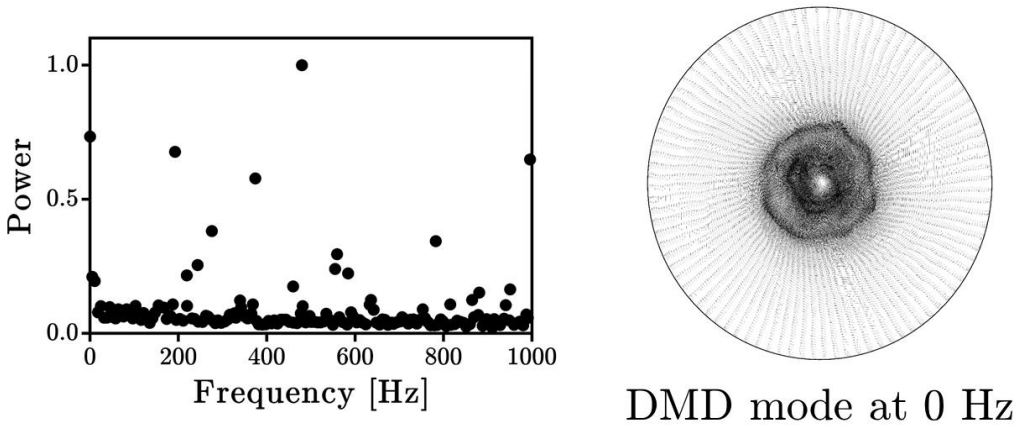

Figure 6.39 Spectrum of frequencies associated with the DMD modes computed for the flow at the axial position 1 in the coal combustor under Oxy27 conditions (left) and steady state flow as depicted by the DMD mode at 0 Hz.

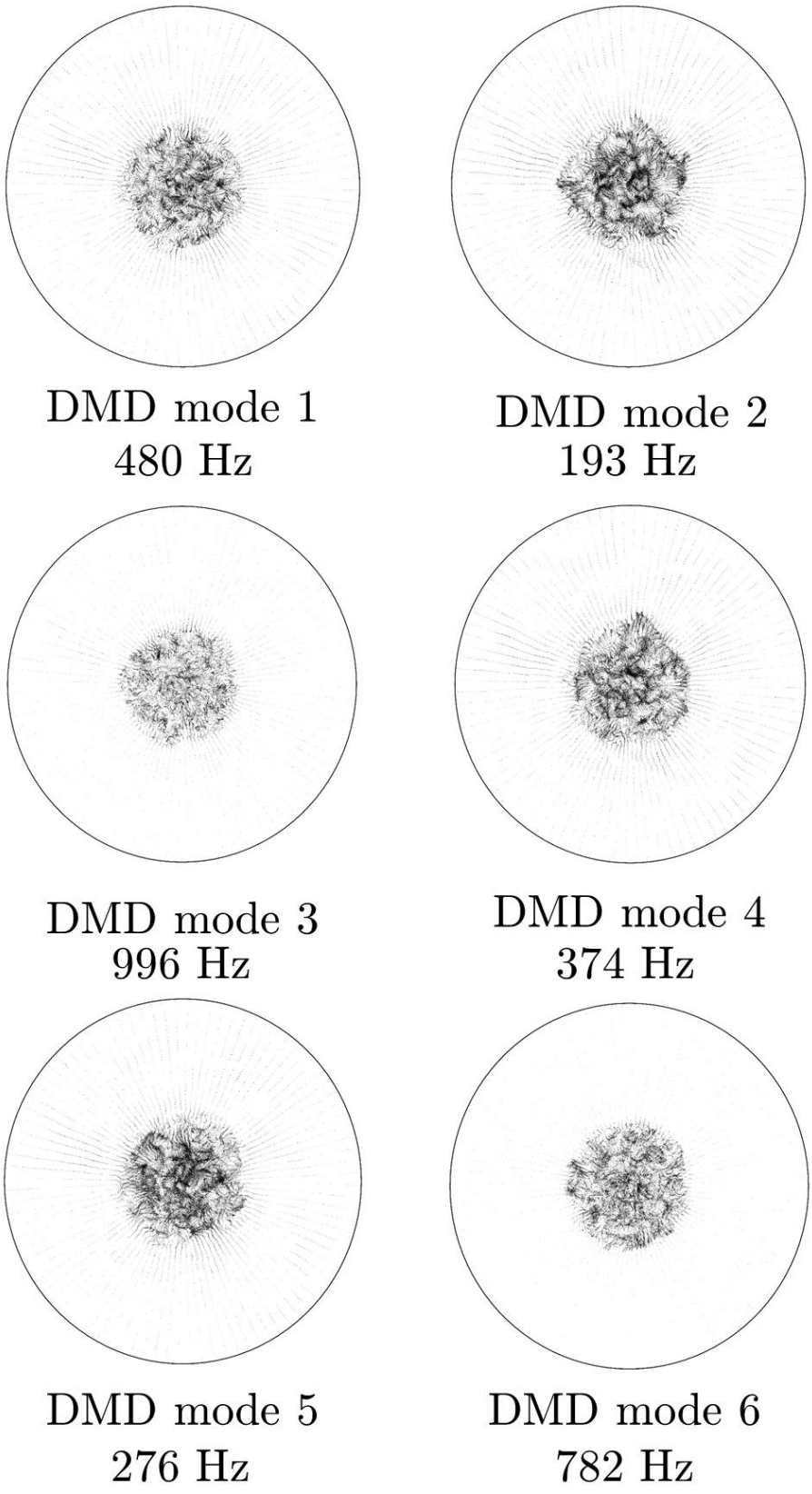

Figure 6.40 DMD modes computed for the results obtained at the axial position 1 for the coal combustor under the Oxy27 conditions.

6.4.4.2. Axial position 2

The spectrum of frequencies generated for the DMD modes for the air case at the axial position 2, shows that the majority of the power of the system is contained in the leading modes, as shown in Figure 6.41. A sharp decrease in the power contained in the DMD modes is observed after the first four modes and after the later fifteen DMD modes. In addition, the steady state DMD mode shows that the shear layer captured for the outer recirculation zone at the axial position 1 vanishes at this location. Furthermore, the effects of the mixing in the flow is observed as the energetic zone induced by the primary flow channel of the burner disseminates and only a remnant of this arrangement prevails. Nevertheless, the flow arrangement is evenly distributed around a single centre of rotation, hence confirming the existence of the main vortex arrangement.

The analysis of the DMD modes computed for the coal combustor under air flow conditions, introduced in Figure 6.42, shows, at the axial position 2, that the frequency range for the most predominant modes is smaller than what it was obtained for the position upstream. The arrangement of fluid structures is similar to that obtained for the axial position 1, as a series of recirculating structures are observed in the central region of the vector plots and their interactions produce high velocity regions in the domain. However, the number of recirculating entities captured in the DMD modes at this axial position is lower and the size of them is bigger than at the previous location, thus suggesting the aggregation of small fluid filaments into larger structures, as it is observed in the isosurfaces used to detect the vortex core region.

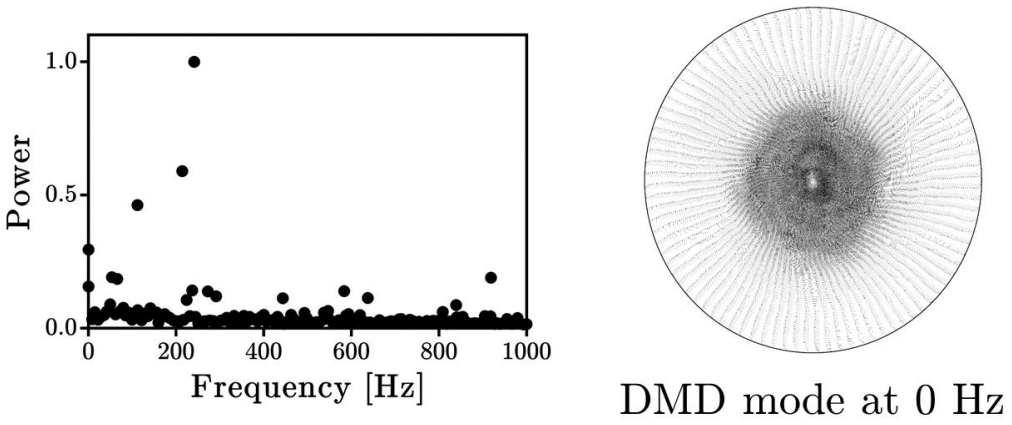

Figure 6.41 Distribution of the power contained in the DMD modes (left) and steady state DMD mode (right) computed for the transient results at the axial position 2 for the air conditions in the coal combustor.

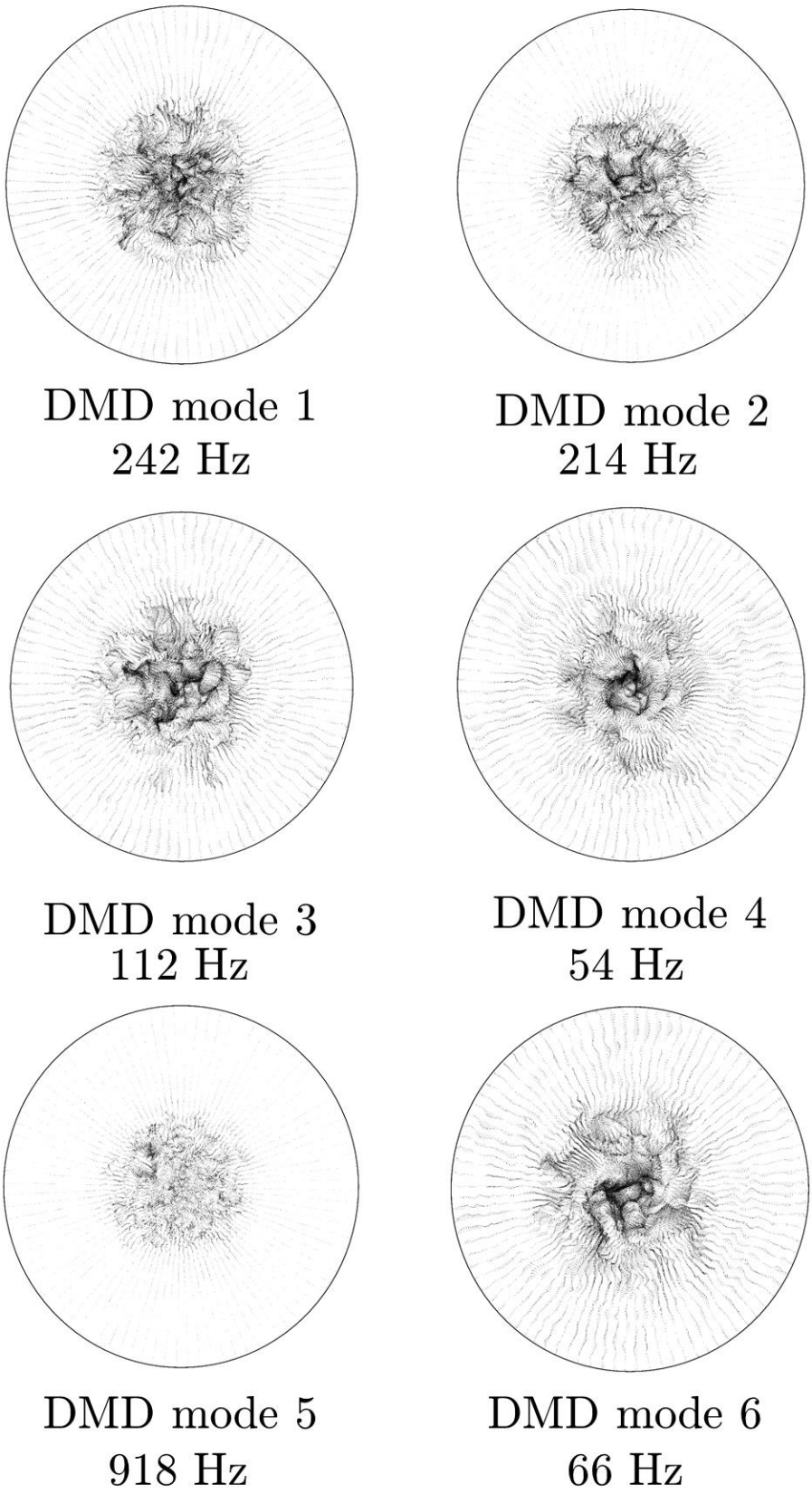

Figure 6.42 DMD modes computed for the flow in the coal combustor at the axial position 2 under air conditions.

The distribution of power in the DMD modes, as obtained for the snapshots obtained at the second axial position of the coal combustor shows that for the Oxy27 conditions, the relevance of dynamic modes with high associated frequencies decreases, as shown in Figure 6.43. In addition, the first two DMD modes are depicted as being more influential in the development of the flow distribution than the rest. The steady state flow, characterised by the DMD mode with 0 Hz of oscillating frequency shows a good arrangement in the swirling motion for the majority of the domain. However, at its centre the vectors produce two distinguishable centres of rotation with similar directions. The overall flow distribution appears to be related to one of them, while the remaining recirculating structure appears to be of a companion type. Some disturbances in the shape of the main swirling jet are produced as a consequence of the two-vortex array, but these are contained in a small region of the fluid and appear to be of a transitional type.

The analysis of the DMD modes for the Oxy27 case, presented in Figure 6.44, shows a difference in the type of the structures captured according to the associated frequency. It is found that the turbulent structures are more cohesive and produce more recognisable patterns for lower associated frequencies, and this agrees with the findings of the analysis of a swirling flow presented in Chapter 5. In contrast, the turbulent structures become disorganised as their associated frequency grows, thus impeding the production of noticeable paths. The chaotic nature of these high-oscillating flow structures suggests that their nature may be numerical rather than a physical interaction of the fluid.

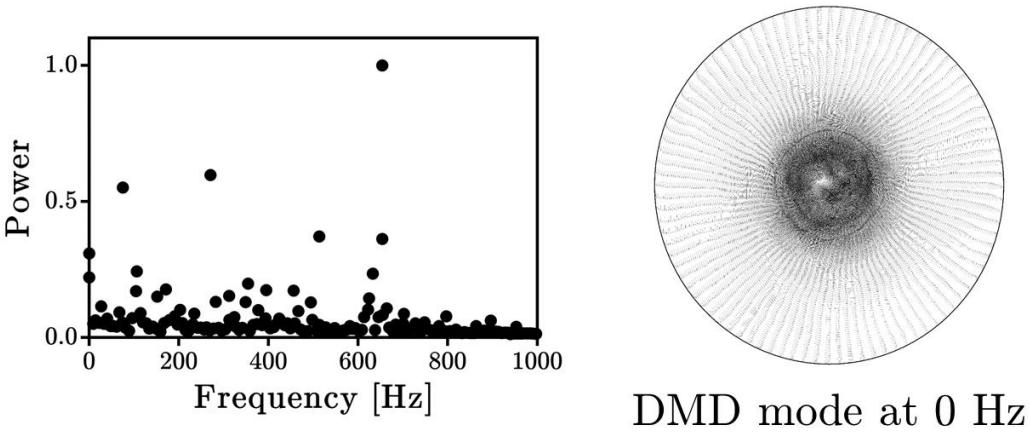

Figure 6.43 Distribution of the power across the DMD modes (left) and steady state DMD mode (right) computed from the results obtained at the axial position 2 in the coal combustor under the Oxy27 conditions.

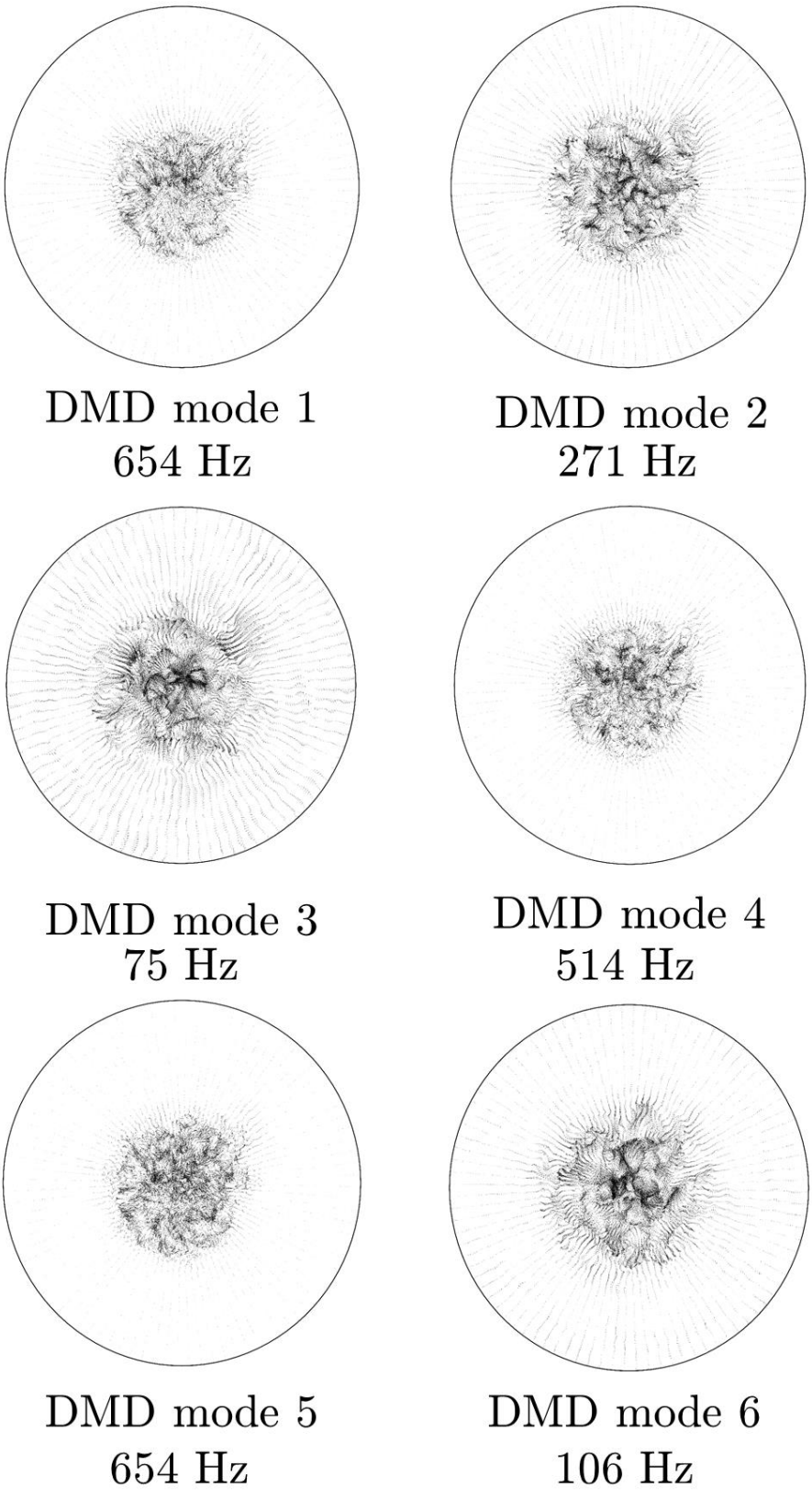

Figure 6.44 The DMD modes calculated for the LES results of the flow at the axial position 2 in the coal combustor under the Oxy27 conditions.

6.4.4.3. Axial position 3

The distribution of the power contained in the DMD modes computed for the flow developed in the coal combustor at the axial position 3, presented in Figure 6.45, shows an increase in the number of relevant frequencies with low associated frequencies. The majority of the frequencies are contained below the 200 Hz mark with a noticeable cluster around 150 Hz. The steady state flow, depicted by the DMD mode at 0 Hz, shows that the flow structure corresponds to a swirling flow, as only a single centre of rotation is observed. The flow appears to be evenly distributed, with a high-velocity region near the centre of rotation of the vortex and this presents small anomalies in its intensity.

The inspection of the DMD modes produced for the transient flow distribution in the coal combustor under air conditions show a close value for the frequency associated with the most relevant DMD modes, and a decrease in the intensity of the interaction of the recirculating structures located at the centre of the domain, thus producing shorter interfaces of high-velocity. In addition, the number of flow structures observed in the predominant modes are lower than that obtained in the previous position analysed, as shown in Figure 6.46. Furthermore, additional structures appear in the near wall region, and these produce disarrangement to some regions of the flow. A noteworthy arrangement was produced for the DMD mode 4, in which two recirculating structures appear to interact around the geometrical centre of the plot and several smaller structures follow the motion in a second concentric row. However, the cohesion of the recirculating structures remain low for the outer row, thus producing scattered structures.

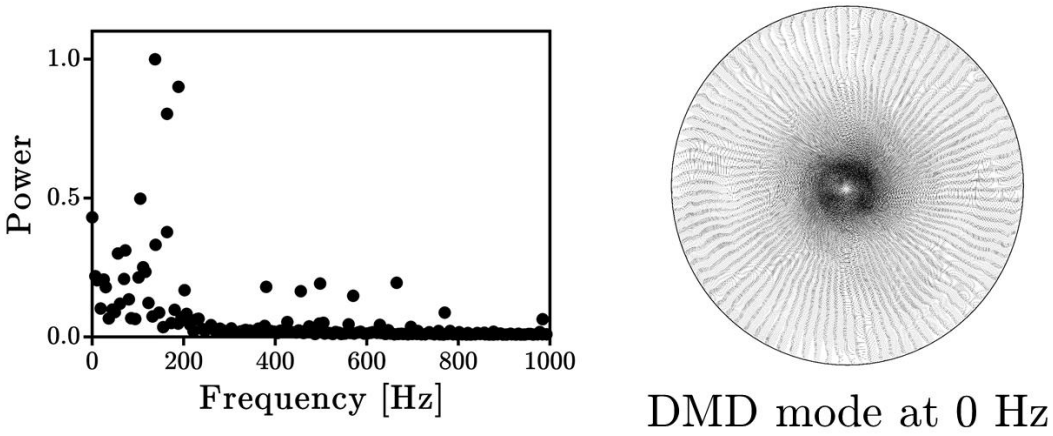

Figure 6.45 Distribution of the power contained in the DMD modes (left) and steady state vector plot (right) computed for the LES results of the flow distribution at the axial position 3 of the coal combustor under air flow conditions.

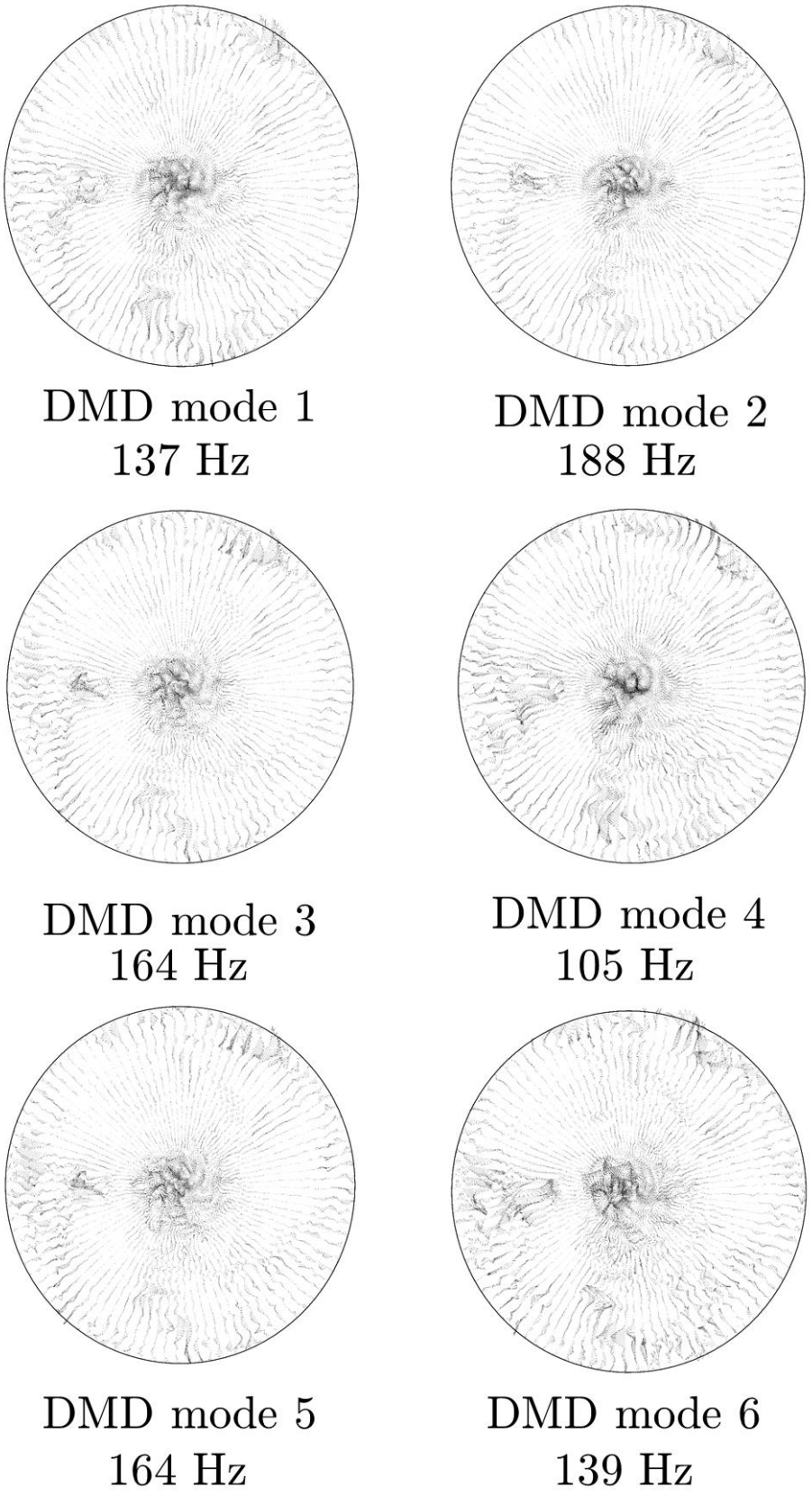

Figure 6.46 The DMD modes produced for the snapshots sampled at the axial position 3 in the LES of the flow in the coal combustor for the air flow conditions.

The spectrum of oscillating frequencies associated to the DMD modes calculated for the transient data obtained at the axial 3 position of the coal furnace, showed that for the Oxy 27 flow conditions, a single dynamic mode is observed, as shown in Figure 6.47. Furthermore, the difference in the power contained in this DMD mode and that estimated for the rest appears to be substantial, thus suggesting that the flow has been effectively mixed and that the flow oscillates at the frequency of the most relevant DMD mode. In addition, the vector plot for the mean velocity components of the flow shows that the steady state of the system is in the form of a rotational movement. The rotation of the flow was predicted to occur around a single axis, as no additional recirculating entities are observed. However, the velocity components for the locations near the outer wall exhibit variations in their magnitudes, thus producing disturbances in the overall swirling motion. Moreover, the centre of rotation was found to be offset from the geometric centre of the furnace, which may indicate asymmetry in the main vortex.

An inspection of the DMD modes produced for the transient results obtained for the Oxy27 flow conditions shows the presence of turbulent structures with recirculating patterns, and these appear to be scattered in the domain. The interaction of the recirculating vortices, produces a region of high-velocity in the central region of the furnace, while the structures located in the outer region appear to produce more chaotic patterns, where no evident interactions of the structures is observed. Furthermore, the effect of the mixing in the flow is observed, as the majority of the DMD modes are calculated in a narrow frequency range in comparison to the previous axial locations.

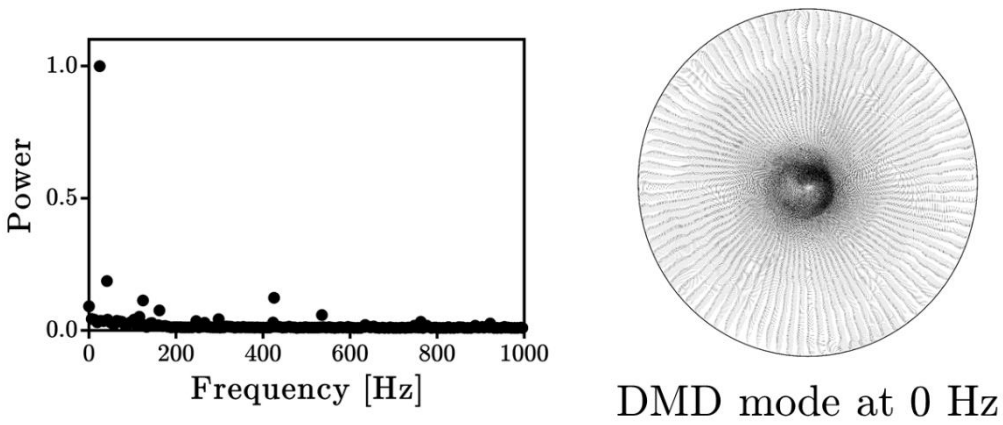

Figure 6.47 Spectrum of frequencies produced by the power contained in the DMD modes (left) and steady state DMD mode (right) calculated for the flow snapshots obtained at the axial position 3 of the coal combustor under the Oxy27 conditions.

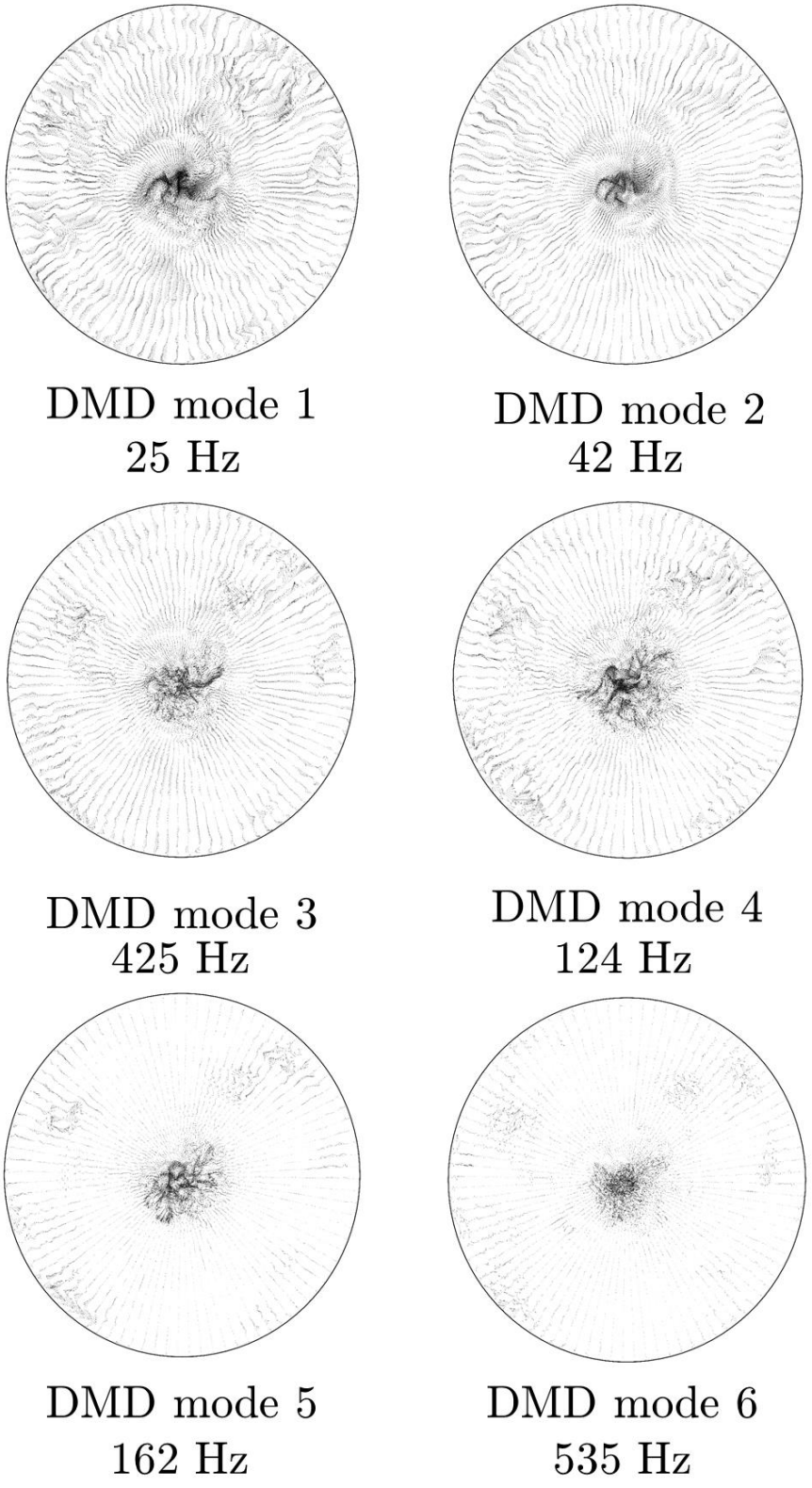

Figure 6.48 The DMD modes calculated for the flow in the coal combustor under the Oxy27 conditions at the axial position 3.

6.4.4.4. Midplane

In agreement with the POD analysis presented in Section 6.4.3, the assessment of the coherence of the flow, using the velocity distributions at the cross-section, is performed in order to analyse the motion of the coherent structures in the axial direction. The distribution of the power in the DMD modes calculated for the flow in the coal furnace under air conditions, is presented in figure 6.49, and shows that the relevant oscillatory modes were scattered across the entire spectrum. However, the contained power remained low after the first fifteen DMD modes. In addition, the steady state flow distribution captured by the DMD mode at 0 Hz shows good agreement with the results obtained from the POD analysis, with the major structures contained in the quarl. Furthermore, the shear layer generated at the interface between the main vortex and the central recirculation zone was distinguished in the near burner region and dispersing it as the flow mixes downstream.

The analysis of the DMD modes obtained for the velocity field at the cross-section showed a large difference to the results of the POD, since in this study a tangle of coherent structures are observed, as shown in Figure 6.50. These structures emerge from the flame holder of the burner and then extend into the combustion chamber. The values for the associated frequencies suggest that the coherent structures recede fast from the burner tip and eventually decrease their oscillations and mix with the slower flow. The cohesion of the flow structures appear to be stronger while in the quarl, thus producing large uninterrupted structures that may be evidence of a precessing vortex cores, as predicted previously by the POD.

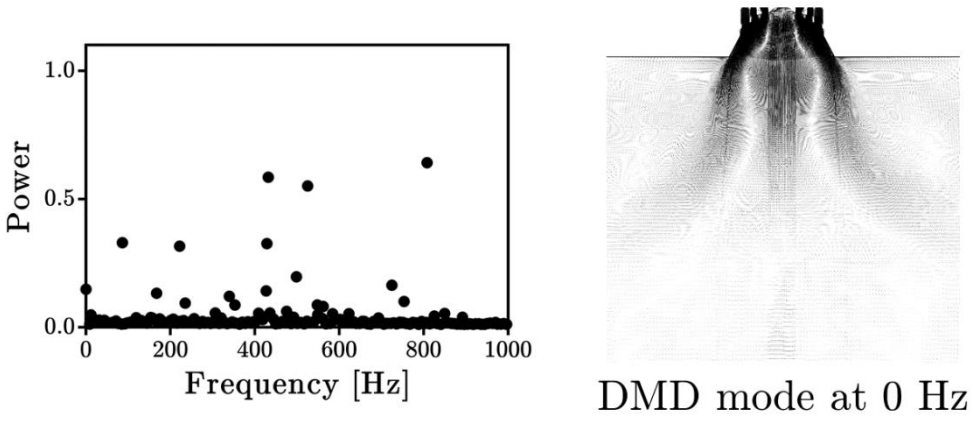

Figure 6.49 Distribution of the power in the computed DMD modes for the flow of air in the coal combustor (left) and steady state of the flow generated by the DMD mode with an associated frequency of 0 Hz (right).

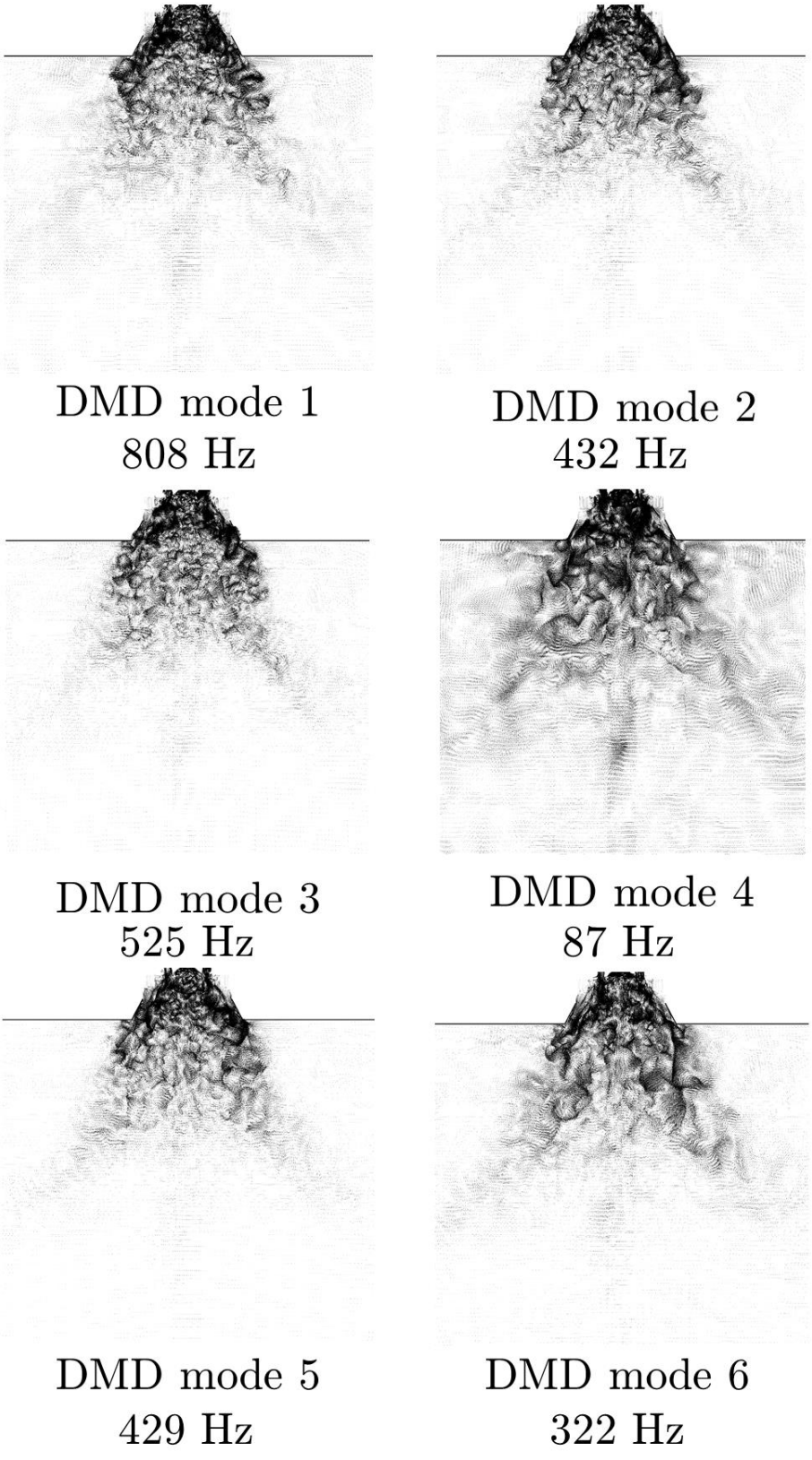

Figure 6.50 The DMD modes obtained at the cross-section of the coal combustor for the LES results for the air case.

The distribution of power in the DMD modes calculated for the snapshots obtained using the cross-section plane of the coal combustor shows, for the Oxy27 case, a decrease in the number of relevant DMD modes in comparison to the distribution produced for the air case. The associated frequencies of the leading DMD modes are predicted to be scattered across the entire spectrum, as shown in Figure 6.51. The steady-state of the flow, shows that the inlet streams mix in the quarl section and enter the combustion chamber as a single swirling jet of high-intensity that disseminates further downstream. However, the extension of the swirling jet in the Oxy27 case is observed as being narrower and longer than its counterpart under the air conditions. Furthermore, the central recirculating zone is observed to contain disturbances in its shape in the axial direction, which corresponds to the misalignments in the centre of rotation perceived for the analyses at the different axial positions previously introduced.

The assessment of the DMD modes produced for the transient data recorded at the cross-section of the coal combustor, is presented in Figure 6.52, and shows a tangle of vortical structures with high vorticity and cohesion that emerge from the flame holder and extend into the combustion chamber. In addition, it is found that the structures with higher associated frequencies are mostly contained near the wall of the quarl, while the slower entities are more dispersed in the domain. Nevertheless, the extension of the turbulent structures appear to be shorter than those depicted for the air case, despite being exhibited as largely cohesive, thus suggesting a large dampening effect for the large structures under the Oxy27 conditions.

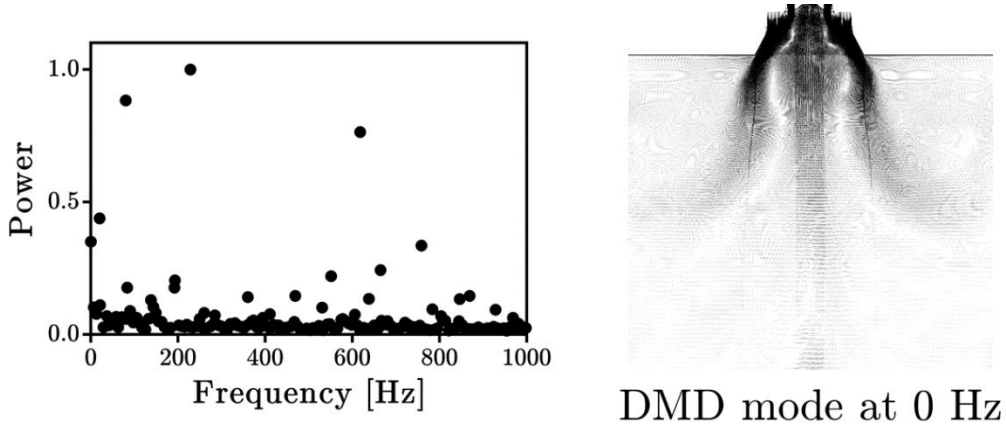

Figure 6.51 Distribution of the power in the DMD modes (left) and steady state DMD mode calculated for the velocity distributions measured at the cross-section of the coal combustor under the Oxy27 flow conditions.

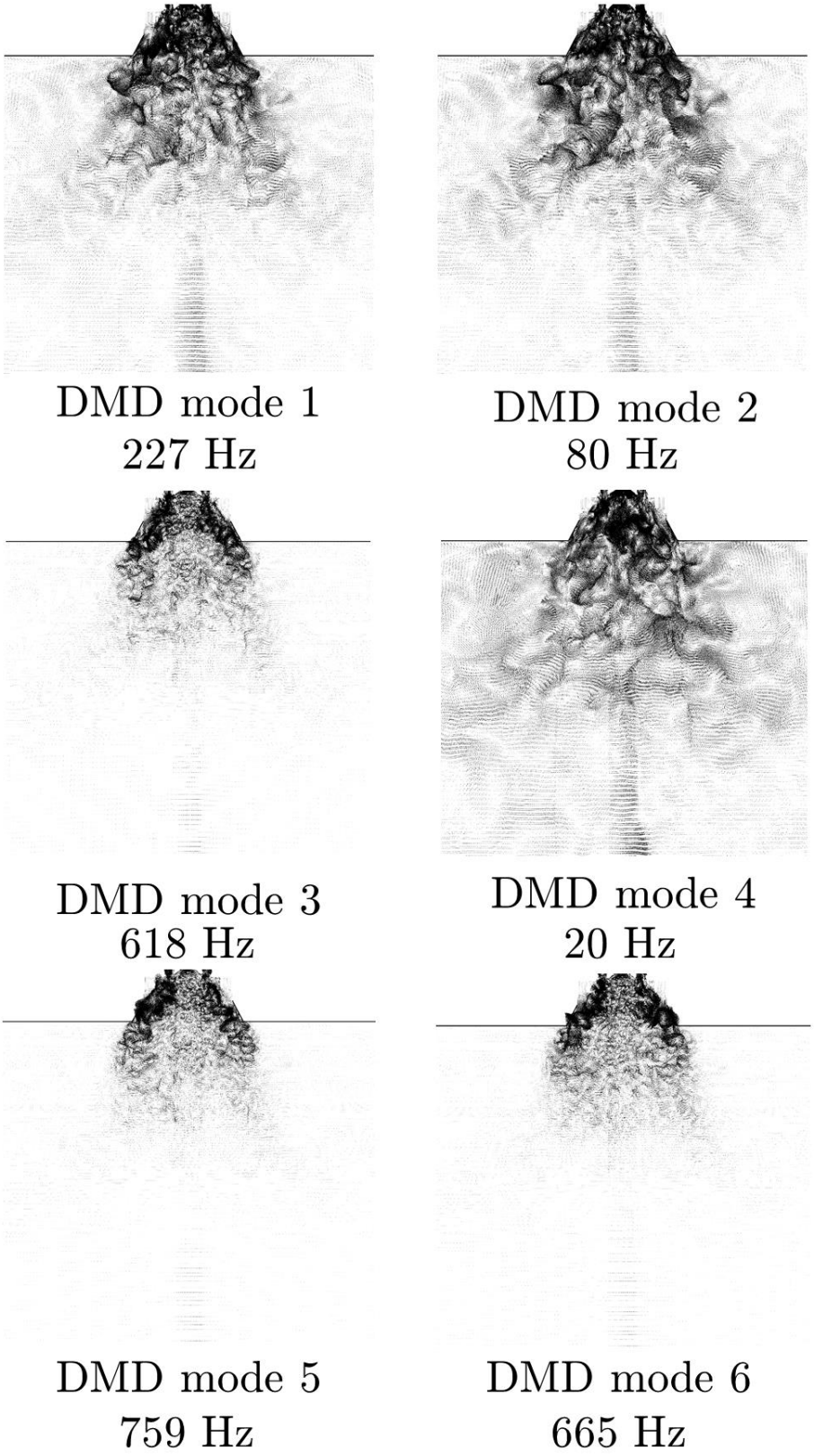

Figure 6.52 The DMD modes generated for the transient results obtained at the cross-section of the coal combustor under the Oxy27 conditions.

6.5. Summary

The coherence of the flow in a coal combustor has been assessed in this chapter by employing the transient data produced by the LES in three different methodologies. The spectral analysis was performed to the signal produced by the fluctuations in the axial velocity of the fluid. These signals were simultaneously recorded using monitor points placed at different locations in the domain. In addition, the instantaneous fluctuations in the flow were recorded at different planar locations and later were used in the calculation of the POD and the DMD. The POD of the transient data was used to account for the spatial coherence of the turbulent structures contained in the flow. Finally, the DMD methodology was employed to obtain a series of dynamic modes that comprise of structures that remain coherent in both time and space. The utilisation of different types of data in the methodologies employed for the analysis of the flow coherence allowed the evaluation of the pertinence of each dataset in the calculation of the flow dynamics and provided a comparison on how each of them characterise the flow.

The transient data used for the coherence assessment was obtained from computational fluid dynamics simulations. The cases studied in these CFD studies comprise of the combustion of coal under air and two oxyfuel conditions, namely Oxy27 and Oxy30. The furnace simulated in these cases was the solid-fuel combustion test facility of the Pilot Advanced Capture Technology (PACT) facilities, which is located in Sheffield, UK. The geometry of the combustion facility were simplified in order to reduce the computing requirements for its simulation. The geometry of the burner, placed on top of the furnace, was not included, instead fully developed profiles for the velocity were set as the inlet conditions. However, the gutters contained in the primary flow channel of the burner was retained in order to incorporate their effect into the overall flow distribution in the furnace and into the flame stability. The three-dimensional mesh used to capture the furnace geometry consisted of 4331721 hexahedral elements and it was generated employing the element size and distributions of similar grids employed for previous calculations.

The CFD calculations employed a RANS approach for the combustion simulations, with the realizable $\kappa - \epsilon$ model as the turbulence model selected. The Menter-Lechner wall functions were employed to capture the boundary layer as their independence on the y^+ value improves the flexibility for its application in complex geometries. The particle tracking was performed using a Lagrangian reference frame that includes the effect of the gravitational force. In addition,

the particle dispersion originated from the velocity fluctuations in the turbulent flow was incorporated into the calculation by the discrete random walk model. The release of volatiles from the coal particles was resolved by a single kinetic rate, whose parameters were set for the 'El Cerrejon coal'. The combustion of the volatile matter was assumed as a two-step reaction, which was computed by the eddy-dissipation model, thus assuming a turbulent-controlled reaction. The combustion of the remaining char particles was simulated by the intrinsic model, with parameters that were set to values tested in previous studies. The radiative heat transfer, which accounts for the most predominant heat transfer mechanism in combustion environments, was modelled by the discrete ordinates model. The calculation of the absorption coefficient in the gaseous phase was made by the full-spectrum correlated k-distribution model.

The prediction of the distribution of chemical species in the furnace was evaluated at three consecutive axial positions. It was found that the concentration of oxygen and carbon dioxide was well predicted for the region close to the burner in the air-fired case. In contrast, a noticeable underprediction of the amount of carbon dioxide was found in both oxyfuel cases, in addition to the overprediction of carbon monoxide in the Oxy30 case showed a delay in the oxidation of CO into CO_2, which appears to be a consequence of the oxyfuel environment. The distribution of species further downstream showed an over prediction of the flow mixing process as the main vortex was depicted as a wider structure than in the experiments. Both the carbon dioxide and the carbon monoxide concentrations, especially within the central recirculation zone, were under predicted at the remaining two axial positions, thus suggesting that the effects of CO related phenomena, that are not included in the analysis, may be relevant. The profiles obtained at the last axial position were mostly flat, thus showing that in the RANS simulations the main vortical entity is diffused in the flow faster than what it was measured experimentally. A similar behaviour for the vortex diffusion was observed for the studies performed to the isothermal swirling-flow rig in Chapter 5, thus suggesting the overprediction of the flow mixing as an inherent characteristic in the RANS approach. Furthermore, the calculated distributions of the temperature and axial velocity in the furnace showed that the Oxy30 better emulated the results for the air combustion, and this agrees with the findings in Chapter 4. In contrast, the aerodynamics for the Oxy27 case showed to be changed, thus producing discrepancies in the location and extent of the recirculation zones. Nevertheless, the distribution of species showed slight differences in the oxyfuel scenarios,

thus suggesting that, despite the alterations to the velocity profile, the combustion rate was similar.

In order to assess the effects of the oxyfuel environment in the stability of the combustor, the air combustion and the Oxy27 cases were selected to compute the LES of their flow, as they exhibited the largest differences in their flow distribution. In the LES of coal combustion, the utilisation of a transient particle tracking is crucial to improve the physical meaning of the results. In addition, corrections to the calculation of the particle trajectories must be included in order to account for the additional forces that act on the particle. Furthermore, the algorithm employed for the simulation of the particle injection must be modified to incorporate the temporal variations in the mass flow, particle distribution and location at the injection boundary. The corresponding reactive LES was set for this study, however the manipulations are complicated, and this is mainly due to the complexity of the numerical models involved, exhibited large computation times for the high-performance computing facilities available. Several methodologies and computational subroutines were developed and tested to decrease the associated computational time in the simulations. The reductions in the computing time achieved by these measures were still not significant enough to ensure the acquisition of the data required for the subsequent analyses under a reasonable amount of time. Therefore, non-reactive LES was employed for the assessment of the stability in the combustor. The mass flow and gas composition for each case analysed was retained and a constant temperature of 300 K was assumed for the domain.

The Sigma SGS model was employed in the LES calculations since it showed a better performance for wall-bounded flows and an improved capability to retain the flow structures developed in the fluid. Furthermore, the spectral synthesiser was employed to induce perturbations to the flow in all of the inlet channels. The time step for the simulations was fixed to 5×10^{-4} s, and the relevant flow scalars were sampled every two time-steps. The total flow time in the simulations was at least 12 s, while the length of the sampled data was 1 s for both of the cases analysed. The presence and type of turbulent structures in the flow was assessed by plotting isosurfaces of three different vortex core detection mechanisms. The size of the structures observed in the flow appears to grow as they recede from the burner and they showed to be largely cohesive. A small cluster of thin fluid filaments was depicted in the quarl section, and these appear to collide and form larger structures. Furthermore, the quarl section appear to influence the mixing process of the streams as the

vortical entities were found to be contained in a single group. Furthermore, the quarl appears to damp the proliferation of large structures in the vicinity of the burner, as these appear further downstream and in a scattered manner, thus reducing their impact in the stability of the system. Nevertheless, the overall flow showed to be arranged around the axis with all the reaming flow structures being of a companion type.

The spectral analysis employed the transient signals recorded at 18 different monitor points placed at three different axial positions in the domain. The results of the spectral analysis produced a distribution of the power spectral density contained in each frequency band, thus allowing us to obtain a discrete spectrum of frequencies. The dominant frequency bands correspond to the primary oscillating mechanisms and account for the repeatability of the flow fluctuations in time which represents the temporal coherence of the system. It was found that the air case produced spectrums with more relevant frequencies, thus depicting the flow as being more unsettled. In addition, the number of relevant frequencies decreased for the axial positions downstream, thus showing that the overall flow eventually finds harmony in its arrangement and becomes coherent in time. Furthermore, the flow for the Oxy27 condition appeared to be oscillating slower than its counterpart for the air case, however this behaviour appear to be related to the slower velocities reached within the furnace.

In addition to the temporal analyses, the coherence of the flow in space was assessed by the POD methodology as an indicator of type and location of the coherent structures in the flow. The calculation of the POD was based on the method of snapshots, where a set of planar representations of the instantaneous flow field were employed. The snapshots consisted of the values for the instantaneous velocity in the three directions of the Cartesian coordinates system and the magnitude of the vorticity. The axial velocity component, normal to the sampling plane in the axial positions, and the vorticity were included in the calculation in order to account for the effect of the flow recirculation and the rotational displacement of the fluid, respectively. The coherent structures captured in the POD modes show recirculation and they appeared to be mostly contained in the central part of the furnace. The interaction of the recirculating structures produced regions where the velocity of the fluid was increased. The number of coherent structures in the domain and their intensity decreased as the flow recedes from the burner. However, the interactions observed for the POD modes with the low number of structures showed to be more pervasive,

thus producing flow arrangements around them. In some POD modes the disposition of the coherent structures suggest the presence of large coherent structures that are intertwined and move in harmony, such as in a double helix precessing vortex core. In addition, the POD was calculated at the cross-section plane using the same composition for the snapshots recorded. It was found that the predominant structures contain recirculation in the axial direction and they originated from the flame-holder at the tip of the burner. Some of the structures observed in the POD modes at the cross-section were shown to be largely cohesive, thus extending their flow filaments into the combustion chamber. Some of the structures showed an indication of the presence of precessing vortex cores, however these were rapidly dissipated within the quarl section.

In order to obtain a temporal characterisation of the turbulent structures in the flow, the DMD was performed on the same data set employed for the POD analysis. As the snapshots contain different scalars, a multivariable DMD methodology was employed for the calculation of the dynamic modes. Furthermore, the DMD modes were sorted based on their decay/growth rate, so that the leading modes contain the most representative structures contained in the flow. The results of the DMD showed agreement with the POD, while predicting that the majority of the turbulent structures of the flow are contained in the central region of the furnace. Moreover, the decrease in the oscillatory frequency associated with the coherent structures decayed as the axial distance from the furnace increased, a characteristic inherent to the dissemination of the main vortex produced in confined swirling flows. The tangle of vortices depicted in the DMD vortices appear to reach equilibrium in a range between 100 and 200 Hz. Furthermore, the structures captured by the DMD modes appeared to be more disorganised than in the POD modes, with no clear evidence of large structures. In addition, the results obtained for the flow snapshots at the cross-section plane showed an arrangement of trailing vortices emerging from the burner and moving into the combustion chamber. These fluid structures were shown to be cohesive while in the quarl section and more prone to be disseminated as they moved further downstream. The lack of large structures in the DMD modes suggest that the coherent predicted by the POD methodology are an aggregate of the motion of the smaller vortices rather than a singular body. These small structures emerge from the burner and move within the swirling stream, where they eventually incorporate similar structures and grow. The overall flow arrangement is strongly retained, despite the presence of these vortices, with a clearly defined rotation of the flow around the furnace axis.

It can be concluded that the effect of the oxyfuel conditions in the aerodynamics of the flow in a coal combustor appeared to be low. The coherence in the analysed flows were high, as discernible patterns were recognised both in time and in space. The coherent structures captured by the methodologies employed were shown to be in the form of fluid filaments of high vorticity. These filaments emerge from the flame holder, eventually undergo shedding and later are transported within the swirling jet. As they progress within the furnace domain, they grow into bigger structures but retain the rotation around the axis of the furnace. The flow distribution caused by the combustor geometry inhibits the formation of larger structures in the near-burner region, which a desirable behaviour in order to enhance the stability of the system. Furthermore, the incorporation of the swirl component in the flow velocity allows the eventual merging of vortices which occurs downstream, thus reducing their influence in the overall flow distribution. Nevertheless, despite the enhancement of the flow stability near the burner, the effect of the larger turbulent structures downstream produce wrinkling in the flame front and potentially disruption in the flame propagation, thus requiring further analysis in order to fully comprehend their impact on the overall combustion process.

7. Conclusions and further work

This thesis has focussed on the assessment of the coherence in swirling flows and coal flames. The complexity of the reactions involved and the intrinsic dynamic nature of turbulent flows compel the development of a reliable methodology for the generation of results that are of statistical significance and can be used to accurately characterise the flow. The availability of high-definition numerical and experimental data require the need to establish techniques that can be applied to a sample of flow scalars regardless on its nature. The accurate characterisation of the swirling flow, and its effects on related phenomena, such as combustion, can be used to evaluate the performance of the system and to predict the efficiency under novel operational parameters, such as those of the oxyfuel conditions. In this thesis, a methodology for characterisation of a flow field in terms of its temporal and spatial coherence was developed. The main conclusions of this study are presented in Section 7.1, and a discussion into the suggested further work is provided in Section 7.2.

7.1. Conclusions

The application of a spiralling motion to a fluid flow triggers large-scale effects, such as an increase in the entrainment capabilities, the growth and decay of the jet and the enhancement of the transport phenomena. Swirling flows are extensively used across a wide variety of industrial applications, such as combustors, and this is due to its inherent benefits in the reaction kinetics and as a stabilisation mechanism for the produced flame. The stability in turbulent flows and flames is an ambiguous concept, and it is often related to the existence of large turbulent structures that are responsible for inducing disequilibrium. A combustor is considered to produce a stable flame if after an alteration in the input parameters does not promote the extinction or flashback of the flame into the inlet plenum. Nevertheless, the combustion phenomena is complex and dynamic in nature and therefore a methodology to quantify its transient behaviour is required

In Chapter 4, a study to characterise the dynamics of a set of swirled coal flames under air and oxyfuel conditions was presented. The study was based on high-speed videos obtained as part of an experimental campaign, from which three flame parameters, namely the perceived luminance, temperature

and oscillation severity index, were calculated. The fluctuations on the perceived luminance and in the flame temperature are among the foremost important parameters measured in combustion systems and due to the relative simplicity in the systems required for its monitoring. In industrial applications, the light emitted by the flame, quantified as the perceived luminance, and its shape are the primary mechanisms for the supervision of the system performance and they are often used by operators to judge the efficiency of the reaction. The quantification of the oscillations prescribed by such flame parameters provide an instrument to obtain significant information regarding their severity and behaviour in time.

The videos obtained in the experimental campaign were sectioned, and a portion of 40 seconds was used in order to obtain consistent results for all the cases tested, thus allowing direct comparisons. The videos were recorded at a frame rate of 200 fps and all the still frames were extracted and manipulated to produce a transient signal. The spectral analysis performed over the transient signals produced a distinguishable cluster of frequencies in the low range of the spectrum, with no further relevant frequency bands beyond 10 Hz. These results suggest that, for this case, the combustion of solid char particles entrained in the swirling flow contributes predominantly in the temporal repeatability, as they exhibit slower reaction kinetics and higher chemiluminescence than the volatile matter. The effects of the gaseous combustion were more evident at the root of the flame, a volatile-rich region, where the oscillatory behaviour was perceived as being more intense and the relevant frequencies appeared dispersed over a wider range of the frequency spectrum for the temperature measurements. Moreover, the altered environment in oxyfuel combustion produced no noticeable changes to the char burning rate, as evidenced in the uniform trend for the weighted frequency of the perceived luminance. In contrast, the oscillation in the temperatures revealed a larger effect of the oxyfuel conditions into the coal combustion process, with a trend for the weighted frequencies that is inversely proportional to the concentration of oxygen. It was found that in order to obtain a temporal coherence of the flame similar to that of the air-fired combustion, the adiabatic flame temperature and the heat transfer profile must be equalised in oxyfuel conditions. The oscillation severity index, a flame parameter that encompasses the changes of the flame front in the colour space and their corresponding standards deviations, was computed in order to account for the extent of the fluctuations in the flame parameters. The results of the

severity index indicated that for the oxycoal flames analysed, the oscillatory behaviour decreases as the oxygen concentration in the domain increases, hence becoming more steady in time. In addition, the calculation of the oscillation severity index demonstrated insensibility to the location and size of the sampled region of the flame, thus increasing its usability in larger and industrial combustion applications, where only a partial sight of the flame front is possible.

The estimation of the temporal repeatability, in conjunction with the evaluation of the oscillation magnitude of the flame parameters, contributes to a better understanding of the combustion dynamics and provides a comprehensive approach to successfully interpret the stability of a flame in terms of quantifiable criterion. The robustness of the methodology for the spectral analyses allows its implementation in flame monitoring systems. However, the dimension-reducing operations involved in the processing of the flame images impose a loss in temporal and spatial data that might be of significant relevance in the evaluation of the flame dynamics. Moreover, the sample-rate used for the data acquisition and the length of the recorded transient signals will modify the extent of the captured spectrum and the width of the frequency bands that comprises it. For the results obtained in this study, it can be concluded that the predominant source of fluctuations is the dynamics of the flow and this is manifested in a low range of the spectrum. The variations that are intrinsic to the combustion kinetics are of a faster nature and their influence will only be noticeable after an increase in the experimental sample rate of at least a hundred times. From an academic standpoint, the increase in the sample rate will yield a better representation of the flame dynamics. However, the amount of data to process will largely increase and so the time for the processing and evaluation of the results, thus reducing the usability of the methodology as a monitoring system.

The resolution of the numerical and experimental data generated for the fluid analyses have increased over time, thus allowing to develop suitable methodologies for their analysis. In Chapter 5, the highly resolved data produced by the LES computations was employed for the assessment of the coherence in a swirling flow. The case analysed was the flow distribution produced in a swirling flow apparatus constructed to resemble the conditions found in a gas combustor. The test rig was part of the Lewis Research Center in the United States, and the results published for the experimental

campaign were used to validate the numerical analysis. The CFD studies comprehended an evaluation on the size and distribution of the mesh elements that was performed over two and three-dimensional domains and that was later used in the generation of the numerical grid employed in the LES. The performance of different RANS turbulence models was compared and the realizable $k - \epsilon$ model emerged as the most stable. The results produced by the RANS models failed to accurately predict the magnitude of the velocity in the central jet and in the regions where recirculation occur while in the LES a better agreement with the experimental data was obtained. Two approaches for the computation of the SGS stresses, namely the Smagorinsky-Lilly and the Sigma models, were used in order to contrast their performance for flows under wall-bounded conditions. It was found that the region closer to the inlet plenum was greatly affected by the flow distribution imposed at the boundary and, more significantly, by the algorithm employed to induce perturbations in the inlet stream. As the flow progresses downstream, and mixing occurs, these synthetic perturbations are less significant to the overall flow arrangement.

The qualitative characterisation of the vortex, carried out by obtaining isosurfaces of the vorticity magnitude, the Q-criterion and the Lambda-2 criterion exhibited a strong dampening for the large-scale turbulent phenomena, such as the vortex breakdown and the precessing vortex core, that are associated to flow instability. Instead, the turbulent structures described by the isosurfaces consisted of small vortical entities in the form of filaments that are tightly intertwined and that move through the domain while retaining the swirling motion of the flow. These structures are often considered as precessing vortex cores themselves, however the alignment of their axes is irregular and difficult to estimate. The turbulent structures were encountered to be contained in the shear layers developed by the interaction of the swirling streams and the central jet and the outer recirculation zone.

The coherence of the flow was evaluated using three different techniques; the spectral analysis, which accounts for the coherence in time; the POD, in order to capture the spatial coherence; and the DMD, which allows the characterisation of the flow by enforcing that the results obtained remain coherent both in time and in space. The spectral analysis was performed to the transient signals obtained at 24 different locations in the domain, while for the POD and DMD analyses a data set composed of matrices, known as

snapshots, containing the instantaneous velocity components at a planar location was obtained. The spectral analysis produced significant differences for the results produced by the two SGS models employed, with the Smagorinsky-Lilly model being highly susceptible to the boundary conditions in the first two axial positions sampled. The last two axial positions revealed the diminish in the spurious oscillations, and produced frequency spectrums with weighted values in a range between 70 and 80 Hz for all the points investigated. In addition to the spectral analysis, cross-correlations of the aforementioned signals were computed in order to establish the level of disarray in the flow. The interdependence of the flow was shown to be high at the first three axial positions, with practically no lag perceived; the cross-correlations, however, showed that the flow becomes unsettled and the overall structure is lost.

The outcome of the POD provided a representation of the distribution of the predominant structures in the domain. The turbulent structures were found to be located in the shear layers for the first three axial positions of the study. In the first two positions, the POD modes predicted an arrangement of small structures with high intensity that are aligned with the rotation of the flow. Further downstream, the dominant structures develop recirculation and are scattered through the domain. The number of POD modes containing a relevant share of the total energy of the system was higher for the axial positions 2 and 3, thus recognising them as the most unsettled positions in the analysis. The path prescribed by the structures, as depicted by the principal POD modes, suggest that the majority of them are self-contained and co-exist alongside others. However, a large degree of cohesion was found for some of them, thus suggesting the displacement of larger entities.

The main drawback in POD analyses is the disregard for the temporal information contained in the set of snapshots of the flow. Consequently, the POD modes calculated are often composed of turbulent structures associated to different oscillation frequencies with their mutual influence mechanisms remaining unclear. The results obtained for the DMD showed good agreement to both the spectral analyses and the POD modes with the relevant DMD modes capturing the recirculating nature of the predominant flow structures and predicting their location in the shear layers. The associ-

ation of a frequency value to the turbulent structures allowed the demonstration of the high-frequency oscillations that influence a significantly smaller portion of the flow while the slower fluctuations dictate the motion of the whole domain. Some of the DMD modes with a high associated frequency produced vector fields in which the identification of discernible patterns was not possible and the most energetic structures were placed within the swirling jet region, thus questioning their physical nature and relevance on the overall flow arrangement.

The spatiotemporal coherence broadens the characterisation of the flow by expanding the dimension of the data employed for its calculation and provides a deep insight into the underlying mechanisms that influences the flow arrangement. The characteristic modes obtained from the DMD combined well the accuracy to recognise patterns in the flow exhibited by the POD and the temporal behaviour captured by the spectral analyses. Nevertheless, as in many methodologies of recent formulation, the results generated by the DMD should be accompanied by supporting experimental data in order to enhance the confidence in the outcome. In DMD analyses, the arrangement of the modes produced is paramount to comprehend the dynamics of the flow. This study employed an arrangement algorithm based on the growth/decay rate exhibited in each mode, however it was shown to be prone to generate modes with high associated frequencies that appear to be less coherent in space. The utilization of filters to the data might alleviate the issue; however, these must be carefully constructed specifically for each application in order to be only relevant to the noise and not to the portion of the signal that has physical relevance. In addition, the comparison of SGS models for the LES showed that perturbations imposed at the inlet boundary vastly affect the entrance region of the domain, thus advising caution while collecting data from this location. Moreover, the Smagorinsky-Lilly model appeared to be prone to induce disarrangement in the high-frequency range, thus producing coherent structures whose nature is uncertain. Finally, the assessment of the flow distribution confirmed that the dampening of the larger turbulent structures enhances the stability of the flow and is a desired state to be achieved in the designing and operation cycles of a combustor, as the overall spiralling motion of the swirl, and the benefit associated to it, are likely to be retained.

The application of the DMD to the transient data obtained by the CFD computations is relevant for the evaluation of the structures developed in the flow. In Chapter 6, the methodology developed for the assessment of the spatiotemporal coherence in swirling flows, as introduced in Chapter 5, was applied to the flow developed in a coal combustor. The geometry of the coal combustion chamber corresponds to that of the solid-fuel combustion test facility of the Pilot Advanced Capture Technology (PACT) facilities located in Sheffield, UK. The CFD studies consisted of steady state simulations for the combustion of coal under air and two different oxyfuel conditions, namely Oxy27 and Oxy30, that assumed an overall oxygen concentrations of 27 and 30 vol%. In accordance to the findings in Chapter 5, the realizable $k - \epsilon$ model with the Menter-Lechner wall functions was selected to account for the turbulent flow. The particle trajectories were estimated using an Euler-Lagrange approach and the discrete random walk approach to include the turbulent dispersion effects. A single rate was assumed for the devolatilisation of the 'El Cerrejon' coal particles, while the gaseous combustion was solved by the eddy-dissipation model with a two-step reaction mechanism. The combustion of the remnant char particles was simulated by the intrinsic model. The radiative heat transfer was accounted for by the discrete ordinate model and the gas radiative properties were estimated by the full-spectrum correlated k-distribution model. The results produced by the steady state approach showed that the heat transfer profile obtained for the air-fired condition is closely related to the Oxy30 case. In addition, the swirling motion in the flow appeared to be strongly retained under combustion conditions, with slight differences in the shape of the main vortex produced for the non-reactive case in the near-burner region.

Two isothermal LES were performed using the inlet flow rates for the air and the Oxy27 cases, respectively. The grid used in the LES was sufficiently refined to be used in reactive studies, and included a detailed representation of the gutters presented in the primary inlet channel. The qualitative characterisation of the vortices generated in the furnace, showed an array of turbulent structures emerging from the burner tip and merging downstream to form larger structures. The turbulent structures depicted in the assessment, as a result of the lower density and viscosity of the fluid, were larger than those obtained for the chamber analysed in Chapter 5. In addition,

they appeared to be mostly contained in the central region of the furnace and exhibited recirculation in their motion.

The spectral analysis of the flow in the coal combustor produced frequency spectrums that were more unsettled for the air case. Furthermore, the number of relevant oscillation frequencies in the spectrum decreased for the axial positions downstream suggesting that the overall flow oscillations found equilibrium, and this agrees with the results obtained in Chapter 5. In addition, the oscillations observed in the Oxy27 were slower than in the air case, a behaviour that appears to be related to the slower velocities reached within the furnace for this condition.

The calculation of the spatial coherence by means of the POD, employed a set of snapshots captured at three different axial locations and at the cross-section plane. The snapshots employed in the analysis were comprised of the three direction of the Cartesian coordinates system and the magnitude of the vorticity. The addition of the vorticity to the snapshots was made in order to incorporate the rotational motion of the fluid in each of the sampled locations. The coherent structures captured by the POD were of a recirculating type and appeared to be located in the central region of the furnace. The interaction of the recirculating structures produced interfaces where the fluid appeared to accelerate. The number of depicted turbulent structures, and their intensity, decreased for the last two axial positions, where a more equalised flow was observed. Furthermore, evidence of the precessing vortex core was observed in some of the POD modes calculated in the axial positions and more predominantly at the cross-section. The coherent structures observed at the cross-section were originated from the burner, showed to be cohesive and long enough to reach the combustion chamber.

The DMD analysis, performed to the same data set used in the POD, showed agreement with the location of the structures developed in the flow, as most of them were placed at the centre of the furnace. In addition, the frequency associated to the most energetic DMD modes, decrease for the axial positions downstream which is a characteristic that appears to be inherent in confined swirling flows. The vortical structures observed in the DMD modes were more chaotic than what it was obtained in the POD. The DMD modes produced a tangle of small vortices with an equilibrium frequency between 100 and 200 Hz at the axial locations. In contrast, the

structures produced at the cross-section contained a wider range of frequencies, and were depicted as trailing vortices emerging from the burner. The cohesion of the turbulent structures were high while in the quarl and diminishing as they recede from the burner. The absence of large structures suggest that the regions of larger influence predicted in the POD were consequence of the aggregate on the effect of smaller turbulent structures. The overall flow structure in the combustor remained arranged around the axis of the furnace, thus producing a singular vortex.

The aerodynamics of the coal combustor appeared to suffer minor disruptions by the implementation of the oxyfuel conditions, as the coherence of the flow in both conditions remained high. The flow structures predicted in the flow produced discernible patterns both in time and in space, thus allowing to associate this values to the operational conditions in the system. The coherent structures produced by the analyses were on the form of small fluid filaments that contain large vorticity values. These filaments are produced by the effect of the flame holder in the burner in the flow. The vortices attach to the tip of the burner and eventually they shed and are transported within the swirling stream into the combustion chamber. As the fluid filaments move within the swirling jet they merge with similar structures and produce larger vortices. These larger vortices are often regarded as a major cause for instabilities in combustion. However, the geometry of the coal combustor has shown to inhibit this phenomena in the near burner region, and the incorporation of the swirling component in the flow ensure that the larger structures that eventually will form are effectively transported out of their most influential region. Despite that the coal combustor produce a stable flow in the near-burner region, the effect of the large vortices in the flame front, and as consequence in the flame propagation, requires further analysis under reactive conditions.

7.2. Further work

The assessment of the spatiotemporal coherence of the flow provides a clear representation of the fundamental mechanisms involved in the arrangement of the flow and contributes in the stipulation of a more comprehensive definition for the stability in fluid flows. The flows investigated in this thesis exhibited good coherence and the results produced were conclusive to categorise them as stable. However, topic for improvement in the techniques

employed have been recognised, and suggested further research subjects based on the findings of the present work are proposed.

Although the results obtained for the spectral analysis based on the flame imaging campaign were consistent, these are highly dependent of the frame rate of the system. An increment in the speed of the camera recording is therefore advisable, however, the frequency threshold where the rapid effects of the combustion phenomena will became evident is uncertain for this case, and might be a high value in the spectrum. The increase in the sample rate will implicate a growth in the amount of data that will be required to be processed, thus reducing the pertinence of the methodology as monitoring system. The common practice to increase the sampling rate in digital cameras is to implement a sub-mapping algorithm to reduce the region captured by the sensor, thus reducing the definition of the images obtained. The effect of the image resolution will be noticeable in the averaging operations and will influence the computation of the frequency spectrum. A study of the influence of the image resolution for the high-intensity regions, such as in the flame front, has not been reported and is consequently advised. In addition, the evaluation of instabilities linked to the geometry and peripheral systems of the combustion chamber, such as resonations, motor frequencies and fuel feeding delays, will allow the reduction in the noise present in the signals and to produce cleaner frequency spectrums. Moreover, the extension of the spectral analysis techniques to different field scalars, such as the pressure fluctuations, will allow us to expand the understanding of the combustion phenomena in the chamber.

The reduced order modelling techniques employed in this thesis produced a clear representation of the structures contained in swirling flows. The standard POD methodology employed in these studies captured the spatial coherence of the flows. However, the lack of temporal information on them reduces their utilisation in the evaluation of highly-dynamic flows. The association of a discrete spectrum of frequencies constructed by realisations of the flow field has been employed to obtain a temporal representation of the POD modes. A comparison of this methodology with the estimations produced by the DMD will allow a better understanding of their differences.

In the DMD studies, the dynamic modes obtained were re-arranged based on their growth/decay rate, thus representing their contribution to the dynamics of the system. Nevertheless, some of the modes predicted as predominant contained high-frequency values but low spatial coherence. This instabilities appeared to be produced numerically, thus complicating their association to the fluid structures depicted in the other modes. The utilisation of a different sorting algorithm will alleviate this issue, however, there is no clear guidelines for this purpose and the generation of indexing procedures remain subjective. Furthermore, the effect of the noise imposed as part of the LES calculation suggest the necessity of a filtering operation to the data prior to their utilisation in the reduced order models, and this needs to be further investigated. In addition, the selection of the flow scalars contained by the snapshots is arbitrary. In this thesis, the velocity components were preferred over the derivative quantities of the flow as their physical relevance and applicability in the reduced order modelling remain unclear. An assessment of these flow variables in the POD and DMD framework is recommended in order to properly associate them to the overall fluid structure. Finally, the data size for each of the snapshots is directly proportional to the mesh size and to the number of variables sampled and these have repercussions in the amount of data to process. The compressed and sparsity-promoted DMD algorithms have been tested for image processing with promising results for a reduced data size, and their performance for highly dynamic systems is still debatable and subject to further tests.

The results produced by the LES computations were able to better predict the distributions of the flow arrangements studied. The study of the spatiotemporal coherence compel the utilisation of temporal, high resolution data in order to obtain a satisfactory representation of the flow field. The inclusion of the flame in the study of the coherence in a coal combustor will alter the size of the recirculation zone and probably supplement additional oscillatory modes to the flow. In order to incorporate the combustion reaction to the LES simulations performed in this thesis, the particle tracking procedure must be modified, as the steady state approach is not capable of accounting for the natural-occurring oscillations in the flow. In addition, the mechanism for the injection of particles into the simulated domain, often based on the mesh resolution, needs to be revised, and a correction for the net amount of particles crossing the inlet boundary must be included. Finally, the cases studied in this work corresponded to flow conditions in

which the stability of the flow was intended, for safety purposes, to be high; an analysis into more stringent aerodynamic profiles will be useful to fully comprehend the operational limit of the combustor and to reveal the viability of oxyfuel combustion under such conditions.

The successful reduction in greenhouse gas emissions is tightly related to the adoption of CCS techniques. In oxyfuel combustion, the utilisation of swirling flows is crucial in the control of pollutants and in the stabilisation the reaction. The concept of stability has been expanded into the spatio-temporal coherence of the flow, which is a definition that can be quantified and incorporated in the experimental and numerical analyses of reacting flows. The possibility to incorporate a comprehensive term for the dynamic behaviour of a combustor will play a key role in the designing and in the adoption of more efficient combustion technologies that eventually will lead to a sustained reduction in pollutants and to the mitigation of the effects associated to them.

Bibliography

[1] World Energy Council, "World Energy Resources," 2013.

[2] British Petroleum, "BP Energy Outlook 2030," British Petroleum, 2013.

[3] British Petroleum, "BP Statistical Review of World Energy," British Petroleum, 2014.

[4] British Petroleum, "BP Energy Outlook Energy 2017," 2017.

[5] EEA, "Reducing air pollution from electricity-generating large combustion plants in the European Union," European Environment Agency, 2013.

[6] IPCC, "Climate change 2014," Interngovernmental panel on climate change, 2014.

[7] Goddard Institute for Space Studies NASA, "Climate Change: Vital Signs of the Planet: Global Temperature." .

[8] D. M. Etheridge, L. P. Steele, R. L. Langenfelds, R. J. Francey, J.-M. Barnola, and V. I. Morgan, "Natural and anthropogenic changes in atmospheric CO $_2$ over the last 1000 years from air in Antarctic ice and firn," *J. Geophys. Res. Atmos.*, vol. 101, no. D2, pp. 4115–4128, Feb. 1996.

[9] NOAA Earth System Research Laboratory, "ESRL Global Monitoring Division - Global Greenhouse Gas Reference Network." .

[10] F. Möller, "On the influence of changes in the CO $_2$ concentration in air on the radiation balance of the Earth's surface and on the climate," *J. Geophys. Res.*, vol. 68, no. 13, pp. 3877–3886, Jul. 1963.

[11] IEA, "Energy and Climate Change," 2015.

[12] United Nations - Framework Convention on Climate Change, "The Paris Agreement," 2015.

[13] United Nations - Framework Convention on Climate Change, "The Paris Agreement - Status of Ratification," 2017.

[14] D. D. Toporov, *Combustion of Pulverised Coal in a Mixture of Oxygen and Recycled Flue Gas*. Elsevier, 2014.

[15] S. A. Rackley, *Carbon capture and storage*, 2nd ed. Elsevier Inc., 2017.

[16] D. Jansen, M. Gazzani, G. Manzolini, E. van Dijk, and M. Carbo, "Pre-combustion CO2 capture," *Int. J. Greenh. Gas Control*, vol. 40, pp. 167–187, Sep. 2015.

[17] B. Dutcher, M. Fan, and A. G. Russell, "Amine-Based CO2 Capture Technology Development from the Beginning of 2013—A Review," *ACS Appl. Mater. Interfaces*, vol. 7, no. 4, pp. 2137–2148, Feb. 2015.

[18] H. Herzog and D. Golomb, "Carbon capture and storage from fossil fuel use," *Encycl. energy*, vol. 1, no. 6562, pp. 277–287, 2004.

[19] A. A. Olajire, "CO2 capture and separation technologies for end-of-pipe applications – A review," *Energy*, vol. 35, no. 6, pp. 2610–2628, Jun. 2010.

[20] D. Y. C. Leung, G. Caramanna, and M. M. Maroto-Valer, "An overview of current status of carbon dioxide capture and storage technologies," *Renew. Sustain. Energy Rev.*, vol. 39, pp. 426–443, Nov. 2014.

[21] B. M. Abraham, J. G. Asbury, E. P. Lynch, and A. P. S. Teotia, "Coal-oxygen process provides CO2 for enhanced recovery," vol. 80, no. 11, 1982.

[22] L. Chen, S. Z. Yong, and A. F. Ghoniem, "Oxy-fuel combustion of pulverized coal: Characterization, fundamentals, stabilization and CFD modeling," *Prog. Energy Combust. Sci.*, vol. 38, no. 2, pp. 156–214, 2012.

[23] R. M. Davidson and S. O. Santos, *Oxyfuel combustion of pulverised coal*. IEA Clean Coal Centre London, UK, 2010.

[24] M. van der Spek, N. H. Eldrup, R. Skagestad, and A. Ramirez,

"Techno-economic Performance of State-of-the-Art Oxyfuel Technology for Low-CO2 Coal-fired Electricity Production," *Energy Procedia*, vol. 114, pp. 6432–6439, Jul. 2017.

[25] B. J. P. Buhre, L. K. Elliott, C. D. Sheng, R. P. Gupta, and T. F. Wall, "Oxy-fuel combustion technology for coal-fired power generation," *Prog. Energy Combust. Sci.*, vol. 31, no. 4, pp. 283–307, Jan. 2005.

[26] E. Croiset and K. V. Thambimuthu, "NOx and SO2 emissions from O2/CO2 recycle coal combustion," *Fuel*, vol. 80, no. 14, pp. 2117–2121, Nov. 2001.

[27] T. Wall *et al.*, "An overview on oxyfuel coal combustion—State of the art research and technology development," *Chem. Eng. Res. Des.*, vol. 87, no. 8, pp. 1003–1016, 2009.

[28] G. Scheffknecht, L. Al-Makhadmeh, U. Schnell, and J. Maier, "Oxy-fuel coal combustion—A review of the current state-of-the-art," *Int. J. Greenh. Gas Control*, vol. 5, pp. S16–S35, Jul. 2011.

[29] J. Gibbins and H. Chalmers, "Carbon capture and storage," *Energy Policy*, vol. 36, no. 12, pp. 4317–4322, Dec. 2008.

[30] N. MacDowell *et al.*, "An overview of CO2 capture technologies," *Energy Environ. Sci.*, vol. 3, no. 11, p. 1645, Oct. 2010.

[31] R. J. Reed, *North American Combustion Handbook: A Basic Reference on the Art and Science of Industrial Heating with Gaseous and Liquid Fuels*, 3rd ed. North American Mfg. Co., 1995.

[32] C. E. Baukal, R. (Robert E. . Schwartz, and John Zink Company., *The John Zink combustion handbook*. CRC Press, 2001.

[33] P. Heil, D. Toporov, H. Stadler, S. Tschunko, M. Förster, and R. Kneer, "Development of an oxycoal swirl burner operating at low O2 concentrations," *Fuel*, vol. 88, no. 7, pp. 1269–1274, Jul. 2009.

[34] N. Kimura, K. Omata, T. Kiga, S. Takano, and S. Shikisima, "The characteristics of pulverized coal combustion in O2/CO2 mixtures for

CO2 recovery," *Energy Convers. Manag.*, vol. 36, no. 6–9, pp. 805–808, Jun. 1995.

[35] T. Kiga *et al.*, "Characteristics of pulverized-coal combustion in the system of oxygen/recycled flue gas combustion," *Energy Convers. Manag.*, vol. 38, pp. S129–S134, Jan. 1997.

[36] J. M. Beer and N. A. Chigier, *Combustion aerodynamics*. Applied Science Publishers Ltd, 1972.

[37] D. Toporov *et al.*, "Detailed investigation of a pulverized fuel swirl flame in CO2/O2 atmosphere," *Combust. Flame*, vol. 155, no. 4, pp. 605–618, Dec. 2008.

[38] R. Correa da Silva, T. Kangwanpongpan, and H. J. Krautz, "Flame pattern, temperatures and stability limits of pulverized oxy-coal combustion," *Fuel*, vol. 115, pp. 507–520, Jan. 2014.

[39] C. M. Coats, "Coherent structures in combustion," *Prog. Energy Combust. Sci.*, vol. 22, no. 5, pp. 427–509, Jan. 1996.

[40] J. Smart, G. Lu, Y. Yan, and G. Riley, "Characterisation of an oxy-coal flame through digital imaging," *Combust. Flame*, vol. 157, no. 6, pp. 1132–1139, Jun. 2010.

[41] M. B. Priestley, *Spectral analysis and time series*. London: London : Academic Press, 1981, 1982.

[42] J. N. Kutz, *Data-Driven Modeling & Scientific Computation: Methods for Complex Systems & Big Data*. New York, NY, USA: Oxford University Press, Inc., 2013.

[43] C. E. Baukal, V. Y. Gershtein, and X. Li, *Computational Fluid Dynamics in Industrial Combustion*, 1st Editio. Boca Raton, FL, 2001.

[44] H. Versteeg and W. Malalasekera, *Introduction to Computational Fluid Dynamics, An : The Finite Volume Method*. Prentice Hall, 2007.

[45] Y. Fei *et al.*, "Evaluation of the potential of retrofitting a coal power plant to oxy-firing using CFD and process co-simulation," *Fuel Process.*

Technol., vol. 131, pp. 45–58, Mar. 2015.

[46] C. Yin and J. Yan, "Oxy-fuel combustion of pulverized fuels: Combustion fundamentals and modeling," *Appl. Energy*, vol. 162, pp. 742–762, Jan. 2016.

[47] P. Edge *et al.*, "Combustion modelling opportunities and challenges for oxy-coal carbon capture technology," *Chem. Eng. Res. Des.*, vol. 89, no. 9, pp. 1470–1493, Sep. 2011.

[48] P. Sagaut, *Large Eddy Simulation for Incompressible Flows: An Introduction*. Springer, 2006.

[49] H. Pitsch, "Large-eddy simulation of turbulent combustion," *Annu. Rev. Fluid Mech.*, vol. 38, no. 1, pp. 453–482, Jan. 2006.

[50] M. Rabaçal *et al.*, "Large Eddy Simulation of coal combustion in a large-scale laboratory furnace," *Proc. Combust. Inst.*, vol. 35, no. 3, pp. 3609–3617, 2015.

[51] B. M. Franchetti, F. Cavallo Marincola, S. Navarro-Martinez, and A. M. Kempf, "Large Eddy Simulation of a 100kWth swirling oxy-coal furnace," *Fuel*, vol. 181, pp. 491–502, 2016.

[52] H. C. Hottel and A. F. Sarofim, *Radiative transfer*. McGraw-Hill, 1967.

[53] C. Yin, "On gas and particle radiation in pulverized fuel combustion furnaces," *Appl. Energy*, vol. 157, pp. 554–561, Nov. 2015.

[54] C. Yin, "Effects of moisture release and radiation properties in pulverized fuel combustion: A CFD modelling study," *Fuel*, vol. 165, pp. 252–259, Feb. 2016.

[55] C. Yin and J. Yan, "Oxy-fuel combustion of pulverized fuels: Combustion fundamentals and modeling," *Appl. Energy*, vol. 162, pp. 742–762, Jan. 2016.

[56] X. Yang *et al.*, "Prediction of the radiative heat transfer in small and large scale oxy-coal furnaces," *Appl. Energy*, vol. 211, pp. 523–537,

Feb. 2018.

[57] P. J. Smith, F. Thomas H., and L. D. Smoot, "Model for pulverized coal-fired reactors," *Symp. Combust.*, vol. 18, no. 1, pp. 1285–1293, Jan. 1981.

[58] B. M. Franchetti, F. Cavallo Marincola, S. Navarro-Martinez, and A. M. Kempf, "Large Eddy simulation of a pulverised coal jet flame," *Proc. Combust. Inst.*, vol. 34, no. 2, pp. 2419–2426, Jan. 2013.

[59] J. Cai, M. Handa, and M. F. Modest, "Eulerian–Eulerian multi-fluid methods for pulverized coal flames with nongray radiation," *Combust. Flame*, vol. 162, no. 4, pp. 1550–1565, Dec. 2014.

[60] F. C. Lockwood and A. P. Salooja, "The prediction of some pulverized bituminous coal flames in a furnace," *Combust. Flame*, vol. 54, no. 1–3, pp. 23–32, Dec. 1983.

[61] B. M. Visser, J. P. Smart, W. L. Van De Kamp, and R. Weber, "Measurements and predictions of quarl zone properties of swirling pulverised coal flames," *Symp. Combust.*, vol. 23, no. 1, pp. 949–955, Jan. 1991.

[62] A. A. F. Peters and R. Weber, "Mathematical Modeling of a 2.4 MW Swirling Pulverized Coal Flame," *Combust. Sci. Technol.*, vol. 122, no. 1–6, pp. 131–182, Jan. 1997.

[63] M. Gharebaghi, R. M. A. Irons, L. Ma, M. Pourkashanian, and A. Pranzitelli, "Large eddy simulation of oxy-coal combustion in an industrial combustion test facility," *Int. J. Greenh. Gas Control*, vol. 5, pp. S100–S110, Jun. 2011.

[64] P. Edge, S. R. Gubba, L. Ma, R. Porter, M. Pourkashanian, and A. Williams, "LES modelling of air and oxy-fuel pulverised coal combustion—impact on flame properties," *Proc. Combust. Inst.*, vol. 33, no. 2, pp. 2709–2716, Jan. 2011.

[65] A. J. Black, "Oxy-fuel Combustion for Carbon Capture using Computational Fluid Dynamics," The University of Leeds, 2014.

[66] G. Olenik, O. T. Stein, and A. Kronenburg, "LES of swirl-stabilised pulverised coal combustion in IFRF furnace No. 1," *Proc. Combust. Inst.*, vol. 35, no. 3, pp. 2819–2828, 2015.

[67] M. Rabaçal *et al.*, "Large Eddy Simulation of coal combustion in a large-scale laboratory furnace," *Proc. Combust. Inst.*, vol. 35, no. 3, pp. 3609–3617, 2015.

[68] A. G. Clements *et al.*, "LES and RANS of air and oxy-coal combustion in a pilot-scale facility: Predictions of radiative heat transfer," *Fuel*, vol. 151, pp. 146–155, Feb. 2015.

[69] M. Rieth, F. Proch, M. Rabaçal, B. M. Franchetti, F. Cavallo Marincola, and A. M. Kempf, "Flamelet LES of a semi-industrial pulverized coal furnace," *Combust. Flame*, vol. 173, pp. 39–56, Nov. 2016.

[70] A. M. Eaton, L. D. Smoot, S. C. Hill, and C. N. Eatough, "Components, formulations, solutions, evaluation, and application of comprehensive combustion models," *Prog. Energy Combust. Sci.*, vol. 25, no. 4, pp. 387–436, Aug. 1999.

[71] P. J. Edge, P. J. Heggs, M. Pourkashanian, and P. L. Stephenson, "Integrated fluid dynamics-process modelling of a coal-fired power plant with carbon capture," *Appl. Therm. Eng.*, vol. 60, no. 1–2, pp. 456–464, Oct. 2013.

[72] S. Black *et al.*, "Effects of firing coal and biomass under oxy-fuel conditions in a power plant boiler using CFD modelling," *Fuel*, vol. 113, pp. 780–786, Nov. 2013.

[73] C. E. Baukal, V. Y. Gershtein, and X. Li, *Computational Fluid Dynamics in Industrial Combustion*, 1st Editio. Boca Rato, FL, 2001.

[74] T. Poinsot, *Theoretical and Numerical Combustion*, 2nd ed. Edwards, 2005.

[75] A. S. Monin, "On the nature of turbulence," *Sov. Phys. Uspekhi*, vol. 21, no. 5, pp. 429–442, May 1978.

[76] Y. C. Li, "On the True Nature of Turbulence," *Math. Intell.*, vol. 29, no. 1, pp. 45–48, Jul. 2007.

[77] Milton Van Dyke, *Van Dyke Album of Fluid Motion*, 1st Edition. The parabolic press, 1982.

[78] H. Tennekes and J. L. Lumley, *A first course in turbulence*. MIT Press, 1972.

[79] P. A. Davidson, *Turbulence : an introduction for scientists and engineers*. Oxford University Press, 2004.

[80] L. F. Richardson and P. Lynch, *Weather Prediction by Numerical Process*. Cambridge: Cambridge University Press, 2007.

[81] S. B. Pope, *Turbulent Flows*. Cambridge University Press, 2000.

[82] A. N. Kolmogorov, "The Local Structure of Turbulence in Incompressible Viscous Fluid for Very Large Reynolds Numbers," *Proc. Math. Phys. Sci.*, vol. 434, no. 1890, pp. 9–13, 1991.

[83] J. H. Ferziger, "Large Eddy Numerical Simulations of Turbulent Flows," *AIAA J.*, vol. 15, no. 9, pp. 1261–1267, 1977.

[84] J. L. Lumley and B. Khajeh-Nouri, "Computational Modeling of Turbulent Transport," *Adv. Geophys.*, vol. 18, pp. 169–192, Jan. 1975.

[85] O. Reynolds, "On the Dynamical Theory of Incompressible Viscous Fluids and the Determination of the Criterion," *Philos. Trans. R. Soc. A Math. Phys. Eng. Sci.*, vol. 186, no. 0, pp. 123–164, Jan. 1895.

[86] A. Favre, "Statistical equations of turbulent gases," *Probl. Hydrodyn. Contin. Mech.*, pp. 213–266, 1969.

[87] W. P. Jones and J. H. Whitelaw, "Calculation methods for reacting turbulent flows: A review," *Combust. Flame*, vol. 48, pp. 1–26, Jan. 1982.

[88] D. C. Wilcox, *Turbulence Modeling for CFD*, no. v. 1. DCW Industries, 2006.

[89] K. Hanjalić, *Turbulence and transport phenomena modelling and simulation*. Delft, The Netherlands: VSSD, 2006.

[90] B. Baldwin and H. Lomax, "Thin-layer approximation and algebraic model for separated turbulentflows," in *16th Aerospace Sciences Meeting*, 1978.

[91] P. Spalart and S. Allmaras, "A one-equation turbulence model for aerodynamic flows," in *30th Aerospace Sciences Meeting and Exhibit*, 1992.

[92] B. E. Launder and D. B. Spalding, *Lectures in mathematical models of turbulence*. Academic Press, 1972.

[93] B. E. Launder and D. B. Spalding, "The numerical computation of turbulent flows," *Comput. Methods Appl. Mech. Eng.*, vol. 3, no. 2, pp. 269–289, 1974.

[94] ANSYS, "ANSYS Release 17.2, Fluent Theory Guide," 2017.

[95] V. Yakhot, S. A. Orszag, S. Thangam, T. B. Gatski, and C. G. Speziale, "Development of turbulence models for shear flows by a double expansion technique," *Phys. Fluids A Fluid Dyn.*, vol. 4, no. 7, pp. 1510–1520, 1992.

[96] J. Fan, L. Qian, Y. Ma, P. Sun, and K. Cen, "Computational modeling of pulverized coal combustion processes in tangentially fired furnaces," *Chem. Eng. J.*, vol. 81, no. 1–3, pp. 261–269, Jan. 2001.

[97] R. Kurose, H. Makino, and A. Suzuki, "Numerical analysis of pulverized coal combustion characteristics using advanced low-NOx burner," *Fuel*, vol. 83, no. 6, pp. 693–703, Apr. 2004.

[98] R. I. Backreedy, L. M. Fletcher, L. Ma, M. Pourkashanian, and A. Williams, "Modelling pulverised coal combustion using a detailed coal combustion model," *Combust. Sci. Technol.*, vol. 178, no. 4, pp. 763–787, Apr. 2006.

[99] L. Chen and A. F. Ghoniem, "Simulation of Oxy-Coal Combustion in a

100 kW th Test Facility Using RANS and LES: A Validation Study," *Energy & Fuels*, vol. 26, no. 8, pp. 4783–4798, Aug. 2012.

[100] T.-H. Shih, W. W. Liou, A. Shabbir, Z. Yang, and J. Zhu, "A New K-epsilon Eddy Viscosity Model for High Reynolds Number Turbulent Flows: Model Development and Validation," NASA, 1994.

[101] S. R. Gubba *et al.*, "Numerical modelling of the co-firing of pulverised coal and straw in a 300 MWe tangentially fired boiler," *Fuel Process. Technol.*, vol. 104, pp. 181–188, Dec. 2012.

[102] J. Szuhánszki *et al.*, "Evaluation of the Performance of a Power Plant Boiler Firing Coal, Biomass and a Blend Under Oxy-fuel Conditions as a CO2 Capture Technique," *Energy Procedia*, vol. 37, pp. 1413–1422, Jan. 2013.

[103] D. C. Wilcox, "Reassessment of the scale-determining equation for advanced turbulence models," *AIAA J.*, vol. 26, no. 11, pp. 1299–1310, Nov. 1988.

[104] F. R. Menter, "Improved two-equation k-omega turbulence models for aerodynamic flows," Moffett Field, CA, United States, Oct. 1992.

[105] D. C. Wilcox, "Formulation of the k-w Turbulence Model Revisited," *AIAA J.*, vol. 46, no. 11, pp. 2823–2838, Nov. 2008.

[106] K. Hanjalic, "Second-Moment Turbulence Closures for CFD: Needs and Prospects," vol. 12, pp. 7–91, 1999.

[107] U. Piomelli, "Large-eddy simulation: achievements and challenges," *Prog. Aerosp. Sci.*, vol. 35, no. 4, pp. 335–362, May 1999.

[108] J. W. Deardorff, "A numerical study of three-dimensional turbulent channel flow at large Reynolds numbers," *J. Fluid Mech.*, vol. 41, no. 02, p. 453, Apr. 1970.

[109] S. A. Orszag and Y.-H. Pao, "Numerical Computation of Turbulent Shear Flows," *Adv. Geophys.*, vol. 18, pp. 225–236, Jan. 1975.

[110] T. S. Lund, "The use of explicit filters in large eddy simulation," *Comput. Math. with Appl.*, vol. 46, no. 4, pp. 603–616, Aug. 2003.

[111] S. T. Bose, P. Moin, and D. You, "Grid-independent large-eddy simulation using explicit filtering," *Phys. Fluids*, vol. 22, no. 10, p. 105103, Oct. 2010.

[112] C. Speziale, "Turbulence Modeling for Time-Dependent RANS and VLES: A Review," *AIAA J.*, vol. 36, no. 2, pp. 173–184, Feb. 1998.

[113] L. Marstorp, "Modelling of subgrid-scale stress and passive scalar flux in large eddy simulations of wall bounded turbulent flows," KTH Royal Iinstitute Of Technology, Stockholm, Sweden, 2008.

[114] M. Germano, "A proposal for a redefinition of the turbulent stresses in the filtered Navier–Stokes equations," *Phys. Fluids*, vol. 29, no. 7, p. 2323, Jun. 1986.

[115] C. G. Speziale, "Galilean invariance of subgrid-scale stress models in the large-eddy simulation of turbulence," *J. Fluid Mech.*, vol. 156, no. 1, p. 55, Jul. 1985.

[116] J. Smagorinsky, "General circulation experiments with the primitive equations," *Mon. Weather Rev.*, vol. 91, no. 3, pp. 99–164, Mar. 1963.

[117] D. K. Lilly, "The representation of small-scale turbulence in numerical simulation experiments," Boulder, Colorado, USA, 1966.

[118] D. K. Lilly, "On the Application of the Eddy Viscosity Concept in the Inertial Sub-range of Turbulence," Boulder, Colorado, USA, 1966.

[119] A. M. Kempf, B. J. Geurts, and J. C. Oefelein, "Error analysis of large-eddy simulation of the turbulent non-premixed sydney bluff-body flame," *Combust. Flame*, vol. 158, no. 12, pp. 2408–2419, Dec. 2011.

[120] E. R. Van Driest, "On Turbulent Flow Near a Wall," *J. Aeronaut. Sci.*, vol. 23, no. 11, pp. 1007–1011, Nov. 1956.

[121] F. Nicoud and F. Ducros, "Subgrid-Scale Stress Modelling Based on the

Square of the Velocity Gradient Tensor," *Flow, Turbul. Combust.*, vol. 62, no. 3, pp. 183–200, 1999.

[122] F. Nicoud, H. B. Toda, O. Cabrit, S. Bose, and J. Lee, "Using singular values to build a subgrid-scale model for large eddy simulations," *Phys. Fluids*, vol. 23, no. 8, p. 085106, 2011.

[123] M. Rieth, F. Proch, O. T. Stein, M. W. A. Pettit, and A. M. Kempf, "Comparison of the Sigma and Smagorinsky LES models for grid generated turbulence and a channel flow," *Comput. Fluids*, vol. 99, pp. 172–181, Jul. 2014.

[124] F. Proch and A. M. Kempf, "Modeling heat loss effects in the large eddy simulation of a model gas turbine combustor with premixed flamelet generated manifolds," *Proc. Combust. Inst.*, vol. 35, no. 3, pp. 3337–3345, Jan. 2015.

[125] A. Rittler, F. Proch, and A. M. Kempf, "LES of the Sydney piloted spray flame series with the PFGM/ATF approach and different sub-filter models," *Combust. Flame*, vol. 162, no. 4, pp. 1575–1598, Apr. 2015.

[126] S. Buhl, F. Dietzsch, C. Buhl, and C. Hasse, "Comparative study of turbulence models for scale-resolving simulations of internal combustion engine flows," *Comput. Fluids*, vol. 156, pp. 66–80, Oct. 2017.

[127] I. B. Celik, Z. N. Cehreli, and I. Yavuz, "Index of Resolution Quality for Large Eddy Simulations," *J. Fluids Eng.*, vol. 127, no. 5, pp. 949–958, Sep. 2005.

[128] S. B. Pope, "Ten questions concerning the large-eddy simulation of turbulent flows," *New J. Phys.*, vol. 6, no. 1, pp. 35–35, Mar. 2004.

[129] C. Meneveau and J. Katz, "Scale-Invariance and Turbulence Models for Large-Eddy Simulation," *Annu. Rev. Fluid Mech.*, vol. 32, no. 1, pp. 1–32, Jan. 2000.

[130] M. Klein, C. Kasten, Y. Gao, and N. Chakraborty, "A-priori direct

numerical simulation assessment of sub-grid scale stress tensor closures for turbulent premixed combustion," *Comput. Fluids*, vol. 122, pp. 1–11, Nov. 2015.

[131] F. Mathey, D. Cokljat, J.-P. Bertoglio, and E. Sergent, "Specification of LES inlet boundary condition using vortex method," 2006.

[132] F. Mathey, D. Cokljat, J. P. Bertoglio, and E. Sergent, "Assessment of the vortex method for Large Eddy Simulation inlet conditions," *Prog. Comput. Fluid Dyn. An Int. J.*, vol. 6, no. 1/2/3, p. 58, 2006.

[133] S. Benhamadouche, N. Jarrin, Y. Addad, and D. Laurence, "Synthetic turbulent inflow conditions based on a vortex method for large-eddy simulation," *Prog. Comput. Fluid Dyn. An Int. J.*, vol. 6, no. 1/2/3, p. 50, 2006.

[134] A. Smirnov, S. Shi, and I. Celik, "Random Flow Generation Technique for Large Eddy Simulations and Particle-Dynamics Modeling," *J. Fluids Eng.*, vol. 123, no. 2, p. 359, Jun. 2001.

[135] A. Kempf, M. Klein, and J. Janicka, "Efficient Generation of Initial- and Inflow-Conditions for Transient Turbulent Flows in Arbitrary Geometries," *Flow, Turbul. Combust. Former. Appl. Sci. Res.*, vol. 74, no. 1, pp. 67–84, Jan. 2005.

[136] L. D. Smoot and P. J. Smith, *Pulverized-coal combustion and gasification*. Boston, MA: Springer US, 1985.

[137] S. A. Morsi and A. J. Alexander, "An investigation of particle trajectories in two-phase flow systems," *J. Fluid Mech.*, vol. 55, no. 02, p. 193, Sep. 1972.

[138] L. L. Baxter and P. J. Smith, "Turbulent Dispersion of Particles: The STP Model," *Energy and Fuels*, vol. 7, no. 6, pp. 852–859, Nov. 1993.

[139] G. I. Taylor, "Diffusion by Continuous Movements," *Proc. London Math. Soc.*, vol. s2-20, no. 1, pp. 196–212, 1922.

[140] A. D. Gosman and E. loannides, "Aspects of Computer Simulation of Liquid-Fueled Combustors," *J. Energy*, vol. 7, no. 6, pp. 482–490, Nov.

1983.

[141] R. Khatami, C. Stivers, K. Joshi, Y. A. Levendis, and A. F. Sarofim, "Combustion behavior of single particles from three different coal ranks and from sugar cane bagasse in O2/N2 and O2/CO2 atmospheres," *Combust. Flame*, vol. 159, no. 3, pp. 1253–1271, Mar. 2012.

[142] L. Chen, S. Z. Yong, and A. F. Ghoniem, "Oxy-fuel combustion of pulverized coal: Characterization, fundamentals, stabilization and CFD modeling," *Prog. Energy Combust. Sci.*, vol. 38, no. 2, pp. 156–214, Apr. 2012.

[143] S. C. Saxena, "Devolatilization and combustion characteristics of coal particles," *Prog. Energy Combust. Sci.*, vol. 16, no. 1, pp. 55–94, Jan. 1990.

[144] P. R. Solomon, M. A. Serio, and E. M. Suuberg, "Coal pyrolysis: Experiments, kinetic rates and mechanisms," *Prog. Energy Combust. Sci.*, vol. 18, no. 2, pp. 133–220, Jan. 1992.

[145] P. R. Solomon and T. H. Fletcher, "Impact of coal pyrolysis on combustion," *Symp. Combust.*, vol. 25, no. 1, pp. 463–474, Jan. 1994.

[146] A. Williams, *Combustion and gasification of coal*. New York, NY, USA: Taylor & Francis, 2000.

[147] P. R. Solomon, T. H. Fletcher, and R. J. Pugmire, "Progress in coal pyrolysis," *Fuel*, vol. 72, no. 5, pp. 587–597, May 1993.

[148] S. Niksa and A. R. Kerstein, "FLASHCHAIN theory for rapid coal devolatilization kinetics. 1. Formulation," *Energy & Fuels*, vol. 5, no. 5, pp. 647–665, Sep. 1991.

[149] S. Niksa, "Predicting the evolution of fuel nitrogen from various coals," *Symp. Combust.*, vol. 25, no. 1, pp. 537–544, Jan. 1994.

[150] S. Niksa, "Predicting the Devolatilization Behavior of any coal from its ultimate analysis," *Combust. Flame*, vol. 100, no. 3, pp. 384–394, Feb. 1995.

[151] T. H. Fletcher, A. R. Kerstein, R. J. Pugmire, and D. M. Grant, "Chemical percolation model for devolatilization. 2. Temperature and heating rate effects on product yields," *Energy & Fuels*, vol. 4, no. 1, pp. 54–60, Jan. 1990.

[152] T. H. Fletcher, A. R. Kerstein, R. J. Pugmire, M. S. Solum, and D. M. Grant, "Chemical percolation model for devolatilization. 3. Direct use of carbon-13 NMR data to predict effects of coal type," *Energy & Fuels*, vol. 6, no. 4, pp. 414–431, Jul. 1992.

[153] T. H. Fletcher, A. R. Kerstein, R. J. Pugmire, M. Solum, and D. M. Grant, "A chemical percolation model for devolatilization: Summary," Livermore, California, 1992.

[154] T. Fletcher and D. Hardesty, "A chemical percolation model for coal devolatilization: Milestone report," May 1992.

[155] M. M. Baum and P. J. Street, "Predicting the Combustion Behaviour of Coal Particles," *Combust. Sci. Technol.*, vol. 3, no. 5, pp. 231–243, Jul. 1971.

[156] H. Kobayashi, J. B. Howard, and A. F. Sarofim, "Coal devolatilization at high temperatures," *Symp. Combust.*, vol. 16, no. 1, pp. 411–425, Jan. 1977.

[157] J. Ballester and S. Jiménez, "Kinetic parameters for the oxidation of pulverised coal as measured from drop tube tests," *Combust. Flame*, vol. 142, no. 3, pp. 210–222, Aug. 2005.

[158] M. V. Gil, J. Riaza, L. Œlvarez, C. Pevida, J. J. Pis, and F. Rubiera, "Kinetic models for the oxy-fuel combustion of coal and coal/biomass blend chars obtained in N2 and CO2 atmospheres," *Energy*, vol. 48, no. 1, pp. 510–518, Dec. 2012.

[159] R. W. Bilger, S. B. Pope, K. N. C. Bray, and J. F. Driscoll, "Paradigms in turbulent combustion research," *Proc. Combust. Inst.*, vol. 30, no. 1, pp. 21–42, Jan. 2005.

[160] K. K. Kuo, *Principles of combustion*. John Wiley, 2005.

[161] I. Glassman and R. A. Yetter, *Combustion*. Academic Press, 2008.

[162] D. Veynante and L. Vervisch, "Turbulent combustion modeling," *Prog. Energy Combust. Sci.*, vol. 28, no. 3, pp. 193–266, Mar. 2002.

[163] University of California -Berkeley, "GRI-Mech 3.0," 2018. [Online]. Available: http://www.me.berkeley.edu/gri˙mech/.

[164] S. P. Burke and T. E. W. Schumann, "Diffusion Flames," *Ind. Eng. Chem.*, vol. 20, no. 10, pp. 998–1004, Oct. 1928.

[165] D. B. Spalding, "Mixing and chemical reaction in steady confined turbulent flames," *Symp. Combust.*, vol. 13, no. 1, pp. 649–657, 1971.

[166] B. F. Magnussen and B. H. Hjertager, "On mathematical modeling of turbulent combustion with special emphasis on soot formation and combustion," *Symp. Combust.*, vol. 16, no. 1, pp. 719–729, 1977.

[167] L. Y. Hu, L. X. Zhou, and J. Zhang, "Large-Eddy Simulation of a Swirling Diffusion Flame Using a SOM SGS Combustion Model," *Numer. Heat Transf. Part B Fundam.*, Feb. 2007.

[168] L. X. Zhou, L. Y. Hu, and F. Wang, "Large-eddy simulation of turbulent combustion using different combustion models," *Fuel*, vol. 87, no. 13–14, pp. 3123–3131, Oct. 2008.

[169] A. Williams, M. Pourkashanian, and J. M. Jones, "Combustion of pulverised coal and biomass," *Prog. Energy Combust. Sci.*, vol. 27, no. 6, pp. 587–610, Jan. 2001.

[170] B. F. Magnussen, "On the structure of turbulence and a generalized eddy dissipation concept for chemical reaction in turbulent flow," American Institute of Aeronautics and Astronautics, St. Loius, Missouri, USA, 1981.

[171] I. R. Gran and B. F. Magnussen, "A Numerical Study of a Bluff-Body Stabilized Diffusion Flame. Part 2. Influence of Combustion Modeling And Finite-Rate Chemistry," *Combust. Sci. Technol.*, vol. 119, no. 1–6, pp. 191–217, Oct. 1996.

[172] C. K. Westbrook and F. L. Dryer, "Simplified Reaction Mechanisms for the Oxidation of Hydrocarbon Fuels in Flames," *Combust. Sci. Technol.*, vol. 27, no. 1–2, pp. 31–43, Dec. 1981.

[173] W. P. Jones and R. P. Lindstedt, "Global reaction schemes for hydrocarbon combustion," *Combust. Flame*, vol. 73, no. 3, pp. 233–249, Sep. 1988.

[174] J. P. Kim, U. Schnell, and G. Scheffknecht, "Comparison of Different Global Reaction Mechanisms for MILD Combustion of Natural Gas," *Combust. Sci. Technol.*, vol. 180, no. 4, pp. 565–592, Feb. 2008.

[175] A. De, E. Oldenhof, P. Sathiah, and D. Roekaerts, "Numerical Simulation of Delft-Jet-in-Hot-Coflow (DJHC) Flames Using the Eddy Dissipation Concept Model for Turbulence–Chemistry Interaction," *Flow, Turbul. Combust.*, vol. 87, no. 4, pp. 537–567, Dec. 2011.

[176] K. Cui, B. Liu, H. Zhang, Y. Wu, K. Matsumoto, and K. Takeno, "Modeling of Pulverized Coal Combustion in Turbulent Flow with the Consideration of Intermediate Reactions of Volatile Matter."

[177] Z. Chen, J. Wen, B. Xu, and S. Dembele, "Extension of the eddy dissipation concept and smoke point soot model to the LES frame for fire simulations," *Fire Saf. J.*, vol. 64, pp. 12–26, Feb. 2014.

[178] Z. Chen, J. Wen, B. Xu, and S. Dembele, "Large eddy simulation of a medium-scale methanol pool fire using the extended eddy dissipation concept," *Int. J. Heat Mass Transf.*, vol. 70, pp. 389–408, Mar. 2014.

[179] J. Floyd, A. M. Kempf, A. Kronenburg, and R. H. Ram, "A simple model for the filtered density function for passive scalar combustion LES," *Combust. Theory Model.*, vol. 13, no. 4, pp. 559–588, Aug. 2009.

[180] N. Peters, "Laminar diffusion flamelet models in non-premixed turbulent combustion," *Prog. Energy Combust. Sci.*, vol. 10, no. 3, pp. 319–339, Jan. 1984.

[181] H. Pitsch, M. Chen, and N. Peters, "Unsteady flamelet modeling of

turbulent hydrogen-air diffusion flames," *Symp. Combust.*, vol. 27, no. 1, pp. 1057–1064, Jan. 1998.

[182] J. Watanabe, T. Okazaki, K. Yamamoto, K. Kuramashi, and A. Baba, "Large-eddy simulation of pulverized coal combustion using flamelet model," *Proc. Combust. Inst.*, vol. 36, no. 2, pp. 2155–2163, Jan. 2017.

[183] X. Wen, Y. Luo, K. Luo, H. Jin, and J. Fan, "LES of pulverized coal combustion with a multi-regime flamelet model," *Fuel*, vol. 188, pp. 661–671, Jan. 2017.

[184] M. Rieth, A. G. Clements, M. Rabaçal, F. Proch, O. T. Stein, and A. M. Kempf, "Flamelet LES modeling of coal combustion with detailed devolatilization by directly coupled CPD," *Proc. Combust. Inst.*, vol. 36, no. 2, pp. 2181–2189, Jan. 2017.

[185] D. Messig, M. Vascellari, and C. Hasse, "Flame structure analysis and flamelet progress variable modelling of strained coal flames," *Combust. Theory Model.*, vol. 21, no. 4, pp. 700–721, Jul. 2017.

[186] G.-S. Liu and S. Niksa, "Coal conversion submodels for design applications at elevated pressures. Part II. Char gasification," *Prog. Energy Combust. Sci.*, vol. 30, no. 6, pp. 679–717, Jan. 2004.

[187] N. M. Laurendeau, "Heterogeneous kinetics of coal char gasification and combustion," *Prog. Energy Combust. Sci.*, vol. 4, no. 4, pp. 221–270, Jan. 1978.

[188] R. E. Mitchell, L. Ma, and B. Kim, "On the burning behavior of pulverized coal chars," *Combust. Flame*, vol. 151, no. 3, pp. 426–436, Nov. 2007.

[189] I. W. Smith, "The combustion rates of coal chars: A review," *Symp. Combust.*, vol. 19, no. 1, pp. 1045–1065, Jan. 1982.

[190] M. A. Field, "Rate of combustion of size-graded fractions of char from a low-rank coal between 1 200ﬂK and 2 000ﬂK," *Combust. Flame*, vol. 13, no. 3, pp. 237–252, Jun. 1969.

[191] I. W. Smith, "The combustion rates of coal chars: A review," *Symp. Combust.*, vol. 19, no. 1, pp. 1045–1065, Jan. 1982.

[192] O. Karlström, A. Brink, M. Hupa, and L. Tognotti, "Multivariable optimization of reaction order and kinetic parameters for high temperature oxidation of 10 bituminous coal chars," *Combust. Flame*, vol. 158, no. 10, pp. 2056–2063, Oct. 2011.

[193] I. W. Smith, "The intrinsic reactivity of carbons to oxygen," *Fuel*, vol. 57, no. 7, pp. 409–414, Jul. 1978.

[194] M. F. Modest, *Radiative Heat Transfer*. Academic Press, 2003.

[195] R. Viskanta, "Radiation heat transfer in combustion systems," *Prog. Energy Combust. Sci.*, vol. 13, no. 2, pp. 97–160, 1987.

[196] F. Lockwood C. and N. Shah G., "A new radiation solution method for incorporation in general combustion prediction procedures," *Symp. Combust.*, vol. 18, no. 1, pp. 1405–1414, 1981.

[197] W. A. Fiveland, "Discrete-Ordinates Solutions of the Radiative Transport Equation for Rectangular Enclosures," *J. Heat Transfer*, vol. 106, no. 4, p. 699, Nov. 1984.

[198] E. H. Chui and G. D. Raithby, "Computation of radiant heat transfer on a non-orthogonal mesh using the finite-volume method," *Numer. Heat Transf. Part B Fundam.*, vol. 23, no. 3, pp. 269–288, Apr. 1993.

[199] J. Y. Murthy and S. R. Mathur, "Finite Volume Method for Radiative Heat Transfer Using Unstructured Meshes," *J. Thermophys. Heat Transf.*, vol. 12, no. 3, pp. 313–321, Jul. 1998.

[200] J. R. Howell, "The Monte Carlo Method in Radiative Heat Transfer," *J. Heat Transfer*, vol. 120, no. 3, p. 547, Aug. 1998.

[201] W. L. Grosshandler and S. L. P. Monteiro, "Attenuation of Thermal Radiation by Pulverized Coal and Char," *J. Heat Transfer*, vol. 104, no. 4, p. 587, Nov. 1982.

[202] L. S. Rothman *et al.*, "The HITRAN 2004 molecular spectroscopic database," *J. Quant. Spectrosc. Radiat. Transf.*, vol. 96, no. 2, pp. 139–204, Dec. 2005.

[203] L. S. Rothman *et al.*, "HITEMP, the high-temperature molecular spectroscopic database," *J. Quant. Spectrosc. Radiat. Transf.*, vol. 111, no. 15, pp. 2139–2150, Oct. 2010.

[204] M. F. Modest, "Narrow-band and full-spectrum k-distributions for radiative heat transfer—correlated-k vs. scaling approximation," *J. Quant. Spectrosc. Radiat. Transf.*, vol. 76, no. 1, pp. 69–83, Jan. 2003.

[205] D. K. Edwards and W. A. Menard, "Comparison of Models for Correlation of Total Band Absorption," *Appl. Opt.*, vol. 3, no. 5, p. 621, May 1964.

[206] C. Yin, S. Singh, and S. Sanchez Romero, "A gas radiation property model applicable to general combustion CFD and its demonstration in oxy-fuel combustion simulation," *Energy Procedia*, vol. 120, pp. 564–571, Aug. 2017.

[207] M. F. Modest, "The Weighted-Sum-of-Gray-Gases Model for Arbitrary Solution Methods in Radiative Transfer," *J. Heat Transfer*, vol. 113, no. 3, pp. 650–656, Aug. 1991.

[208] C. Yin, "Refined Weighted Sum of Gray Gases Model for Air-Fuel Combustion and Its Impacts," *Energy & Fuels*, vol. 27, no. 10, pp. 6287–6294, Oct. 2013.

[209] L. J. Dorigon, G. Duciak, R. Brittes, F. Cassol, M. Galarça, and F. H. R. França, "WSGG correlations based on HITEMP2010 for computation of thermal radiation in non-isothermal, non-homogeneous H2O/CO2 mixtures," *Int. J. Heat Mass Transf.*, vol. 64, pp. 863–873, Sep. 2013.

[210] C. Yin, L. C. R. Johansen, L. A. Rosendahl, and S. K. Kær, "New Weighted Sum of Gray Gases Model Applicable to Computational Fluid Dynamics (CFD) Modeling of Oxy−Fuel Combustion: Derivation,

Validation, and Implementation," *Energy & Fuels*, vol. 24, no. 12, pp. 6275–6282, Dec. 2010.

[211] R. Johansson, B. Leckner, K. Andersson, and F. Johnsson, "Account for variations in the H2O to CO2 molar ratio when modelling gaseous radiative heat transfer with the weighted-sum-of-grey-gases model," *Combust. Flame*, vol. 158, no. 5, pp. 893–901, May 2011.

[212] G. Krishnamoorthy, "A new weighted-sum-of-gray-gases model for oxy-combustion scenarios," *Int. J. Energy Res.*, vol. 37, no. 14, pp. 1752–1763, Nov. 2013.

[213] T. Kangwanpongpan, F. H. R. França, R. Corrêa da Silva, P. S. Schneider, and H. J. Krautz, "New correlations for the weighted-sum-of-gray-gases model in oxy-fuel conditions based on HITEMP 2010 database," *Int. J. Heat Mass Transf.*, vol. 55, no. 25–26, pp. 7419–7433, Dec. 2012.

[214] M. H. Bordbar, G. Węcel, and T. Hyppänen, "A line by line based weighted sum of gray gases model for inhomogeneous CO2–H2O mixture in oxy-fired combustion," *Combust. Flame*, vol. 161, no. 9, pp. 2435–2445, Sep. 2014.

[215] L. Pierrot, A. Soufiani, and J. Taine, "Accuracy of narrow-band and global models for radiative transfer in H2O, CO2, and H2O-CO2 mixtures at high temperature," *J. Quant. Spectrosc. Radiat. Transf.*, vol. 62, no. 5, pp. 523–548, Jul. 1999.

[216] R. Porter, F. Liu, M. Pourkashanian, A. Williams, and D. Smith, "Evaluation of solution methods for radiative heat transfer in gaseous oxy-fuel combustion environments," *J. Quant. Spectrosc. Radiat. Transf.*, vol. 111, no. 14, pp. 2084–2094, Sep. 2010.

[217] T. Kangwanpongpan, "Contribution to CFD Modeling of Lignite Oxy-fuel Combustion with Special Focus on Radiation Properties," Brandenburg University of Technology, Cottbus-Senftenberg, 2013.

[218] P. Edge, S. R. Gubba, L. Ma, R. Porter, M. Pourkashanian, and A.

Williams, "LES modelling of air and oxy-fuel pulverised coal combustion—impact on flame properties," *Proc. Combust. Inst.*, vol. 33, no. 2, pp. 2709–2716, Jan. 2011.

[219] M. F. Modest and H. Zhang, "The Full-Spectrum Correlated-k Distribution for Thermal Radiation From Molecular Gas-Particulate Mixtures," *J. Heat Transfer*, vol. 124, no. 1, pp. 30–38, Feb. 2002.

[220] S. Mazumder and M. F. Modest, "Application of the full spectrum correlated-k distribution approach to modeling non-gray radiation in combustion gases," *Combust. Flame*, vol. 129, no. 4, pp. 416–438, Jun. 2002.

[221] A. G. Clements, "Modelling mercury oxidation and radiative heat transfer in oxy-coal environments," The University of Leeds, 2016.

[222] R. Demarco, J. L. Consalvi, A. Fuentes, and S. Melis, "Assessment of radiative property models in non-gray sooting media," *Int. J. Therm. Sci.*, vol. 50, no. 9, pp. 1672–1684, Sep. 2011.

[223] J. L. Consalvi, R. Demarco, A. Fuentes, S. Melis, and J. P. Vantelon, "On the modeling of radiative heat transfer in laboratory-scale pool fires," *Fire Saf. J.*, vol. 60, pp. 73–81, Aug. 2013.

[224] A. G. Clements, R. Porter, A. Pranzitelli, and M. Pourkashanian, "Evaluation of FSK models for radiative heat transfer under oxyfuel conditions," *J. Quant. Spectrosc. Radiat. Transf.*, vol. 151, pp. 67–75, Jan. 2015.

[225] P. R. Solomon, R. M. Carangelo, P. E. Best, J. R. Markham, and D. G. Hamblen, "Analysis of particle emittance, composition, size and temperature by FT-i.r. emission/transmission spectroscopy," *Fuel*, vol. 66, no. 7, pp. 897–908, Jul. 1987.

[226] S. Manickavasagam and M. P. Menguc, "Effective optical properties of pulverized coal particles determined from FT-IR spectrometer experiments," *Energy & Fuels*, vol. 7, no. 6, pp. 860–869, Nov. 1993.

[227] M. P. Menguc and R. Viskanta, "On the Radiative Properties of

Polydispersions : A Simplified Approach," *Combust. Sci. Technol.*, vol. 44, no. 3–4, pp. 143–159, Dec. 1985.

[228] A. G. Blokh, *Heat transfer in steam boiler furnaces*. New York, NY: Hemisphere Publishing, 1987.

[229] A. A. Townsend, *The structure of turbulent shear flow*, 2nd Editio. Cambridge University Press, 1976.

[230] E. C. Ifeachor and B. W. Jervis, *Digital signal processing: A practical approach*, 2nd Editio. New Jersey: Prentice Hall, 2002.

[231] V. K. Ingle and J. G. Proakis, *Digial signal processing using MATLAB*, Interanati. Ontario, Canada, 2007.

[232] J. W. Cooley and J. W. Tukey, "An algorithm for the machine calculation of complex Fourier series," *Math. Comput.*, vol. 19, no. 90, p. 297, Apr. 1965.

[233] J. R. Buck, M. M. Daniel, and A. C. Singer, *Computer Explorations in Signals and Systems Using MATLAB*, 2nd Editio. Upper Saddle River, NJ, USA: Prentice Hall, 2002.

[234] P. Stoica and M. Randolph, *Spectral Analysis of Signals*. Upper Saddle River, NJ, USA: Prentice Hall, 2005.

[235] L. C. Berselli, *Mathematics of large eddy simulation of turbulent flows*. Berlin, Germany: Springer Berlin Heidelberg, 2006.

[236] Y. Zhiyin, "Large-eddy simulation: Past, present and the future," *Chinese J. Aeronaut.*, vol. 28, no. 1, pp. 11–24, Feb. 2015.

[237] J. Sheng, H. Meng, and R. O. Fox, "A large eddy PIV method for turbulence dissipation rate estimation," *Chem. Eng. Sci.*, vol. 55, no. 20, pp. 4423–4434, Oct. 2000.

[238] R. Gilbert and D. A. Johnson, "Evaluation of FFT-based cross-correlation algorithms for PIV in a periodic grooved channel," *Exp. Fluids*, vol. 34, no. 4, pp. 473–483, Apr. 2003.

[239] J. M. Foucaut, J. Carlier, and M. Stanislas, "PIV optimization for the study of turbulent flow using spectral analysis," *Meas. Sci. Technol.*,

vol. 15, no. 6, pp. 1046–1058, Jun. 2004.

[240] H. Schmidt and U. Schumann, "Coherent structure of the convective boundary layer derived from large-eddy simulations," *J. Fluid Mech.*, vol. 200, no. 1, p. 511, Mar. 1989.

[241] Y. Dai, T. Kobayashi, and N. Taniguchi, "Large eddy simulation of plane turbulent jet flow using a new outflow velocity boundary condition," *JSME Int. J. Ser. B*, vol. 37, no. 2, pp. 242–253, May 1994.

[242] S. Khanna and J. Brasseur, "Analysis of Monin–Obukhov similarity from large-eddy simulation," *J. Fluid Mech.*, vol. 345, pp. 251–286, 1997.

[243] H. Su, R. H. Shaw, and K. T. Paw U, "Two-point correlation analysis of neutrally stratified flow within and above a forest from large-eddy simulation," *Boundary-Layer Meteorol.*, vol. 94, no. 3, pp. 423–460, Mar. 2000.

[244] F. Rütten, W. Schröder, and M. Meinke, "Large-eddy simulation of low frequency oscillations of the Dean vortices in turbulent pipe bend flows," *Phys. Fluids*, vol. 17, no. 3, p. 035107, Mar. 2005.

[245] P. J. Schmid, "Dynamic mode decomposition of numerical and experimental data," *J. Fluid Mech.*, vol. 656, pp. 5–28, Aug. 2010.

[246] J. L. Lumley, "The structure of inhomogeneous turbulence," *Atmos. Turbul. Wave Propag.*, pp. 166–178, 1967.

[247] H. Chen, D. L. Reuss, and V. Sick, "On the use and interpretation of proper orthogonal decomposition of in-cylinder engine flows," *Meas. Sci. Technol.*, vol. 23, no. 8, p. 085302, Aug. 2012.

[248] K. Pearson, "On lines and planes of closest fit to systems of points in space," *London, Edinburgh, Dublin Philos. Mag. J. Sci.*, vol. 2, no. 11, pp. 559–572, Nov. 1901.

[249] H. Hotelling, "Analysis of a complex of statistical variables into principal components.," *J. Educ. Psychol.*, vol. 24, no. 6, pp. 417–441,

1933.

[250] Karhunen, "Zur Spektraltheorie stochastischer Prozesse," *Ann. Acad. Sci. Fenn.*, vol. 37, 1946.

[251] M. Loeve, "Funcions aleatoire de second ordre," *Comptes Rendus Acad. Sci*, p. 220, 1945.

[252] G. H. Golub, *Matrix computations*, 4th editio. Baltimore, Maryland: The Johns Hopkins University Press, 2013.

[253] L. Sirovich, "Analysis of turbulent flows by means of the empirical eigenfunctions," *Fluid Dyn. Res.*, vol. 8, no. 1–4, pp. 85–100, Oct. 1991.

[254] Y. C. Liang, H. P. Lee, S. P. Lim, W. Z. Lin, K. H. Lee, and C. G. Wu, "Proper orthogonal decomposition and its applications - Part I: Theory," *J. Sound Vib.*, vol. 252, no. 3, pp. 527–544, May 2002.

[255] G. Golub and W. Kahan, "Calculating the Singular Values and Pseudo-Inverse of a Matrix," *J. Soc. Ind. Appl. Math. Ser. B Numer. Anal.*, vol. 2, no. 2, pp. 205–224, Jan. 1965.

[256] P. A. Businger and G. H. Golub, "Algorithm 358: singular value decomposition of a complex matrix [F1, 4, 5]," *Commun. ACM*, vol. 12, no. 10, pp. 564–565, Oct. 1969.

[257] G. H. Golub and C. Reinsch, "Singular Value Decomposition and Least Squares Solutions*," *Numer. Math.*, vol. 14, pp. 403–420, 1970.

[258] N. Grosjean, L. Graftieaux, M. Michard, W. Hübner, C. Tropea, and J. Volkert, "Combining LDA and PIV for turbulence measurements in unsteady swirling flows," *Meas. Sci. Technol.*, vol. 8, no. 12, pp. 1523–1532, Dec. 1997.

[259] J. P. Bonnet *et al.*, "Collaborative testing of eddy structure identification methods in free turbulent shear flows," *Exp. Fluids*, vol. 25, no. 3, pp. 197–225, Aug. 1998.

[260] L. Graftieaux, M. Michard, and N. Grosjean, "Combining PIV, POD and vortex identification algorithms for the study of unsteady

turbulent swirling flows," *Meas. Sci. Technol.*, vol. 12, no. 9, pp. 1422–1429, Sep. 2001.

[261] P. Druault and C. Chaillou, "Use of Proper Orthogonal Decomposition for reconstructing the 3D in-cylinder mean-flow field from PIV data," *Comptes Rendus Mécanique*, vol. 335, no. 1, pp. 42–47, Jan. 2007.

[262] M. Legrand, J. Nogueira, A. Lecuona, S. Nauri, and P. A. Rodríguez, "Atmospheric low swirl burner flow characterization with stereo PIV," *Exp. Fluids*, vol. 48, no. 5, pp. 901–913, May 2010.

[263] S. Park, A. Wachsman, A. Annaswamy, A. Ghoniem, B. Pang, and K. Yu, "Experimental Study of POD-based Control for Combustion Instability Using a Linear Photodiode Array," in *42nd AIAA Aerospace Sciences Meeting and Exhibit*, 2004.

[264] J. Wäsle, A. Winkler, and T. Sattelmayer, "Spatial Coherence of the Heat Release Fluctuations in Turbulent Jet and Swirl Flames," *Flow, Turbul. Combust.*, vol. 75, no. 1–4, pp. 29–50, Dec. 2005.

[265] M. Stöhr, R. Sadanandan, and W. Meier, "Phase-resolved characterization of vortex–flame interaction in a turbulent swirl flame," *Exp. Fluids*, vol. 51, no. 4, pp. 1153–1167, Oct. 2011.

[266] M. Wierman, B. Pomeroy, T. Feldman, W. Hallum, and W. Anderson, "Application of Proper Orthogonal Decomposition to Light Intensity Measurements of Combustion Instability," in *48th AIAA/ASME/SAE/ASEE Joint Propulsion Conference & Exhibit*, 2012.

[267] A. M. Steinberg, C. M. Arndt, and W. Meier, "Parametric study of vortex structures and their dynamics in swirl-stabilized combustion," *Proc. Combust. Inst.*, vol. 34, no. 2, pp. 3117–3125, Jan. 2013.

[268] O. Choi and M. C. Lee, "Investigation into the combustion instability of synthetic natural gases using high speed flame images and their proper orthogonal decomposition," *Int. J. Hydrogen Energy*, vol. 41, no. 45, pp. 20731–20743, Dec. 2016.

[269] I. S. Anufriev, O. V. Sharypov, A. A. Dekterev, E. Y. Shadrin, and A. P. Papulov, "Study of flow structure in a four-vortex furnace model," *Thermophys. Aeromechanics*, vol. 24, no. 6, pp. 849–855, Nov. 2017.

[270] X. Lu, S. Wang, H. Sung, S. Hsieh, and V. Yang, "Large-eddy simulations of turbulent swirling flows injected into a dump chamber," *J. Fluid Mech.*, vol. 527, pp. 171–195, Mar. 2005.

[271] S. Wang, V. Yang, G. Hsiao, S. Hsieh, and H. C. Mongia, "Large-eddy simulations of gas-turbine swirl injector flow dynamics," *J. Fluid Mech.*, vol. 583, p. 99, Jul. 2007.

[272] K. K. J. Ranga Dinesh and M. P. Kirkpatrick, "Study of jet precession, recirculation and vortex breakdown in turbulent swirling jets using LES," *Comput. Fluids*, vol. 38, no. 6, pp. 1232–1242, Jun. 2009.

[273] P. Rudolf and D. Štefan, "Decomposition of the swirling flow field downstream of Francis turbine runner," *IOP Conf. Ser. Earth Environ. Sci.*, vol. 15, no. 6, p. 062008, Nov. 2012.

[274] Y. Yang and S. K. Kær, "Large-eddy simulations of the non-reactive flow in the Sydney swirl burner," *Int. J. Heat Fluid Flow*, vol. 36, pp. 47–57, Aug. 2012.

[275] M. T. Parra-Santos, V. Vuorinen, R. Perez-Dominguez, R. Szasz, and F. Castro-Ruiz, "Aerodynamic characterization of isothermal swirling flows in combustors," *Int. J. Energy Environ. Eng.*, vol. 5, no. 2–3, p. 85, Jul. 2014.

[276] P. G. Cizmas, A. Palacios, T. O'Brien, and M. Syamlal, "Proper-orthogonal decomposition of spatio-temporal patterns in fluidized beds," *Chem. Eng. Sci.*, vol. 58, no. 19, pp. 4417–4427, Oct. 2003.

[277] H.-G. Sung, "Combustion dynamics in a model lean-premixed gas turbine with a swirl stabilized injector," *J. Mech. Sci. Technol.*, vol. 21, no. 3, pp. 495–504, Mar. 2007.

[278] Y. Lang, A. Malacina, L. T. Biegler, S. Munteanu, J. I. Madsen, and S. E. Zitney, "Reduced Order Model Based on Principal Component

Analysis for Process Simulation and Optimization," *Energy & Fuels*, vol. 23, no. 3, pp. 1695–1706, Mar. 2009.

[279] K. K. J. Ranga Dinesh, K. W. Jenkins, M. P. Kirkpatrick, and W. Malalasekera, "Modelling of instabilities in turbulent swirling flames," *Fuel*, vol. 89, no. 1, pp. 10–18, Jan. 2010.

[280] R. Munipalli, X. Zhu, S. Menon, and J. Hesthaven, "Model Reduction Opportunities in Detailed Simulations of Combustion Dynamics," in *52nd Aerospace Sciences Meeting*, 2014.

[281] P. J. Schmid, "Application of the dynamic mode decomposition to experimental data," *Exp. Fluids*, vol. 50, no. 4, pp. 1123–1130, Apr. 2011.

[282] K. K. Chen, J. H. Tu, and C. W. Rowley, "Variants of dynamic mode decomposition: Boundary condition, Koopman, and Fourier analyses," *J. Nonlinear Sci.*, vol. 22, no. 6, pp. 887–915, Dec. 2012.

[283] J. L. Proctor, S. L. Brunton, and J. N. Kutz, "Dynamic mode decomposition with control," *SIAM J. Appl. Dyn. Syst.*, vol. 15, no. 1, pp. 142–161, Jan. 2016.

[284] J. N. Kutz, J. H. Tu, J. L. Proctor, and S. L. Brunton, "Compressed sensing and dynamic mode decomposition," *J. Comput. Dyn.*, vol. 2, no. 2, pp. 165–191, Dec. 2016.

[285] J. H. Tu, C. W. Rowley, D. M. Luchtenburg, S. L. Brunton, and J. N. Kutz, "On Dynamic Mode Decomposition: Theory and Applications," Nov. 2013.

[286] M. R. Jovanović, P. J. Schmid, and J. W. Nichols, "Sparsity-promoting dynamic mode decomposition," *Phys. Fluids*, vol. 26, no. 2, p. 024103, Feb. 2014.

[287] S. Lombardi, K. Bizon, A. S. Coghe, F. Cozzi, and G. Continillo, "DMD analysis of experimental PIV data of a swirled jet," in *International Colloquium on the Dynamics of Explosions and Reactive Systems*, 2015.

[288] H. Carlsson, C. Carlsson, L. Fuchs, and X. S. Bai, "Large eddy simulation and extended dynamic mode decomposition of flow-flame interaction in a lean premixed low swirl stabilized flame," *Flow, Turbul. Combust.*, vol. 93, no. 3, pp. 505–519, Oct. 2014.

[289] T. Grenga, J. F. MacArt, and M. E. Mueller, "Dynamic mode decomposition of a direct numerical simulation of a turbulent premixed planar jet flame: convergence of the modes," *Combust. Theory Model.*, vol. 22, no. 4, pp. 795–811, Jul. 2018.

[290] S. Ghosal, V. Ramanan, S. Sarkar, S. R. Chakravarthy, and S. Sarkar, "Detection and Analysis of Combustion Instability From Hi-Speed Flame Images Using Dynamic Mode Decomposition," in *ASME 2016 Dynamic Systems and Control Conference, Volume 1*, 2016, p. V001T12A005.

[291] F. Richecoeur, L. Hakim, A. Renaud, and L. Zimmer, "DMD algorithms for experimental data processing in combustion," *Proceeding 2012 Summer Progr.*, pp. 459–468, 2012.

[292] G. Kewlani, "Large eddy simulations of premixed turbulent flame dynamics : combustion modeling, validation and analysis," Massachusetts Institute of Technology, 2014.

[293] A. Abou-Taouk, S. Sadasivuni, D. Lörstad, G. Bulat, and L. E. Eriksson, "CFD analysis and application of dynamic mode decomposition for resonant-mode identification and damping in an SGT-100 DLE combustion system," *Proc. Eur. Combust. Meet.*, 2015.

[294] F. Lacombe and Y. Méry, "Mixed acoustic-entropy combustion instabilities in a model aeronautical combustor: Large eddy simulation and reduced order modeling," *J. Eng. Gas Turbines Power*, vol. 140, no. 3, p. 031506, Oct. 2017.

[295] P. Palies, R. Cheng, D. Dustin, and I. Milos, "Dynamic mode decomposition (DMD) application to premixed low swirl injector flames," in *68th Annual Meeting of the APS Division of Fluid Dynamics*, 2015.

[296] J.-F. Bourgouin, J. Moeck, D. Durox, and T. Schuller, "Sensitivity of swirling flows to small changes in the swirler geometry," *Comptes Rendus Mécanique*, vol. 341, no. 1–2, pp. 211–219, Jan. 2013.

[297] E. Motheau, F. Nicoud, and T. Poinsot, "Mixed acoustic–entropy combustion instabilities in gas turbines," *J. Fluid Mech.*, vol. 749, pp. 542–576, Jun. 2014.

[298] J. M. Quinlan and B. T. Zinn, "Transverse combustion instabilities: Modern experimental techniques and analysis," in *50th AIAA/ASME/SAE/ASEE Joint Propulsion Conference*, 2014.

[299] A. Ghani, T. Poinsot, L. Gicquel, and G. Staffelbach, "LES of longitudinal and transverse self-excited combustion instabilities in a bluff-body stabilized turbulent premixed flame," *Combust. Flame*, vol. 162, no. 11, pp. 4075–4083, Nov. 2015.

[300] C. Huang, W. E. Anderson, M. E. Harvazinski, and V. Sankaran, "Analysis of self-excited combustion instabilities using decomposition techniques," *AIAA J.*, vol. 54, no. 9, pp. 2791–2807, Sep. 2016.

[301] R. Rajasegar *et al.*, "Extended proper orthogonal decomposition (EPOD) and dynamic mode decomposition (DMD) for analysis of mesoscale burner array flame dynamics," in *2018 AIAA Aerospace Sciences Meeting*, 2018.

[302] P. Rosin, "The Laws Governing the Fineness of Powdered Coal," *J. Inst. Fuel.*, vol. 7, pp. 29–36, 1933.

[303] M. A. Habib and J. H. Whitelaw, "Velocity Characteristics of Confined Coaxial Jets With and Without Swirl," *J. Fluids Eng.*, vol. 102, no. 1, p. 47, Mar. 1980.

[304] B. V Johnson and J. C. Bennett, "Mass and Momentum Turbulent Transport Experiments with Confined Coaxial Jets," East Hartford, CT, United States, 1981.

[305] B. Johnson and R. Roback, "Mass and momentum turbulent transport experiments with confined swirling coaxial jets. I," in *20th Joint*

Propulsion Conference, 1984.

[306] Y. Huang, Y. Yan, G. Lu, and A. Reed, "On-line flicker measurement of gaseous flames by image processing and spectral analysis," *Meas. Sci. Technol.*, vol. 10, no. 8, pp. 726–733, Aug. 1999.

[307] G. Lu, G. Gilabert, and Y. Yan, "Vision based monitoring and characterisation of combustion flames," *J. Phys. Conf. Ser.*, vol. 15, no. 1, pp. 194–200, Jan. 2005.

[308] P. Molcan, G. Lu, T. Le Bris, Y. Yan, B. Taupin, and S. Caillat, "Characterisation of Biomass and Coal Co-Firing on a 3 MWth Combustion Test Facility using Flame Imaging and Gas/Ash Sampling Techniques," *Fuel*. Elsevier Science Ltd., 14-Apr-2009.

[309] L. G, Y. Y, and W. DD, "Advanced monitoring, characterisation and evaluation of gas-fired flames in a utility boiler," *J. Inst. Energy*, vol. 73, no. 494, pp. 43–49, 2000.

[310] D. Sun, G. Lu, H. Zhou, and Y. Yan, "Flame stability monitoring and characterization through digital imaging and spectral analysis," *Meas. Sci. Technol.*, vol. 22, no. 11, p. 114007, Nov. 2011.

[311] G. Lu, Y. Yan, M. Colechin, and R. Hill, "Monitoring of Oscillatory Characteristics of Pulverized Coal Flames Through Image Processing and Spectral Analysis," *IEEE Trans. Instrum. Meas.*, vol. 55, no. 1, pp. 226–231, Feb. 2006.

[312] A. González-Cencerrado, B. Peña, and A. Gil, "Coal flame characterization by means of digital image processing in a semi-industrial scale PF swirl burner," *Appl. Energy*, vol. 94, pp. 375–384, Jun. 2012.

[313] A. González-Cencerrado, A. Gil, and B. Peña, "Characterization of PF flames under different swirl conditions based on visualization systems," *Fuel*, vol. 113, pp. 798–809, Nov. 2013.

[314] N. Syred, "A review of oscillation mechanisms and the role of the precessing vortex core (PVC) in swirl combustion systems," *Prog.*

Energy Combust. Sci., vol. 32, no. 2, pp. 93–161, Jan. 2006.

[315] S. Black, J. Szuhánszki, L. Ma, D. B. Ingham, and M. Pourkashanian, "LES of a 250 kW oxy-coal burner: an investigation into flame stability," in *OCC3 Conference*, 2013.

[316] R. C. Gonzalez, R. E. Woods, and S. L. Eddins, *Digital Image Processing Using MATLAB*, 2n Edition. Upper Saddle River, NJ, USA: Prentice-Hall, Inc., 2010.

[317] G. Lu, Y. Yan, S. Cornwell, M. Whitehouse, and G. Riley, "Impact of co-firing coal and biomass on flame characteristics and stability," *Fuel*, vol. 87, no. 7, pp. 1133–1140, Jun. 2008.

[318] H. C. Hottel and F. P. Broughton, "Determination of True Temperature and Total Radiation from Luminous Gas Flames," *Ind. Eng. Chem. Anal. Ed.*, vol. 4, no. 2, pp. 166–175, Apr. 1932.

[319] F. Jorgensen and M. Zuiderwyk, "Two-colour pyrometer measurement of the temperature of individual combusting particles," *J. Phys. E Sci. Instruments J. Phys. E Sci. Instrum. J. Phys. E Sci. Instrum*, vol. 18, no. 18, 1985.

[320] G. Lu, H. C. Bheemul, and Y. Yan, "Concurrent measurements of temperature and soot concentration of pulverised coal flames," in *IMTC 2001. Proceedings of the 18th IEEE Instrumentation and Measurement Technology Conference. Rediscovering Measurement in the Age of Informatics (Cat. No.01CH 37188)*, vol. 2, pp. 1221–1226.

[321] D. Sun, G. Lu, H. Zhou, Y. Yan, and S. Liu, "Quantitative Assessment of Flame Stability Through Image Processing and Spectral Analysis," *IEEE Trans. Instrum. Meas.*, vol. 64, no. 12, pp. 3323–3333, Dec. 2015.

[322] R. C. Gonzalez and R. E. Woods, *Digital Image Processing*, 2nd ed. Boston, MA, USA: Addison-Wesley Longman Publishing Co., Inc., 2001.

[323] International Telecommunication Union, "Recommendation ITU-R BT.601-7, Studio encoding parameters of digital television for standard

4:3 and wide-screen 16:9 aspect ratios.," 2015.

[324] K. L. Cashdollar, "Three-wavelength pyrometer for measuring flame temperatures," *Appl. Opt.*, vol. 18, no. 15, p. 2595, Aug. 1979.

[325] R. D. Larrabee, "Spectral Emissivity of Tungsten†," *J. Opt. Soc. Am.*, vol. 49, no. 6, p. 619, Jun. 1959.

[326] G. Lu and Y. Yan, "Temperature Profiling of Pulverized Coal Flames Using Multicolor Pyrometric and Digital Imaging Techniques," *IEEE Trans. Instrum. Meas.*, vol. 55, no. 4, pp. 1303–1308, Aug. 2006.

[327] D. Sun, G. Lu, H. Zhou, and Y. Yan, "Flame stability monitoring and characterization through digital imaging and spectral analysis," *Meas. Sci. Technol.*, vol. 22, no. 11, p. 114007, Nov. 2011.

[328] D. Sun, G. Lu, H. Zhou, X. Li, and Y. Yan, "A simple index based quantitative assessment of flame stability," in *2013 IEEE International Conference on Imaging Systems and Techniques (IST)*, 2013, pp. 190–193.

[329] N. Otsu, "A Threshold Selection Method from Gray-Level Histograms," *IEEE Trans. Syst. Man. Cybern.*, vol. 9, no. 1, pp. 62–66, Jan. 1979.

[330] T. Wall *et al.*, "An overview on oxyfuel coal combustion—State of the art research and technology development," *Chem. Eng. Res. Des.*, vol. 87, no. 8, pp. 1003–1016, Aug. 2009.

[331] O. V. Mitrofanova, G. D. Podzorov, and I. G. Pozdeeva, "Vortex structure of swirl flows," *Int. J. Heat Mass Transf.*, vol. 65, pp. 225–234, Oct. 2013.

[332] A. K. Gupta, D. G. Lilley, and N. Syred, "Swirl flows," *Tunbridge Wells, Kent, England, Abacus Press. 1984, 488 p.*, 1984.

[333] T. Loiseleux, J. M. Chomaz, and P. Huerre, "The effect of swirl on jets and wakes: Linear instability of the Rankine vortex with axial flow," *Phys. Fluids*, vol. 10, no. 5, p. 1120, Sep. 1998.

[334] B. Guo, T. A. G. Langrish, and D. F. Fletcher, "Simulation of

Turbulent Swirl Flow in an Axisymmetric Sudden Expansion," *AIAA J.*, vol. 39, no. 1, pp. 96–102, Jan. 2001.

[335] S. Wang, V. Yang, G. Hsiao, S. Hsieh, and H. C. Mongia, "Large-eddy simulations of gas-turbine swirl injector flow dynamics," *J. Fluid Mech.*, vol. 583, p. 99, Jul. 2007.

[336] R. Mullyadzhanov, M. Hadžiabdić, and K. Hanjalić, "LES Investigation of the Hysteresis Regime in the Cold Model of a Rotating-Pipe Swirl Burner," *Flow, Turbul. Combust.*, vol. 94, no. 1, pp. 175–198, Jan. 2015.

[337] H. Zhang, C. Han, T. Ye, J. Zhang, and Y. Chen, "Large eddy simulation of unconfined turbulent swirling flow," *Sci. China Technol. Sci.*, vol. 58, no. 10, pp. 1731–1744, Oct. 2015.

[338] S. Clees, J. Lewalle, M. Frederick, and J. O'Connor, "Vortex Core Dynamics in a Swirling Jet Near Vortex Breakdown," in *2018 AIAA Aerospace Sciences Meeting*, 2018.

[339] H. E. Fiedler, "Coherent structures in turbulent flows," *Prog. Aerosp. Sci.*, vol. 25, no. 3, pp. 231–269, Jan. 1988.

[340] S. V. Pantakar and D. B. Spalding, "A calculation procedure for heat, mass and momentum transfer in three-dimensional parabolic flows," *Numer. Predict. Flow, Heat Transf. Turbul. Combust.*, pp. 54–73, Jan. 1983.

[341] F. Proch, M. W. A. Pettit, T. Ma, M. Rieth, and A. M. Kempf, "Investigations on the Effect of Different Subgrid Models on the Quality of LES Results," Springer, Cham, 2015, pp. 141–147.

[342] J. Jeong and F. Hussain, "On the identification of a vortex," *J. Fluid Mech.*, vol. 285, no. 1, p. 69, Feb. 1995.

[343] Y. Dubief and F. Delcayre, "On coherent-vortex identification in turbulence," *J. Turbul.*, vol. 1, p. N11, Jan. 2000.

[344] A. Ruggles and J. Kelman, "Unsteady vortex breakdown in an

atmospheric swirl stabilised combustor. Part 1: Chamber behaviour," *Combust. Flame*, vol. 162, no. 2, pp. 388–407, 2015.

[345] S. Panchev, *Random functions and turbulence*, 1st Editio. Pergamon Press, 1971.

[346] P. Holmes, J. L. Lumley, and G. Berkooz, *Turbulence, coherent structures, dynamical systems and symmetry*, 1st Editio. Cambridge, UK: Cambridge University Press, 1996.

[347] K. Taira *et al.*, "Modal Analysis of Fluid Flows: An Overview," *AIAA J.*, vol. 55, no. 12, pp. 4013–4041, Dec. 2017.

[348] I. Mezić, "Spectral Properties of Dynamical Systems, Model Reduction and Decompositions," *Nonlinear Dyn.*, vol. 41, no. 1–3, pp. 309–325, Aug. 2005.

[349] D. Duke, J. Soria, and D. Honnery, "An error analysis of the dynamic mode decomposition," *Exp. Fluids*, vol. 52, no. 2, pp. 529–542, Feb. 2012.

[350] N. Syred and J. M. Beér, "Combustion in swirling flows: A review," *Combust. Flame*, vol. 23, no. 2, pp. 143–201, Oct. 1974.

[351] R. Stanger *et al.*, "Oxyfuel combustion for CO2 capture in power plants," *Int. J. Greenh. Gas Control*, vol. 40, pp. 55–125, Sep. 2015.

[352] G. Gouesbet and A. Berlemont, "Eulerian and Lagrangian approaches for predicting the behaviour of discrete particles in turbulent flows," *Prog. Energy Combust. Sci.*, vol. 25, no. 2, pp. 133–159, Apr. 1999.

[353] A. Pranzitelli, A. G. Clements, A. Duncan, R. Porter, L. Ma, and M. Pourkashanian, "Development and application of a novel radiation property model for oxy-coal combustion," in *3rd Oxyfuel Combustion Conference - OCC3*, 2013.

[354] A. L. Brown and T. H. Fletcher, "Modeling soot derived from pulverized coal," 1998.

[355] L. Gallen, A. Felden, E. Riber, and B. Cuenot, "Lagrangian tracking of

soot particles in LES of gas turbines," *Proc. Combust. Inst.*, Jun. 2018.

[356] G. Berkooz, P. Holmes, and J. L. Lumley, "The proper orthogonal decomposition in the analysis of turbulent flows," *Annu. Rev. Fluid Mech*, vol. 25, pp. 539–75, 1993.

[357] C. Duwig and L. Fuchs, "Large eddy simulation of vortex breakdown/flame interaction," *Phys. Fluids*, vol. 19, no. 7, p. 075103, Jul. 2007.

[358] D. M. Markovich, S. S. Abdurakipov, L. M. Chikishev, V. M. Dulin, and K. Hanjalić, "Comparative analysis of low- and high-swirl confined flames and jets by proper orthogonal and dynamic mode decompositions," *Phys. Fluids*, vol. 26, no. 6, p. 065109, Jun. 2014.

[359] K. Oberleithner *et al.*, "Three-dimensional coherent structures in a swirling jet undergoing vortex breakdown: stability analysis and empirical mode construction," *J. Fluid Mech.*, vol. 679, pp. 383–414, Jul. 2011.